Wind Speed Preview Measurement and Estimation for Feedforward Control of Wind Turbines

by

Eric J. Simley

B.S., University of Colorado Boulder, 2010

M.S., University of Colorado Boulder, 2010

A thesis submitted to the

Faculty of the Graduate School of the

University of Colorado in partial fulfillment

of the requirements for the degree of

Doctor of Philosophy

Department of Electrical, Computer, and Energy Engineering

2015

This thesis entitled:
Wind Speed Preview Measurement and Estimation for Feedforward Control of Wind Turbines
written by Eric J. Simley
has been approved for the Department of Electrical, Computer, and Energy Engineering

Lucy Y. Pao

Dr. Patrick J. Moriarty

Date

The final copy of this thesis has been examined by the signatories, and we find that both the content and the form meet acceptable presentation standards of scholarly work in the above mentioned discipline.

Simley, Eric J. (Ph.D., Electrical Engineering)

Wind Speed Preview Measurement and Estimation for Feedforward Control of Wind Turbines

Thesis directed by Prof. Lucy Y. Pao

Wind turbines typically rely on feedback controllers to maximize power capture in below-rated conditions and regulate rotor speed during above-rated operation. However, measurements of the approaching wind provided by Light Detection and Ranging (lidar) can be used as part of a preview-based, or feedforward, control system in order to improve rotor speed regulation and reduce structural loads. But the effectiveness of preview-based control depends on how accurately lidar can measure the wind that will interact with the turbine.

In this thesis, lidar measurement error is determined using a statistical frequency-domain wind field model including wind evolution, or the change in turbulent wind speeds between the time they are measured and when they reach the turbine. Parameters of the National Renewable Energy Laboratory (NREL) 5-MW reference turbine model are used to determine measurement error for a hub-mounted circularly-scanning lidar scenario, based on commercially-available technology, designed to estimate rotor effective uniform and shear wind speed components. By combining the wind field model, lidar model, and turbine parameters, the optimal lidar scan radius and preview distance that yield the minimum mean square measurement error, as well as the resulting minimum achievable error, are found for a variety of wind conditions. With optimized scan scenarios, it is found that relatively low measurement error can be achieved, but the attainable measurement error largely depends on the wind conditions. In addition, the impact of the induction zone, the region upstream of the turbine where the approaching wind speeds are reduced, as well as turbine yaw error on measurement quality is analyzed.

In order to minimize the mean square measurement error, an optimal measurement prefilter is employed, which depends on statistics of the correlation between the preview measurements and the wind that interacts with the turbine. However, because the wind speeds encountered by the turbine

are unknown, a Kalman filter-based wind speed estimator is developed that relies on turbine sensor outputs. Using simulated lidar measurements in conjunction with wind speed estimator outputs based on aeroelastic simulations of the NREL 5-MW turbine model, it is shown how the optimal prefilter can adapt to varying degrees of measurement quality.

Dedication

To my parents Jeff and Mary Simley for their unending support and encouragement.

Acknowledgements

One of the joys of my time in graduate school has been the opportunity to work with so many talented and kind people. Foremost, I would like to extend my gratitude to Prof. Lucy Pao for guiding me through my academic journey the past five years. Without her wisdom as well as the direction and encouragement that she has provided, the research accomplishments presented in this thesis simply would not have been possible. I have learned an incredible amount from Prof. Pao about how to conduct and communicate research, and she has provided me with countless valuable opportunities. Her dedication to her students is truly remarkable.

It has been a great honor to work with Dr. Alan Wright from the National Renewable Energy Laboratory (NREL), whose leadership, support, and knowledge of wind turbine control systems were invaluable during this research. I would also like to thank the rest of my dissertation committee, Dr. Patrick Moriarty, Prof. Julie Lundquist, Prof. Jason Marden, and Prof. Scott Palo, for their time and for the valuable advice they offered regarding this research. Dr. Moriarty and Prof. Lundquist deserve special mention for their effort reviewing the first draft of this thesis.

I would like to thank Dr. Rod Frehlich, Neil Kelley, and Bonnie Jonkman for their assistance with understanding the basics of lidar, atmospheric turbulence, and the NREL design codes that were utilized during this research. Without their help, this project certainly wouldn't have got off the ground so quickly. The opportunity to work with computational fluid dynamics (CFD) data during this work greatly expanded the topics I was able to explore. I would like to extend my gratitude to Dr. Pieter Gebraad, Dr. Paul Fleming, and Dr. Matthew Churchfield from NREL for their contributions generating, providing, and explaining the CFD data used in this thesis. Many

thanks to Dr. Ned Patton from the National Center for Atmospheric Research as well for providing initial CFD data used early on during the project.

One of the most memorable periods of my research project was the ten months I spent at the Danish Technical University (DTU) Wind Energy department performing lidar field measurements as a Fulbright fellow. I am indebted to Prof. Jakob Mann and Prof. Torben Mikkelsen for hosting me during my visit and to Nikolas Angelou, Dr. Mikael Sjöholm, Anders Tegtmeier Pedersen, and the rest of the remote sensing team at DTU Wind Energy for allowing me the opportunity to work with their lidar systems and for sharing their vast knowledge of remote sensing. Additionally, my visit to Denmark was an amazing cultural experience, thanks to the welcoming environment created by all of the graduate students and postdocs at DTU.

I cannot thank Dr. David Schlipf from the University of Stuttgart enough for all of the suggestions and ideas that he gave me related to our common research interests. The path that my research followed was shaped in part by the many enlightening conversations we had throughout the years. I owe my gratitude to Fiona Dunne for the input she provided on this research, particularly related to determining when lidar measurements are beneficial in a feedforward control scenario. I have been truly fortunate to work with such a talented and friendly group of graduate students in Prof. Pao's lab. I would like to thank Jake Aho, Fiona Dunne, Dan Zalkind, Andrew Buckspan, Dr. Shervin Shajiee, Dr. Jason Laks, Dr. Hua Zhong, and all my other former and current labmates for their support, for the advice they offered, and for making graduate school such a fun experience. Additional thanks are extended to the rest of the NREL-sponsored feedforward control team that I worked with, including Prof. Kathryn Johnson, Dr. Na Wang, and Andy Scholbrock.

Special thanks go to all of my friends for their support throughout the years. To Jeff, Dan, Ellis, Sam, and so many more for all of the adventures we shared together in the mountains of Colorado when I wasn't in the lab. Hien Nguyen, thank you for always being there for me and for letting me learn from you how to successfully complete a PhD! Finally, I owe my deepest gratitude to my wonderful family, especially my Mom, Dad, and brother Kevin, for their support and encouragement. I could not have made it through this journey without them.

Contents

Chapter

Tables

Table

Figures

Figure

Chapter 1

Introduction

As one of the fastest growing sources of electricity production, wind energy generation accounted for nearly 4% of global electricity demand by the end of 2013 [1]. According to statistics provided by the Global Wind Energy Council, between 2004 and 2014 global installed wind capacity has increased nearly eightfold from approximately 48 GW to 370 GW with average annual capacity increases of 23% [2]. In the United States, wind power represented 33% of new generation capacity between 2007 and 2013, allowing the technology to meet 4.5% of the U.S.'s current electricity demand [3]. A 2008 report published by the U.S. Department of Energy proposed a roadmap for achieving 20% of the U.S.'s electricity demand using wind generation by 2030 [4]. One factor that can help reduce the cost of wind energy, facilitating the strong growth in wind generation capacity necessary to achieve such a target, is the advancement in wind turbine control technology. Advanced control systems on wind turbines can help increase power capture and decrease structural loads [5]. As wind turbines continue to grow in size, yielding large flexible rotors that encounter inhomogeneous turbulent wind inflow, advanced control systems that reduce structural loads can lower the cost of energy by decreasing operation and maintenance costs or allowing the turbine to be constructed with less material [5]. The remainder of this chapter will introduce the basics of wind turbine control, discuss recent research into control systems that utilize preview information about the wind inflow, and outline the contributions of this thesis to the advancement of such wind speed preview-based control systems.

1.1 Wind Turbine Control Background

Modern horizontal axis wind turbines are designed to operate in different control regions depending on the wind speed [5, 6]. For very low wind speeds, the available power in the wind is too low to justify operating the turbine due to turbine system losses. These very low wind speeds comprise control region 1. At the turbine's "cut-in" wind speed, the turbine begins generating power. For wind speeds between cut-in and the turbine's "rated" wind speed, referred to as region 2, the control objective is to maximize power production. At the rated wind speed, the power captured by the turbine matches the power output rating of the turbine's generator. For wind speeds above the rated wind speed, forming region 3, the control objective is to regulate the generated power to its rated value, so that the generator and other turbine components are not damaged. The power produced by a turbine can be described using the following simple formula derived using momentum theory:

$$P = \frac{1}{2}\rho A U^3 C_P\left(\lambda, \beta\right), \tag{1.1}$$

where ρ is the air density, A represents the rotor area of the turbine, U is the wind speed, and C_P is the turbine's power coefficient as a function of the tip-speed ratio λ and blade pitch angle β [7]. Tip-speed ratio is defined as the ratio between the speed of the blade tips as they rotate and the wind inflow speed U. The coefficient of power C_P determines the fraction of the available power in the wind that is extracted by the turbine rotor, and cannot exceed the theoretical Betz limit of ~ 0.59 [7].

The principle control actuators available on a typical variable-speed pitch-regulated wind turbine are the generator, which can be commanded to produce a desired torque, the blade pitch angle, which alters the rotor's aerodynamic characteristics, and the yaw motor, which is used to orient the turbine rotor into the wind direction to maximize power capture [5, 6]. In region 2, blade pitch angle is kept at the optimal value (zero degrees) and generator torque is typically controlled to sufficiently balance the aerodynamic torque to maintain the optimal tip-speed ratio, thereby maximizing C_P and producing power proportional to U^3. In region 3, the control objective

is to regulate power capture by keeping generator torque and rotor speed constant. The blade pitch angle is controlled to reduce the aerodynamic efficiency of the rotor so that C_P decreases in proportion to the inverse of U^3, maintaining constant power. When the wind speed exceeds a "cut-out" wind speed, defining the upper limit of region 3, the turbine is shut down to avoid damage to the turbine's components. During turbine operation, the yaw motor is used to track changes in wind direction, typically very slowly to avoid harmful gyroscopic forces [5].

The behavior of a turbine throughout the different control regions is illustrated in Fig. 1.1 for the National Renewable Energy Laboratory (NREL) 5-MW reference turbine model [8], which is used as the wind turbine model throughout the rest of this thesis. The power output, rotor speed, generator torque command, and blade pitch command are plotted as a function of wind speed from the NREL 5-MW reference turbine's cut-in wind speed of 3 m/s through the rated wind speed of 11.4 m/s to the cut-out wind speed of 25 m/s. The turbine signals were generated using NREL's FAST aeroelastic simulation code [9]. Note that the NREL 5-MW model's baseline control system further divides region 2 into regions 1.5, 2, and 2.5, where regions 1.5 and 2.5 are suboptimal transition regions between regions 1, 2, and 3 [8]. In region 2, generator torque is controlled to achieve the optimal tip-speed ratio of ~ 7.55. In region 3, generator torque is held constant, and blade pitch angle is controlled to regulate the rotor speed to its rated value of 12.1 RPM, maintaining the rated power output of 5 MW.

A typical wind turbine control system relies on generator speed feedback, which is related to the rotor speed through the drivetrain's gear ratio, to control generator torque and blade pitch angle, as shown in Fig. 1.2. The yaw motor, on the other hand, is typically used to correct the turbine's orientation after the yaw error, obtained from wind vane measurements on the turbine's nacelle, integrated over time exceeds a threshold [6]. In region 2, a control law is often employed whereby the generator torque command is equal to the square of the generator speed multiplied by a torque constant [5, 6]. When the torque constant is selected properly, this control law allows the rotor speed to vary such that the optimal tip-speed ratio is tracked. In region 3, generator torque is typically held constant and blade pitch angle is controlled to regulate rotor speed using

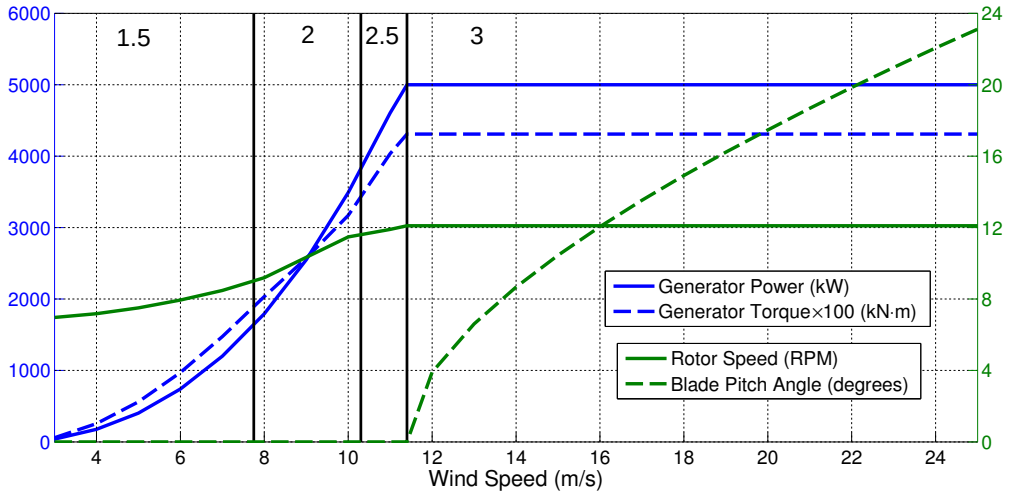

Figure 1.1: Generated power and rotor speed as well as the steady-state generator torque and blade pitch control actions throughout the operational range of the NREL 5-MW reference turbine [8] from the cut-in wind speed of 3 m/s to cut-out at 25 m/s. All signals were generated using the National Renewable Energy Laboratory's FAST code [9]. The true generator torque command is multiplied by a factor of 100 as presented. The turbine's operational range is divided into regions 1.5, 2, 2.5, and 3.

a form of proportional-integral-derivative (PID) control [5, 6]. The baseline blade pitch controller for the NREL 5-MW reference turbine uses proportional-integral (PI) control to regulate the error between the true rotor speed and the rated rotor speed of 12.1 RPM to zero as the wind speed fluctuates [8]. Thus in above-rated conditions, the wind speed acts not only as the source of power for the turbine, but also as a disturbance, due to its turbulent nature.

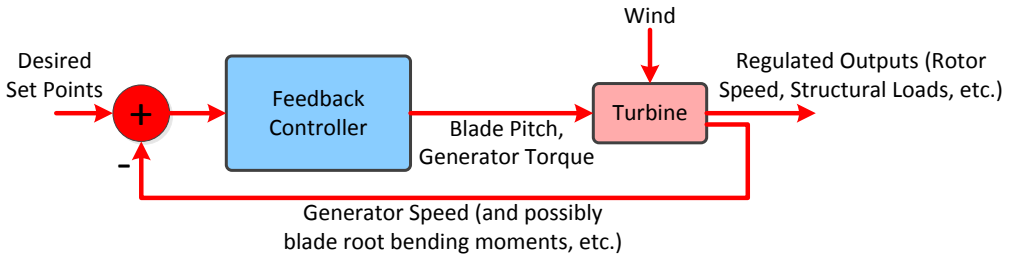

Figure 1.2: A typical wind turbine feedback control loop. Generator speed feedback is used to control generator torque in below-rated conditions (region 2) to track the optimal tip-speed ratio. Blade pitch control using generator speed feedback is employed in above-rated conditions (region 3) to regulate rotor speed to its rated value. Fluctuations in the wind speed act as a disturbance at the turbine.

Standard region 3 blade pitch control systems rely on collective pitch control. That is, assuming a three-bladed turbine such as the NREL 5-MW model, all three blades are pitched using the same command. However, as wind turbines grow larger, the wind inflow they encounter becomes less homogenous; vertical wind shear, the increase in wind speed with height caused by the atmospheric boundary layer, as well as spatially varying turbulent structures can result in the three blades encountering significantly different wind speeds as they rotate. To address these issues, a second category of blade pitch control, individual pitch control (IPC), has been explored [10, 11]. In IPC, the three blades are pitched independently to alleviate the time-varying structural loads experienced by each blade as they rotate through the wind shear and spatially varying turbulence. Measurements of bending moment loads at each blade, using sensors such as strain gauges, can be used as inputs to IPC controllers.

1.2 Preview-Based Control of Wind Turbines using Lidar

A drawback to wind turbine control based on feedback only is that the wind disturbance must first act on the turbine before a corrective control action can be made. To address this delay, feedforward control has been proposed, whereby a preview measurement of the wind disturbance is used directly as an input to the controller (see Fig. 1.3 (a)). Original work in feedforward control focused on regulating power capture in fluctuating wind conditions using preview measurements provided by an upstream meteorological tower [12]. Later, research concentrated on using Light Detection and Ranging (lidar) technology to remotely sense the wind speeds from the turbine's nacelle [13]. Lidar anemometry, which uses the Doppler shift of laser light that scatters off of aerosols in the wind to estimate wind velocities, was first demonstrated several decades ago. But only in the past decade has the cost been reduced to the point where the technology can be employed in wind turbine control applications due to the adoption of relatively inexpensive optical fiber technology from the telecommunications industry [13].

Lidar-based control has been investigated for use in both below-rated and above-rated conditions. In below-rated region 2 control, turbine-mounted lidar measurements have been proposed for

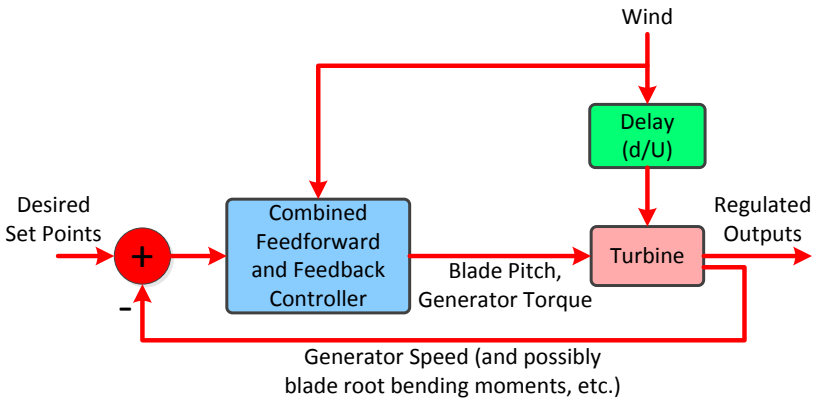

(a) Ideal feedforward control.

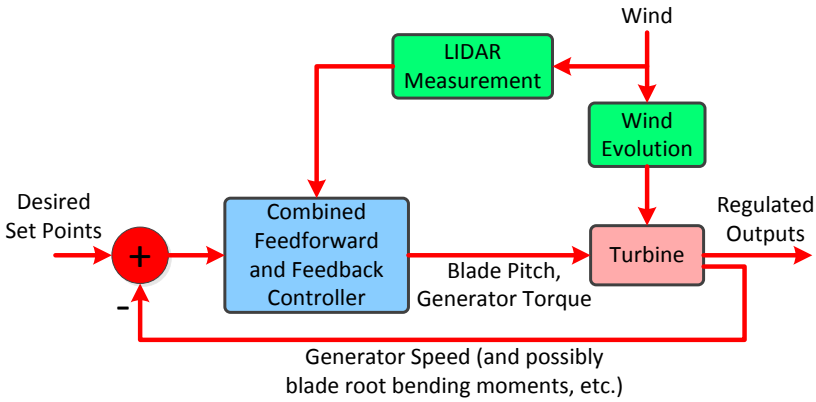

(b) Feedforward control with measurement error sources.

Figure 1.3: Combined feedforward/feedback control scenarios using wind speed preview information. (a) Ideal preview measurement scenario where the wind disturbance at the turbine is equal to the input to the controller with a delay of d/U, where d is the preview distance and U is the mean wind speed. (b) Realistic preview measurement scenario including lidar measurement errors and wind evolution effects.

correcting yaw error [14, 15, 16] and increasing power capture [14, 17, 18, 19]. Through simulation, Kragh *et al.* [15] found that a scanning lidar system can effectively estimate 10-minute average yaw error with median errors of only a few degrees regardless of mean wind speed or turbulence intensity. Recent field testing performed by Fleming *et al.* [16] showed that a bias in the yaw angle reported by the wind vane could be identified using lidar measurements. After correcting for the bias, an increase in power capture was observed, and it was estimated that annual energy production for the turbine could be increased by 2.4%. As pointed out by Bossanyi *et al.* [18] and Fleming *et al.* [16], lidars can be used to simply calibrate the turbine's yaw measurement system once, and do

not need to be employed for this purpose during the entire lifetime of the turbine. Lidar-assisted feedforward control in below-rated conditions has been shown to provide a small increase in power capture ($0.1-2\%$) through better tracking of the optimal tip-speed ratio. However, as concluded by Bossanyi *et al.* [18] the increased power and torque fluctuations caused by more aggressive tip-speed ratio tracking would likely outweigh the modest increase in power. Furthermore, Schlipf *et al.* [19] find that the additional structural loads caused by aggressively tracking the optimal tip-speed ratio make lidar-based control in region 2 unattractive.

Recently, much of the lidar preview-based control research has focused on regulating rotor speed and mitigating structural loads in region 3, where potential for significant load reduction has been shown [18], [20]–[37]. As with feedback control, lidar-assisted control in region 3 can be classified as either collective pitch or individual pitch control. Preview-based collective pitch control strategies use the lidar measurements to estimate the effective wind speed that the entire rotor will experience to regulate rotor speed and reduce loads [18, 22, 24], [29]–[33], [35, 36]. Individual blade pitch control, however, allows for reduction of the loads experienced by each separate blade, which could also be transferred to non-rotating components on the turbine [18, 21], [23]–[28], [34, 37]. As discussed in Laks *et al.* [25] and Dunne *et al.* [28], IPC controller designs can either use information from lidar measurements to estimate the wind speeds local to each individual rotating blade independently [24, 26, 34], or to estimate "non-rotating" wind quantities such as the effective collective (rotor average), linear horizontal shear, and linear vertical shear components of the wind experienced by the rotor [18, 21, 37]. An advantage of using estimates of the non-rotating collective and shear components is that it is easier to create linear time-invariant models of the turbine dynamics, that can be used for model-based control, for these disturbances than for the wind disturbances local to each blade [38]. Furthermore, simple PI controllers can be designed to reduce once-per-revolution (1P) loads caused by horizontal and vertical shear disturbances, whereas controllers that use wind measurements local to each blade must be designed to reject cyclic disturbances [18, 25]. Control systems that incorporate non-rotating wind disturbances often rely on the "multiblade coordinate transformation," explained in Bir [38], to transform the

non-rotating blade pitch commands to mitigate loads caused by the shear components into pitch commands for each specific blade.

Lidar preview-based controller designs proposed in the literature range from simple "model-inverse" feedforward controllers to more complex model predictive controllers (MPC). The simple model-inverse feedforward collective pitch controller discussed in Schlipf *et al.* [30] essentially uses a lookup table to determine the steady-state pitch angle that would result in zero rotor speed error given the preview wind speed measurement (similar to the plot of pitch angle vs. wind speed in Fig. 1.1). The preview information provided by the lidar is used to overcome the delay caused by the pitch actuator dynamics, which is typically less than 1 s [28]. Additional preview time is used to filter the lidar measurement signal to remove the components that are uncorrelated with the wind disturbance at the rotor. As shown in Schlipf *et al.* [30] and Dunne and Pao [32], better rotor speed regulation typically results in reduced structural loads as well.

More advanced controllers proposed in the literature are designed to explicitly reduce structural loads and to penalize blade pitch activity, so that rotor speed regulation and load reduction do not come at the cost of excessive pitch actuator wear. For example, $\mathcal{H}_2$ optimal controllers are designed to minimize a quadratic cost function of a vector of system variables [32, 34, 35]. The cost function used in Dunne and Pao [32] includes rotor speed error and pitch activity, the $\mathcal{H}_2$ control design in Laks *et al.* [34] also penalizes flapwise blade bending, and the design proposed in Kristalny *et al.* [35] places a penalty on the rotor thrust, so that tower oscillations will be reduced. Finally, MPC controllers that incorporate lidar-based wind preview information are designed to optimize the control actions using the predicted system dynamics over a finite horizon time [23, 27, 30, 31, 36]. In addition to minimizing a cost function to reduce structural loads and other system variables, MPC allows hard constraints to be imposed, such as pitch rate limitations or the maximum allowable rotor speed [31]. While more advanced controllers such as $\mathcal{H}_2$ and MPC designs can be formulated for any amount of preview time, Laks *et al.* [34] find that the performance of an $\mathcal{H}_2$ optimal controller saturates at a preview time of 0.5 s for simulations of a 550 kW turbine. Similarly, Bottasso *et al.* [36] discovered that a preview window of 1 s was sufficient for MPC using

simulations of a 3 MW turbine. Despite the apparent advantages of more advanced controllers, as revealed in Schlipf *et al.* [30], simple model-inverse feedforward controllers can nearly match the performance of more advanced MPC controllers, yet require a much simpler design process.

Preliminary simulation-based research on lidar-based controllers included the assumption that upstream wind speeds could be measured perfectly [20, 25, 26]). An additional assumption was that the measured wind speeds would reach the turbine unchanged after a delay time of d/U, where d is the preview distance and U is the mean wind speed (see Fig. 1.3 (a)). The next generation of lidar-based control simulations contained realistic lidar models including spatial averaging of the wind speeds along the lidar beam and the limitation to line-of-sight measurements (discussed in Chapter 4) [15, 22, 23, 24, 39]. Recently, control simulations have included models of the important source of error commonly referred to as "wind evolution" (discussed in Chapter 3) [34, 35, 36, 40]. Wind evolution describes how the wind speeds change, or evolve, as they travel downstream toward the turbine. The more realistic lidar measurement scenario including wind evolution is shown in Fig. 1.3 (b). An additional source of measurement error that has recently been included in simulation is uncertainty in the time delay for the measured wind to reach the rotor [33, 41]; Dunne *et al* [41] determine the reduction in measurement error that is possible if knowledge of the time-varying time delay is available. Many recent lidar-based control designs account for measurement error by filtering the lidar signal to remove the components of the measurement that are uncorrelated with the wind that arrives at the rotor [30, 42, 43, 44] or by including the measurement correlation directly in the optimal control derivation, as in Dunne and Pao [32].

Although the previously discussed research on lidar-based control was performed using computer simulations, recent field testing was performed at NREL's National Wind Technology Center (NWTC) to help determine whether the simulated load reductions could be realized in practice. During 2012, simple model-inverse feedforward controllers designed to regulate rotor speed were tested using nacelle-mounted lidars on NREL's 2-bladed 600 kW CART2 turbine [44] as well as the 3-bladed 550 kW CART3 turbine [43]. In both studies, the feedforward control signals were added to the baseline feedback control actions. In Schlipf *et al.* [44], the authors found that feedforward

control resulted in a rotor speed standard deviation reduction of 30% on the CART2 turbine. Scholbrock *et al.* [43] also found improved rotor speed regulation and additionally observed a decrease in tower fore-aft bending. Scholbrock *et al.* [43] point out that with the improved rotor speed regulation at low frequencies provided by feedforward control, the feedback controller could be made less aggressive by reducing its PI gains. Lower PI gains could result in less pitch activity, causing reduced structural loads on the turbine, a strategy originally proposed by Bossanyi *et al.* [18].

1.2.1 Lidar Measurement Strategies

A number of lidar systems have been developed in the past decade, both commercially and for research purposes, for use as part of preview-based control strategies. Harris *et al.* [45] performed the first turbine-mounted lidar test using a continuous-wave (CW) lidar (see Chapter 4) mounted on top of the nacelle. This lidar was simply configured to stare straight ahead into the wind and focus at a particular distance. Rettenmeier *et al.* [46] employ a customized WindCube pulsed lidar system (explained in Chapter 4) that is also mounted on top of the nacelle. The pulsed lidar provides measurements at 5 ranges along the beam between 40 m and 200 m, can sample at a rate of approximately 6 Hz, and can be aimed in any direction in front of the rotor using a mirror with two axes of motion. This pulsed lidar was used for the field tests performed on the CART2 turbine described in Schlipf *et al.* [44], where it was programmed to scan a circular pattern with a rotational period of ∼1-2 s. A lidar developed by BlueScout Technologies, that measures the wind using three fixed beam directions to estimate the horizontal wind speed and direction and vertical wind speed at three different ranges, was used for the CART3 field experiments described in Scholbrock *et al.* [43]. Mikkelsen *et al.* [47] have developed a circularly-scanning modified ZephIR CW lidar, with a 50 Hz sampling rate and a 1 s scan period configured using either a 53 m focus distance with a 30° cone angle or a 103 m focus distance with a 15° cone angle, that can be mounted in the hub, or spinner, of a turbine. This lidar placement allows for continuous measurements without periodic blockage from passing blades. A similar, but more complex, spinner lidar discussed in Sjöholm *et al.* [48] relies on two beam-redirecting prisms rotating at different speeds to measure

400 locations, distributed within the rotor disk area upstream of the turbine, every second. The information provided by such a lidar can be used to determine two-dimensional spatial structures in the wind inflow. Recently, Pedersen *et al.* [49] have tested a CW lidar mounted directly on a turbine blade with a focus distance of only 5 m, allowing for direct measurement of the local wind speed and angle-of-attack that a section of the rotating blade will experience.

1.3 Thesis Objectives and Contributions

The primary objective of the research presented in this thesis is to understand how accurately lidar can be used to provide preview measurements of the wind speed disturbances that interact with a wind turbine. This research objective was motivated by the need for more realistic analysis of preview-based wind turbine control systems to determine if improvements in load reduction are still achievable with realistic measurement errors. In general, the objectives of this research can be divided into two categories: the development of realistic lidar measurement and wind field models, which are used to determine the error between the preview wind speed measurements and the wind that arrives at the turbine, and the optimization of the lidar measurement strategy to minimize measurement error given the constraints imposed by the lidar and wind field models. The ultimate goal of this research is to show that even when accounting for realistic preview measurement error sources, through optimization of the measurement scenario and proper filtering of the preview measurement signals, relatively low measurement errors can be achieved allowing the effective use of preview-based control.

A diagram of the measurement scenario investigated in this research, including the major sources of measurement error, is provided in Fig. 1.4, where the region enclosed by the dashed line indicates the scope of the research discussed in this thesis. A lidar is used to measure the wind upstream of the turbine, yielding the measurement signal w_m. The wind that is measured by the lidar will change as it travels downstream toward the rotor, denoted by the "wind evolution" block. Error between the turbine's yaw angle and the wind direction, when unaccounted for, produces additional error between the lidar measurement and the wind encountered by the turbine. Finally,

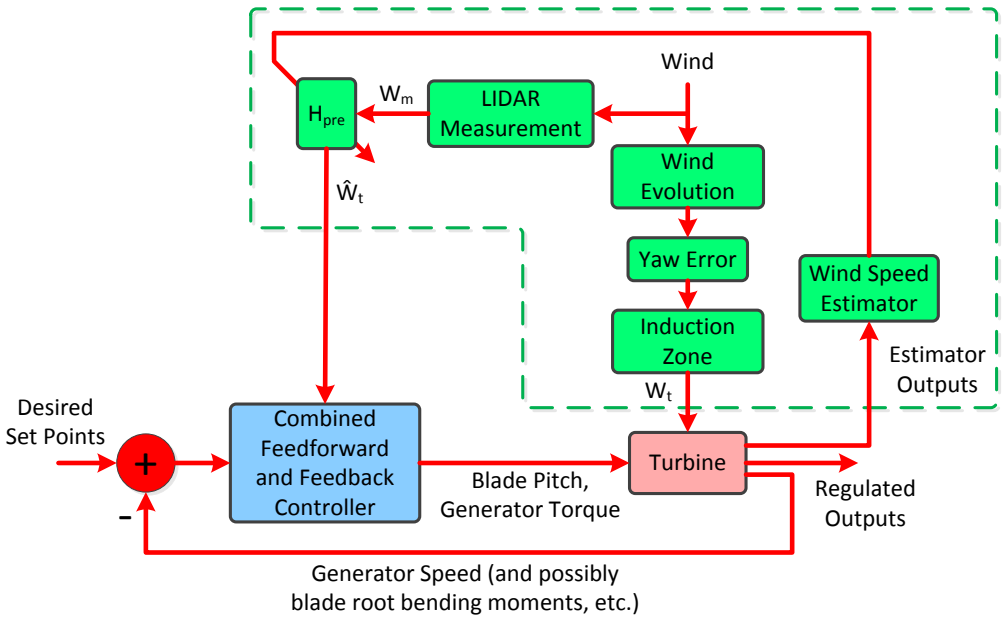

Figure 1.4: Combined feedforward/feedback control scenario including details of the preview measurement process. After the lidar measures the wind speeds in front of the wind turbine, the wind continues to be altered by wind evolution and the wind turbine's induction zone before it interacts with the rotor, where it is represented by w_t. Potential yaw error creates another source of measurement error. The lidar measurement w_m is filtered using a minimum mean square error prefilter H_{pre} which yields an estimate $\hat{w}_t$ of the wind disturbance that will arrive at the rotor, and $\hat{w}_t$ is used as an input to the feedforward controller. The prefilter transfer function adapts based on statistics of the correlation between w_m and w_t, where past values of w_t are estimated using a wind speed estimator relying on measured turbine outputs.

the induction zone, the region upstream of the turbine where the wind is influenced by the rotor, creates additional potential for alteration of the wind inflow. A significant contribution of this research is the development of methods to determine the error between w_m and the wind w_t that arrives at the turbine by incorporating the aforementioned error sources. A further contribution of this research is the design and implementation of a "prefilter" H_{pre} that is used to provide a minimum mean square error (MMSE) estimate of w_t, indicated by $\hat{w}_t$. As will be explained, the MMSE prefilter transfer function depends on statistics of the correlation between w_m and w_t. To determine the true wind disturbances that interact with the turbine, a wind speed estimator is implemented, which uses a dynamic model of the wind turbine to estimate the wind disturbances that produced the measured turbine outputs. As indicated in Fig. 1.4, information from the wind

speed estimator is therefore used to adapt the measurement prefilter.

A more detailed list of the major contributions of this thesis is provided below, where the relationship between the research and the work of other authors is explained and unique contributions are highlighted.

- A framework is provided for calculating the power spectrum of a turbine variable of interest, assuming ideal feedforward control and the use of a MMSE prefilter, as a function of measurement coherence, which describes the correlation between the lidar measurement and the true wind disturbance as a function of frequency. While the same MMSE prefilter has also been proposed by Schlipf *et al.* [44, 50], the analysis presented in this thesis shows how the filter minimizes the variance of the turbine variable of interest and how the resulting controller performance is related to the measurement coherence.

- A statistical frequency domain model of wind evolution is developed based on the behavior of turbulence simulated by researchers at NREL using computational fluid dynamics (CFD). Other wind evolution models have been proposed [51, 52], as well as applied to lidar-based control analysis [36, 40, 50], but either lack validation from realistic wind measurements or do not include a dependence on the specific wind conditions. The model developed in this thesis is a function of commonly-used wind speed and turbulence statistics and is based on realistic physics-based CFD simulations, although field measurements are still required for full validation.

- The impact of a wind turbine's upstream induction zone on wind speed preview measurement error is assessed using CFD simulation data produced by researchers at NREL. Little previous work has been performed to assess how the induction zone impacts lidar preview measurement quality aside from investigations of the mean velocity reduction upstream of the rotor [53, 54, 55]. The work in this thesis additionally reveals how wind speed direction and turbulence are altered in the induction zone along with the implications for lidar measurement quality.

- A method is developed for determining the spectra of "rotor effective" wind speed quantities, i.e., the rotor average wind speed and the effective linear horizontal and vertical shears across the rotor, by treating the rotor as three rotating blades and averaging wind speeds along each blade weighted according to the spanwise contribution to a turbine variable of interest, e.g., aerodynamic torque or the blade root bending moment. This wind speed modeling strategy is in contrast to previous work, which treats the single rotor effective wind speed as containing contributions from wind speeds over the entire rotor disk area, neglecting blade rotational effects [50, 56].

- Methods are developed for calculating the measurement coherence between a circularly-scanning lidar measurement and the wind encountered by a rotating blade, as well as the coherence between estimates of rotor effective wind quantities based on three circularly-scanning lidar measurements and the true wind quantities experienced by the rotor. The frequency-domain methods used to calculate measurement coherence are similar to the methods used in Schlipf *et al.* [50], although here the rotational effects of three discrete blades are included, and measurement coherence for the shear components is additionally investigated.

- Using the developed wind evolution model, a circularly-scanning lidar scenario (used to estimate rotor effective wind quantities) is optimized to minimize mean square measurement error. Although previous lidar scenario optimizations have been performed [50], here the dependence of the optimal scan parameters as well as the measurement error on wind conditions, such as mean wind speed and turbulence intensity, is determined. The impact of yaw error on measurement coherence is also shown.

- A wind speed estimator that uses turbine outputs to estimate the rotor effective wind disturbances is designed and implemented in simulation. Its merits and shortcomings are discussed. The developed estimator is based on Kalman filtering, which has been employed in previous wind speed estimation designs [57]–[60]. In this work, however, emphasis is

placed on designing an estimator that can accurately determine the wind speeds in the bandwidth of importance for blade pitch control applications, i.e., up to roughly 1 Hz for the NREL 5-MW reference turbine model [28, 31].

- A method for determining the MMSE H_{pre} measurement filter coefficients using statistics regarding the correlation between the lidar measurement signal w_m and the "true" wind disturbances w_t at the turbine provided by the wind speed estimator is developed. Previous lidar-assisted controller implementations used during field testing have included similar adaptive filtering components by fitting first or second-order low-pass filters to the estimated transfer function from the lidar measurement to the wind speed disturbance at the turbine [43, 44]. In the work presented here, the filters are explicitly derived to minimize mean square measurement error using time-domain statistics, while taking advantage of all of the available preview time. The necessary time that it takes for the MMSE prefilter coefficients to adapt to changing wind conditions is also analyzed.

1.4 Organization of Thesis

The remainder of the thesis is organized as follows. Chapter 2, which is based on work published in Simley and Pao [42], provides an analysis of the effectiveness of an ideal feedforward controller incorporated into a feedback control loop as a function of the preview measurement error. It is shown that for large measurement error, feedforward control can harm the system's performance. However, when a MMSE lidar measurement filter is introduced, feedforward control will always reduce the variance of an output error variable of interest as long as the preview measurement contains some correlation with the true wind disturbance. The dependence of the spectrum of a turbine output variable, and its variance, on the measurement coherence is discussed.

Motivated by the frequency-domain metric of measurement coherence, a statistical frequency-domain wind field model is presented in Chapter 3. A spatial coherence model describing wind evolution, also described in Simley and Pao [61] is presented in Section 3.2. Section 3.3, which

includes results published in Simley *et al.* [62], contains a description of a wind turbine's induction zone, i.e., the region upstream of the rotor where wind speeds are reduced. In Section 3.4 the concept of a "blade effective wind speed" is proposed, which allows the combined impact of the wind speeds encountered along the entire length of a blade to be quantified using a single wind speed value. The chapter concludes with a discussion of how rotor effective wind disturbances, including the rotor average wind speed and horizontal and vertical shear components can be calculated using the concept of blade effective wind speeds. All blade and rotor effective wind speed variables are defined using parameters of the NREL 5-MW reference turbine model [8], which is the turbine model that is assumed in all of the analyses throughout the thesis.

Chapter 4 is devoted to the lidar modeling process, where CW and pulsed lidar models based on commercially-available designs are discussed. Lidar basics, including the spatial averaging of wind speeds along the lidar beam which is inherent to the measurement process and is referred to as "range weighting," are discussed in Section 4.1. In Section 4.2, the sources of lidar measurement error that are present in the hub-mounted circularly-scanning lidar scenario investigated in this thesis are analyzed, including the limitation to line-of-sight measurements, wind evolution, range weighting, and the use of a lidar measurement to estimate blade effective wind speed. For each source of error, a derivation of the measurement coherence is included, based on methods published in Simley *et al.* [63]. Many of the error sources discussed in this chapter were originally analyzed using time-domain statistics in Simley *et al.* [39].

By combining the lidar measurement process described in Chapter 4 with the wind field model discussed in Chapter 3, a method for calculating measurement coherence for a three-beam circularly-scanning lidar scenario used to estimate the rotor average wind speed and the effective shear components is presented in Chapter 5. Section 5.1 describes measurement coherence between circularly-scanning lidar measurements and the wind encountered by a single rotating blade, based on research originally presented in Simley and Pao [64], while Section 5.2 extends this approach to the calculation of measurement coherence for rotor effective quantities using a unique lidar measurement for each blade. In Section 5.3, calculations of measurement coherence are used to optimize

the preview distance and scan radius of the lidar system to minimize measurement error. Additionally, the impacts of the induction zone and yaw error on measurement error are analyzed. Finally, Section 5.4 reveals the optimal scan parameters and achievable measurement error as a function of mean wind speed and turbulence intensity, providing useful lidar system design guidelines.

Chapter 6, based on Simley and Pao [65], describes the development and analysis of a wind speed estimator, which uses turbine sensor measurements to estimate the rotor effective wind disturbances encountered by the turbine. The correlation between the lidar measurements and the estimated wind disturbances at the turbine is used to determine the optimal MMSE prefilter coefficients so that uncorrelated components of the measurement are filtered out. A description of the developed Kalman filter-based wind speed estimator is given in Section 6.2. The performance of the estimator, evaluated using aeroelastic simulations and analyzed in the frequency domain, is presented in Section 6.4, where the impact of different aerodynamic models used in simulation is discussed. Sections 6.6 and 6.7 show how the introduction of delay in the wind speed estimator as well as the use of gain scheduling can reduce estimation error.

While much of the thesis focuses on determining lidar measurement error directly through frequency-domain analysis, Chapter 7 contains results from time-domain simulations. Section 7.1 begins the chapter by showing the measurement error resulting from simulated lidar measurements in a large-eddy simulation (LES) wind field generated by NREL, presented in Simley *et al.* [62]. The LES wind field includes the impact of the wind turbine's induction zone, allowing the measurement error caused by the induction zone to be assessed. In Section 7.2, which includes work published in Laks *et al.* [34], a method for simulating wind fields including the effects of wind evolution is described. Section 7.2.1 compares the measurement coherence obtained from time-domain simulations in evolving wind fields with the coherence calculated directly using frequency-domain techniques. An approach used to calculate the optimal measurement prefilter coefficients based on the correlation between the lidar measurement signal and the estimated wind speed disturbances at the turbine, briefly discussed in Simley and Pao [42], is presented in Section 7.3. Because some estimation time is required to determine the measurement correlation statistics used to define the

prefilter coefficients, Section 7.3.2 analyzes the effectiveness of the prefilter, in terms of the reduction in mean square measurement error, as a function of the time allowed to estimate the filter coefficients.

Concluding remarks and recommendations for future research are included in Chapter 8. Finally, an appendix is included, which describes lidar field measurements of the induction zone upstream of a 225 kW turbine performed during Spring 2014 at the Danish Technical University (DTU) Wind Energy department's Risø campus (also presented in Simley *et al.* [66]).

Chapter 2

Simplified Feedforward Control Scenario and Optimal Measurement Filtering

In this chapter, the performance of a simplified ideal feedforward control scenario is analyzed in terms of statistics describing the preview measurement quality. First, the conditions on measurement error for which ideal feedforward control provides benefit over feedback-only control are derived. Next, it is shown that by employing an optimal measurement filter, the feedforward control scenario will always improve system performance as long as the correlation between the preview measurement and the true disturbance at the turbine is non-zero and the feedforward controller contains no modeling errors. The performance of the control system is characterized by the variance of an output variable of interest, and is determined using the coherence between the preview measurement and the true disturbance, where coherence describes the correlation between the two signals as a function of frequency. The analyses presented in this chapter motivate the use of the coherence function as one of the primary metrics for preview measurement quality throughout the rest of the thesis. Practical issues related to implementing the optimal measurement filter are also discussed.

2.1 Simplified Ideal Feedforward Control

The derivation of feedforward controller performance presented in this chapter uses the combined feedforward/feedback wind turbine control scenario for above-rated operation shown in Fig. 2.1, where it is assumed that the wind turbine and controller dynamics are linear about the operating point at the mean wind speed U. Blade pitch (β) and generator torque (τ_{gen}) con-

trol loops using the feedback measurement y_{FF} regulate an output variable y (such as generator speed or power production error), which represents the deviation from a setpoint. Typically generator speed is used as the feedback measurement, but other measurements can be used for more advanced control, such as blade root bending moment measurements for individual pitch control. The feedback control loop is designed for the mean wind speed U such that any wind speed deviation acts as a disturbance w_t on the turbine plant P. The feedback control loop, where C_{FB} indicates the controller, is augmented with a blade pitch feedforward controller C_{FF} which uses the preview wind disturbance measurement w_m, provided by a lidar, to form a feedforward blade pitch command β_{FF}. As the original upstream wind w_{orig}, which is measured by the lidar, travels downstream toward the turbine it will change due to wind evolution, and potentially the other sources of distortion indicated in Fig. 1.4, until it interacts with the turbine as w_t after a delay of roughly d/U where d is the preview distance upstream of the turbine. A prefilter H_{pre} can be introduced between the lidar measurement stage and the feedforward controller to provide an estimate $\hat{w}_t$ of the wind disturbance. In this section, however, the feedforward controller is analyzed assuming perfect measurements ($w_m = w_t$) and $H_{pre} = 1$ ($\hat{w}_t = w_m$).

When feedforward is not used ($C_{FF} = 0$), the output variable y is given by

$$y = T_{yw_t} w_t, \tag{2.1}$$

where T_{yw_t} represents the closed-loop transfer function from the wind disturbance to y, indicated by the region inside of the dashed box in Fig. 2.1. With the introduction of feedforward control, y becomes a function of both w_t and w_m:

$$y = T_{yw_t} w_t + T_{y\beta_{FF}} C_{FF} w_m, \tag{2.2}$$

where $T_{y\beta_{FF}}$ represents the transfer function from the feedforward blade pitch command to y. When the measurements are perfect ($w_m = w_t$) and there is perfect plant modeling, the feedforward controller that completely cancels the effect of the disturbance w_t on the turbine is given by

$$C_{FF} = -T_{y\beta_{FF}}^{-1} T_{yw_t}, \tag{2.3}$$

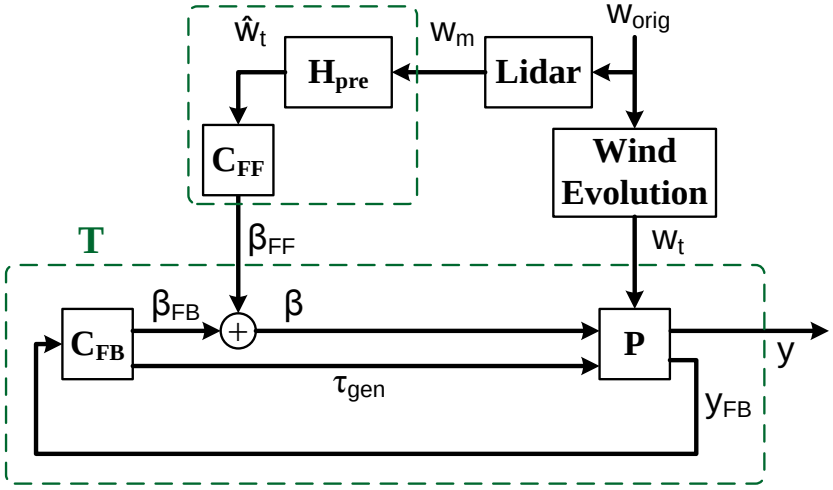

Figure 2.1: Feedforward control scenario block diagram. The dashed box encloses a blade pitch (β) and generator torque (τ_{gen}) feedback control loop where P represents the wind turbine plant and C_{FB} indicates the feedback controller. The output y represents an output error variable, which is intended to be regulated to 0. The feedforward controller is indicated by the C_{FF} block and H_{pre} is the prefilter used to form an estimate $\hat{w}_t$ of the wind disturbance w_t at the turbine based on the LIDAR measurement w_m. w_m is formed by measuring the original upstream wind speed w_{orig}, which becomes w_t after experiencing wind evolution and arriving at the turbine.

which yields the output $y = 0$ in (2.2). In reality, possible non-minimum phase zeros in $T_{y\beta_{FF}}$ can cause C_{FF} to be unstable [26]. Therefore, the ideal C_{FF} often cannot be realized and model inverse approximation techniques beyond the scope of this thesis must be used [24, 26]. Furthermore, plant modeling errors and the desire for low-order controller dynamics can prevent the implementation of the ideal feedforward controller. For the analyses in this chapter, however, it is simply assumed that $C_{FF} = -T_{y\beta_{FF}}^{-1} T_{yw_t}$. When the ideal feedforward controller is used but the preview measurements are imperfect ($w_m \neq w_t$), the output is given by

$$y = T_{yw_t} (w_t - w_m) . \tag{2.4}$$

2.1.1 Power Spectral Density, Cross-Power Spectral Density, and Coherence Definitions

Before proceeding with the feedforward control analysis for imperfect measurements, some statistical frequency domain functions that are used throughout the chapter and the rest of the

thesis are defined in this section, for both continuous-time (CT) and discrete-time (DT) variables. First, the definitions will be provided for CT variables. For wide-sense stationary (WSS) stochastic processes $a\,(t)$ and $b\,(t)$, the cross-correlation function is defined as

$$R_{ab}(t) = \lim_{T\to\infty} \frac{1}{T} \int_{-T/2}^{T/2} a(\tau + t) b^*(\tau) d\tau, \tag{2.5}$$

where t represents the time lag between the two variables and $\{\}^*$ indicates complex conjugation [67, 68]. Note that because a and b are WSS, the cross-correlation statistics depend only on the time difference between a and b and not the absolute time. When $a = b$, (2.5) yields the autocorrelation function of variable a. The cross-power spectral density (CPSD) between a and b is defined as the Fourier transform of the two variables' cross-correlation function:

$$S_{ab}\,(f) = \mathcal{F}\{R_{ab}(t)\}, \tag{2.6}$$

where the Fourier transform relating a time-domain variable $a\,(t)$ to the frequency domain variable $A\,(f)$ [68, 69], represented by the operator $\mathcal{F}\{\}$, is defined as

$$A(f) = \int_{-\infty}^{\infty} a(t) e^{-j2\pi t f} dt. \tag{2.7}$$

When $a = b$, the CPSD is equivalent to the power spectral density (PSD) $S_{aa}\,(f)$, which describes how the power contained in the signal a is distributed as a function of frequency. Finally, the magnitude-squared coherence $\gamma^2_{ab}\,(f)$ [69], which relies on CPSD and PSD functions to describe the correlation between two signals a and b as a function of frequency, is defined as

$$\gamma^2_{ab}\,(f) = \frac{|S_{ab}\,(f)|^2}{S_{aa}\,(f)\,S_{bb}\,(f)}. \tag{2.8}$$

The magnitude-squared coherence, or simply coherence, takes on values between 0 and 1 where a value of 0 indicates that a and b are completely uncorrelated at a particular frequency, while a value of 1 indicates that a and b are perfectly correlated. A coherence value of 1 does not necessarily mean that the magnitudes of the two variables are equivalent at a particular frequency, nor that their phases are aligned.

Many of the derivations presented in this thesis rely on an alternative definition of the CPSD (and therefore PSD) [69], which is given as:

$$S_{ab}(\tau) = \lim_{T\to\infty} \frac{1}{2T} \mathbf{E}\left[A_T\left(f\right) B_T^*\left(f\right)\right], \tag{2.9}$$

where $A_T\left(f\right)$ is the Fourier transform of the time-windowed signal $a_T\left(t\right)$, defined as

$$a_T(t) = \begin{cases} a(t), & \text{if } |t| \leq T \\ 0, & \text{otherwise.} \end{cases} \tag{2.10}$$

This alternative definition suggests that the CPSD between signals a and b can be estimated as the mean of the product between the Fourier transforms of finite-length samples of signals a and b, while applying the complex conjugate to the Fourier transforms of signal b. As the window length of the finite-length samples, parametrized by T, approaches infinity, the CPSD estimate converges to the true CPSD. Equation (2.9) provides a convenient definition of the CPSD because it allows $S_{ab}\left(f\right)$ to be determined completely in the frequency domain using representations of the Fourier transforms of signals a and b.

Some of the derivations presented in this thesis utilize DT representations of variables. The discrete-time analogues to the spectrum definitions for CT variables are provided here. For WSS random sequences $a\left[n\right]$ and $b\left[n\right]$, the CPSD as a function of the frequency ω in units of radians/sample [67, 68] is defined as

$$S_{ab}\left(\omega\right) = \mathcal{F}\{R_{ab}\left[n\right]\}, \tag{2.11}$$

where the DT cross-correlation function $R_{ab}\left[n\right]$ is defined as

$$R_{ab}\left[n\right] = \lim_{N\to\infty} \frac{1}{2N+1} \sum_{m=-N}^{N} a[m+n]b^*[m], \tag{2.12}$$

and the DT Fourier transform $\mathcal{F}\left\{\ \right\}$ is given by

$$A(\omega) = \sum_{n=-\infty}^{\infty} a\left[n\right] e^{-j\omega n}. \tag{2.13}$$

Note that as with the CT case, when $a = b$, (2.12) produces the DT autocorrelation function. Similar to (2.9), the CPSD can be alternatively defined [69] as

$$S_{ab}(\omega) = \lim_{N\to\infty} \frac{1}{2N+1} \mathbf{E}\left[A_N\left(\omega\right) B_N^*\left(\omega\right)\right], \tag{2.14}$$

where $A_N(\omega)$ represents the Fourier transform of the windowed DT function

$$a_N[n] = \begin{cases} a[n], & \text{if } |n| \leq N \\ 0, & \text{otherwise.} \end{cases} \tag{2.15}$$

2.1.2 Measurement Error with Imperfect Measurements

Due to the effects of the lidar measurement process, wind evolution, and other potential error sources, along with the spatial averaging of the wind caused by the area of the turbine rotor, in general $w_m \neq w_t$. Here, the variance of y will be derived in the discrete-time frequency domain using (2.4) and the property that the integral over the power spectrum of a variable is equal to its variance [67]:

$$\text{Var}(y) = \frac{1}{\pi}\int_0^\pi |T_{yw_t}(\omega)|^2 \, \mathbf{E}\left[|W_t(\omega) - W_m(\omega)|^2\right] d\omega. \tag{2.16}$$

Note that (2.16) relies on the alternative CPSD definition expressed in (2.14), where the notation indicating the limit as the window length approaches infinity is excluded for simplicity. In general, throughout the remainder of the thesis PSD and CPSD functions will be written as the expectation of the product of Fourier transforms of variables by employing (2.9) for CT signals and (2.14) for DT signals, while similarly leaving out the assumed limit as the window length approaches infinity. In the frequency domain, the mean square error (MSE) of the measurement present in (2.16), equivalent to the PSD of $w_t - w_m$, can be described as

$$\mathbf{E}\left[|W_t(\omega) - W_m(\omega)|^2\right] = S_{tt}(\omega) + S_{mm}(\omega) - 2\Re\{S_{tm}(\omega)\}, \tag{2.17}$$

where $S_{tt}(\omega)$ is the PSD of the wind disturbance w_t, $S_{mm}(\omega)$ is the PSD of the lidar measurement w_m, and $S_{tm}(\omega)$ is the CPSD between w_t and w_m. Note that (2.17) relies on the linearity property of the Fourier transform [67].

When feedforward is not used, the variance of y based on (2.1) is simply

$$\text{Var}(y) = \frac{1}{\pi}\int_0^\pi |T_{yw_t}(\omega)|^2 \, S_{tt}(\omega) \, d\omega. \tag{2.18}$$

By comparing (2.16) and (2.17) with (2.18), the frequencies where feedforward control with $\hat{w}_t = w_m$ is beneficial can be found. Feedforward control reduces the variance of y at the frequencies where

(2.19) is satisfied:

$$S_{tt}(\omega) + S_{mm}(\omega) - 2\Re\{S_{tm}(\omega)\} < S_{tt}(\omega). \tag{2.19}$$

Equation (2.19) can be rearranged into a simpler form:

$$\frac{1}{2} < \frac{\Re\{S_{tm}(\omega)\}}{S_{mm}(\omega)}. \tag{2.20}$$

2.2 Optimal Feedforward Controller for Imperfect Preview Measurements

By introducing the linear prefilter H_{pre}, shown in Fig. 2.1, to form an estimate of w_t based on the measured w_m, the variance of the output variable y can be reduced below the variance given by (2.16). Here it is shown that with imperfect disturbance measurements, the optimal linear feedforward control scenario can be formed using the ideal feedforward controller in (2.3) in series with an optimal prefilter. The optimal feedforward controller $C_{FF,opt}$ is found as the transfer function C_{FF} that minimizes the variance of y as described in (2.2):

$$C_{FF,opt} = \arg\min_{C_{FF}} \mathbf{E}\left[\left|T_{yw_t}w_t + T_{y\beta_{FF}}C_{FF}w_m\right|^2\right], \tag{2.21}$$

where $\mathbf{E}\left[\left|T_{yw_t}w_t + T_{y\beta_{FF}}C_{FF}w_m\right|^2\right]$ can be described in the frequency domain as

$$\begin{aligned}
&\mathbf{E}\left[\left|T_{yw_t}(\omega)W_t(\omega) + T_{y\beta_{FF}}(\omega)C_{FF}(\omega)W_m(\omega)\right|^2\right] \\
&\quad = \left|T_{yw_t}(\omega)\right|^2 S_{tt}(\omega) + \left|T_{y\beta_{FF}}(\omega)\right|^2 \left|C_{FF}(\omega)\right|^2 S_{mm}(\omega) \\
&\qquad + T_{yw_t}(\omega)C^*_{FF}(\omega)T^*_{y\beta_{FF}}(\omega)S_{tm}(\omega) + T_{y\beta_{FF}}(\omega)C_{FF}(\omega)T^*_{yw_t}(\omega)S^*_{tm}(\omega).
\end{aligned} \tag{2.22}$$

In the frequency domain, the solution to (2.21) is

$$C_{FF,opt}(\omega) = -T^{-1}_{y\beta_{FF}}(\omega)T_{yw_t}(\omega)\frac{S_{tm}(\omega)}{S_{mm}(\omega)}. \tag{2.23}$$

Equation (2.23) reveals that the optimal linear feedforward controller can be described by the ideal feedforward controller C_{FF} in (2.3) in series with the prefilter

$$H_{pre}(\omega) = \frac{S_{tm}(\omega)}{S_{mm}(\omega)}. \tag{2.24}$$

The filter H_{pre} given in (2.24) is in fact the non-causal minimum mean square error (MMSE) Wiener filter [70] for estimating a variable w_t given w_m. The use of the prefilter in (2.24) to improve lidar-assisted feedforward control has also been proposed by Schlipf *et al.* [44, 50], where the filter is meant to act as an estimate of the transfer function from the lidar measurement to the true wind disturbance.

The optimal feedforward controller presented in (2.23) was derived under the constraint that C_{FF} is linear. Here, it will be shown that under the assumption that the closed-loop transfer functions T_{yw_t} and $T_{y\beta_{FF}}$ are linear and that w_m and w_t are jointly Gaussian random variables [68, 70], which they are modeled as throughout this thesis, C_{FF} in (2.23) is the optimal controller that minimizes output variance among all possible controllers, both linear and nonlinear.

A more general form of the output y with combined feedforward/feedback control can be written as

$$y = T_{yw_t} w_t + y_{FF}\left(w_m\right), \tag{2.25}$$

where $y_{FF}\left(w_m\right)$ represents the additional output caused by the feedforward control action based on the measurement w_m. The variance of y will be minimized if $y_{FF}\left(w_m\right)$ is a MMSE estimate of $-T_{yw_t} w_t$. Because w_m and w_t are jointly Gaussian random variables, w_m and $-T_{yw_t} w_t$ are also jointly Gaussian, since a linear combination of Gaussian random variables (resulting from the linear operator $-T_{yw_t}$) is also Gaussian [68]. Therefore, the linear Wiener filtering operation (given in (2.24) for variables w_m and w_t) can be used to provide the MMSE estimate of $-T_{yw_t} w_t$ based on w_m [70]. The resulting estimator can be written as the following filtering operation on w_m:

$$\begin{aligned} y_{FF,opt}\left(w_m\right) &= \tfrac{S_{-T_{yw_t} w_t, w_m}}{S_{mm}} w_m \\ &= -T_{yw_t} \tfrac{S_{tm}}{S_{mm}} w_m \\ &= -T_{y\beta_{FF}} T_{y\beta_{FF}}^{-1} T_{yw_t} \tfrac{S_{tm}}{S_{mm}} w_m \\ &= T_{y\beta_{FF}} C_{FF,opt} w_m. \end{aligned} \tag{2.26}$$

The second line of (2.26) uses the following property: $S_{Ha,b}\left(\omega\right) = H\left(\omega\right) S_{ab}\left(\omega\right)$ for any linear transfer function $H\left(\omega\right)$ [68]. The third and fourth lines of (2.26) show that the optimal output

y caused by feedforward control action is equivalent to the output that is produced using the feedforward controller derived in (2.23).

2.2.1 Optimal Measurement Error with Imperfect Measurements

When the optimal feedforward controller (2.23) is utilized, the PSD of y using the optimal prefilter $H_{pre}(\omega) = \frac{S_{tm}(\omega)}{S_{mm}(\omega)}$ is equal to

$$\begin{aligned} S_{yy}(\omega) &= \mathbf{E}\left[\left|\mathcal{F}\left\{T_{yw_t}\left(w_t - H_{pre}w_m\right)\right\}\right|^2\right] \\ &= \left|T_{yw_t}(\omega)\right|^2 \mathbf{E}\left[\left|W_t(\omega) - H_{pre}(\omega) W_m(\omega)\right|^2\right] \\ &= \left|T_{yw_t}(\omega)\right|^2 \mathbf{E}\left[\left|W_t(\omega) - \tfrac{S_{tm}(\omega)}{S_{mm}(\omega)} W_m(\omega)\right|^2\right] \\ &= \left|T_{yw_t}(\omega)\right|^2 S_{tt}(\omega)\left(1 - \gamma_{tm}^2(\omega)\right), \end{aligned} \tag{2.27}$$

where $\gamma_{tm}^2(\omega)$ is the magnitude-squared coherence between the lidar measurement and the true disturbance at the turbine:

$$\gamma_{tm}^2(\omega) = \frac{\left|S_{tm}(\omega)\right|^2}{S_{tt}(\omega) S_{mm}(\omega)}. \tag{2.28}$$

Using the optimal prefilter, the MSE, as a function of frequency, between $\hat{w}_t$ and w_t is given by

$$\mathbf{E}\left[\left|W_t(\omega) - H_{pre}(\omega) W_m(\omega)\right|^2\right] = S_{tt}(\omega)\left(1 - \gamma_{tm}^2(\omega)\right). \tag{2.29}$$

Integrating (2.27) yields the minimum output variance that can be achieved:

$$\mathrm{Var}(y) = \frac{1}{\pi}\int_0^{\pi} \left|T_{yw_t}(\omega)\right|^2 S_{tt}(\omega)\left(1 - \gamma_{tm}^2(\omega)\right) d\omega. \tag{2.30}$$

Comparing the optimal variance in the frequency domain from (2.30) with (2.18) reveals that as a function of frequency, the relative reduction in the variance of y using optimal feedforward control compared to no feedforward control is provided by the simple expression

$$\frac{\mathrm{Var}\left(Y_{C_{FF}=C_{FF,opt}}(\omega)\right)}{\mathrm{Var}\left(Y_{C_{FF}=0}(\omega)\right)} = 1 - \gamma_{tm}^2(\omega). \tag{2.31}$$

Equation (2.30) reveals that by employing the optimal prefilter, the variance of the output variable will be reduced at all frequencies where the measurement coherence is greater than zero. At

frequencies where the coherence is equal to zero, the prefilter removes all of the lidar measurement content, and therefore the feedforward control action, to avoid harming the control system performance. Thus by introducing the optimal prefilter to the feedforward control scenario, feedforward control will never increase the output variance, even for very large measurement error.

2.3 Minimum Mean Square Error Measurement Filter with Preview Time Constraints

In practice, the prefilter in (2.24) that produces the optimal $\mathrm{Var}\,(y)$ given in (2.30) cannot be implemented because of finite preview time. The MMSE H_{pre} in (2.24) can result in a non-causal impulse response requiring infinite preview time. However, time-domain techniques can be used to find the MMSE Wiener filter for estimating w_t with preview constraints imposed. Because the lidar measures the upstream wind a time interval of approximately d/U before the wind reaches the turbine, a maximum of $f_s d/U$ samples of filter preview exist, where f_s is the lidar sampling rate. If $n = 0$ represents the time sample when the wind speed of interest is measured, the prefilter can operate on the lidar measurement from $n = -\infty$ to $n = f_s d/U$. Letting N_p indicate the chosen number of samples of filter preview and N_h represent the number of samples of filter history, or memory, an estimate of w_t can be formed using the finite impulse response filter h_{pre} as

$$\hat{w}_t\,[n] = \sum_{k=-N_h}^{N_p} h_{pre}\,[-k]\,w_m\,[n+k]\,. \tag{2.32}$$

Given the filter constraint of $h_{pre}\,[n] = 0$ for $n < -N_p$ and $n > N_h$, the MMSE Wiener filter is found by solving the discrete-time Wiener-Hopf [70] equation

$$\boldsymbol{h_{pre}} = \boldsymbol{R_{mm}^{-1} R_{tm}} \tag{2.33}$$

for the vector of filter coefficients $\boldsymbol{h_{pre}}$. The positive semidefinite Toeplitz matrix $\boldsymbol{R_{mm}}$ contains values of the lidar measurement autocorrelation function $R_{mm}\,[n]$:

$$\boldsymbol{R_{mm}} = \begin{bmatrix} R_{mm}\,[0] & \cdots & R_{mm}\,[N_h+N_p] \\ \vdots & \ddots & \vdots \\ R_{mm}\,[N_h+N_p] & \cdots & R_{mm}\,[0] \end{bmatrix}. \tag{2.34}$$

The vector $\boldsymbol{R_{tm}}$ contains values of the cross-correlation function $R_{tm}[n]$ between w_t and w_m:

$$\boldsymbol{R_{tm}} = \begin{bmatrix} R_{tm}[-N_p] & \cdots & R_{tm}[N_h] \end{bmatrix}^T. \tag{2.35}$$

When using the optimal prefilter $\boldsymbol{h_{pre}}$ described in (2.33) with filter preview and memory constraints, the MSE in $\hat{w}_t$ is easily calculated [70] using

$$\mathbf{E}\left[(w_t - \hat{w}_t)^2\right] = R_{tt}[0] - \boldsymbol{R_{tm}}^T \boldsymbol{R_{mm}}^{-1} \boldsymbol{R_{tm}}. \tag{2.36}$$

2.3.1 Minimum Output Variance Measurement Filter with Preview Time Constraints

While the optimal prefilter without preview time constraints (2.24) produces both the MMSE estimate of the true wind disturbance and the minimum output variance when combined with the ideal feedforward controller, the MMSE filter derived with preview time constraints (2.33) is not guaranteed to achieve the minimum output variance. For example, because of preview time constraints the filter in (2.33) cannot, in general, minimize measurement error at all frequencies. Although the filter minimizes MSE as much as possible given the time constraints, it does not necessarily minimize error at the frequencies that have the greatest impact on output variance, i.e., where $|T_{yw_t}(\omega)|^2$ is large.

Following the expression given in (2.4), the output variance can be written in the time domain as

$$\begin{aligned} \mathrm{Var}(y) &= \mathbf{E}\left[|t_{yw_t} * (w_t - h_{pre} * w_m)|^2\right] \\ &= \mathbf{E}\left[|t_{yw_t} * w_t - h_{pre} * (t_{yw_t} * w_m)|^2\right], \end{aligned} \tag{2.37}$$

where t_{yw_t} represents the impulse response of the closed-loop transfer function T_{yw_t} and $*$ indicates convolution. Note that the second line of (2.37) uses the linearity and commutative properties of the convolution operator [67].

The second line of (2.37) can be interpreted as the MSE between $\tilde{w}_t$ and $h_{pre}\tilde{w}_m$ using the

following definitions:

$$\tilde{w}_t = t_{yw_t} * w_t \tag{2.38a}$$

$$\tilde{w}_m = t_{yw_t} * w_m. \tag{2.38b}$$

Therefore the variance of y can be minimized given filter time constraints using the traditional Wiener filtering methods described in the previous section. Specifically, the minimum variance filter can be found using the following Wiener-Hopf equation:

$$\boldsymbol{h_{pre}} = \boldsymbol{R}_{\tilde{\boldsymbol{m}}\tilde{\boldsymbol{m}}}^{-1} \boldsymbol{R}_{\tilde{\boldsymbol{t}}\tilde{\boldsymbol{m}}}, \tag{2.39}$$

where $\boldsymbol{R}_{\tilde{\boldsymbol{m}}\tilde{\boldsymbol{m}}}$ and $\boldsymbol{R}_{\tilde{\boldsymbol{t}}\tilde{\boldsymbol{m}}}$ are defined in terms of the variables $\tilde{w}_t$ and $\tilde{w}_m$. Analogous to (2.36), the variance of y resulting from the prefilter defined in (2.39) combined with the ideal feedforward controller can be expressed as

$$\mathrm{Var}\,(y) = R_{\tilde{t}\tilde{t}}\,(0) - \boldsymbol{R}_{\tilde{\boldsymbol{t}}\tilde{\boldsymbol{m}}}{}^{T} \boldsymbol{R}_{\tilde{\boldsymbol{m}}\tilde{\boldsymbol{m}}}{}^{-1} \boldsymbol{R}_{\tilde{\boldsymbol{t}}\tilde{\boldsymbol{m}}}. \tag{2.40}$$

2.4 Discussion and Conclusions

As discussed in this chapter, the performance of a feedforward control system strongly depends on the accuracy of the preview disturbance measurements. A simple model-inverse feedforward control scenario was analyzed in this chapter, where the objective is to minimize the variance of an output error variable. Such lidar-based feedforward control scenarios are of interest in the wind turbine control community. For example, in the field tests discussed in Schlipf *et al.* [44] and Scholbrock *et al.* [43] feedforward collective blade pitch controllers were added to existing feedback loops to improve rotor speed regulation. The results of this chapter indicate that if a controller is designed assuming perfect preview measurements, then under certain conditions the presence of measurement error can cause the feedforward controller to harm the control system's performance. However, if a MMSE measurement prefilter formed using knowledge of the measurement error statistics is employed, feedforward control will always reduce output variance at frequencies

where the measurement coherence is non-zero; when coherence is zero, the filter blocks all feedforward control action so as not to harm the system's performance. Even for control scenarios that are more complex than the simple model-inverse feedforward scenario presented here, the MMSE prefilter can still be employed to minimize measurement error, where the resulting MSE can be characterized using the measurement coherence function. As a result, much of the remainder of this thesis is devoted to determining values of measurement coherence and MSE, assuming optimal prefiltering, that are likely to be achieved in realistic measurement scenarios. Finally, the optimal prefilter discussed in this chapter depends on statistics of the error between the lidar measurement and the true wind disturbance, yet the true wind disturbance that interacts with the turbine cannot be directly measured. Instead, as explained in Chapter 6, a wind speed estimator using measurable turbine outputs can be used to estimate the true wind disturbances. Part of Chapter 7 focuses on how the optimal prefilter with preview time constraints can be derived based on the lidar measurements and wind speed estimator outputs.

Acknowledgements

Assistance from Fiona Dunne, with respect to determining when the ideal model-inverse feedforward controller leads to improved control system performance, is greatly appreciated. Her input helped inspire the spectrum-based analysis of feedforward controller performance in this chapter.

Chapter 3

Wind Field Modeling

The behavior of a wind field can be characterized using frequency-domain statistics describing the power spectra of the wind speeds at individual points in space as well as the correlation between wind speeds at different locations. A common assumption made in wind field modeling is that turbulent wind speeds are distributed as Gaussian random variables [71]–[74], in which case the wind field model can be completely described using power spectra and spatial coherence functions for all points in space relevant to the wind turbine. Time-domain realizations of wind fields with the chosen frequency-domain statistics can be generated using techniques described in Veers [72] and Mann [74], where the Veers method is implemented in NREL's TurbSim stochastic wind field generator [71]. Commonly-used power spectra and spatial coherence functions for modeling the wind field are described in Section 3.1. However, common wind field models do not include spatial coherence in the longitudinal direction (mean wind direction), instead relying on the assumption that wind speeds remains perfectly correlated as they travel downstream at the mean wind speed. A more realistic longitudinal coherence model, used in this research, is presented in Section 3.2. A simple model of how the flow upstream of a turbine, in the turbine's "induction zone," is affected by the presence of the rotor is included in Section 3.3. Finally, models of the effective wind speed variables experienced by a wind turbine, which are relevant to control, are defined in Sections 3.4 and 3.5. Section 3.4 defines the effective wind speed experienced by a single blade, using the the three-bladed NREL 5-MW reference wind turbine model analyzed in this thesis as an example, while Section 3.5 describes how "rotor effective" wind speed variables can be described using three

"blade effective" wind speeds for a three-bladed wind turbine.

3.1 Turbulence Models

The coordinate system used to define the wind field is shown in Fig. 3.1, where the longitudinal x direction is aligned with the mean wind direction, the transverse y direction is perpendicular to x in the horizontal direction, and the z direction is aligned vertically. These coordinate axes are defined such that x is negative upstream of the rotor, y is positive on the left side of the turbine hub when viewing the turbine from upstream, and the positive z direction points upward. Therefore, the x, y, and z directions are identical to the commonly-used boundary-layer meteorology convention of streamwise, cross-stream, and vertical directions. While some wind field definitions place the origin of this coordinate system at the base of the turbine tower [71], in the definition used here the origin is in the center of the rotor at the turbine's hub. Wind speed values are described using a three-dimensional vector where the longitudinal u, transverse y, and vertical w components are aligned with the x, y, and z directions, respectively. The dimensions of the NREL 5-MW reference wind turbine model used in this thesis are included in Fig. 3.1, where the turbine's hub-height z_{HH} is 90 m above the base of the tower, the rotor diameter is $D = 126$ m, and therefore the rotor radius, or blade span, is $R = 63$ m [8]. Although the NREL 5-MW reference model contains a rotor shaft tilt angle of 5° and a rotor precone angle of 2.5° to avoid tower strikes by the blades [8], these angles are ignored for simplicity in most of the analyses in this thesis. As a result, when the turbine is aligned with the wind direction (zero yaw error), the x axis is perpendicular to the rotor plane.

Frequency-domain wind field statistics are defined under the assumption that the wind speeds remain stationary for the period of time when the wind field is analyzed. That is, the power spectrum and spatial correlation statistics are time-invariant while the wind field is analyzed. Wind speeds throughout the wind field are characterized by their mean values as well as their turbulent fluctuations. Unless otherwise stated, the mean transverse and vertical wind speeds are assumed to be zero, while the mean longitudinal wind speed at the turbine's hub-height is denoted

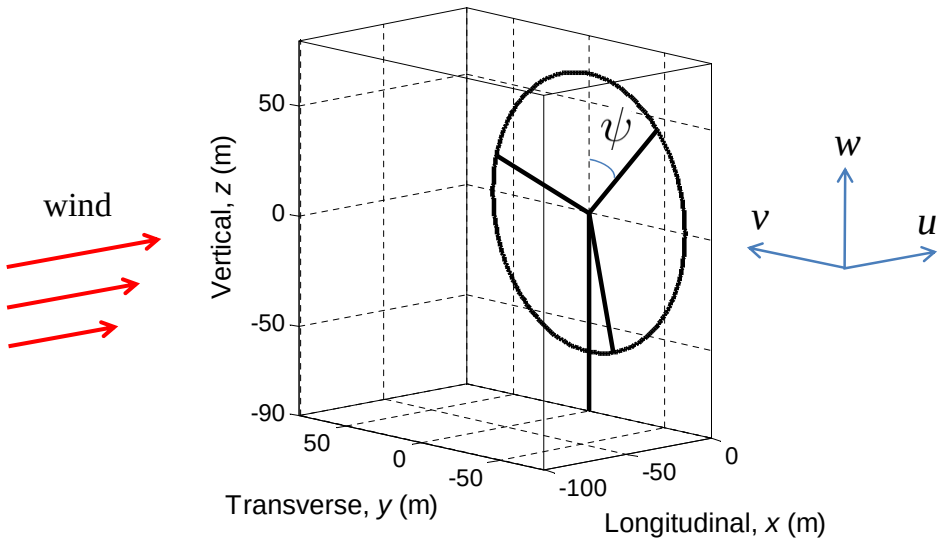

Figure 3.1: Coordinate system used for the wind field definition, where the positive longitudinal x direction is aligned with the mean wind direction and the transverse y and vertical z directions are perpendicular to x. The wind speed vector is comprised of the longitudinal u, transverse v, and vertical w components, which are aligned with the x, y, and z directions, respectively. The origin of the coordinate system is defined as the turbine's hub location. Therefore, the base of the tower is located at $z = -z_{HH}$, where z_{HH} is the height of the hub above the ground. When there is zero yaw error and the vertical tilt angle of the rotor is ignored, which is assumed during most of the analyses in this thesis, then the turbine's rotor is perpendicular to the longitudinal x direction. The dimensions of the NREL 5-MW reference turbine model used throughout this thesis are shown, where $z_{HH} = 90$ m and the rotor diameter is $D = 126$ m (the rotor radius is $R = 63$ m). Finally, the azimuth angle ψ of a blade within the rotor plane is defined as 0 at the top of its rotation and increasing in the clockwise direction when the rotor is viewed from upstream.

as U. Although the atmospheric boundary layer where wind turbines are located typically contains vertical wind shear, i.e., the variation of mean wind speed with height, typically increasing with height [71], wind shear is ignored in most of the analyses in this thesis. Instead, it is assumed that the mean wind speed U applies to all locations in the wind field. This simplification is made because lidar measurements of the mean shear component are perfectly correlated with the mean shear that interacts with the turbine and therefore do not contribute to measurement error; only time-varying wind speed components contribute to measurement error, assuming optimal measurement prefiltering is employed. Furthermore, by ignoring mean wind shear wind fields can be potentially treated as "axisymmetric," which allows the frequency-domain calculations of measurement error

to be greatly simplified, as explained in Section 5.1. However, by assuming zero mean wind shear, measurement errors caused by wind speeds measured at different heights arriving at the rotor after different time delays are not included.

3.1.1 Power Spectra

Power spectra are used to define the frequency content of turbulence. Two standard turbulence definitions used throughout this thesis are provided here, including the Kaimal and von Kármán models [71, 75]. The Kaimal turbulence model, defined in the International Electrotechnical Commission (IEC) standard [75] and implemented in TurbSim [71], is described by the following power spectrum:

$$S_{KK}(f) = \frac{4\sigma_K^2 L_K/U}{(1+6fL_K/U)^{5/3}}, \tag{3.1}$$

where $K \in \{u, v, w\}$ represents the wind component, σ_K is the standard deviation of the wind speed, and L_K is the integral length scale of the turbulence, defined as

$$L_K = \frac{U}{\sigma_K^2}\int_0^\infty R_{KK}(t)\,dt, \tag{3.2}$$

with $R_{KK}(t)$ representing the autocorrelation function of the time-varying component of the wind. As defined by the IEC standard [75], L_K is determined as

$$L_K = \begin{cases} 5.67 \cdot \min(60\,\text{m},\, z_{HH}), & K = u \\ 1.89 \cdot \min(60\,\text{m},\, z_{HH}), & K = v \\ 0.462 \cdot \min(60\,\text{m},\, z_{HH}), & K = w, \end{cases} \tag{3.3}$$

where z_{HH} is the turbine's hub height. For the Kaimal model, the mean wind speed U and u component standard deviation σ_u are free parameters, while the v and w component standard deviations are defined as $\sigma_v = 0.8\sigma_u$ and $\sigma_w = 0.5\sigma_u$.

The von Kármán turbulence power spectrum is defined as

$$S_{uu}(f) = \frac{4\sigma_u^2 L_u/U}{\left(1+71\,(fL_u/U)^2\right)^{5/6}} \tag{3.4}$$

for the u component and

$$S_{KK}(f) = \frac{2\sigma_K^2 L_K/U}{\left(1 + 71\,(fL_K/U)^2\right)^{11/6}}\left(1 + 189\,(fL_K/U)^2\right) \tag{3.5}$$

for $K \in \{v, w\}$, where the integral length scale is defined as

$$L_K = 2.45 \cdot \min(60\,\text{m}, z_{HH}) \tag{3.6}$$

for all three wind components. The turbulence standard deviations of all three components are treated as being equal ($\sigma_w = \sigma_v = \sigma_u$), although in the atmospheric boundary layer it is more realistic to have $\sigma_u > \sigma_v > \sigma_w$ [71, 73]. As opposed to the Kaimal spectral model, the von Kármán model contains isotropic turbulence in the transverse and vertical directions, i.e., the v and w turbulence statistics are identical. Note that the Kaimal and von Kármán models use a single set of power spectra to describe wind speeds at all points in the wind field. Other models such as NREL's Great Plains low-level jet model [71], analyzed in Simley *et al.* [39], contain turbulence spectra that vary with height.

Fig. 3.2 provides plots of the power spectral densities of all three wind components for the Kaimal and von Kármán turbulence models using the NREL 5-MW model's rated wind speed $U = 11.4$ m/s and u component turbulence intensity $TI_u = 15\%$, roughly equivalent to the IEC Normal Turbulence Model Class C turbulence intensity [71]. Note, however, that the turbulence intensity simply scales the power spectra. Turbulence intensity (TI) is defined as the ratio between the turbulence standard deviation and the mean longitudinal wind speed expressed as a percentage. Thus the corresponding u component standard deviation is $\sigma_u = 1.71$ m/s. The PSDs are normalized by frequency in Fig. 3.2 (b). By multiplying a spectrum by frequency, the visible area under the curve between any two frequencies represents the fraction of the turbulence power contained in that frequency band when compared to the total area under the curve. As revealed in Fig. 3.2, the primary differences between the turbulence spectra are at low frequencies; at high frequencies, the spectra approach a $f^{-5/3}$ slope. For the Kaimal model, the smaller length scales for the v and w components result in smaller spatial scales, or more of the turbulence power being concentrated at

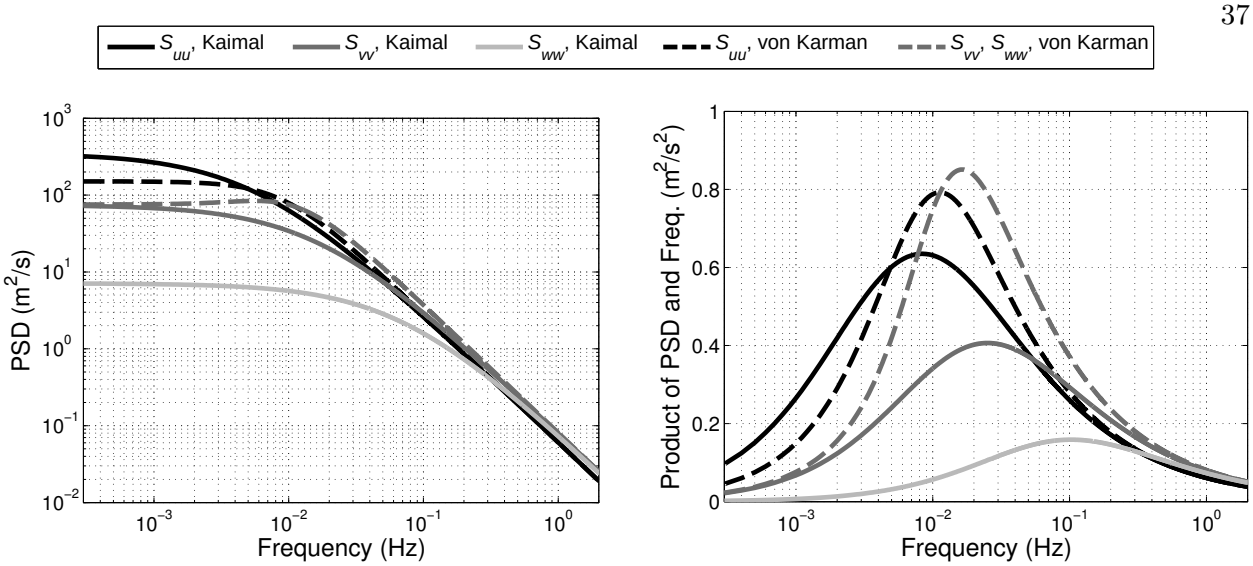

(a) Power spectral density.

(b) Product of power spectrum and frequency.

Figure 3.2: Turbulence power spectral densities for the Kaimal and von Kármán models for all three wind components. (a) Unaltered power spectral densities. (b) Power spectral densities multiplied by frequency revealing the dominant frequencies of the turbulence. All spectra are generated with $U = 11.4$ m/s and $TI_u = 15\%$.

higher frequencies. The lower variance of the v and w components can be noted as well, keeping in mind that the integrated power spectrum is equal to the variance. As defined in (3.1), (3.4), and (3.5), the variance is equal to the one-sided integral of the power spectrum from 0 Hz to ∞. For the von Kármán turbulence model, the dominant frequencies for the v and w components are slightly higher than for the u component, even though the variance is the same for all three components.

3.1.2 Spatial Coherence

To complete the frequency-domain wind field model, the correlation between wind speeds at different spatial locations must be defined. In the IEC standard [75], the correlation as a function of frequency between wind speeds at two points $\vec{x}_1$ and $\vec{x}_2$ is defined using the following magnitude-squared coherence function:

$$\gamma^2_{yz,K_{\vec{x}_1}K_{\vec{x}_2}}(f) = \exp\left(-2\alpha\sqrt{\left(\frac{f\Delta_{yz}}{U}\right)^2 + \left(\beta\frac{\Delta_{yz}}{L_K}\right)^2}\right), \tag{3.7}$$

where $\vec{x} = [x, y, z]$, Δ_{yz} is the distance between the two points in the y and z directions:

$$\Delta_{yz} = \sqrt{(y_2 - y_1)^2 + (z_2 - z_1)^2}, \tag{3.8}$$

$\alpha = 12$, and $\beta = 0.12$. Note that this spatial coherence formula does not include any dependence on the spatial separation in the x direction, which will be discussed later. In the IEC standard, (3.7) only applies to the u component ($K = u$), while the spatial correlation for $K \in \{v, w\}$ is defined as zero for any $\Delta_{yz} > 0$:

$$\gamma^2_{yz,K_{\vec{x}_1}K_{\vec{x}_2}}(f) = \begin{cases} 1, & [y_1, z_1] = [y_2, z_2] \\ 0, & [y_1, z_1] \neq [y_2, z_2]\,. \end{cases} \tag{3.9}$$

However, for the analyses in this thesis, it is assumed that the spatial coherence formula presented in (3.7) applies to all wind components ($K \in \{u, v, w\}$). Including non-zero spatial correlation for $\Delta_{yz} > 0$ is believed to be a more realistic approach, as confirmed by the field measurements that led to the development NREL's Great Plains-Low Level Jet model [71]. Following the suggestions in the IEC standard [71, 75], the correlation between different wind speed components (i.e., $K_1 \neq K_2$) is assumed to be zero regardless of spatial separation.

Spatial coherence curves calculated using (3.7) are plotted in Fig. 3.3 for the u, v, and w components, using the integral length scale values defined by the Kaimal and von Kármán turbulence models in (3.3) and (3.6), for spatial separations of $\Delta_{yz} = 15.75$ m, 31.5 m, and 63 m (0.25, 0.5, and 1 R for the NREL 5-MW reference turbine). In addition to decaying as frequency increases, the spatial coherence decreases as the spatial separation Δ_{yz} increases. As exhibited by the coherence curves for the v and w components using the Kaimal turbulence models, the spatial coherence decreases as the turbulence length scale becomes smaller as well.

The lack of any dependence on spatial separations in the x direction in the spatial coherence formula in (3.7) stems from the traditional application of Taylor's frozen turbulence hypothesis [76] in wind field simulation [71]–[74]. Taylor's hypothesis is a simplification used to relate the behavior of wind speeds along the longitudinal direction to the time behavior of the wind speed at a fixed point through the mean wind speed U, resulting in the following relationship between the

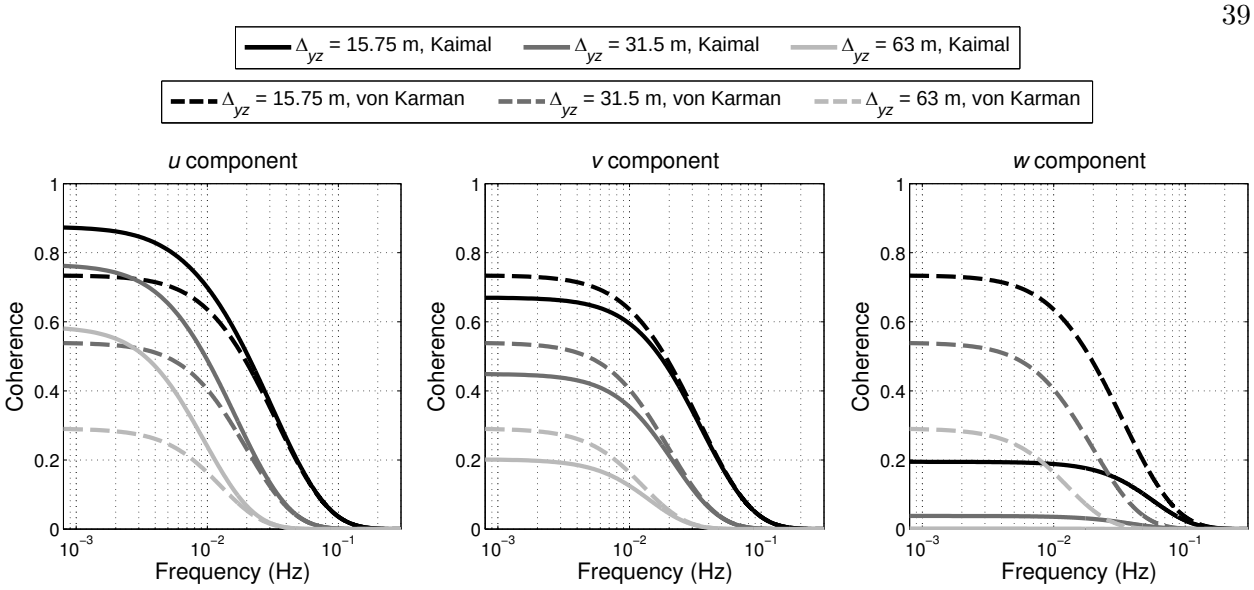

Figure 3.3: Transverse and vertical spatial coherence curves for the u, v, and w components using parameters from the Kaimal and von Kármán turbulence models for spatial separations of Δ_{yz} = 15.75 m, 31.5 m, and 63 m (0.25 R, 0.5 R, and 1 R) with U = 11.4 m/s.

longitudinal position of a wind speed variable and its time index:

$$\vec{u}_{[x+\delta_x,\,y,\,z]}\,(t) = \vec{u}_{[x,\,y,\,z]}\,(t - \delta_x/U)\,, \tag{3.10}$$

where $\vec{u} = [u, v, w]$. Equation (3.10) states that for fixed y and z coordinates, the value of a wind speed variable at a longitudinal location shifted by δ_x is equal to the value of the original wind speed shifted in time by δ_x/U. In other words, by applying Taylor's hypothesis, turbulent wind speeds simply "march" downstream at the mean wind speed without changing. As a result, for fixed y and z coordinates, the spatial coherence is equal to 1 regardless of the longitudinal separation. The spatial coherence between wind speed component K at any two locations $\vec{x}_1$ and $\vec{x}_2$ is therefore simplified as

$$\gamma^2_{K_{\vec{x}_1} K_{\vec{x}_2}}(f) = \gamma^2_{yz,K_{\vec{x}_1} K_{\vec{x}_2}}(f). \tag{3.11}$$

While the spatial coherence is unaffected by the longitudinal separation, the phase between wind speeds at two different locations depends solely on the longitudinal separation according to traditional wind field modeling methods [71]–[74]. As long as wind speeds at two different locations

have the same longitudinal position, the average phase difference between them is 0. By solving the coherence equation (2.8) for the magnitude of the CPSD and applying the proper phase shift, the cross spectrum between the wind speed component K at locations $\vec{x}_1$ and $\vec{x}_2$ can be expressed as

$$S_{K_{\vec{x}_1}K_{\vec{x}_2}}(f) = \sqrt{S_{K_{\vec{x}_1}K_{\vec{x}_1}}(f)\, S_{K_{\vec{x}_2}K_{\vec{x}_2}}(f)\, \gamma^2_{K_{\vec{x}_1}K_{\vec{x}_2}}(f)}\, e^{j2\pi(x_2-x_1)f/U}, \tag{3.12}$$

where the phase is given by the time lag $(x_2 - x_1)/U$ between the two wind speeds using Taylor's hypothesis multiplied by the angular frequency.

3.2 Wind Evolution Modeling

While Taylor's frozen turbulence hypothesis is acceptable in traditional wind turbine simulation, where the range of longitudinal locations experienced by the rotor is very small, it is less appropriate for the analysis of preview-based control of wind turbines. Measurement error can be underestimated by assuming that the measured wind simply marches toward the rotor without changing or "evolving." Thus models of "wind evolution" have been employed using spatial coherence formulas for spatial separations in the longitudinal direction, denoted as $\gamma^2_{x,K_{\vec{x}_1}K_{\vec{x}_2}}(f)$. Section 3.2.1 describes existing wind evolution models that have been used for lidar-assisted control investigations, including their potential shortcomings, while Sections 3.2.2 and 3.2.3 describe a wind evolution model based on wind speed data from computational fluid dynamics (CFD) simulations performed by researchers at NREL. Finally, Section 3.2.4 discusses methods for combining longitudinal coherence formulas that describe wind evolution with the spatial coherence function described in the previous section to form a complete three-dimensional spatial coherence definition.

3.2.1 Existing Longitudinal Coherence Models

A simple exponential decay coherence formula proposed by Davenport [77] and extended to the longitudinal direction by Pielke and Panofsky [52], which depends on the product between wavenumber, longitudinal separation, and a decay parameter α, has been used to introduce wind evolution to calculations of the coherence between lidar measurements and the wind that reaches

the rotor [50, 63]:

$$\gamma^2_{x,K_{\vec{x}_1}K_{\vec{x}_2}}(f) = e^{-\alpha\Delta_x f/U}, \tag{3.13}$$

where $\Delta_x = |x_1 - x_2|$. The values of the unitless decay parameter α presented by Pielke and Panofsky [52] for the exponential decay model range from approximately 10 to 50. Schlipf *et al.* [50] find that a decay parameter of 0.4 matches field measurements quite well, but the specific wind conditions that were analyzed are not specified. Furthermore, it is unclear how the α parameter depends on turbulence statistics.

An analytic expression for longitudinal coherence in neutral atmospheric conditions, derived by Kristensen [51], has been used to create four-dimensional stochastic wind fields for assessing the impact of wind evolution on lidar-based control [34, 36, 40]. The Kristensen model for the u component is given by

$$\gamma^2_{x,u_{\vec{x}_1}u_{\vec{x}_2}}(f) = e^{-2\alpha G(fL_u/U)}\left(1 - e^{-\left(2\alpha\min\{\alpha,1\}(fL_u/U)^2\right)^{-1}}\right)^2, \tag{3.14}$$

where

$$G(fL_u/U) = (33)^{-2/3}\frac{(33fL_u/U)^2(33fL_u/U + 3/11)^{1/2}}{(33fL_u/U + 1)^{11/6}} \tag{3.15}$$

and

$$\alpha = \frac{\sigma}{U}\frac{\Delta_x}{L_u}. \tag{3.16}$$

The Kristensen model depends on the mean wind speed U, the integral length scale L_u, the longitudinal separation Δ_x, and σ, which is defined as

$$\sigma = \sqrt{\sigma_u^2 + \sigma_v^2 + \sigma_w^2}. \tag{3.17}$$

The definition of σ is related to the turbulent kinetic energy (TKE):

$$\text{TKE} = \frac{1}{2}\left(\sigma_u^2 + \sigma_v^2 + \sigma_w^2\right). \tag{3.18}$$

While the Kristensen model depends on atmospheric parameters, it has not been validated by field measurements or CFD simulations. Similar to the transverse-vertical spatial coherence formula in (3.7), in both the Pielke and Panofsky as well as Kristensen longitudinal coherence formulas the

coherence decays with increasing frequency, indicating that the high-frequency, small turbulence scales decay faster than the low-frequency, large scales, and also with increasing spatial separation, since the turbulent structures have more time to evolve.

In the remainder of this section, longitudinal coherence curves are calculated for a collection of wind fields representing a variety of mean wind speeds, turbulence intensities, and atmospheric stability categories generated using large-eddy simulation (LES), a type of CFD. The LES wind fields were provided by NREL and were generated using NREL's Simulator fOr Wind Farm Applications (SOWFA) tool [78]. A simple coherence model similar to (3.7) is then fit to the calculated coherence curves to determine how the model parameters depend on atmospheric conditions.

3.2.2 Large-Eddy Simulation Wind Fields

A collection of twelve LES wind fields provided and generated by researchers at NREL is used to determine longitudinal spatial coherence curves for a variety of wind conditions. The wind fields were generated using NREL's SOWFA tool [78], which combines a CFD solver based on OpenFOAM [79] with NREL's FAST aeroelastic code to simulate the two-way interaction between the atmospheric boundary layer and a turbine. Note that in this section, only data produced by the LES portion of SOWFA are utilized; there are no wind turbines located in the portions of the wind fields analyzed. A domain volume of 3 km $\times$ 3 km $\times$ 1 km was used to develop the atmospheric boundary layers. To reduce the computational time, a grid resolution of 12 m was used for most of the domain, but the wind speeds analyzed are located in a 3 m-resolution grid refinement zone. Although time steps of 0.02 s were used during simulation, the data analyzed here are only sampled once per second. The final wind field segments used to calculate coherence curves in this section are horizontal planes at the NREL 5-MW reference turbine's hub height of 90 m, extending 385 m in the longitudinal x direction and 370 m in the transverse y direction. While the original LES simulations were generated for thousands of seconds to allow boundary layer development, the segments used for analysis range from 470 to 670 s.

Of the twelve wind conditions simulated, half contain approximately 8 m/s mean wind speeds

(wind field IDs 1–6) and half contain approximately 12 m/s mean wind speeds (IDs 7–12). For the two mean wind speed categories, neutral, unstable, and stable conditions were simulated for both a low turbulence case representative of offshore conditions [80], implemented using a surface roughness of $2 \cdot 10^{-4}$ m, and a high turbulence case representative of onshore conditions, using a surface roughness of 0.2 m. Atmospheric stability is defined by the vertical gradient of potential temperature, such that negative gradients, typical of daytime conditions onshore when the surface is being heated, define unstable conditions while positive gradients, common at night onshore, describe stable conditions [80, 81]. Neutral stability occurs when the potential temperature remains constant with height and turbulence is primarily generated by shear caused by the interaction between the wind flow and the rough surface. In unstable conditions, buoyancy forces tend to produce amplified turbulence, while in stable conditions, disturbances in the flow are dampened, leading to lower turbulence levels [80]. The unstable cases were generated using a surface heating rate of 1 K/hr while the stable wind fields contain a heating rate of -1 K/hr. Further information about SOWFA and the LES simulation environment can be found in [80] and [82].

Additional details for all LES wind fields are provided in Table 3.1, including the turbulent kinetic energy, the integral length scale for all wind components, and the turbulence intensity values for all wind speed components. The integral length scales were calculated by integrating $R_{KK}(t)$ up to the first zero crossing as described in [83]. Examples of planes of instantaneous wind speeds for all three stability classes in the $U \approx 12$ m/s, high turbulence category are provided in Fig. 3.4, where the different length scales can be compared.

3.2.3 Development of a Longitudinal Coherence Model

An attempt was made to validate the Pielke and Panofsky coherence model and the Kristensen formula using the coherence curves calculated from the LES wind fields. However, the values of the decay parameter α presented in Pielke and Panofsky [52] produce spatial coherence that is much too low compared to the LES-based calculations, and it is unknown how the decay parameter depends on specific atmospheric conditions. Contrarily, when using values of σ and L_u calculated from

Table 3.1: Details of the twelve LES wind fields (IDs 1 through 12) including mean wind speed (U), stability (N: neutral, U: unstable, S: stable), turbulent kinetic energy, u, v, and w component integral length scales, and u, v, and w component turbulence intensities (TI_u, TI_v, and TI_w). All statistics are for a height of 90 m.

ID	U (m/s)	Stab.	TKE ($\mathrm{m}^2/\mathrm{s}^2$)	L_u (m)	L_v (m)	L_w (m)	TI_u (%)	TI_v (%)	TI_w (%)
1	8.0	N	0.20	71	37	29	5.5	4.3	3.6
2	8.0	U	0.44	178	156	74	6.9	7.1	6.2
3	8.0	S	0.03	28	19	16	2.1	2.0	1.2
4	8.2	N	0.72	96	46	25	10.3	7.9	6.4
5	8.2	U	1.73	241	231	110	12.8	15.3	10.8
6	8.0	S	0.13	33	19	17	4.7	3.6	2.4
7	12.0	N	0.38	115	45	23	5.3	3.8	3.1
8	12.2	U	1.05	211	156	128	7.3	7.4	5.9
9	11.9	S	0.20	42	21	19	3.9	2.9	2.0
10	11.7	N	1.65	186	35	40	11.8	7.5	6.7
11	10.6	U	2.08	230	90	62	14.1	10.1	8.4
12	11.9	S	0.93	56	26	20	8.5	6.2	4.7

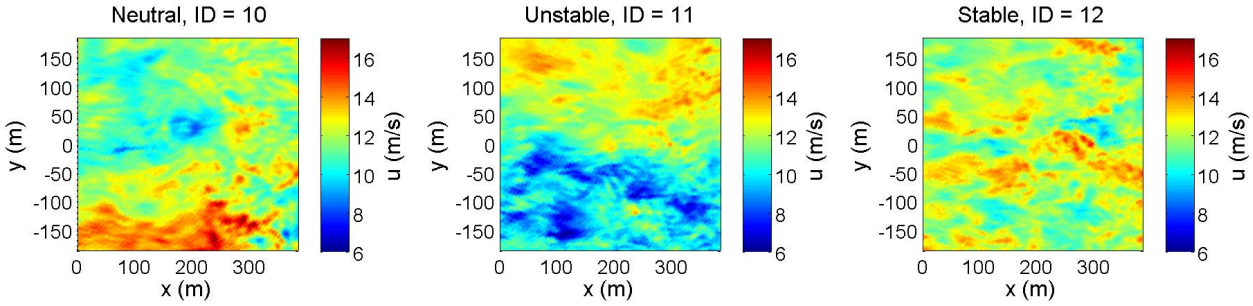

Figure 3.4: Examples of instantaneous u velocities in neutral, unstable, and stable LES wind fields (IDs 10, 11, and 12) at a height of 90 m with mean wind speeds of approximately 12 m/s and u component turbulence intensities of 11.8%, 14.1%, and 8.5%, respectively.

the LES data, the Kristensen model [51] was found to overestimate the coherence. In Fig. 3.5, u component coherence curves calculated using neutral LES wind field 1 are compared with coherence curves based on the Kristensen model using U, σ, and L_u values calculated from the LES data for longitudinal separations of 31.5 m, 63 m, 126 m, and 252 m (0.25, 0.5, 1, and 2 D for the NREL 5-MW model). The LES-based coherence curves shown in Fig. 3.5, as well as those discussed in the rest of this section, were calculated using Welch's modified periodogram method [84] with a Hamming window and 120 s data segments. The spectra are calculated using 550 pairs of wind speed time series separated by the desired longitudinal distance of Δ_x within the wind fields. As can be seen in Fig. 3.5, the Kristensen model clearly overestimates the LES-based coherence curves.

Examples of longitudinal coherence curves calculated for LES wind conditions representing the three stability cases are shown by the black curves in Fig. 3.6, once again for pairs of wind speeds with longitudinal separations of Δ_x = 31.5 m, 63 m, 126 m, and 252 m. An additional problem with the Pielke and Panofsky as well as Kristensen models is that as frequency approaches zero, coherence always approaches 1, but as is evident in the stable coherence curves in Fig. 3.6, this is not always realistic. A suitable coherence model should therefore allow for non-unity coherence

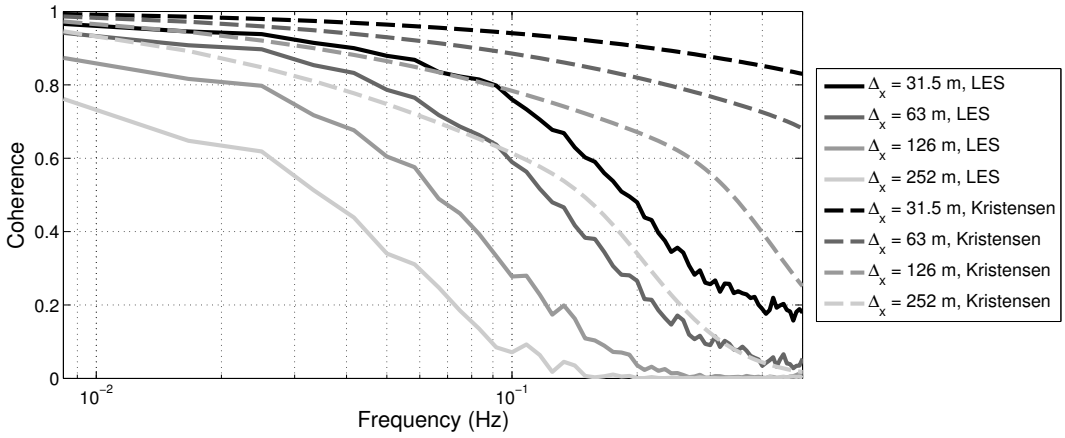

Figure 3.5: Comparison between longitudinal u component coherence curves calculated using LES wind field 1 (see Table 3.1) and coherence curves given by the Kristensen coherence formula for longitudinal separations of Δ_x = 31.5 m, 63 m, 126 m, and 252 m. The Kristensen formula parameters, determined from the LES wind field are U = 8 m/s, σ = 0.63 m/s, and L_u = 71 m.

at 0 Hz (DC).

The coherence formula similar to (3.7) developed by Thresher [85] for transverse and vertical separations, and included in various forms in the IEC standard [75] and TurbSim [71] contains a parameter that creates a bias at DC preventing coherence from approaching 1. This coherence formula, with Δ_x representing the separation distance between wind speeds at points $\vec{x}_1$ and $\vec{x}_2$ in the transverse and vertical plane in the original definition [85], but indicating a longitudinal separation distance when applied here as a longitudinal coherence function, is defined as

$$\gamma^2_{x,K_{\vec{x}_1}K_{\vec{x}_2}}(f) = \exp\left(-a\sqrt{\left(\frac{f\Delta_x}{U}\right)^2 + (b\Delta_x)^2}\right), \tag{3.19}$$

with a and b serving as tuning parameters. When $b = 0$, (3.19) is identical to the Pielke and Panofsky model. To determine if (3.19) is a suitable formula, the expression is fit to the LES-based coherence curves by tuning a and b. Note that only longitudinal coherence for the u component

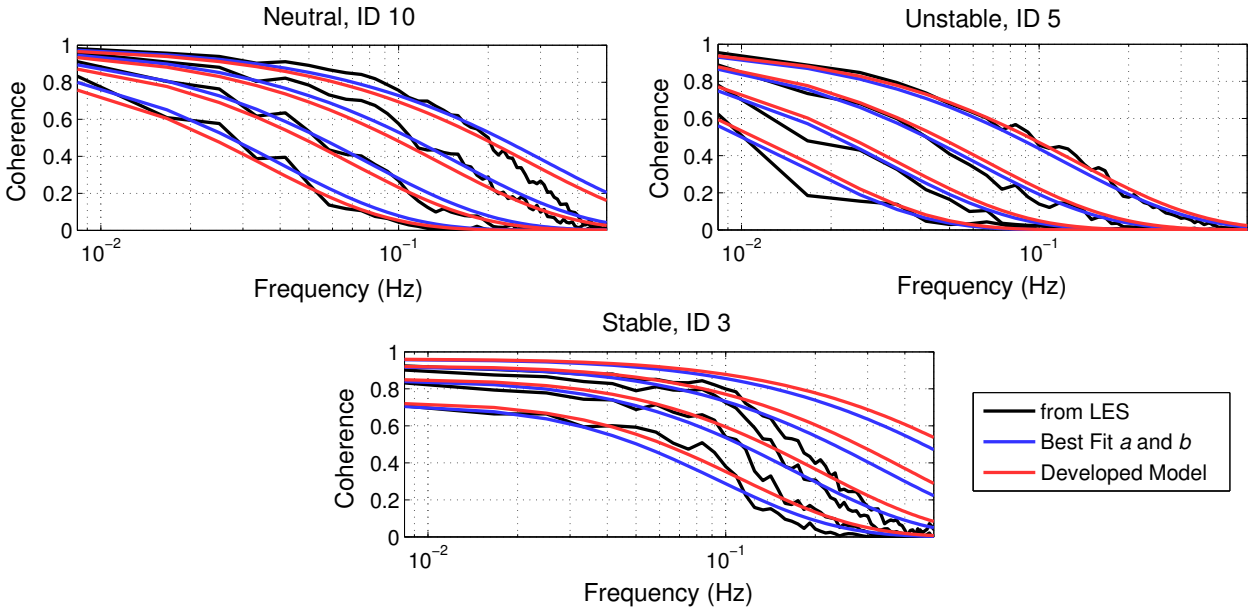

Figure 3.6: Longitudinal coherence curves for wind field IDs 10 (neutral, high wind speed, high turbulence), 5 (unstable, low wind speed, high turbulence), and 3 (stable, low wind speed, low turbulence). Coherence curves calculated from the LES wind fields are compared with the coherence formula in (3.19), using the best fit a and b parameters for each wind field, and the coherence model in (3.21) using a_1 =8.4, $a_2 = 0.05$, $b_1 = 0.25$, and $b_2 = 1.24$. Ordered from top to bottom in each plot, the coherence curves represent longitudinal separations of $\Delta_x = 31.5$ m, 63 m, 126 m, and 252 m.

is analyzed in this thesis. For each wind condition, a pair of a and b parameters is chosen by minimizing the following objective function:

$$J(a,b) = \frac{1}{\int_0^{f_{max}} S_{uu}(f)\,df} \sum_{k=1}^{N} \int_0^{f_{max}} S_{uu}(f) \left(\gamma^2_{x,u_{\vec{x}_1}u_{\vec{x}_2}}(f,\Delta_{x,k}) - \gamma^2_{x,u_{\vec{x}_1}u_{\vec{x}_2},\mathrm{LES}}(f,\Delta_{x,k})\right)^2 df. \tag{3.20}$$

The objective function in (3.20) sums the integrated square errors between the LES-based calculated coherence curves and the longitudinal coherence formula $\gamma^2_{x,u_{\vec{x}_1}u_{\vec{x}_2}}(f,\Delta_{x,k})$ in (3.19), weighted by the power spectrum $S_{uu}(f)$ of the u component calculated from the LES wind data, over N different longitudinal separations. An integration limit of $f_{max} = 0.5$ Hz, equal to half the sampling frequency of the LES data, is used. Weighting the errors by the PSD helps ensure that error is low at the frequencies where most of the power in the wind is concentrated. The sum of the errors is normalized by the integral of $S_{uu}(f)$ so that values of $J(a,b)$ for different wind conditions can be meaningfully compared. The three longitudinal separations of $\Delta_x = 63$ m, 126 m, and 252 m (0.5 D, 1 D, and 2 D for the NREL 5-MW reference turbine) were chosen for the objective function because prior research indicates that the optimal measurement distance for preview-based control applications is likely to fall in this range [39, 62]. Examples of the resulting best fit coherence curves are shown by the blue curves in Fig. 3.6.

The best fit a and b parameters found using (3.20) were compared with several atmospheric variables calculated from the LES wind fields to determine their relationship to the wind conditions. It was found that a is a strong linear function of the ratio between σ and U. The b parameter, which determines the value that the coherence approaches as frequency approaches 0, is strongly proportional to the inverse of the integral length scale. Fig. 3.7 contains the best fit a and b parameters organized by stability class as functions of σ/U and L_u, respectively. Along with the best fit parameters, Fig. 3.7 shows the best fit curves relating a and b to σ/U and L_u. The a parameter is described as $a = a_1\sigma/U + a_2$ and b is expressed in a power-law form: $b = b_1 L_u^{-b_2}$. The final form of the developed longitudinal coherence function is given as:

$$\gamma^2_{x,K_{\vec{x}_1}K_{\vec{x}_2}}(f) = \exp\left(-\left(a_1\frac{\sigma}{U} + a_2\right)\sqrt{\left(\frac{f\Delta_x}{U}\right)^2 + \left(b_1 L_u^{-b_2}\Delta_x\right)^2}\right), \tag{3.21}$$

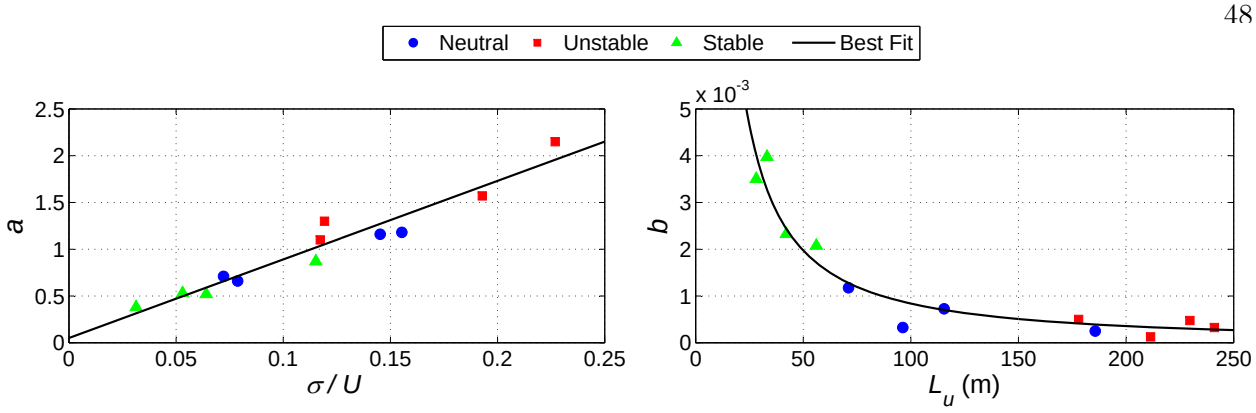

Figure 3.7: Best fit a and b coherence parameters from (3.19) for all twelve wind fields separated by stability class along with the best fit curves describing a as a function of σ/U and b as a function of L_u.

where the best fit parameters relating a and b to σ/U and L_u are $a_1 = 8.4$, $a_2 = 0.05$, $b_1 = 0.25$, and $b_2 = 1.24$. Examples of coherence curves using the model in (3.21) are provided by the red curves in Fig. 3.6.

Several interesting trends are revealed by the developed longitudinal coherence function. First, if the impact of L_u is ignored, relative changes in U will affect coherence more than relative changes in Δ_x due to the dependence of the a parameter on mean wind speed. This behavior is also present in the Kristensen model, but not in the Pielke and Panofsky formula, which depends on Δ_x and U only through Δ_x/U. Second, as integral length scale decreases and more of the energy in the wind is concentrated at small length scales, the value of coherence approached as f approaches 0 decreases as well. Since stable boundary layers tend to produce small length scales, as revealed by Fig. 3.7, low frequency coherence decreases during stable conditions. Finally, as can be seen in Fig. 3.6, the coherence model is unable to capture the sharp decrease in coherence above a certain frequency apparent in the stable condition as well as for the 31.5 m separation in the neutral condition. To summarize the quality of fit for the developed coherence model, Table 3.2 contains errors based on the objective function in (3.20) for each wind condition.

As illustrated in Fig. 3.6 as well as Table 3.2, the developed wind evolution model matches the measured coherence curves very well for certain wind conditions (e.g., unstable wind field 5),

Table 3.2: Errors between the developed coherence model in (3.21) and the LES-based coherence curves, calculated using (3.20).

ID	1	2	3	4	5	6	7	8	9	10	11	12
Model Error ($\times 10^{-3}$)	3.4	4.2	11.4	17.8	7.3	6.9	2.4	12.4	3.6	7.7	7.5	10.7

and not as well for others (e.g., stable wind field 3). Additional improvements can be made to the coherence formula, such as introducing a term to account for the sharp decline in coherence at high frequencies visible for wind field 3. Furthermore, validation of the evolution model would benefit from wind conditions with a larger range of mean wind speeds and larger ratios of σ/U.

3.2.4 Combining Transverse-Vertical and Longitudinal Spatial Coherence

It is unclear how the longitudinal coherence formula in (3.21) should be combined with the transverse-vertical coherence formula in (3.7) to form a three-dimensional spatial coherence function. Initial investigations of the effect of wind evolution on lidar measurement error used the assumption that the spatial coherence between wind speeds at points $\vec{x}_1$ and $\vec{x}_2$ is equal to the product of the longitudinal coherence and the transverse-vertical coherence [18, 34, 50, 64]:

$$\gamma^2_{K_{\vec{x}_1}K_{\vec{x}_2}}(f) = \gamma^2_{x,K_{\vec{x}_1}K_{\vec{x}_2}}(f)\gamma^2_{yz,K_{\vec{x}_1}K_{\vec{x}_2}}(f). \tag{3.22}$$

However, an alternate method for combining the two coherence formulas is discussed here, which is inspired by the exponential decay form of the individual coherence functions. By representing the longitudinal coherence at a specific frequency as $\exp(-a_x)$ and the transverse-vertical coherence as $\exp(-a_{yz})$, the exponents can be combined as $\exp\left(-\sqrt{a_x^2 + a_{yz}^2}\right)$ to form the three-dimensional coherence. In contrast, by combining the separate coherence functions using their product, the three-dimensional spatial coherence is equivalent to $\exp(-(a_x + a_{yz}))$. In a more general form, this method, which creates a new exponent using the root-of-sum-of-squares (RSS) of the transverse-vertical and longitudinal exponents is given by

$$\gamma^2_{K_{\vec{x}_1}K_{\vec{x}_2}}(f) = \exp\left(-\sqrt{\log\left(\gamma^2_{x,K_{\vec{x}_1}K_{\vec{x}_2}}(f)\right)^2 + \log\left(\gamma^2_{yz,K_{\vec{x}_1}K_{\vec{x}_2}}(f)\right)^2}\right). \tag{3.23}$$

The RSS method can be interpreted as an extension of the transverse-vertical coherence formula in (3.7), where the decay exponent depends on the Euclidean distance between the two points in the y and z directions. If the a and b parameters of the longitudinal coherence formula in (3.21) match those of (3.7), then the RSS method would imply that the three-dimensional spatial coherence is a function of the three-dimensional Euclidean distance. Since the parameters are different, though, the RSS method represents a more general form for combining spatial coherences.

The product and RSS methods for combing spatial coherence curves are compared in Fig. 3.8. Using neutral, high-turbulence LES wind field 4, described in Table 3.1, coherence curves calculated at a fixed height of 90 m for all four combinations of $\Delta_{yz} \in \{7.875 \text{ m}, 15.75 \text{ m}\}$ (0.125 R and 0.25 R) and $\Delta_x \in \{15.75 \text{ m}, 252 \text{ m}\}$ (0.125 D and 2 D) are compared with the product and RSS methods for combining the individually calculated longitudinal and transverse-vertical coherence curves. As can be seen in Fig. 3.8, the product method tends to underestimate the true spatial coherence, while the RSS approach is much more accurate. Accordingly, the RSS method for creating three-dimensional spatial coherence is used for the frequency-domain analyses in this thesis.

Finally, while combining a longitudinal coherence formula with an existing transverse-vertical coherence model is convenient for forming a simplified statistical definition of a wind field, other methods of defining spatial coherence in all three dimensions exist. For example, a spectral wind field definition developed by Wilczek *et al.* [86] describes the u component coherence in the longitudinal and transverse dimensions using one unifying analytic formula.

3.3 Induction Zone Modeling

Due to the extraction of energy from the wind by a wind turbine, the induced velocities both upstream and downstream of the turbine are reduced compared to the freestream wind speed. As derived using a simple actuator disk model of a horizontal axis wind turbine in steady flow [7], a turbine's power coefficient C_P, defined in (1.1), is a function of the axial induction factor a, where a is defined as the fraction of the freestream wind speed U_∞ that the wind speed is reduced by at

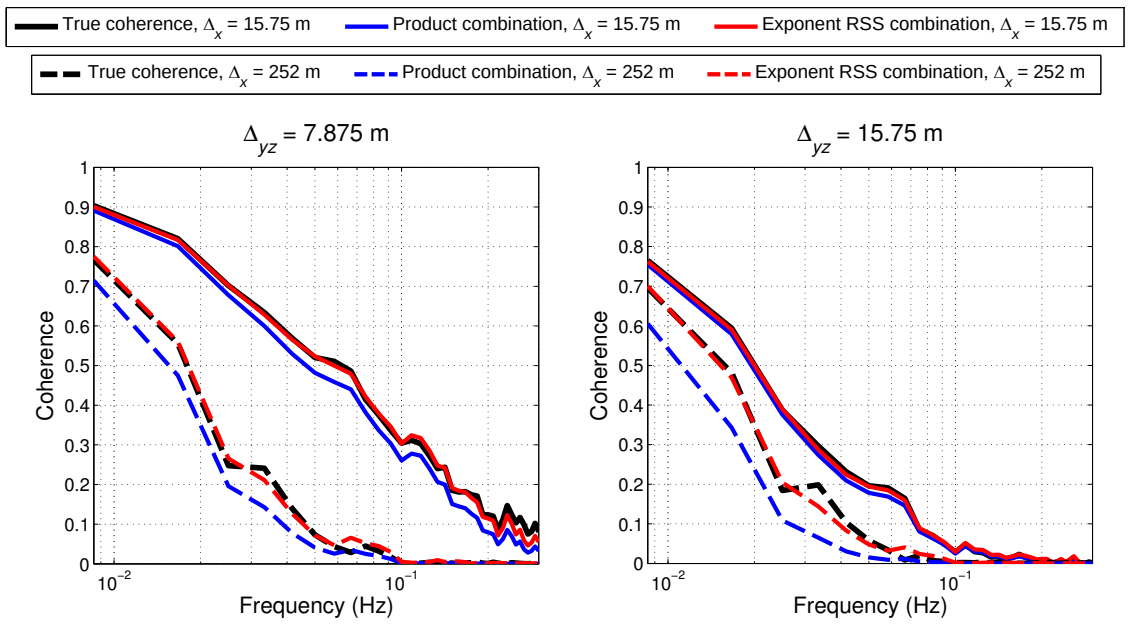

Figure 3.8: Combined transverse-vertical and longitudinal coherence curves for transverse-vertical separations $\Delta_{yz} = 7.875$ m and 15.75 m with longitudinal separations $\Delta_x = 15.75$ m and 252 m determined from LES wind field 4. The true coherence curves (black) are compared with the product of the measured transverse-vertical and longitudinal coherence curves (blue) and the exponential decay coherence formula using the root-of-sum-of-squares (RSS) of the transverse-vertical and longitudinal decay constants (red).

the rotor disk:

$$a = \frac{U_\infty - U_{disk}}{U_\infty}, \tag{3.24}$$

where U_{disk} is the wind speed at the rotor disk. Specifically, using linear momentum theory [7], the coefficient of power C_P can be expressed as

$$C_P = 4a\,(1-a)^2\,. \tag{3.25}$$

The well-known optimal induction factor which maximizes power capture is $a = 1/3$. As explained in Medici *et al.* [53], vortex sheet theory can be applied to the actuator disk model to determine the velocities at all distances upstream and downstream of the rotor. Using this vortex sheet theory formula [53], the wind speeds along the "symmetry axis", which passes through the center of the rotor disk perpendicular to the disk, are shown in Fig. 3.9 expressed in terms of a and plotted as a function of the distance from the rotor in units of rotor diameters D. The region upstream of the

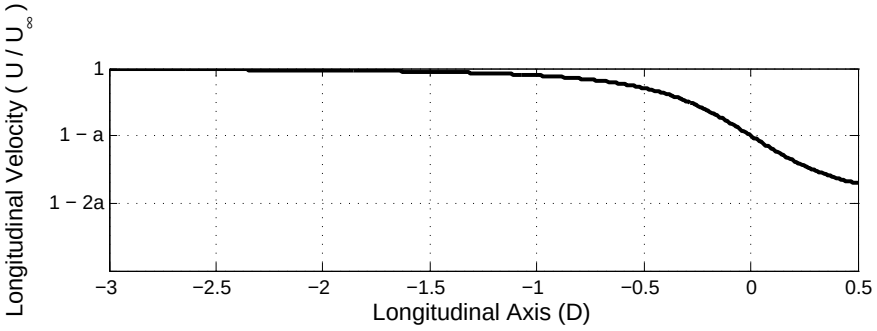

Figure 3.9: Example of mean longitudinal velocities along the axis perpendicular to the rotor center expressed in terms of freestream mean wind speed U_∞ and axial induction factor a. The velocities are calculated assuming an actuator disk in steady flow using the formula based on vortex sheet theory presented in Medici *et al.* [53].

rotor where the induced wind speeds are reduced is called the "upstream induction zone" or simply the "induction zone." In addition to the reduction in longitudinal wind speed in the induction zone, application of conservation of mass indicates that a streamtube passing around the rotor disk expands as the distance upstream of the rotor decreases [7]. Thus the mean radial wind speeds (perpendicular to the longitudinal direction, oriented away from the rotor center) are non-zero close to the rotor to produce this expansion. The rest of this section is devoted to describing a model of the induction zone for the full region upstream of the rotor, not confined to the symmetry axis, that can be used to analyze the impact on lidar measurement quality.

3.3.1 Development of an Induction Zone Model based on Large-Eddy Simulation

The impact of the induction zone on lidar measurements is investigated using NREL's SOWFA code [78] with the NREL 5-MW reference turbine model [8]. As discussed in Section 3.2.2, SOWFA models the two-way interaction between the wind and the turbine using LES coupled with FAST. As opposed to FAST, which only calculates the induced velocities at the blade locations, this allows an induction zone to develop upstream of the rotor. As explained in Simley *et al.* [62], the wind turbine aerodynamic effects are modeled using an actuator line representation of the blades. Each blade is treated as a line that rotates through the wind field. Each line is divided into small

segments, each with a center point. Velocity is sampled at the center point of each line segment and passed to FAST. The aerodynamics module in FAST uses airfoil lift and drag tables to compute the aerodynamic forces at each blade section. Those forces are then passed both to the structural dynamics module in FAST and also back to SOWFA's CFD solver. The CFD solver applies the computed blade forces along the actuator lines as body forces. These body forces create the axial induction zone, the rotor wake, and blade root and tip vortices. The impact of the nacelle and tower on the flow is not modeled however.

A 1000 s simulation of the rotor-wind field interaction was produced by researchers at NREL using neutral, low-turbulence LES wind condition 1 with $U = 8$ m/s described in Table 3.1. At the below-rated wind speed $U = 8$ m/s, the 5-MW reference turbine operates at its maximum coefficient of power ($C_P = \sim$0.48), yielding an axial induction factor of ~ 0.18 according to (3.25). More details about the specific simulation parameters can be found in Simley *et al.* [62]. The mean velocity field near the turbine produced by this simulation, including the flow perturbed by the turbine, is shown in Figure 3.10. The U component reductions upstream of the turbine clearly vary with the radial distance from the rotor center. The U velocities also vary with height, due to the vertical wind shear across the height of the rotor present in the LES wind field. The radial wind speed components, which are oriented away from the rotor center, perpendicular to the longitudinal direction, (V in the top view plot and W in the side view plot) illustrate the expansion of the wind field around the rotor due to conservation of mass. As revealed by the mean W velocities in the top view plot and the V velocities in the side view plot, the mean tangential velocities, aligned with the rotor's rotational direction, are zero upstream of the rotor, but strong downstream of the rotor in the turbine's wake. The non-zero tangential velocities indicate wake rotation, which is caused by tangentially induced velocities at the rotor [7].

Whereas Fig. 3.10 revealed the behavior of the mean wind speeds upstream of the turbine, Fig. 3.11 contains plots of the wind speed standard deviations in the induction zone for all three wind components. While the standard deviation of the turbulence is heavily impacted by the rotor in the turbine's wake, there is little effect upstream of the rotor. The turbulence standard deviation

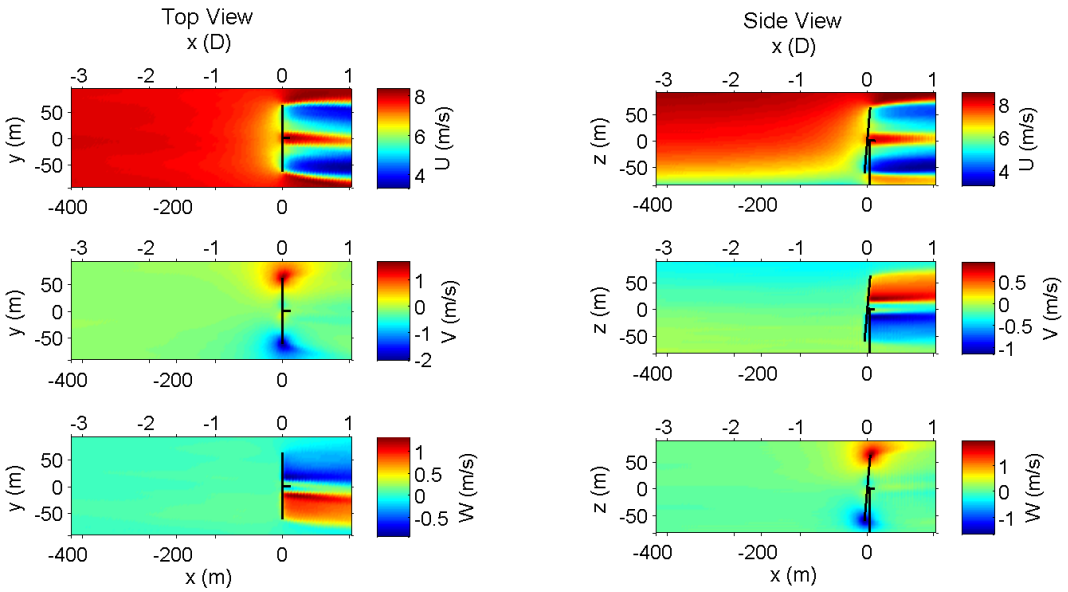

Figure 3.10: Mean U, V, and W component wind speeds near the NREL 5-MW reference turbine in neutral LES wind field 1, with freestream mean wind speed $U = 8$ m/s, generated using SOWFA. The x coordinates are expressed in meters as well as rotor diameters ($D = 126$ m).

increases close to the rotor in the upstream induction zone, but in the region farther upstream of the rotor where lidar preview measurements are likely to occur (43–154 m, or 0.34–1.22 D, upstream of the rotor, as revealed in Chapter 5), there is very little change in the turbulence.

A model of the mean velocity changes in the induction zone based on the LES results shown in Figs. 3.10 and 3.11 is created by averaging the mean longitudinal and radial wind speeds on both sides of the rotor at hub height. Thus the induction zone model is a function of the longitudinal location and radial distance from the rotor center, assuming symmetry about the x axis. Because the mean tangential velocities and turbulence standard deviations are not significantly altered upstream of the turbine, they are not included in the simplified induction zone model. Fig. 3.12 contains the mean longitudinal wind speed reductions, expressed as a fraction of the freestream mean wind speed U_∞, and wind direction changes that comprise the induction zone model. Specifically, Fig. 3.12 (b) illustrates the wind direction changes caused by non-zero mean radial wind speeds using streamlines passing through the mean flow field.

Note that the induction zone behavior shown in Fig. 3.12 corresponds to a specific turbine

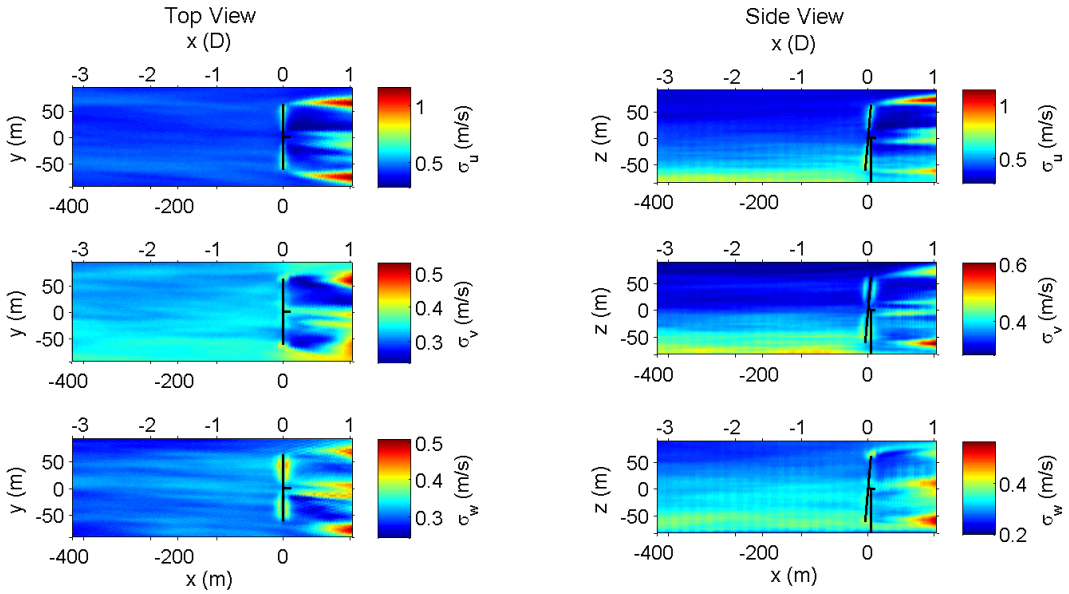

Figure 3.11: Standard deviations of the u, v, and w components near the NREL 5-MW reference turbine in neutral LES wind field 1, with freestream mean wind speed $U = 8$ m/s, generated using SOWFA. The x coordinates are expressed in meters as well as rotor diameters ($D = 126$ m).

operating point, with an axial induction factor of $a = \sim 0.18$. When the wind speed exceeds 11.4 m/s, the NREL 5-MW reference turbine's rated wind speed, however, the axial induction factor decreases in order to regulate power capture. Thus, the induction zone behavior for an arbitrary mean freestream wind speed is determined by assuming that the mean wind speed changes are linearly related to the axial induction factor. Note that while the vortex sheet theory formula presented in Medici *et al.* [53] describes the velocity reductions along the symmetry axis as being linearly related to the induction factor, further analysis using LES is required to determine if the velocity reductions as well as radial wind speeds at all locations in the induction zone can be reasonably approximated as being linearly related to a as well. If δ_x represents the longitudinal position upstream of the rotor and δ_{yz} indicates the radial position, then the mean wind speed $U(\delta_x, \delta_{yz})$ for a specific axial induction factor a corresponding to mean freestream wind speed U_∞ is determined by

$$U(\delta_x, \delta_{yz}) = U_\infty \left(1 - \frac{a}{a_0}\left(1 - \frac{U_0(\delta_x, \delta_{yz})}{U_{\infty,0}}\right)\right), \tag{3.26}$$

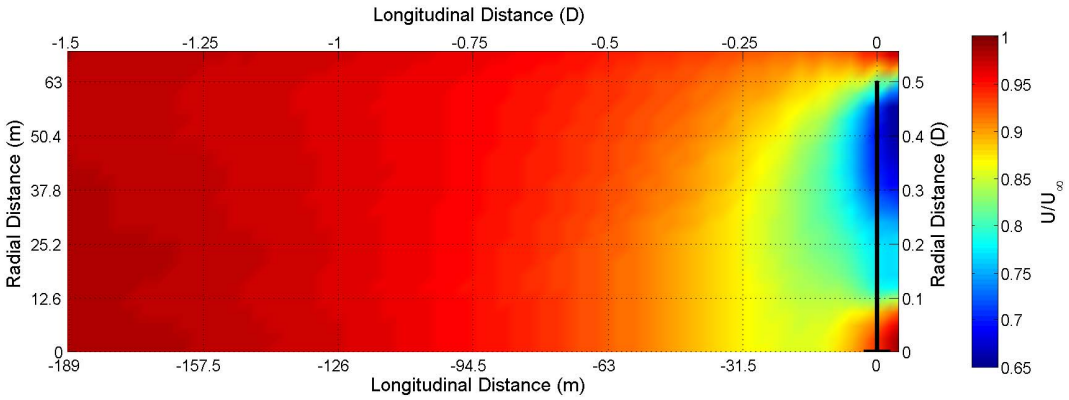

(a) Mean velocity reductions in the induction zone.

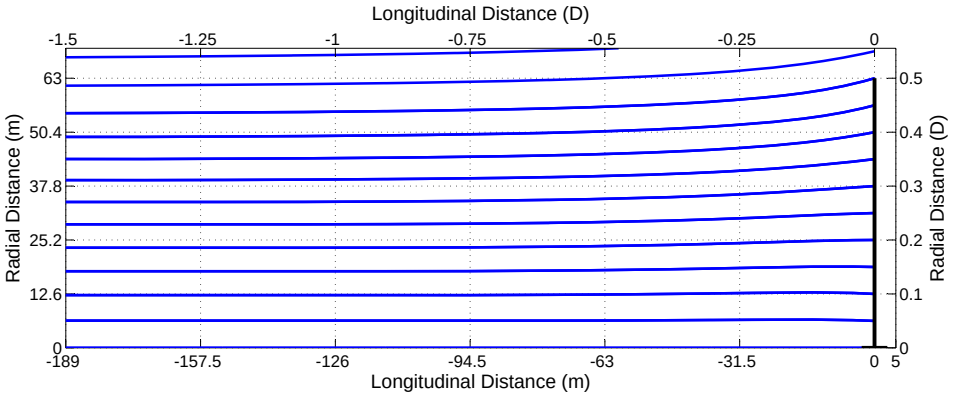

(b) Streamlines of the mean wind velocities in the induction zone.

Figure 3.12: Axisymmetric model of the induction zone based on the NREL 5-MW reference turbine in neutral LES wind field 1, with freestream mean wind speed $U = 8$ m/s, generated using SOWFA. (a) Mean longitudinal wind speed reductions normalized by the freestream wind speed $U_\infty = 8$ m/s. (b) Streamlines created using the mean longitudinal and radial wind velocities.

where $U_{\infty,0} = 8$ m/s, $a_0 = 0.18$, and $U_0\left(\delta_x, \delta_{yz}\right)/U_{\infty,0}$ corresponds to the velocity reductions plotted in Fig. 3.12 (a). Similarly, the radial wind speed $V\left(\delta_x, \delta_{yz}\right)$ is determined as

$$V\left(\delta_x, \delta_{yz}\right) = \frac{a}{a_0}\frac{U_\infty}{U_{\infty,0}} V_0\left(\delta_x, \delta_{yz}\right), \tag{3.27}$$

where $V_0\left(\delta_x, \delta_{yz}\right)$ represents the mean radial wind speeds corresponding to $a_0 = 0.18$ and $U = 8$ m/s. The corrected radial velocity is then projected onto the proper transverse and vertical directions, depending on the specific position (i.e., azimuth angle) in the wind field.

In addition to the CFD-based analysis of the induction zone presented in this section, Appendix A contains results, based on Simley *et al.* [66], from a field measurement campaign performed

at the Danish Technical University's Wind Energy department where three ground-based scanning lidars were used to measure the mean velocities and turbulence characteristics in the induction zone of a 225 kW 27 meter rotor diameter wind turbine for a range of mean wind speeds. The field measurements confirm many of the trends identified in this section, particularly that non-zero mean radial wind components are present near the rotor due to the expansion of the wind inflow around the rotor, that the mean tangential velocities in the induction zone are zero, and that as the mean wind speed increases, causing the turbine's induction factor to decrease, the longitudinal velocity reductions and wind direction changes in the induction zone become smaller. Measurements of turbulence statistics upstream of the rotor show little change in the standard deviation of the tangential wind component in the induction zone, but a slight decrease in the standard deviation of the u component and a slight increase in the standard deviation of the radial component. Since most of the change in turbulence statistics occurs within 0.5 D of the rotor, however, it is unlikely that the change in turbulence standard deviation will significantly affect lidar measurement quality.

3.3.2 The Impact of the Induction Zone on Wind Evolution

Although there is very little change in the standard deviation of the turbulence components in the induction zone, except very close to the rotor, the induction zone does affect the longitudinal coherence describing wind evolution. The impact of the induction zone on wind evolution is assessed by calculating longitudinal coherence in the SOWFA-generated LES wind field analyzed in this section for different longitudinal separations along the streamlines shown in Fig. 3.12 (b), both inside and outside of the induction zone. Specifically, the coherence curves are calculated using wind speeds at pairs of points upstream of the rotor separated by the desired longitudinal distance Δ_x such that the points farthest downstream are longitudinally located at x_0 (thus the upstream points are longitudinally located at $x_0 - \Delta_x$). By varying the offset x_0 from the rotor hub position, the dependence of the longitudinal coherence within the induction zone on the proximity to the rotor can be determined. For longitudinal separations of Δ_x = 31.5 m, 63 m, 126 m, and 252 m (0.25, 0.5, 1, and 2 D), Fig. 3.13 contains coherence curves for longitudinal offsets x_0 between 0

and -63 m (-0.5 D), as well as the freestream coherence, using pairs of wind speeds at hub height across the entire transverse span of the rotor. The freestream coherence curves are calculated using longitudinal offsets x_0 between -252 m and -378 m (2 to 3 D upstream of the rotor).

As revealed by Fig. 3.13, the longitudinal coherence decreases as the offset x_0 approaches the rotor, indicating that wind evolution is more severe within the induction zone than in the freestream flow. The decrease in measurement coherence is particularly large for offsets of $x_0 = 0$, at the rotor plane. Note that a peak in the coherence curve for $\Delta_x = 31.5$ m and $x_0 = 0$ occurs at 0.45 Hz because this is the blade passage frequency at the below-rated mean wind speed $U = 8$ m/s; the points in the wind field used to calculate the coherence curve are sufficiently close to the rotor to experience periodic induced wind speeds at the blade passage frequency. Some reduction in

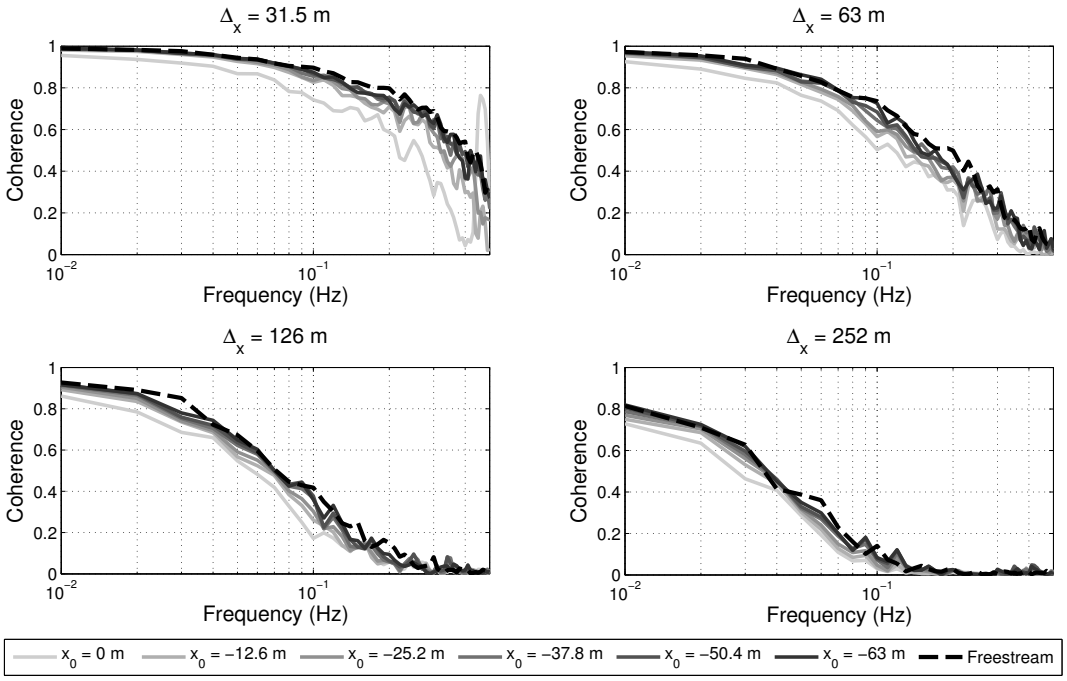

Figure 3.13: Longitudinal coherence curves measured both inside and outside of the induction zone of the NREL 5-MW reference turbine generated using SOWFA with neutral LES wind field 1 for longitudinal separations of $\Delta_x = 31.5$ m, 63 m, 126 m, and 252 m. The coherence curves are generated for different longitudinal offsets x_0 from the hub location between 0 and -63 m using wind speeds across the entire transverse span of the rotor at hub height. The freestream coherence curves are generated using wind speed pairs with longitudinal offsets x_0 between 252 and 378 m upstream of the hub location.

longitudinal coherence is expected within the induction zone, however, because of the reduced mean wind speeds. As revealed by the developed coherence model in (3.21), as the mean wind speed is reduced, the longitudinal coherence decays. Therefore, to correct for the mean wind speed reduction in the induction zone, the developed longitudinal coherence formula is modified using the effective mean wind speed

$$U' = \Delta t_{\vec{x}_1,\vec{x}_2}/\Delta'_x, \tag{3.28}$$

where $\Delta t_{\vec{x}_1,\vec{x}_2}$ indicates the transit time between the wind at points $\vec{x}_1$ and $\vec{x}_2$, calculated by tracing the point closest to the rotor upstream along its mean streamline to the same longitudinal position as the other point. The modified Δ'_x represents the distance that the point closest to the rotor travels along its mean streamline beginning at the longitudinal location of the other point. Thus U' yields a lower mean wind speed that slightly reduces longitudinal coherence.

Furthermore, it has been observed that the temporal frequency content of the turbulence in the induction zone is roughly the same as in the freestream flow. Therefore, the assumption is made that the spatial scale of the turbulence in the longitudinal direction is reduced, and the integral length scale parameter used in the developed coherence model is modified by applying the multiplicative factor U'/U_∞.

In Fig. 3.14, the longitudinal coherence based on the developed model in (3.21) using modified mean wind speed and length scale parameters representative of the behavior in the induction zone is compared to the true measured coherence curves. Specifically, the coherence formula in (3.19) is fit to the measured freestream coherence curves by tuning the a and b parameters such that (3.20) is minimized for each individual longitudinal separation. Next, the best fit coherence formulas are corrected using the modified mean wind speeds and length scales in the induction zone for each longitudinal separation and compared to the measured coherence curves. As can be seen in Fig. 3.14, the drop in longitudinal coherence in the induction zone cannot be explained by the change in the effective mean wind speed alone; additional characteristics of the induction zone contribute to the loss of longitudinal coherence. However, since it is unknown how the longitudinal

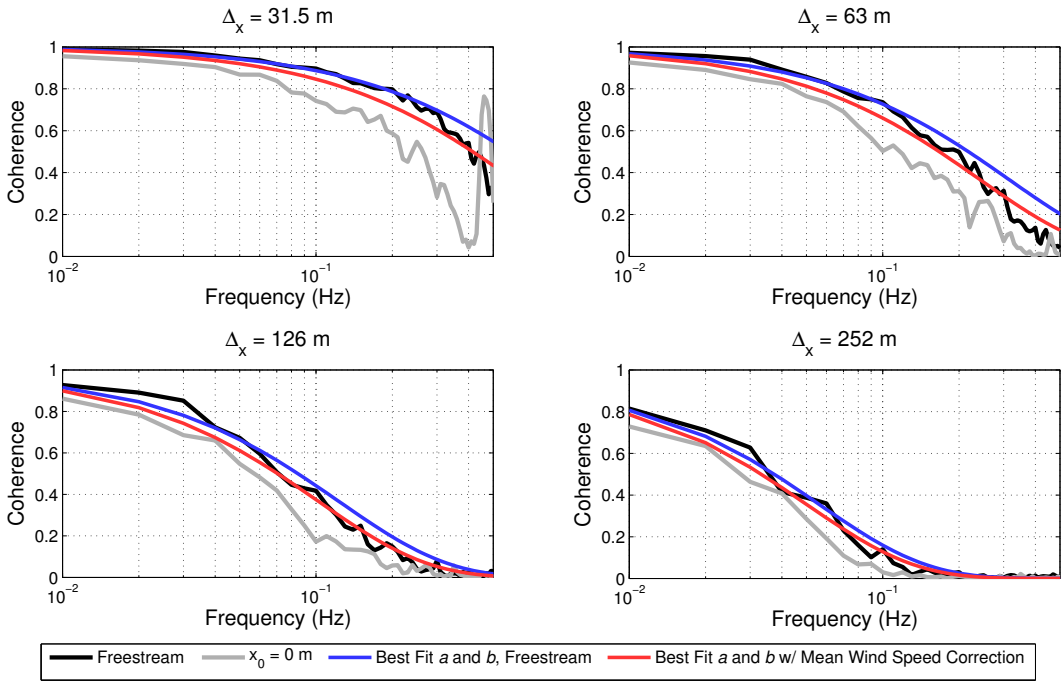

Figure 3.14: Longitudinal coherence curves measured both inside and outside of the induction zone of the NREL 5-MW reference turbine generated using SOWFA with neutral LES wind field 1 for longitudinal separations of $\Delta_x = 31.5$ m, 63 m, 126 m, and 252 m. The coherence curves inside of the induction zone are generated for a longitudinal offset from the hub location of $x_0 = 0$ using wind speeds across the entire transverse span of the rotor at hub height. The freestream coherence curves are generated using wind speed pairs with longitudinal offsets x_0 between 252 m and 378 m upstream of the hub location. Coherence curves given by the coherence formula in (3.19) are fit to the longitudinal coherence curves measured outside of the induction zone using the best fit a and b parameters for each individual longitudinal separation (blue). The best fit coherence curves with modified mean wind speeds U, accounting for the true transit times along the longitudinal distances Δ_x in the induction zone are shown in red.

coherence loss changes for different wind conditions, the calculations of measurement error in this thesis using the induction zone model will simply incorporate the modified mean wind speed and length scale parameters.

3.4 Blade Effective Wind Speeds

Sections 3.1 and 3.2 provide a statistical description of the wind field in which a turbine operates. This section and the next present approaches for modeling the wind speed variables of interest for control purposes that a turbine experiences. One approach for modeling the time-

varying "rotor effective wind speeds" experienced by a turbine is to calculate some spatial average of the spatially-varying turbulent wind speeds over the entire rotor disk area. In Schlipf *et al.* [31], the rotor effective wind speed is determined by averaging the cube of the longitudinal wind speeds over the rotor disk area weighted by the radially-dependent local contribution to power capture at each location. The wind speeds are cubed to reflect the dependence of the turbine's power capture on the cubed wind speed (see (1.1)). The final rotor effective wind speed is formed by taking the cube-root of this average. In this section, an alternate way of defining the wind speeds encountered by the rotor is proposed by treating the rotor as three discrete rotating blades rather than a solid disk. Section 3.5 presents a method for determining rotor effective wind speed variables using three "blade effective wind speeds."

A blade effective weighting function is formed by averaging the wind speeds along the span of the blade, where the spanwise weighting function is based on the local contribution of wind speed changes to some variable of interest. For example, wind speeds could be weighted according to the spanwise contribution to torque, thrust, or out-of-plane blade root bending moment produced along the blade. First, the distribution of torque production along the blade will be calculated due to the interest in regulating rotor speed during above-rated operation, which is heavily dependent on the aerodynamic rotor torque. Following the same calculation approach, the spanwise contribution to the out-of-plane blade root bending moment will be analyzed as well, due to the interest in mitigating blade root bending moments using individual pitch control.

The spanwise dependence on torque production along a blade can be calculated using the blade element momentum (BEM) theory approach implemented in NREL's AeroDyn aerodynamics solver [87] as well as NREL's WT_Perf rotor performance code [88]. For a given mean wind speed, rotor speed, and blade pitch angle, WT_Perf calculates a number of variables for different rotor azimuth angles (indicated by the angle ψ in Fig. 3.1) as a function of the discrete spanwise blade segment. At spanwise position q and azimuth angle ψ_i, AeroDyn and WT_Perf use BEM methods to calculate the local torque production $\delta Q\left(q, \psi_i\right)$ and relate the torque to the local coefficient of

torque $C_Q(q,\psi_i)$ through the following equation:

$$\begin{aligned}\delta Q(q,\psi_i) &= \tfrac{1}{N_b N_\psi}\tfrac{1}{2}\rho U^2 C_Q(q,\psi_i)\, A_{Ann}(q)\, q \\ &\approx \tfrac{1}{N_b N_\psi}\tfrac{1}{2}\rho U^2 C_Q(q,\psi_i)\, 2\pi q^2 \delta q,\end{aligned} \tag{3.29}$$

where U is the wind speed, ρ is the air density, and $A_{Ann}(q)$ is the area of the annulus swept out by the blade segment centered at a distance q along the blade. For normalization purposes, N_b is the number of blades comprising the rotor and N_ψ is the number of azimuth angle segments that the rotor is divided into for analysis. The second line of (3.29) results from linearization of the annulus area as $2\pi q\delta_q$, where δ_q is the width of the spanwise segment.

Airfoil parameters for the NREL 5-MW reference turbine at 17 spanwise locations [8] are used to calculate the torque production and coefficient of torque for 24 evenly spaced azimuth angles using WT_Perf. The torque and C_Q values are then averaged over all azimuth angles to form average torque values as a function of spanwise position:

$$\begin{aligned}\delta Q(q) &= \sum_{i=1}^{N_\psi} \frac{1}{N_b N_\psi}\frac{1}{2}\rho U^2 C_Q(q,\psi_i)\, 2\pi q^2 \delta q \\ &= \tfrac{1}{N_b}\tfrac{1}{2}\rho U^2 C_Q(q)\, 2\pi q^2 \delta q.\end{aligned} \tag{3.30}$$

After eliminating all constants in (3.30), the torque production as a function of spanwise position q along the blade is proportional to

$$Q(q) \sim C_Q(q)\, q^2. \tag{3.31}$$

By employing the same approach using WT_Perf, the spanwise contribution to the out-of-plane blade root bending moment $M_{root,y}$ can be calculated by multiplying the spanwise contribution to rotor thrust by the spanwise position q. Because the coefficient of thrust C_T is defined in a similar manner as the coefficient of torque in AeroDyn and WT_Perf, the contribution to the out-of-plane blade root bending moment as a function of spanwise position q along the blade is simply proportional to

$$M_{root,y}(q) \sim C_T(q)\, q^2. \tag{3.32}$$

Fig. 3.15 illustrates the spanwise contribution to torque production and blade root bending moment using (3.31) and (3.32) calculated with WT_Perf for a variety of mean wind speeds U

using parameters for the NREL 5-MW reference turbine model. As plotted, the spanwise weighting functions are normalized by the peak value of the $U = 11.4$ m/s curve. At the rated wind speed 11.4 m/s, the blade pitch angle is zero and the torque production is almost a linear function of spanwise position, neglecting tip and root losses [7]. At the rated wind speed, the contribution to blade root bending moment is approximately proportional to the square of the spanwise position along the blade. As the wind speed increases above 11.4 m/s, rotor speed is held constant and the blades are pitched to maintain 5 MW of power capture, resulting in more of the torque production and contribution to blade root bending occurring closer to the inboard portion of the blades. At the cut-out wind speed $U = 25$ m/s [8], the outboard region of the blade in fact produces enough drag to negatively contribute to torque production; similarly, the rotor thrust is directed in the upstream direction at the outboard section of the blades. Note that in below-rated conditions, where blade pitch angle is held at zero and the tip-speed ratio is almost constant (near the optimal value to maximize power capture), the spanwise weighting functions are very similar to the curves shown for the rated wind speed $U = 11.4$ m/s.

While the curves in Fig. 3.15 show how the torque production and contribution to out-of-

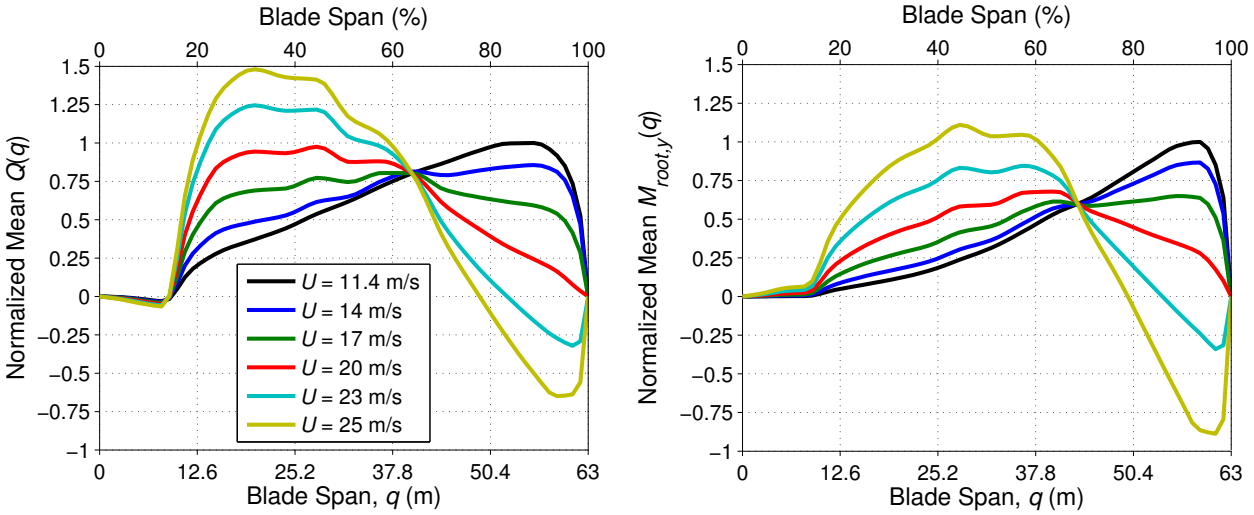

Figure 3.15: Normalized spanwise contribution to torque production and the out-of-plane blade root bending moment for the NREL 5-MW reference turbine for mean wind speeds between the rated wind speed $U = 11.4$ m/s and the cut-out wind speed $U = 25$ m/s.

plane bending moment is distributed along the blade for different above-rated operating points, the weighting variable used to define the time-varying blade effective wind speed in this thesis is the spanwise contribution of the *deviation* of the wind speed to *changes* in the torque or blade root bending along the blade. Because of the need to use linear weighting functions when performing the power spectrum and measurement coherence calculations in Chapters 4 and 5, a linearized blade effective wind speed definition is used, neglecting the dependence of the blade aerodynamics on the square of the wind speed. The torque produced by a blade, for example, can be expressed in linearized form as the mean torque produced at a specific mean wind speed U, mean rotor speed $\overline{\omega}_{rot}$, and mean pitch angle $\overline{\beta}$ plus the linearized change in torque caused by deviations of the wind speeds along the blade ($u'(q)$), rotor speed (ω'_{rot}), and pitch angle (β') from their mean values:

$$Q(u, \omega_{rot}, \beta) = \overline{Q}(U, \overline{\omega}_{rot}, \overline{\beta}) + \int_0^R \frac{\delta Q(q)}{\delta u} u'(q) dq + \frac{\delta Q}{\delta \omega_{rot}} \omega'_{rot} + \frac{\delta Q}{\delta \beta} \beta', \tag{3.33}$$

where $u'(q)$ represents the deviation of the wind speed as a function of the spanwise position along the blade, R is the rotor radius, and $\frac{\delta Q(q)}{\delta u}$ represents the partial derivative of the torque production at spanwise position q with respect to changes in the wind speed. The linearized blade effective wind speed u_b is defined as the single effective wind speed deviation from U present along the entire span of the blade that would produce the same linearized aerodynamic torque as the actual spatial distribution of wind speeds at a given time. By replacing $u'(q)$ with u_b in (3.33) such that the linearized torque production remains unchanged, the linearized blade effective wind speed can be expressed as

$$u_b = \frac{\int_0^R \frac{\delta Q(q)}{\delta u} u'(q) dq}{\int_0^R \frac{\delta Q(q)}{\delta u} dq}. \tag{3.34}$$

In a more general form, the linearized blade effective wind speed for azimuth angle ψ in the rotor plane, formed by treating the blade as an infinitely thin line in space and ignoring the vertical tilt angle of the rotor as well as the rotor precone angle, can be written as

$$u_{b,\psi} = \int_0^R W_b(q)\, u_{q\bar{b}} dq, \tag{3.35}$$

where $W_b(q)$ is the spanwise dependent blade effective weighting function and $u_{q\vec{b}}$ represents the longitudinal wind speed at $q\vec{b}$ with $\vec{b}$ defined as the azimuth angle-dependent unit vector $\vec{b} = [0, -\sin\psi, \cos\psi]$. The torque-based blade effective weighting function described in (3.34) is equivalent to

$$W_b(q) = \frac{\frac{\delta Q(q)}{\delta u}}{\int_0^R \frac{\delta Q(q)}{\delta u} dq}. \tag{3.36}$$

In a similar manner, the blade effective weighting function based on the spanwise sensitivity of the contribution to the out-of-plane blade root bending moment along the blade to changes in the wind speed can be written as

$$W_b(q) = \frac{\frac{\delta M_{root,y}(q)}{\delta u}}{\int_0^R \frac{\delta M_{root,y}(q)}{\delta u} dq}. \tag{3.37}$$

Note that for simplicity, the transverse v and vertical w wind speed components are not included in the calculation of blade effective wind speed because they do not affect the rotor aerodynamics as much as the dominant u component [87]. However, as the mean wind speed increases in above-rated conditions, the sensitivity of the torque and thrust produced by the rotor to changes in angle-of-attack along the blade becomes larger. Therefore, the v and w wind components are expected to have more of an impact on the rotor aerodynamics at higher mean wind speeds during above-rated operation.

The blade effective weighting functions based on spanwise sensitivity of torque production or contribution to the out-of-plane blade root bending moment to wind speed deviations given in (3.36) and (3.37), calculated using WT_Perf, are provided in Fig. 3.16 for the same rated and above-rated mean wind speeds (and corresponding pitch angles) for which the curves in Fig. 3.15 are shown. Although the blade effective weighting functions are defined such that they integrate to 1 over the span of the blade, they are plotted normalized by the peak value of the $U = 11.4$ m/s curves. Contrary to the behavior of the weighting functions plotted in Fig. 3.15 based on the total spanwise contribution to torque and blade root bending at the mean operating conditions, the blade effective weighting functions based on the sensitivity of these variables to wind speed

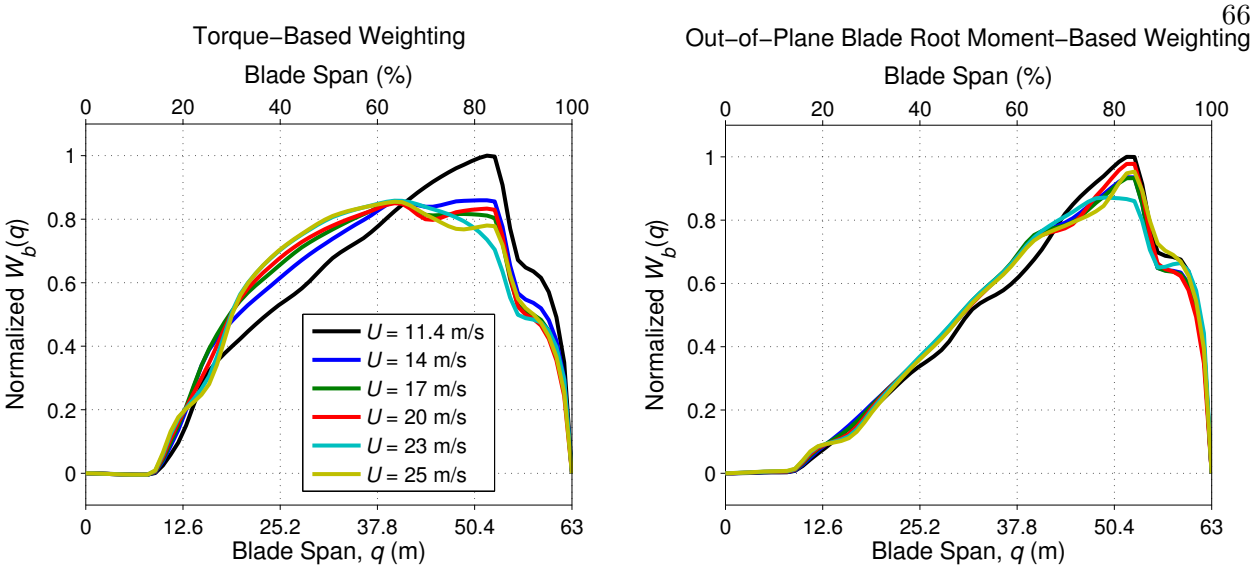

Figure 3.16: Normalized blade effective weighting functions for the NREL 5-MW reference turbine model based on the sensitivity of both the spanwise torque production, as well as the spanwise contribution to the out-of-plane blade root bending moment, to changes in wind speed for mean wind speeds between the rated wind speed of $U = 11.4$ m/s and the cut-out wind speed of $U = 25$ m/s.

fluctuations, shown in Fig. 3.16, do not vary significantly as the mean wind speed increases above the rated wind speed. Essentially, while the spanwise contribution to torque and blade root bending varies considerably as the wind speed increases and the blades are pitched more to regulate power capture, thus shifting more of the contribution to the inboard section of the blades, the spanwise sensitivity to changes in the wind speeds remain almost constant, with the emphasis remaining on the outboard region of the blade regardless of the operating condition. The largest exception is for the torque sensitivity-based weighting functions close to the rated wind speed of $U = 11.4$ m/s, where the outboard section of the blade is emphasized even more than at higher wind speeds. Note that the blade effective weighting functions in below-rated conditions, where the blade pitch angle is kept at zero and the tip-speed ratio is approximately constant, are very similar to the weighting functions at the rated wind speed, resulting in similar aerodynamic behavior regardless of the specific mean wind speed.

3.5 Rotor Effective Wind Speeds

In this section, it is shown how three blade effective wind speeds can be used to determine rotor effective wind speed variables including the effective uniform wind speed and linear horizontal and vertical shear components. The individual blade effective wind speeds are converted into rotor effective variables because it is more common to design control systems that mitigate the effect of rotor-scale wind disturbances rather than disturbances local to individual rotating blades. For example, the multiblade coordinate (MBC) transform [38] allows individual pitch control to be used to reject rotor effective shear disturbances [10, 11] in addition to the effective uniform wind speed across the rotor. Furthermore, linear models of wind turbine dynamics used for model-based control are more accurate when calculated in the "non-rotating" frame after applying the MBC transform [38]. The three blade effective wind speed variables are therefore transformed into an equivalent rotor effective uniform, or hub-height, component u_{hh} and variables describing the slope of the linear horizontal (Δ_h) and vertical (Δ_v) shears across the rotor in units of m/s/m or 1/s. Thus the wind speed at a point in space $\vec{x}$ can be written as $u = u_{hh} + \Delta_h y + \Delta_v z$, where u_{hh} is the wind speed at the hub location, which is also the origin.

By treating the wind field as consisting only of u_{hh}, Δ_h, and Δ_v components and applying (3.35), the blade effective wind speed for blade i and rotor azimuth angle ψ can be written as

$$u_{b_i,\psi} = u_{hh} + \int_0^R W_b(q) \left(\cos\left(\psi + \frac{(i-1)\,2\pi}{3} \right) \Delta_v q - \sin\left(\psi + \frac{(i-1)\,2\pi}{3} \right) \Delta_h q \right) dq, \tag{3.38}$$

where the azimuth angle of blade i is defined as $\psi + (i-1)\,2\pi/3$. Using (3.38), the three blade effective wind speeds can be related to u_{hh}, Δ_h, and Δ_v through the following matrix equation:

$$\begin{bmatrix} u_{b_1,\psi} \\ u_{b_2,\psi} \\ u_{b_3,\psi} \end{bmatrix} = T(\psi) \begin{bmatrix} u_{hh} \\ \Delta_h \\ \Delta_v \end{bmatrix}, \tag{3.39}$$

where

$$T(\psi) = \begin{bmatrix} 1 & -\int_0^R W_b(q)\sin(\psi)qdq & \int_0^R W_b(q)\cos(\psi)qdq \\ 1 & -\int_0^R W_b(q)\sin\left(\psi+\frac{2\pi}{3}\right)qdq & \int_0^R W_b(q)\cos\left(\psi+\frac{2\pi}{3}\right)qdq \\ 1 & -\int_0^R W_b(q)\sin\left(\psi+\frac{4\pi}{3}\right)qdq & \int_0^R W_b(q)\cos\left(\psi+\frac{4\pi}{3}\right)qdq \end{bmatrix} \tag{3.40}$$

is similar to the MBC transformation matrix discussed in Bir [38].

Because $T(\psi)$ in (3.40) is an invertible matrix, the effective u_{hh}, Δ_h, and Δ_v components can be found for any three blade effective wind speeds:

$$\begin{bmatrix} u_{hh} \\ \Delta_h \\ \Delta_v \end{bmatrix} = T^{-1}(\psi) \begin{bmatrix} u_{b_1,\psi} \\ u_{b_2,\psi} \\ u_{b_3,\psi} \end{bmatrix}, \tag{3.41}$$

where

$$T^{-1}(\psi) = \begin{bmatrix} \frac{1}{3} & \frac{1}{3} & \frac{1}{3} \\ -\frac{2\sin(\psi)}{3\int_0^R W_b(q)\,qdq} & -\frac{2\sin\left(\psi+\frac{2\pi}{3}\right)}{3\int_0^R W_b(q)\,qdq} & -\frac{2\sin\left(\psi+\frac{4\pi}{3}\right)}{3\int_0^R W_b(q)\,qdq} \\ \frac{2\cos(\psi)}{3\int_0^R W_b(q)\,qdq} & \frac{2\cos\left(\psi+\frac{2\pi}{3}\right)}{3\int_0^R W_b(q)\,qdq} & \frac{2\cos\left(\psi+\frac{4\pi}{3}\right)}{3\int_0^R W_b(q)\,qdq} \end{bmatrix}. \tag{3.42}$$

Equation (3.41) reveals that for a given azimuth angle ψ, three arbitrary blade effective wind speeds can be transformed into equivalent rotor effective hub-height and linear shear components. Thus any spatial distribution of wind speeds encountered by the rotor at a particular instance can be equivalently described as u_{hh}, Δ_h, and Δ_v components through the use of linear blade effective wind speeds. As the blades rotate through the spatially-varying turbulent wind field, the blade effective wind speeds change, producing time-varying rotor effective wind components. Finally, the shear components are transformed into the alternate definitions used in the AeroDyn [87] and FAST [9] simulation codes:

$$\delta_h = D \cdot \Delta_h / u_{hh} \tag{3.43a}$$

$$\delta_v = D \cdot \Delta_v / u_{hh}, \tag{3.43b}$$

where δ_h and δ_v describe the difference in the wind speeds across the rotor disk in the horizontal and vertical directions normalized by the hub-height wind speed.

In the remainder of this thesis, the blade effective weighting function based on the spanwise sensitivity of torque production to changes in wind speed, defined in (3.36), is used to determine the rotor effective hub-height component, to reflect the impact of u_{hh} on rotor torque, and therefore rotor speed fluctuations, which can be addressed using collective pitch control. On the other hand, the horizontal and vertical shear components are determined using the blade effective weighting function based on the sensitivity of the out-of-plane blade root bending moment to wind speed deviations, given in (3.37), since shear has a larger impact on blade root bending moments, which can be addressed using individual pitch control, than on rotor torque.

3.6 Discussion and Conclusions

This chapter presented a statistical frequency-domain wind field definition including wind evolution through a developed longitudinal coherence model based on CFD simulations. A simplified model of the mean wind speed behavior in the turbine's upstream induction zone was created based on results from NREL's SOWFA code, which simulates the two-way interaction between wind turbines and the atmospheric boundary layer. This induction zone model will be applied in Chapter 5 to determine how lidar measurement quality is affected by the induced velocities upstream of the rotor. Further induction zone results based on field measurements can be found in Appendix A. Although it was observed that the induction zone also causes the severity of wind evolution to increase close to the rotor, further work is required to determine how the change in wind evolution depends on the specific turbine operating conditions and wind conditions. Finally, the rotor effective hub-height and linear horizontal and vertical shear components that are of interest in wind turbine control applications, and which are to be estimated using lidar measurements, are defined using the concept of blade effective wind speeds. In order to create this rotor effective wind speed model, however, the blade effective wind speed definition is simplified by assuming that the aerodynamic torque is a linear function of the wind speeds along the blade and that the v and

w components do not affect the torque production. In Chapter 7, the accuracy of the simplified linear rotor effective wind speed modeling approach is assessed through comparison with the estimated hub-height and shear components resulting from aeroelastic wind turbine simulations using the wind speed estimator described in Chapter 6. The frequency-domain wind field model and the rotor effective wind component definitions are applied in Chapter 5 to determine lidar measurement coherence for different wind conditions and lidar configurations using the lidar model described in the next chapter.

Acknowledgements

Dr. Paul Fleming is greatly acknowledged for providing the SOWFA-generated LES data used to develop the wind evolution model in Section 3.2. The SOWFA data used to analyze the induction zone in Section 3.3 was generated and provided by Dr. Pieter Gebraad, whose effort is greatly appreciated. Finally, assistance from Dr. Matthew Churchfield, who provided additional SOWFA data used to investigate the induction zone and wind evolution, and who also helped explain the SOWFA simulation approach, is tremendously appreciated as well.

Chapter 4

Lidar Modeling

4.1 Lidar Background

Various optical and acoustical methods exist for remotely measuring wind speeds, including incoherent "direct detection" lidar (light detection and ranging), coherent Doppler lidar, and sodar (sonic detection and ranging) [13]. Sodar relies on detecting the echo from emitted sound waves reflecting off of temperature and velocity fluctuations in the wind [13]. The Doppler shift of the echo is then used to determine the velocity of the wind. However, the background noise as well as the presence of spurious echos from the ground, etc. make sodar an unattractive option for turbine-mounted wind speed measurements [13]. Both incoherent and coherent lidar technologies rely on detecting the light emitted along a laser beam that is backscattered off of aerosols flowing in the wind, using the basic assumption that the aerosols travel at the same speed as the wind. Incoherent lidar relies on measuring the intensity of the backscattered light along the beam direction [13, 89]. By tracking how the distribution of the backscattered light intensity along the beam changes over time, the velocity of the aerosols, and thus the wind, can be determined. However, due to the cost and size of direct detection lidars, coherent Doppler lidar technology, which is relatively inexpensive and accurate, has comprised the majority of commercial and research lidars developed for wind energy applications [13, 89, 90].

Coherent lidar uses the Doppler shift of light that is backscattered off of aerosols in the wind and collected by the lidar's telescope to determine the velocity of the wind projected along the lidar beam direction, also known as the "line-of-sight" velocity [13, 89, 90]. Representing the

line-of-sight velocity detected by the lidar as u_{los}, the frequency of the backscattered light is equal to the frequency of the emitted laser beam plus the following Doppler shift:

$$\delta f = \frac{2u_{los}}{\lambda}, \tag{4.1}$$

where λ is the laser wavelength, typically in the infrared around 1.5 μm [89]. A heterodyne receiver is used to mix the transmitted reference laser signal with the backscattered signal. An intensity proportional to the square of the sum of these two signals is measured by a photodetector, yielding a constant term as well as a term that is proportional to $\cos(\delta f)$ [89]. By mixing the THz-band backscattered signal down to the baseband, the heterodyne receiver allows the $\cos(\delta f)$ term to be digitally sampled so that the Doppler shift frequency can be determined [89, 90]. Through (4.1), the magnitude of the line-of-sight wind velocity can be estimated in a straightforward manner.

The two main coherent lidar technologies that are widely used in wind turbine control applications are continuous-wave (CW) lidar [89] and pulsed lidar [90], which can both be implemented using relatively inexpensive fiber technology developed for the telecommunications industry. In CW lidar systems, continuously emitted laser light is focused at a specific distance along the beam, and the majority of the backscattered light is reflected off of aerosols near the focus distance. By changing the focus distance using a focus motor which moves the end of the laser-emitting fiber relative to the telescope lens, CW lidars can measure the wind at multiple ranges [89]. Pulsed lidars, by contrast, can measure the wind at multiple ranges along the beam simultaneously. A pulsed lidar emits a short pulse of laser light (on the order of 200 ns [91]) and collects the backscattered light for some duration of time [90]. The wind speed at a particular distance F can be determined by measuring the Doppler shift of a segment of the backscattered signal measured $2F/c$ s after the pulse was emitted, where c is the speed of light and $2F/c$ is the round-trip travel time from the lidar to the range of interest. By separating the measured backscattered signal into multiple time segments, the velocities at a corresponding set of "range gates" can be estimated.

In this section, models of two commercially available lidars are compared: a CW lidar model based on the ZephIR 300 lidar [89, 91] and a pulsed lidar model similar to the WindCube WLS7 [90,

91]. Both manufacturers have developed lidars designed for measuring the wind profile using an upward-oriented ground-based configuration as well as for control applications using a forward-staring nacelle-mounted configuration. The ZephIR 300 CW lidar technology is capable of providing velocity measurements at a rate of 50 Hz, but is limited to focus distances of less than approximately 200 m [89]. On the other hand, the pulsed lidar is capable of measuring wind velocities at 30 m-wide range gates for distances from 40 m to several hundred meters, but samples the wind velocity at a slower rate, on the order of 1 Hz [90]. In general, however, pulsed lidars can measure at distances on the order of several km, while CW lidars are limited to a few hundred meters due to inherent optical limitations [89, 90]. In the remainder of this thesis, a model of the ZephIR CW lidar is used to analyze preview measurement error for control applications because of the higher sampling rate and the need to only measure up to 100-200 m upstream of the turbine. However, further details of the WindCube pulsed lidar are provided in Section 4.1.1 for comparison.

4.1.1 Range Weighting

Neither CW nor pulsed lidar technologies are capable of measuring the wind speed at a single point in space. Rather than only detecting the wind speed at the focus distance (CW) or the center of the range gate (pulsed), wind speed values in a volume along the entire length of the laser beam contribute to the detected line-of-sight velocity, forming a "range-weighted" measurement. Since the transverse dimension of the laser beam is very narrow compared to the along-range length of the sampling volume, the sampling volume can be treated as an infinitely thin beam. The range weighting measurement process can be described as the integral of line-of-sight wind speeds along the lidar beam weighted according to a range weighting function $W_\ell\,(F, s)$, where F is the measurement distance and s represents the range along the beam:

$$u_\ell = \int_0^\infty u_{los}(s) W_\ell(F, s) ds, \tag{4.2}$$

with u_ℓ representing the lidar measurement [92].

For a CW lidar, when the effects of refractive turbulence on laser propagation are ignored [92],

the CW range weighting function for a focus distance F is given by

$$W_\ell(F,s) = \begin{cases} \dfrac{K_N}{s^2 + (1-\frac{s}{F})^2 R_R^2}, & \text{if } s \geq 0 \\ 0, & \text{otherwise,} \end{cases} \tag{4.3}$$

where R_R is the Rayleigh range and K_N is a normalizing constant so that

$$\int_{-\infty}^{\infty} W_\ell(F,s)ds = 1. \tag{4.4}$$

The Rayleigh range, which is defined here as the distance it takes for the cross-sectional area of a collimated Gaussian beam emitted from the lidar telescope to double, is given by

$$R_R = \frac{\pi a_2^2}{\lambda}, \tag{4.5}$$

where λ is the laser wavelength and a_2 is the e^{-2} intensity radius of the Gaussian laser beam [92]. The analyses in this thesis assume $\lambda = 1.565$ μm and $a_2 = 2.8$ cm, which are similar to the parameters of the ZephIR 300 Doppler lidar system [89].

Although pulsed lidar systems do not rely on focusing a laser at the range of interest as CW systems do, their spatial averaging can be similarly described by a range weighting function. The shape of the pulse emitted by a pulsed system can usually be approximated as Gaussian:

$$I_n(F,s) = \frac{1}{\sqrt{\pi} r_p} e^{-\frac{(F-s)^2}{r_p^2}}, \tag{4.6}$$

where F, although not the "focus distance" as it is for CW lidars, represents the distance to the center of the range gate of interest and the e^{-1} half-width of the pulse r_p is given by

$$r_p = \frac{\Delta r}{2\sqrt{\ln(2)}}, \tag{4.7}$$

where Δr is the Full-Width-at-Half-Maximum (FWHM) pulse width [93]. Backscattered light returns are integrated as the Gaussian pulse travels through the range gate volume according to the range weighting function

$$W_\ell(F,s) = \frac{1}{\Delta p} \int_{-\frac{\Delta p}{2}}^{+\frac{\Delta p}{2}} I_n(F, s+p)dp, \tag{4.8}$$

where Δp is the size of the range gate. After integrating (4.8), in terms of the "Erf" function, the range weighting function for a range gate centered at a distance F away from the lidar [91, 93] is given by

$$W(F,s) = \frac{1}{2\Delta p}\left\{\text{Erf}\left(\frac{s-F+\frac{\Delta p}{2}}{r_p}\right) - \text{Erf}\left(\frac{s-F-\frac{\Delta p}{2}}{r_p}\right)\right\}. \tag{4.9}$$

The approximate parameters for the commercially available WindCube WLS7 lidar are $\Delta r = 30$ m and $\Delta p = 30$ m [91]. The Windcube lidar is actually a hybrid focused/pulsed system with the focus at a range of about 100 m. This hybrid nature alters the range weighting function slightly from the derivation in (4.6) through (4.9), but the range weighting function in (4.9) is a good approximation for the range gate near $F = 100$ m.

Examples of the range weighting functions in (4.3) and (4.9) for the CW lidar model based on the ZephIR 300 with focus distances of $F = 50$ m, 125 m, and 200 m and the pulsed lidar model based on the WindCube WLS7 are provided in Fig. 4.1. The full-width-at-half-maximum (FWHM) of the CW lidar's range weighting function scales with the square of the focus distance and can be approximated as $0.0013 \cdot F^2$. For very short focus distances the lidar measurements are close to point measurements, but at distances greater than 200 m the lidar beam cannot be focused effectively, leading to the limitation on the measurement distance of approximately 200 m. The pulsed lidar's range weighting function, on the other hand, is constant regardless of the range gate distance. As discussed in Simley *et al.* [39], the error caused by range weighting is roughly equivalent for the CW and pulsed lidars at a focus distance of $F = 135$ m. For greater focus distances, the CW lidar measurement spatially averages the wind more than the pulsed lidar. In Sections 4.2.3 and 4.2.4, the impact of range weighting on measurement coherence will be analyzed.

4.1.2 Determining Velocities from Lidar Doppler Spectra

The lidar wind speed measurement process is not as simple as the weighting integral in (4.2) suggests. In reality, a Doppler spectrum is calculated which contains energy at Doppler shift frequencies corresponding to the velocities encountered along the lidar beam weighted by the range weighting function, as well as background noise. Background noise sources include dark noise

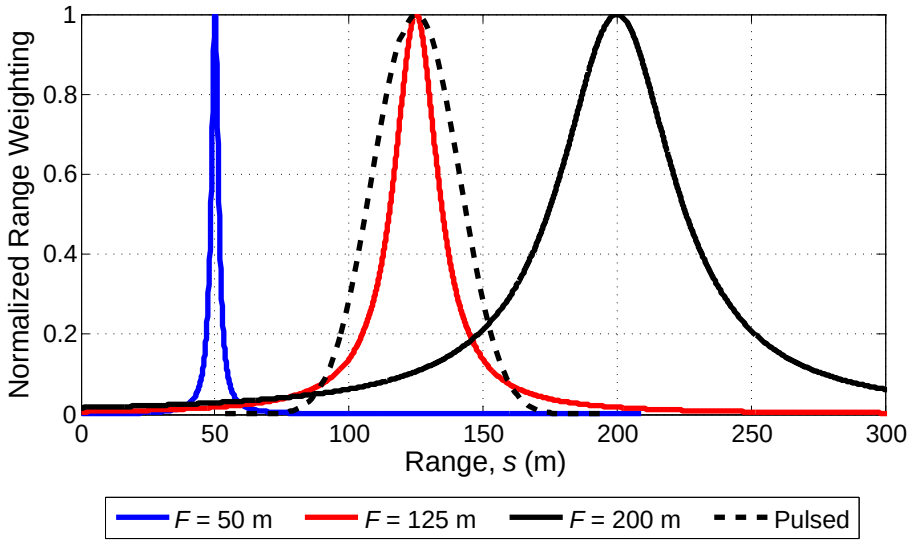

Figure 4.1: Normalized lidar range weighting functions for a CW lidar with focus distances of $F = 50$ m, 125 m, and 200 m and a pulsed lidar with range weighting that is independent of measurement distance.

produced by the photodetector and signal amplifier during the detection process and photon shot noise due to the random generation of photons at the photodetector [89, 92], both discussed in Pitter *et al.* [89]. Note that the signal-to-noise ratio of the Doppler spectrum is independent of the focus distance [89], which is not the case with pulsed lidars. Because the backscattered light detected by the lidar is very weak, many Doppler spectra are averaged together to reduce the noise level, forming a spectrum that can be used to estimate the true wind velocity. For the ZephIR CW lidar with a sampling rate of 50 Hz, approximately 4,000 individual spectra calculated from 5 μs segments of data are averaged during each sample period [91]. By sampling the baseband signal using an analog-to-digital converter with a 100 MHz sampling rate, 512 samples yielding 256 discrete frequency bins contribute to each Doppler spectrum [89, 94]. The resulting frequency resolution of 0.195 MHz produces a velocity resolution of $\sim$0.15 m/s using the Doppler shift formula (4.1). As explained in Angelou *et al.* [94], the Doppler spectrum obtained at each time step is normalized by the mean background noise spectrum, which, for example, can be calculated over a period of $\sim$60 s, resulting in a whitened noise floor, i.e., equal noise power in each frequency bin.

Once a Doppler spectrum with a whitened noise floor is obtained, the line-of-sight velocity needs to be estimated. Fig. 4.2 contains a whitened Doppler spectrum (in blue) obtained during one sampling period using the short-range WindScanner lidar [95] developed by the Danish Technical University Wind Energy department (DTU Wind Energy). Note that the Doppler frequency axis is represented in terms of the equivalent velocity using (4.1). The WindScanner lidar, which is based on a modified ZephIR CW lidar, mixes the detected signal during the heterodyne process such that zero Doppler shift results in a detected frequency of 27 MHz rather than 0 Hz [94]. This way, negative velocities produce frequencies less than 27 MHz while positive velocities cause detected frequencies greater than 27 MHz. Without the use of an intermediate frequency in the heterodyne process, the lidar cannot distinguish the sign of the velocity, as is the case in the commercially available ZephIR lidar [89]. To separate the true velocity Doppler spectrum from the remaining noise floor, a threshold above the mean value of 1 is defined, such that values of the spectrum greater than the threshold level are attributed to the detected wind velocities. The threshold value can be as high as five times the standard deviation of the noise floor above the mean value of 1 [94], which is a conservative value used in the ZephIR lidar [89]. The threshold value shown in Fig. 4.2 (solid black) is defined as twice the noise standard deviation above the mean spectrum level, resulting in the true Doppler spectrum estimate shown in red.

Given the thresholded Doppler spectrum shown in Fig. 4.2, there are three common ways of estimating the line-of-sight velocity. The simplest method, the maximum (max.) estimate, represented as the dashed black line, treats the location of the peak of the Doppler spectrum as the measured velocity. The centroid estimation method, indicated by the dashed green line, treats the spectrum values as masses and uses the centroid velocity based on the mass distribution as the line-of-sight velocity estimate. Finally, the median method, shown as the dashed magenta line, finds the Doppler velocity that divides the integrated spectrum into two equal areas. These estimation methods are compared in more detail in Angelou *et al.* [94]. The max. method is susceptible to spurious spikes in the spectrum, and does not necessarily represent the velocity region where most of the spectrum's energy is concentrated. The centroid method, which is appropriate for

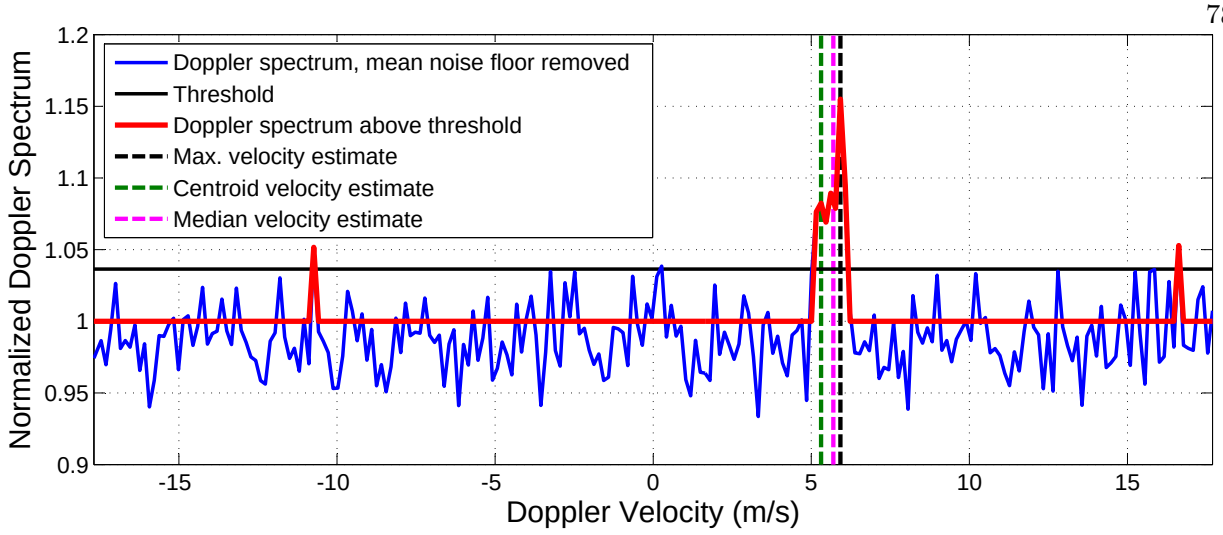

Figure 4.2: Example of a Doppler spectrum used to estimate the line-of-sight velocity measured by a DTU Wind Energy Short-Range WindScanner lidar with $F = 61.4$ m. The spectrum normalized by the mean noise floor (blue) is used to estimate the standard deviation of the remaining noise. Spectrum values above a threshold, defined here as twice the noise standard deviation plus the mean value of 1 (solid black), are treated as the part of the Doppler spectrum caused by detected wind speeds. The thresholded Doppler spectrum (red) is used to estimate the line-of-sight velocity using the max. method (dashed black), centroid method (dashed green), and median method (dashed magenta).

very high signal-to-noise ratios, is susceptible to spurious noise at Doppler velocities far from the main concentration of spectrum energy (e.g., the spike near -11 m/s), and can produce distorted velocity estimates. The median method is recommended as a more robust estimation technique [94]. It should be noted that while the range weighting equation in (4.2) corresponds to the centroid method, the median method produces similar estimates in the absence of noise [96]. Therefore, the lidar measurement process will still be analyzed using the range weighting integral in (4.2), which is easily described analytically.

In addition to the noise floor in the Doppler spectrum, an additional source of measurement noise exists, called spectral broadening [96, 97]. If a single discrete wind velocity is detected along the lidar beam, then the bandwidth of the Doppler spectrum will be inversely proportional to the sampling period. In the general case where different velocities along the beam contribute to the spectrum, spectral broadening will still occur, which increases as the sampling period becomes

smaller. Since the Doppler spectra are calculated using a short sampling period of $\sim$5 μs, the resulting spectrum will be somewhat broadened. Additionally, for a scanning lidar beam or a beam direction that is not aligned with the wind direction, the time that an aerosol is illuminated by the laser beam could be reduced to less than the sampling period, causing further spectral broadening [96]. When determining the line-of-sight velocity from the Doppler spectrum, spectral broadening causes additional uncertainty in the velocity estimate [97]. In Simley *et al.* [39], the white noise floor of the velocity measurement signal caused by spectral broadening and other spectral noise present in measurements obtained using a spinner-mounted circularly-scanning CW lidar [47] is estimated. The resulting standard deviation of the measurement noise is estimated to be between 0.02 and 0.2 m/s. While this noise is dominant at high frequencies, other error sources, such as wind evolution, are dominant in the bandwidth of interest for wind turbine control (up to $\sim$1 Hz). Therefore lidar measurement noise is ignored in the rest of the analyses in this thesis.

4.2 Lidar Measurement Scenario and Error Sources

In the remainder of this chapter, various sources of lidar measurement error are discussed using the hub-mounted circularly-scanning lidar measurement scenario shown in Fig. 4.3 and demonstrated on a utility-scale wind turbine by Mikkelsen *et al.* [47]. The lidar is used to estimate the longitudinal u component of the wind by measuring the line-of-sight velocity at a preview distance d upstream of the turbine along a circle with scan radius r. It is assumed that the scan circle is centered around the x axis, (i.e., zero yaw error is assumed). The CW range weighting function is illustrated using the magenta curve along the lidar beam. Rotating lidar measurements are analyzed in Chapter 5, while stationary measurements are assumed in the rest of this chapter. Lidar measurement quality is analyzed using parameters for the NREL 5-MW reference turbine with rotor diameter $D = 126$ m (and rotor radius $R = 63$ m). However, the 5° rotor shaft tilt and 2.5° rotor precone angle are ignored [8].

In the following sections, various lidar measurement error sources are analyzed in terms of their impact on measurement coherence. Section 4.2.1 discusses the error caused by estimating

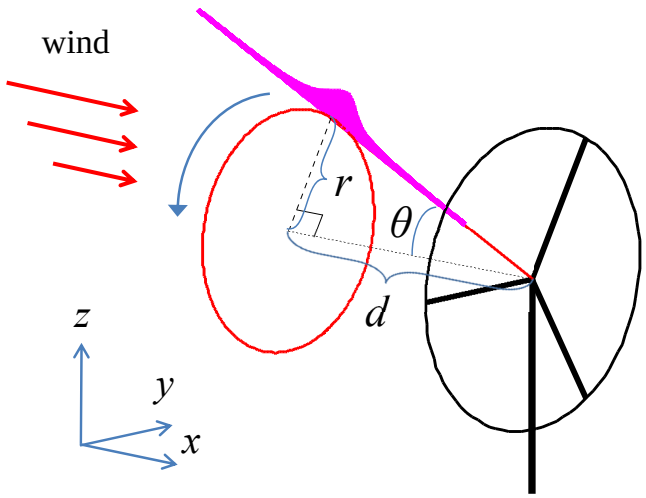

Figure 4.3: Hub-mounted circularly-scanning lidar scenario for a CW lidar showing the preview distance d, scan radius r, and measurement cone angle θ.

the u component of the wind at a single point from a line-of-sight measurement. Section 4.2.2 additionally includes the impact of wind evolution, while the effect that range weighting has on measurement quality is analyzed in Section 4.2.3. Finally, in Section 4.2.4, measurement error is analyzed for lidar measurements of blade effective wind speed. The strategy used for deriving measurement coherence given a frequency domain wind field model is to express all power spectra or cross-spectra involving lidar measurements or blade effective wind speeds as linear combinations of individual cross-spectra between wind speeds at two discrete points, using the definitions in Chapter 3. This general strategy for "semi-analytically" determining measurement coherence was originally developed in Schlipf *et al.* [50] and expanded upon in Simley *et al.* [63] and Simley and Pao [64].

4.2.1 Line-of-Sight Measurement Errors

Without range weighting, the line-of-sight wind speed measurement u_ℓ at the location

$$\vec{x}_2 = [-d, -r\sin(\psi), r\cos(\psi)] \tag{4.10}$$

along the scan circle, assuming a hub-mounted lidar, can be written as the projection of the wind speed vector onto the lidar beam direction:

$$u_\ell = -\ell_x u_{\vec{x}_2} - \ell_y v_{\vec{x}_2} - \ell_z w_{\vec{x}_2}, \tag{4.11}$$

where

$$\vec{\ell} = [\ell_x, \ell_y, \ell_z] \tag{4.12}$$

is the unit vector oriented in the direction that the lidar beam is pointing using the coordinate system shown in Fig. 3.1. Note that the negative signs appear in (4.11) because the velocity vector is projected along the direction *opposite* the direction the lidar is pointing to form the line-of-sight velocity. Using the line-of-sight measurement, an estimate of the longitudinal u component, which generally has the greatest impact on the aerodynamic response of the rotor, is formed. By assuming that the typically smaller v and w components are zero, the u component can be estimated by dividing the line-of-sight measurement by $-\ell_x$:

$$\begin{aligned} \hat{u}_{\vec{x}_2} &= -\tfrac{1}{\ell_x} u_\ell \\ &= u_{\vec{x}_2} + \tfrac{\ell_y}{\ell_x} v_{\vec{x}_2} + \tfrac{\ell_z}{\ell_x} w_{\vec{x}_2}. \end{aligned} \tag{4.13}$$

As revealed in (4.13), the transverse and vertical wind speed components act as error sources during estimation of the u component. As the lidar cone angle $\theta = \arctan(r/d)$ increases, the ratios ℓ_y/ℓ_x and ℓ_z/ℓ_x become larger causing the line-of-sight errors to increase. As the cone angle approaches zero ($r/d \to 0$), the line-of-sight errors become negligible.

If the objective is to estimate the u component at the point $\vec{x}_2$, then the measurement coherence between $\hat{u}_{\vec{x}_2}$ and $u_{\vec{x}_2}$, using CT Fourier transform theory, is defined as

$$\gamma^2_{u_{\vec{x}_2}\hat{u}_{\vec{x}_2}}(f) = \frac{\left|S_{u_{\vec{x}_2}\hat{u}_{\vec{x}_2}}(f)\right|^2}{S_{u_{\vec{x}_2}u_{\vec{x}_2}}(f)\, S_{\hat{u}_{\vec{x}_2}\hat{u}_{\vec{x}_2}}(f)}. \tag{4.14}$$

The cross-spectrum $S_{u_{\vec{x}_2}\hat{u}_{\vec{x}_2}}(f)$ can be calculated using the CPSD definition in (2.9), with the implicit expectation operation and limit as the window length approaches infinity excluded for simplicity, as

$$\begin{aligned} S_{u_{\vec{x}_2}\hat{u}_{\vec{x}_2}}(f) &= U_{\vec{x}_2}(f)\left(U^*_{\vec{x}_2}(f) + \tfrac{\ell_y}{\ell_x} V^*_{\vec{x}_2}(f) + \tfrac{\ell_z}{\ell_x} W^*_{\vec{x}_2}(f)\right) \\ &= S_{u_{\vec{x}_2}u_{\vec{x}_2}}(f), \end{aligned} \tag{4.15}$$

where the second line is a result of the assumed zero correlation between the u and v as well as u and w components discussed in Chapter 3. Similarly, the PSD $S_{\hat{u}_{\vec{x}_2}\hat{u}_{\vec{x}_2}}(f)$ can be written as

$$\begin{aligned} S_{\hat{u}_{\vec{x}_2}\hat{u}_{\vec{x}_2}}(f) &= \left(U_{\vec{x}_2}(f) + \tfrac{\ell_y}{\ell_x}V_{\vec{x}_2}(f) + \tfrac{\ell_z}{\ell_x}W_{\vec{x}_2}(f)\right)\left(U^*_{\vec{x}_2}(f) + \tfrac{\ell_y}{\ell_x}V^*_{\vec{x}_2}(f) + \tfrac{\ell_z}{\ell_x}W^*_{\vec{x}_2}(f)\right) \\ &= S_{u_{\vec{x}_2}u_{\vec{x}_2}}(f) + \tfrac{\ell_y^2}{\ell_x^2}S_{v_{\vec{x}_2}v_{\vec{x}_2}}(f) + \tfrac{\ell_z^2}{\ell_x^2}S_{w_{\vec{x}_2}w_{\vec{x}_2}}(f), \end{aligned} \tag{4.16}$$

where the nine individual Fourier transform products comprising the first line simplify to three power spectra, defined by the turbulence model, since it is assumed that different components of the wind vector are uncorrelated with each other.

By combining the derived spectra, the measurement coherence resulting from line-of-sight errors is given by

$$\gamma^2_{u_{\vec{x}_2}\hat{u}_{\vec{x}_2}}(f) = \frac{S^2_{u_{\vec{x}_2}u_{\vec{x}_2}}(f)}{S_{u_{\vec{x}_2}u_{\vec{x}_2}}(f)\left(S_{u_{\vec{x}_2}u_{\vec{x}_2}}(f) + \frac{\ell_y^2}{\ell_x^2}S_{v_{\vec{x}_2}v_{\vec{x}_2}}(f) + \frac{\ell_z^2}{\ell_x^2}S_{w_{\vec{x}_2}w_{\vec{x}_2}}(f)\right)}. \tag{4.17}$$

As the lidar cone angle θ approaches zero, resulting in perfect lidar alignment with the longitudinal direction, the ratios ℓ_y/ℓ_x and ℓ_z/ℓ_x approach 0 and the measurement coherence approaches 1. On the other hand, as the measurement angle θ approaches 90°, yielding a beam direction perpendicular to the longitudinal direction, ℓ_y/ℓ_x and ℓ_z/ℓ_x approach infinity and the measurement coherence diminishes to zero.

4.2.2 Combining Line-of-Sight Errors and Wind Evolution Errors

If instead of estimating the u component upstream of the turbine at the same location as the measurement point $\vec{x}_2 = [-d, -r\sin(\psi), r\cos(\psi)]$, an estimate of the u component at $\vec{x}_1 = [0, -r\sin(\psi), r\cos(\psi)]$, downstream of the measurement point at the rotor plane, is desired, then the measurement coherence will depend on the amount of wind evolution. The resulting measurement coherence can be expressed by replacing the CPSD $S_{u_{\vec{x}_2}\hat{u}_{\vec{x}_2}}(f)$ in (4.15) with $S_{u_{\vec{x}_1}\hat{u}_{\vec{x}_2}}(f)$ and the PSD of the true u component $S_{u_{\vec{x}_2}u_{\vec{x}_2}}(f)$ with $S_{u_{\vec{x}_1}u_{\vec{x}_1}}(f)$:

$$\gamma^2_{u_{\vec{x}_1}\hat{u}_{\vec{x}_2}}(f) = \frac{\left|S_{u_{\vec{x}_1}u_{\vec{x}_2}}(f)\right|^2}{S_{u_{\vec{x}_1}u_{\vec{x}_1}}(f)\left(S_{u_{\vec{x}_2}u_{\vec{x}_2}}(f) + \frac{\ell_y^2}{\ell_x^2}S_{v_{\vec{x}_2}v_{\vec{x}_2}}(f) + \frac{\ell_z^2}{\ell_x^2}S_{w_{\vec{x}_2}w_{\vec{x}_2}}(f)\right)}, \tag{4.18}$$

where the individual CPSD functions are formed using the definition in (3.12). As a result, the CPSDs in (4.18) are functions of the wind speed PSDs and the longitudinal coherence model describing wind evolution provided in Chapter 3.

Measurement coherence curves illustrating the individual and combined effects of line-of-sight errors and wind evolution on measurement quality are shown in Fig. 4.4. Coherence is calculated for three scan geometries containing preview distances d = 31.5 m, 63 m, and 126 m (0.25 D, 0.5 D, and 1 D for the NREL 5-MW reference model), all with a scan radius of r = 44.1 m (0.7 R). The von Kármán turbulence model is used along with the developed longitudinal coherence formula described in Section 3.2.3 for the rated mean wind speed U = 11.4 m/s, turbulence intensity TI = 15%, and integral length scales $L_u = L_v = L_w$ =147 m. The solid curves represent the combined effects of line-of-sight and wind evolution errors given by (4.18), while the dashed curves are calculated for line-of-sight errors only, as in (4.17), and the dotted curves represent the longitudinal coherence loss due to wind evolution alone.

The dashed coherence curves for line-of-sight errors in Fig. 4.4 show that as the preview

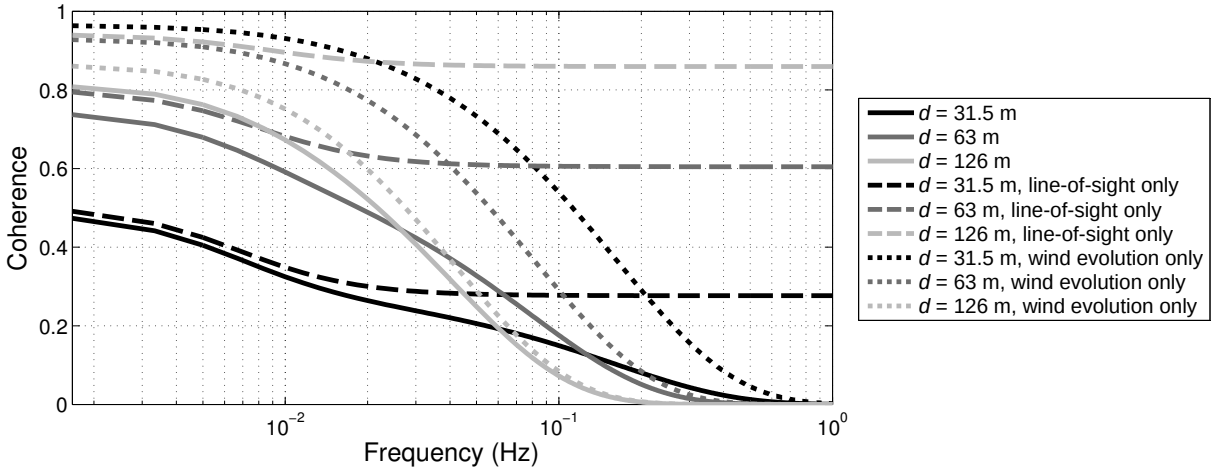

Figure 4.4: Lidar measurement coherence between the u component at a point with spanwise position 44.1 m and lidar measurements with r = 44.1 m and d = 31.5 m, 63 m, and 126 m for both line-of-sight and wind evolution errors (solid), line-of-sight errors only (dashed), and wind evolution errors only (dotted). Lidar range weighting is not included. The von Kármán turbulence model is used with U = 11.4 m/s, TI = 15%, and L_u =147 m.

distance increases for a fixed scan radius (causing the measurement angle θ to decrease) the measurement coherence increases, as explained in the previous section. Note that the coherence is higher at low frequencies because the power spectrum of the v and w components is lower relative to the spectrum of the u component at these frequencies, as shown in Fig. 3.2. Therefore, the v and w components corrupt the u component estimate less at low frequencies than at high frequencies where the v and w components contain more energy than the u component. In contrast, the coherence curves representing wind evolution decrease as the preview distance increases. Thus two opposing trends contribute to measurement coherence. As preview distance increases, the measurement angle becomes smaller and line-of-sight errors are reduced, but coherence drops due to wind evolution. As shown by the solid curves that include both error sources, as preview distance increases the low-frequency coherence becomes larger due to less line-of-sight error, but the coherence begins to decay at lower frequencies because of greater wind evolution effects. For large measurement angles measurement coherence is dominated by line-of-sight errors, while for large preview distances and small cone angles coherence is dominated by wind evolution.

When analyzing the impact of measurement coherence on the mean square measurement error, the power spectrum of the wind speed to be estimated must be taken into account, as discussed in Section 2.2.1. Since the energy in the power spectra of wind is concentrated at low frequencies, it is advantageous to decrease the measurement angle in order to increase low-frequency coherence and reduce the overall MSE. Beyond a certain optimal preview distance, however, the additional benefit of reducing the measurement angle diminishes and wind evolution causes the overall measurement error to increase.

4.2.3 The Effect of Range Weighting on Measurement Error

By combining the range weighting equation in (4.2) with the line-of-sight measurement equation in (4.11), a range-weighted line-of-sight lidar measurement can be described as

$$u_\ell = -\int_0^\infty W_\ell\left(F, s\right)\left(\ell_x u_{s\vec{\ell}} + \ell_y v_{s\vec{\ell}} + \ell_z w_{s\vec{\ell}}\right) ds. \tag{4.19}$$

An estimate of the u component at the lidar's focus point $\vec{x}_2 = [-d, -r\sin(\psi), r\cos(\psi)]$ using (4.13) can therefore be represented as

$$\hat{u}_{\vec{x}_2} = \int_0^\infty W_\ell(F,s)\left(u_{s\vec{\ell}} + \frac{\ell_y}{\ell_x}v_{s\vec{\ell}} + \frac{\ell_z}{\ell_x}w_{s\vec{\ell}}\right)ds. \tag{4.20}$$

In order to calculate the measurement coherence between a lidar measurement at $\vec{x}_2$ and the wind speed at a point directly downstream at the rotor plane $\vec{x}_1 = [0, -r\sin(\psi), r\cos(\psi)]$, given by

$$\gamma^2_{u_{\vec{x}_1}\hat{u}_{\vec{x}_2}}(f) = \frac{\left|S_{u_{\vec{x}_1}\hat{u}_{\vec{x}_2}}(f)\right|^2}{S_{u_{\vec{x}_1}u_{\vec{x}_1}}(f)\,S_{\hat{u}_{\vec{x}_2}\hat{u}_{\vec{x}_2}}(f)}, \tag{4.21}$$

the CPSD $S_{u_{\vec{x}_1}\hat{u}_{\vec{x}_2}}(f)$ and PSD $S_{\hat{u}_{\vec{x}_2}\hat{u}_{\vec{x}_2}}(f)$ involving the range weighting integral need to be established.

Using the linearity property of the Fourier transform [67], the CPSD $S_{u_{\vec{x}_1}\hat{u}_{\vec{x}_2}}(f)$ can be written as

$$\begin{aligned} S_{u_{\vec{x}_1}\hat{u}_{\vec{x}_2}}(f) &= U_{\vec{x}_1}(f)\int_0^\infty W_\ell(F,s)\left(U^*_{s\vec{\ell}}(f) + \frac{\ell_y}{\ell_x}V^*_{s\vec{\ell}}(f) + \frac{\ell_z}{\ell_x}W^*_{s\vec{\ell}}(f)\right)ds \\ &= \int_0^\infty W_\ell(F,s)\,S_{u_{\vec{x}_1}u_{s\vec{\ell}}}(f)\,ds, \end{aligned} \tag{4.22}$$

where the second line is made possible by distributing the Fourier transform $U_{\vec{x}_1}(f)$ inside of the integral and by the modeling assumption that the u component is uncorrelated with the v and w components. The individual CPSDs $S_{u_{\vec{x}_1}u_{s\vec{\ell}}}(f)$ in (4.22) can be determined using the CPSD definition in (3.12) and the three-dimensional spatial coherence formula given by (3.23). The PSD $S_{\hat{u}_{\vec{x}_2}\hat{u}_{\vec{x}_2}}(f)$, again using linearity of the Fourier transform, can be expressed as a double integral over the range along the lidar beam:

$$\begin{aligned} S_{\hat{u}_{\vec{x}_2}\hat{u}_{\vec{x}_2}}(f) &= \left(\int_0^\infty W_\ell(F,s)\left(U_{\vec{x}_2}(f) + \frac{\ell_y}{\ell_x}V_{\vec{x}_2}(f) + \frac{\ell_z}{\ell_x}W_{\vec{x}_2}(f)\right)ds\right)\ldots \\ &\quad \ldots\cdot\left(\int_0^\infty W_\ell(F,s)\left(U^*_{\vec{x}_2}(f) + \frac{\ell_y}{\ell_x}V^*_{\vec{x}_2}(f) + \frac{\ell_z}{\ell_x}W^*_{\vec{x}_2}(f)\right)ds\right) \\ &= \int_0^\infty\int_0^\infty W_\ell(F,q)\,W_\ell(F,s)\left(S_{u_{q\vec{\ell}}u_{s\vec{\ell}}}(f) + \frac{\ell_y^2}{\ell_x^2}S_{v_{q\vec{\ell}}v_{s\vec{\ell}}}(f) + \frac{\ell_z^2}{\ell_x^2}S_{w_{q\vec{\ell}}w_{s\vec{\ell}}}(f)\right)dqds, \end{aligned} \tag{4.23}$$

where the product of two integrals in the first line is equivalently expressed as a double integral over the product of the integrands in the second line. As in (4.16), the presence of only three CPSDs

in the integrand of the second line results from the assumption that different components of the wind are uncorrelated with each other. While the measurement coherence curves without range weighting are presented analytically, since they depend only on the PSD and spatial coherence functions presented in Chapter 3, the integrals in the CPSD and PSD equations (4.22) and (4.23) with range weighting are difficult to solve. Therefore, the measurement coherence calculations are performed "semi-analytically," as discussed in Schlipf *et al.* [50], by discretizing the integration variables and approximating the integrals as summations. For the calculations performed in this thesis the range weighting range variables are discretized using a 2 m step size, which was found to only significantly distort the spectral calculations above $\sim$2 Hz.

In Fig. 4.5, the calculations of measurement coherence including line-of-sight errors and wind evolution without range weighting are compared with measurement coherence calculations including range weighting using (4.22) and (4.23) for a fixed scan radius $r = 44.1$ m and the three preview distances $d = 31.5$ m, 63 m, and 126 m for TI = 15% (Fig. 4.5 (a)) as well as a low turbulence intensity case with TI = 2% (Fig. 4.5 (b)). The range weighting functions are calculated using the CW weighting function presented in (4.3), and plotted in Fig. 4.1.

For TI = 15%, Fig. 4.5 (a) shows that with the addition of lidar range weighting the measurement coherence increases. For the low turbulence intensity TI = 2%, however, measurement coherence decreases when range weighting is introduced. The turbulence intensity only influences the coherence calculations through the longitudinal coherence formula (3.21) describing wind evolution, where coherence decreases as turbulence intensity increases. For the high turbulence case, range weighting improves measurement coherence by averaging over the spatially-varying v and w components along the beam, effectively reducing their impact on the line-of-sight errors. Although spatial averaging of the u component along the beam degrades the measurement coherence, the benefit of reducing the impact of the v and w components outweighs the resulting coherence drop. However, when the turbulence intensity is very low and wind evolution is not as severe, range weighting causes a slight degradation in measurement coherence. When wind evolution is not as significant of an error source, the drop in measurement correlation due to spatial averaging of the

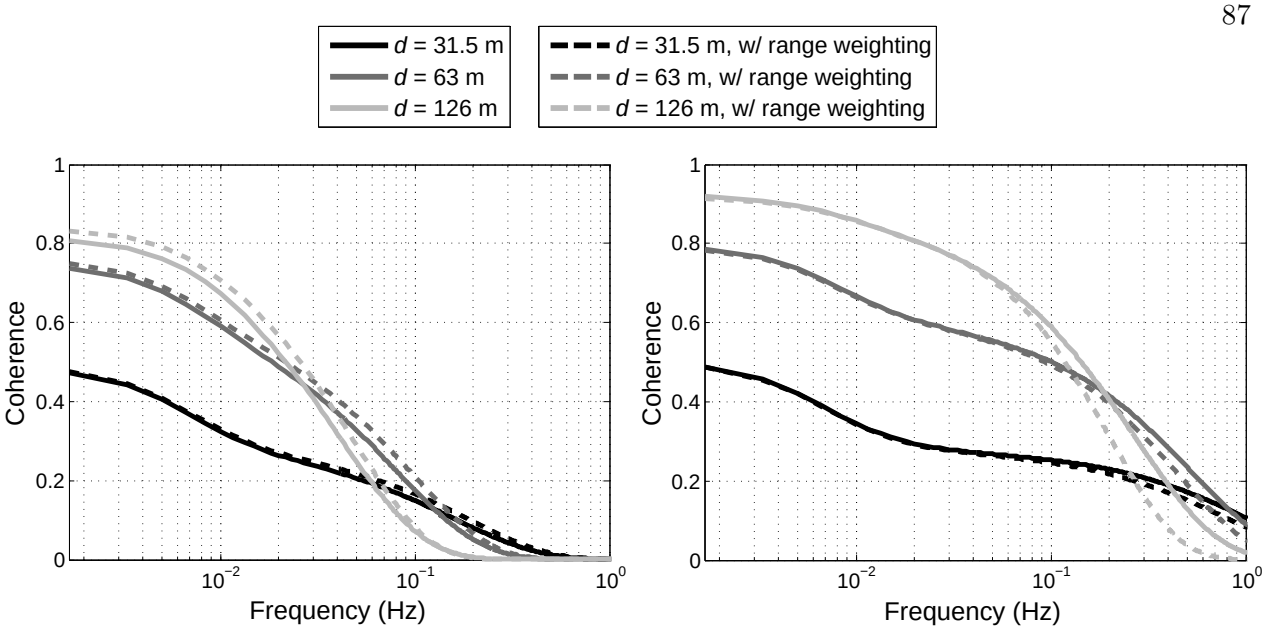

(a) TI = 15%. (b) TI = 2%.

Figure 4.5: Lidar measurement coherence between the u component at a point with spanwise position 44.1 m and lidar measurements with $r = 44.1$ m and $d = 31.5$ m, 63 m, and 126 m for line-of-sight and wind evolution errors both without (solid) and with (dashed) lidar range weighting. Measurement coherence curves for two different wind conditions are provided: (a) TI = 15% and (b) TI = 2%. The von Kármán turbulence model is used with $U = 11.4$ m/s and L_u =147 m.

u component becomes more pronounced compared to the benefit gained by averaging the v and w components along the beam, causing the slight drop in coherence. In general, lidar range weighting has a much smaller impact on measurement coherence than line-of-sight effects or wind evolution, and should not necessarily be thought of as an error source.

It should be noted that if the objective is to use the lidar to measure the mean wind speed, range weighting can potentially lead to incorrect measurements when non-zero mean vertical wind shear is present. For example, if the lidar is oriented such that wind speeds at different heights are detected along the beam, the mean wind speed measured by the lidar might not correspond to the true mean wind speed at the focus location in the presence of nonlinear mean shear. If the mean wind shear is linear, on the other hand, the range weighted average mean wind speed detected along the lidar beam will be equal to the true mean wind speed. However, since the analyses of measurement error in this thesis focus on the time-varying turbulent components of the wind, errors

due to mean wind shear are not investigated further.

4.2.4 Measurement Errors for Blade Effective Wind Speeds

In the previous sections measurement coherence was derived assuming that the objective was to estimate the longitudinal wind velocity at a single point. But measurements of the blade effective wind speed, which includes the approximate effects of how the wind field interacts with the turbine aerodynamically, are more useful for wind turbine control applications. Repeating the definition in Section 3.4 for reference, the linear blade effective wind speed at azimuth angle ψ in the rotor plane can be expressed as

$$u_b = \int_0^R W_b(q)\, u_{q\vec{b}} dq, \tag{4.24}$$

where $\vec{b} = [0, -\sin\psi, \cos\psi]$ and $u_{q\vec{b}}$ indicates the longitudinal wind component at the location $q\vec{b}$. If a lidar measurement at point $\vec{x}_2 = [-d, -r\sin(\psi), r\cos(\psi)]$ is used to provide an estimate $\hat{u}_b$ of u_b, then the measurement coherence

$$\gamma^2_{u_b\hat{u}_b}(f) = \frac{|S_{u_b\hat{u}_b}(f)|^2}{S_{u_bu_b}(f)\, S_{\hat{u}_b\hat{u}_b}(f)} \tag{4.25}$$

can be calculated by determining the CPSD $S_{u_b\hat{u}_b}(f)$ and the PSD $S_{u_bu_b}(f)$. Note that the lidar measurement PSD $S_{\hat{u}_b\hat{u}_b}(f)$ is given by the formula in (4.23).

By combining the definitions in (4.19) and (4.24), the CPSD $S_{u_b\hat{u}_b}(f)$ can be written as

$$\begin{aligned} S_{u_b\hat{u}_b}(f) &= \left(\int_0^R W_b(q)\, U_{q\vec{b}}(f)\, dq\right)\left(\int_0^\infty W_\ell(F,s)\left(U^*_{s\vec{\ell}}(f) + \frac{\ell_y}{\ell_x}V^*_{s\vec{\ell}}(f) + \frac{\ell_z}{\ell_x}W^*_{s\vec{\ell}}(f)\right)ds\right) \\ &= \int_0^R\int_0^\infty W_b(q)\, W_\ell(F,s)\, S_{u_{q\vec{b}}u_{s\vec{\ell}}}(f)\, ds, \end{aligned} \tag{4.26}$$

again using the property that the product of two integrals can be expressed as the double integral over the product of the integrands. The second line of (4.26) results from the assumed zero correlation between u and either v or w. Following the approach used in (4.23), the PSD $S_{u_bu_b}(f)$ can

be written as

$$\begin{aligned} S_{u_b u_b}(f) &= \left(\int_0^R W_b(q)\, U_{q\vec{b}}(f)\, dq\right) \cdot \left(\int_0^R W_b(q)\, U^*_{q\vec{b}}(f)\, dq\right) \\ &= \int_0^R \int_0^R W_b(q)\, W_b(s)\, S_{u_{q\vec{b}} u_{s\vec{b}}}(f)\, dqds. \end{aligned} \tag{4.27}$$

Similar to the spectrum calculations for range weighted lidar measurements described in Section 4.2.3, spectra involving blade effective weighting function integrals must be solved semi-analytically by discretizing the spanwise integration variable. For the results presented in this thesis the spanwise variable q in (4.24) is discretized using a step size of 1 m. Furthermore, the range weighting function is truncated at 5% of its peak value to limit the length along the beam over which wind speeds are integrated.

For the same two turbulence intensity values analyzed in Fig. 4.5, blade effective wind speed measurement coherence curves calculated for scan parameters $d = 31.5$ m, 63 m, and 126 m with $r = 44.1$ m, are shown in Fig. 4.6 both with and without lidar range weighting included. The torque sensitivity-based blade effective weighting function $W_b(q)$ defined in (3.36) and shown in Fig. 3.16 for the mean wind speed $U = 11.4$ m/s is used in the calculations. The coherence curves reveal the same general trends as in Fig. 4.4, i.e., as the measurement angle θ decreases, the low-frequency coherence becomes higher, but as the the preview distance increases the coherence begins to decay at lower frequencies due to additional wind evolution. However, unlike the measurement coherence curves in Fig. 4.5, lidar range weighting improves measurement coherence for *both* turbulence intensity cases. While it can't necessarily be concluded that range weighting is *always* beneficial when measuring blade effective wind speeds, the results in Fig. 4.6 suggest that range weighting helps approximate the spatial averaging of wind speeds along the blade, thereby enhancing measurement coherence.

4.3 Discussion and Conclusions

The first half of this chapter provided a description of the lidar measurement process including the estimation of velocity from a detected Doppler spectrum. Lidar range weighting, the spatial

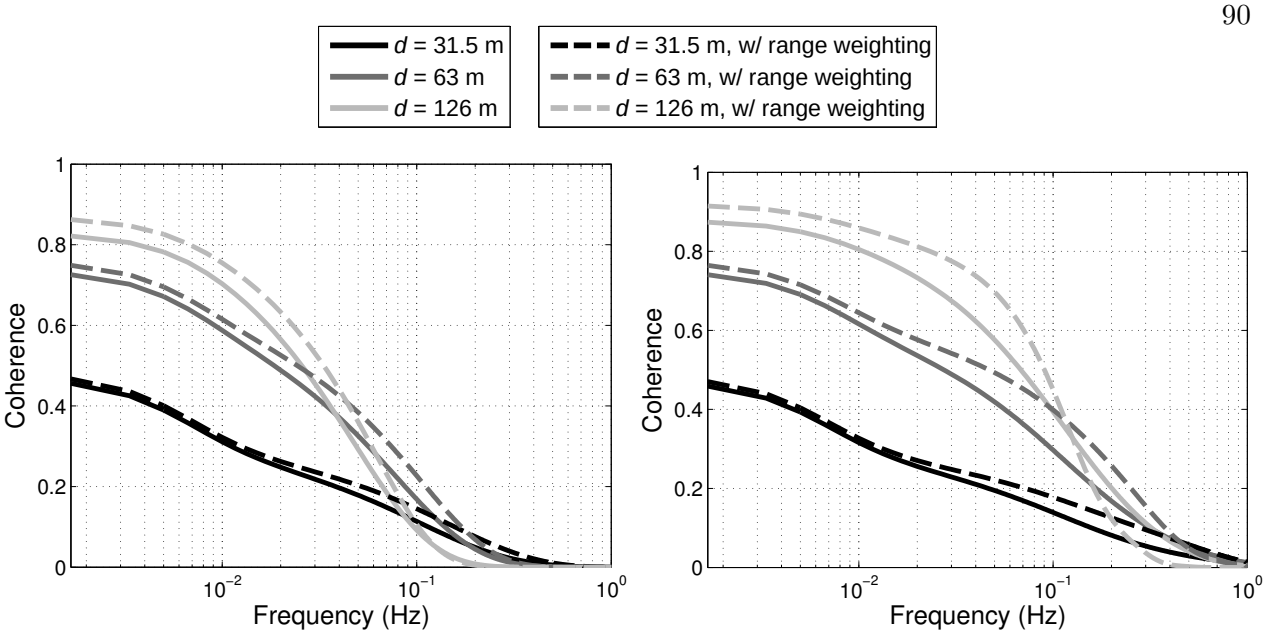

(a) TI = 15%. (b) TI = 2%.

Figure 4.6: Lidar measurement coherence between blade effective wind speeds and lidar measurements with $r = 44.1$ m and $d = 31.5$ m, 63 m, and 126 m for line-of-sight and wind evolution errors both without (solid) and with (dashed) lidar range weighting. Measurement coherence curves for two different wind conditions are provided: (a) TI = 15% and (b) TI = 2%. The von Kármán turbulence model is used with $U = 11.4$ m/s and L_u =147 m.

averaging of wind speeds along the lidar beam, was presented for CW and pulsed lidar technologies. Various measurement noise sources inherent to the lidar technology were discussed, but it was concluded that other error sources including line-of-sight effects and wind evolution are dominant, and that it is not necessary to include the lidar measurement noise in calculations of measurement error. In the second half of the chapter, the process through which measurement coherence can be determined, including line-of-sight effects, wind evolution, range weighting, and the spatial averaging caused by the blade effective wind speed definition, was described. Measurement and blade effective wind speed power spectra as well as measurement coherence can be calculated using only the statistical frequency-domain wind field definition presented in Chapter 3 together with definitions of the lidar range weighting function and the blade effective weighting function. Examples of measurement coherence were provided, illustrating the effects of various error sources assuming a CW lidar based on the commercially developed ZephIR system, which is the model

assumed in the rest of this thesis.

The relative impacts of the different error sources investigated in this chapter are summarized in Table 4.1 for measurements of the u component at a single point with a spanwise position of 44.1 m, as in Sections 4.2.1 through 4.2.3, as well blade effective wind speed, as in Section 4.2.4, using the von Kármán turbulence model with $U = 11.4$ m/s, TI = 15%, and L_u =147 m. Specifically, normalized mean square measurement errors are provided for the following combinations of error sources: line-of-sight effects only, wind evolution effects only, line-of-sight and wind evolution effects together, line-of-sight effects with lidar range weighting, and finally line-of-sight and wind evolution effects together with range weighting. As will be explained more in Chapter 5, the mean square measurement error values are calculated by integrating the power spectrum of the measurement MSE given by (2.29), assuming the optimal MMSE measurement filter is employed, up to a bandwidth of 1 Hz (the approximate bandwidth of interest for blade pitch control applications for the NREL 5-MW reference turbine model). The MSEs are then normalized by the variances of the true wind speed variables that are being estimated with lidar measurements, similarly calculated by integrating the power spectra of the wind speed variables up to a bandwidth of 1 Hz.

Table 4.1 shows the tradeoff between the dominant line-of-sight and wind evolution error sources, revealing the importance of decreasing the measurement angle θ to reduce measurement error. Although not shown in Table 4.1, beyond some preview distance greater than 126 m, measurement error including both line-of-sight effects and wind evolution effects will begin to increase due to the intensification of wind evolution. The measurement error values with all error sources included underscore the idea that lidar range weighting can help reduce measurement error, especially for measurements of blade effective wind speed, and should not necessarily be considered as an error source.

It should be noted that while the general trends of the dependence of measurement error on measurement angle, preview distance, etc. are expected to hold for arbitrary wind conditions, the specific normalized measurement errors listed in Table 4.1 are only valid for the particular wind conditions analyzed here. Depending on the specific wind field parameters, the magnitudes of the

Table 4.1: Normalized mean square measurement errors, assuming optimal measurement filtering, between lidar measurements and point wind speeds at a spanwise position of 44.1 m as well as blade effective wind speeds for different combinations of error sources with $r = 44.1$ m and $d = 31.5$ m, 63 m, and 126 m. All mean square measurement errors are normalized by the variance of the wind speed variable of interest. The von Kármán turbulence model is used with $U = 11.4$ m/s, TI = 15%, and L_u =147 m.

Point Wind Speeds

d (m)	Line-of-Sight	Wind Evo.	Line-of-Sight + Wind Evo.	Line-of-Sight + Range Weighting	All Error Sources
31.5	0.64	0.18	0.69	0.65	0.68
63	0.31	0.28	0.49	0.35	0.47
126	0.10	0.53	0.46	0.19	0.43

Blade Effective Wind Speeds

d (m)	Line-of-Sight	Wind Evo.	Line-of-Sight + Wind Evo.	Line-of-Sight + Range Weighting	All Error Sources
31.5	0.67	0.16	0.67	0.65	0.66
63	0.39	0.20	0.43	0.35	0.40
126	0.22	0.29	0.35	0.16	0.30

errors can change. For example, the magnitude of the errors caused by line-of-sight effects will grow as the ratio between the turbulence intensity of both the v and w components and the u component of interest increases. Furthermore, the magnitude of the errors caused by wind evolution will increase as the turbulent kinetic energy increases, since TKE determines how quickly the longitudinal coherence decays as a function of longitudinal separation as well as frequency. For fixed turbulence length scales, changes in mean wind speed are expected to have a relatively small impact on measurement error, however; higher values of U shift more of the energy in the wind speed variables to higher frequencies, as revealed by the power spectrum definitions in Section 3.1.1, but the longitudinal coherence function describing wind evolution, given by (3.21), decays at higher frequencies as well, such that that the overall measurement error is not expected to change significantly.

Although a circularly-scanning lidar scenario (see Fig. 4.3) was assumed in this chapter, only measurement coherence between stationary lidar measurements and wind speeds or blade effective wind speeds at fixed locations was described. However, in addition to illustrating the basic trends of various measurement error sources, the stationary power spectra and coherence calculations pre-

sented in this chapter form the building blocks of the calculations of mean square measurement error between circularly scanning lidar measurements and rotor effective hub-height and shear components, based on three rotating blades, described in Chapter 5. Finally, by calculating measurement coherence for different scan radii and preview distances, the lidar scenario can be optimized for different wind conditions, as is discussed in the next chapter.

Acknowledgements

The contributions of Dr. Rod Frehlich toward determining typical levels of lidar measurement noise for a circularly-scanning turbine-mounted lidar are greatly appreciated. A broader discussion of the measured noise levels based on Dr. Frehlich's work is included in Simley *et al.* [39].

Chapter 5

Frequency Domain Calculations of Rotor Effective Wind Speed and Lidar Measurement Coherence

In Section 4.2 of the previous chapter, lidar measurement coherence calculations were presented for stationary lidar measurements as well as point wind speeds or blade effective wind speeds at fixed azimuth angles ψ in the scan circle and rotor plane. To model the rotor effective hub-height and linear shear components relevant to control applications outlined in Section 3.5, however, wind speed spectra must be calculated for rotating blade effective wind speeds. Similarly, the spectra of circularly-scanning lidar measurements must be determined. A method for calculating the power spectra and measurement coherence for a single rotating lidar measurement/blade effective wind speed pair is described in Section 5.1, using the assumption that the lidar measurement and blade rotate at the same fixed speed, i.e., the desired rotor speed at the specific turbine operating point analyzed. As with the derivation provided in Section 4.2, the rotational spectra and coherence are calculated using the frequency-domain wind field definition provided in Chapter 3 along with specific range weighting and blade effective weighting functions. This method for calculating rotational spectra is extended in Section 5.2 to the calculation of power spectra and measurement coherence for the rotor effective u_{hh}, δ_h, and δ_v components, defined using three rotating blade effective wind speeds. Lidar-based estimates of the rotor effective wind speeds are formed using three circularly-scanning lidar measurements, one corresponding to each blade. This measurement scenario is shown in Fig. 5.1 where ψ_t represents the azimuth angle of the turbine rotor and ψ_m indicates the azimuth angle of the lidar measurements. Note that the three lidar measurement

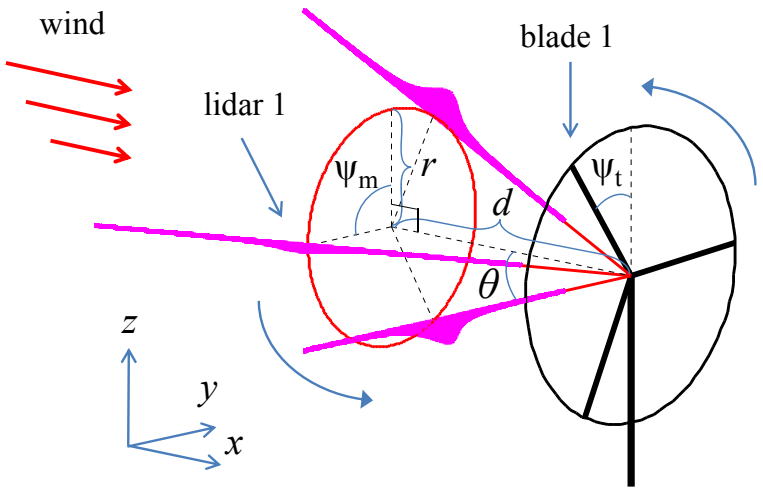

Figure 5.1: Hub-mounted circularly-scanning three-beam lidar scenario using CW lidars with preview distance d and scan radius r resulting in measurement cone angle θ. The three beam directions are separated by 120° azimuth intervals. The instantaneous azimuth angle of the turbine rotor is indicated by ψ_t while the lidar measurement azimuth angle is represented by ψ_m.

points are evenly spaced in the scan circle and that the rotor (and thus the lidar measurement locations) rotates clockwise when viewing the turbine from upstream.

In the second half of the chapter, the developed methods for calculating the spectra and measurement coherence for rotor effective wind components are used to optimize the lidar measurement scenario for different wind conditions. Section 5.3 presents an optimization over the lidar scan radius and preview distance variables for a specific wind condition by finding the scan configuration that minimizes mean square measurement error. In Sections 5.3.1 and 5.3.2, the impact of the induction zone model presented in Section 3.3 as well as degradation in measurement error caused by turbine yaw error are discussed. Finally, the dependence of the optimal scan parameters and the corresponding achievable measurement error on the wind condition is analyzed in Section 5.4. Specifically, the influence of mean wind speed, turbulence intensity, and turbulence length scale on the optimized scan scenario is investigated, providing guidelines that can be used for the development of lidar systems for preview-based control.

5.1 Calculating Rotating Blade Effective Wind Speed Spectra and Measurement Coherence

A method for calculating the rotational power spectra and cross-spectra necessary to determine lidar measurement coherence is described in this section, based on work presented in Simley and Pao [64]. All calculations are derived assuming discrete-time signals and the DT Fourier definitions provided in Section 2.1.1. Treating the wind speeds and lidar measurements as DT signals allows the rotational spectra to be determined computationally, by replacing integrals with summations. To simplify the spectrum calculations, the rotational speed of the blades and lidar measurements is assumed to be fixed at 12.1 RPM, the NREL 5-MW reference turbine's rated rotor speed. The sampling frequency of all DT signals is assumed to be approximately that of the ZephIR CW lidar, which the lidar model used for analysis is based on. Although the commercially available ZephIR lidar samples at a rate of 50 Hz [89], a slightly faster sampling frequency of 50.82 Hz is assumed for the calculations in this chapter. This sampling frequency results in an integer number ($N = 252$) of discrete azimuth angles per rotational period of $\sim$4.96 s corresponding to the 12.1 RPM rotor speed. Furthermore, selecting a number of discrete azimuth angles N that is divisible by 6 allows some of the calculations to be simplified. Although sampling the CT wind speed signals can result in aliasing, the sampling frequency of 50.82 Hz is high enough to capture most of the energy in the wind time series, and any aliasing effects that might occur are ignored for simplicity.

By breaking the scan circle and rotor into N discrete azimuth angles, rotating signals can be formed by sequentially sampling N different "stationary" signals around the circle such that each signal corresponding to a fixed azimuth angle is sampled once every N time steps. If $a_\psi[n]$ represents a stationary signal at azimuth angle ψ, then a signal formed by sampling $a_\psi[n]$ every N-th time step, with values at all other time steps defined as 0 and with the first non-zero sample for $n \geq 0$ beginning at $n = \psi N/2\pi$, can be written as

$$a_{s,\psi}[n] = \left(\sum_{k=-\infty}^{\infty} \delta\left[n - \frac{\psi N}{2\pi} - kN \right] \right) \cdot a_\psi[n], \tag{5.1}$$

where $\delta[n]$ is the Kronecker delta function:

$$\delta[n] = \begin{cases} 1, & \text{if } n = 0 \\ 0, & \text{otherwise.} \end{cases} \tag{5.2}$$

Using (5.1), the rotational signal $a_r[n]$ formed by sequentially sampling the N stationary signals $a_{\psi_m}[n]$ around the scan circle or rotor for $m \in \{1, \ldots, N\}$, with sample $n = 0$ corresponding to an azimuth angle of 0, can simply be described as

$$a_r[n] = \sum_{m=0}^{N-1} a_{s,\psi_m}[n]. \tag{5.3}$$

By applying the Fourier property equating the Fourier transform of the product of two signals to the convolution of the individual Fourier transforms, as well as the time shift property [67], the Fourier transform of the sampled stationary signal $a_\psi[n]$ in (5.1) is given by

$$\begin{aligned} A_{s,\psi}(\omega) &= \tfrac{1}{N} \int_{-\pi}^{\pi} \left(e^{-j(\omega-\phi)\frac{\psi N}{2\pi}} \sum_{k=-\frac{N}{2}}^{\frac{N}{2}} \delta\left(\omega - \phi - \frac{2\pi k}{N}\right) \right) A_\psi(\phi)\, d\phi \\ &= \tfrac{1}{N} \sum_{k=-\frac{N}{2}}^{\frac{N}{2}} e^{-jk\psi} A_\psi\left(\omega - \frac{2\pi k}{N}\right). \end{aligned} \tag{5.4}$$

The first line of (5.4) is formed by taking advantage of the following Fourier transform pair [67]:

$$\mathcal{F}\left\{ \sum_{k=-\infty}^{\infty} \delta[n - kN] \right\} = \frac{2\pi}{N} \sum_{k=-\frac{N}{2}}^{\frac{N}{2}} \delta\left(\omega - \frac{2\pi k}{N}\right), \tag{5.5}$$

where $\delta(\omega)$ is the CT Dirac delta function:

$$\delta(\omega) = \begin{cases} 1, & \text{if } \omega = 0 \\ 0, & \text{otherwise.} \end{cases} \tag{5.6}$$

Finally, letting $\psi_m = 2\pi m/N$ and utilizing the derivation of $A_{s,\psi}(\omega)$ in (5.4), the Fourier transform of the rotating signal $a_r[n]$ defined in (5.3) is given by

$$A_r(\omega) = \frac{1}{N} \sum_{m=0}^{N-1} \left(\sum_{k=-\frac{N}{2}}^{\frac{N}{2}} e^{-j\psi_m k} A_{\psi_m}\left(\omega - \frac{2\pi k}{N}\right) \right). \tag{5.7}$$

While (5.7) provides a method for calculating the Fourier transform of a rotational signal using the Fourier transforms of N stationary signals, the CPSD between two rotating signals must be derived in order to calculate rotational power spectra and measurement coherence based on the frequency-domain wind field definition presented in Chapter 3. By implicitly applying the CPSD definition in (2.14) and using the Fourier transform $A_r(\omega)$ derived in (5.7), the CPSD between two rotating signals $a_r[n]$ and $b_r[n]$ can be expressed as

$$\begin{aligned} S_{a_r b_r}(\omega) &= \tfrac{1}{N^2}\left[\sum_{m=0}^{N-1}\left(\sum_{i=-\frac{N}{2}}^{\frac{N}{2}} e^{-j\psi_m i} A_{\psi_m}\left(\omega - \frac{2\pi i}{N}\right)\right)\right]\cdot\left[\sum_{n=0}^{N-1}\left(\sum_{k=-\frac{N}{2}}^{\frac{N}{2}} e^{j\psi_n k} B^*_{\psi_n}\left(\omega - \frac{2\pi k}{N}\right)\right)\right] \\ &= \tfrac{1}{N^2}\sum_{m=0}^{N-1}\sum_{n=0}^{N-1}\left(\sum_{k=-\frac{N}{2}}^{\frac{N}{2}} e^{j(\psi_n-\psi_m)k} S_{a_{\psi_m} b_{\psi_n}}\left(\omega - \frac{2\pi k}{N}\right)\right), \end{aligned} \tag{5.8}$$

where the double summation over i and k in the first line collapses to a single summation in the second line using the assumption that different frequency components of the two signals are uncorrelated with each other, i.e., $A_{\psi_m}(\omega_1)$ is uncorrelated with $B^*_{\psi_n}(\omega_2)$ unless $\omega_1 = \omega_2$ for all m and n. This assumption is also made in common stochastic wind field simulation techniques [71, 74].

The formula presented in (5.8) allows the calculation of the CPSD of two rotational signals, but requires the calculation of the fixed-azimuth angle CPSDs $S_{a_{\psi_m} b_{\psi_n}}(\omega)$ for every pair of azimuth angles. Calculating N^2 individual fixed-azimuth angle CPSDs can be very computationally expensive because each CPSD corresponding to lidar measurement and blade effective wind speed variables can further require double summations over the number of discrete points along the blade or lidar beam, as shown in (4.23), (4.26), and (4.27). However, under the condition that each fixed-azimuth angle CPSD $S_{a_{\psi_m} b_{\psi_n}}(\omega)$ only depends on the absolute difference between the two azimuth angles $|n-m|$, the following simplification can be made to the formula in (5.8):

$$\begin{aligned} S_{a_r b_r}(\omega) &= \tfrac{2}{N^2}\sum_{m=1}^{N-1}\left((N-m)\sum_{k=-\frac{N}{2}}^{\frac{N}{2}} \cos\left((\psi_m - \psi_0)\,k\right) S_{a_{\psi_0} b_{\psi_m}}\left(\omega - \frac{2\pi k}{N}\right)\right) \\ &\quad + \tfrac{1}{N}\sum_{k=-\frac{N}{2}}^{\frac{N}{2}} S_{a_{\psi_0} b_{\psi_0}}\left(\omega - \frac{2\pi k}{N}\right), \end{aligned} \tag{5.9}$$

where $\psi_0 = 0$ can be assumed without loss of generality. The simplified rotational CPSD formula in (5.9) requires only a single summation over the N azimuth angles, greatly reducing the computational complexity of the required calculations. More importantly, only N fixed-azimuth angle CPSDs need to be determined to calculate the rotational CPSD, reducing the computational burden by a factor of N.

While not all wind fields and measurement scenarios lend themselves to the necessary condition that $S_{a_{\psi_m} b_{\psi_n}}(\omega)$ depends only on $|n-m|$ for all m and n allowing the simplified formula in (5.9) to be used, the following wind field characteristics are sufficient, assuming the circularly-scanning lidar scenario shown in Fig. 5.1:

- All turbulence power spectra and spatial coherence functions are independent of location in space.
- The transverse v and vertical w component turbulence power spectra and spatial coherence functions are identical.
- Zero yaw error is present, i.e., the turbine rotor is aligned with the longitudinal x direction.
- No wind shear or wind veer (height-dependent wind direction) are present.

Wind fields satisfying these properties are referred to as "axisymmetric," because the cross-spectrum between wind speeds at any two points remains unchanged if the points are rotated by any amount around the longitudinal x axis. The von Kármán turbulence model discussed in Chapter 3 meets these requirements because the v and w component spectra are identical, while the Kaimal model does not, since the transverse and vertical component spectra are different. So that the Kaimal spectral model, which is more widely utilized in the wind turbine control community, can be used with the simplified formula in (5.9), it is modified for the calculations in this chapter. Specifically, the power spectrum of the v and w components is treated as the average of the original individual v and w component power spectra. Additionally, the integral length scale describing the v and w components is treated as $\left(0.5\left(L_v^{-1} + L_w^{-1}\right)\right)^{-1}$, where L_v and L_w are the original separate length

scales, to reflect the dependence of the spatial coherence formulas on the inverse of the length scale.

Finally, the formula presented in (5.9) can be used to calculate the rotational blade effective wind speed PSD $S_{u_{b,r}u_{b,r}}(\omega)$, rotational lidar measurement PSD $S_{\hat{u}_{b,r}\hat{u}_{b,r}}(\omega)$, and rotational CPSD $S_{u_{b,r}\hat{u}_{b,r}}(\omega)$ necessary to calculate the measurement coherence between a rotating lidar measurement and rotating blade effective wind speed.

5.2 Calculating Rotating Rotor Effective Wind Speed Spectra and Measurement Coherence

Building on the rotational CPSD formula developed in the previous section, a method for calculating the spectra of the rotor effective u_{hh}, δ_h, and δ_v components derived from three rotating blade effective wind speeds is provided in this section. The formulas for calculating the effective hub-height and linear shear components derived in (3.41) and (3.42) are provided again here:

$$u_{hh,\psi} = \frac{1}{3}\left(u_{b_1,\psi} + u_{b_2,\psi} + u_{b_3,\psi}\right) \tag{5.10a}$$

$$\Delta_{h,\psi} = -\frac{2}{3\int_0^R W_b(q)\,qdq}\left(\sin(\psi)u_{b_1,\psi} + \sin\left(\psi+\frac{2\pi}{3}\right)u_{b_2,\psi} + \sin\left(\psi+\frac{4\pi}{3}\right)u_{b_3,\psi}\right) \tag{5.10b}$$

$$\Delta_{v,\psi} = \frac{2}{3\int_0^R W_b(q)\,qdq}\left(\cos(\psi)u_{b_1,\psi} + \cos\left(\psi+\frac{2\pi}{3}\right)u_{b_2,\psi} + \cos\left(\psi+\frac{4\pi}{3}\right)u_{b_3,\psi}\right), \tag{5.10c}$$

where $u_{b_i,\psi}$ indicates the blade effective wind speed for blade i when the rotor, or equivalently blade 1, is at azimuth angle ψ. The Δ_h and Δ_v components represent the slope of the linear shear across the rotor disk in units of 1/s. Using the three lidar measurements illustrated in Fig. 5.1, one for each blade denoted as $\hat{u}_{b_1,\psi}$, $\hat{u}_{b_2,\psi}$, and $\hat{u}_{b_3,\psi}$, lidar-based estimates of these variables can be formed using

$$\hat{u}_{hh,\psi} = \frac{1}{3}\left(\hat{u}_{b_1,\psi} + \hat{u}_{b_2,\psi} + \hat{u}_{b_3,\psi}\right) \tag{5.11a}$$

$$\hat{\Delta}_{h,\psi} = -\frac{2}{3r}\left(\sin(\psi)\hat{u}_{b_1,\psi} + \sin\left(\psi+\frac{2\pi}{3}\right)\hat{u}_{b_2,\psi} + \sin\left(\psi+\frac{4\pi}{3}\right)\hat{u}_{b_3,\psi}\right) \tag{5.11b}$$

$$\hat{\Delta}_{v,\psi} = \frac{2}{3r}\left(\cos(\psi)\hat{u}_{b_1,\psi} + \cos\left(\psi+\frac{2\pi}{3}\right)\hat{u}_{b_2,\psi} + \cos\left(\psi+\frac{4\pi}{3}\right)\hat{u}_{b_3,\psi}\right), \tag{5.11c}$$

where dividing the shear component measurements by the scan radius r serves the purpose of providing estimates of the slope of the shear.

Relying on the $u_{hh,\psi}$, and $\hat{u}_{hh,\psi}$ definitions in (5.10) and (5.11), for fixed azimuth angles ψ_m and ψ_n, the CPSD between any two rotor effective or lidar-estimated hub-height component variables can be expressed using CPSDs between individual blade effective or lidar measurement variables as

$$S_{a_{u_{hh},\psi_m} b_{u_{hh},\psi_n}}(\omega) = \frac{1}{9}\sum_{i=1}^{3}\sum_{k=1}^{3} S_{a_{b_i,\psi_m} b_{b_k,\psi_n}}(\omega), \tag{5.12}$$

where $a_{u_{hh}}$, $b_{u_{hh}} \in \{u_{hh}, \hat{u}_{hh}\}$ and a_b, $b_b \in \{u_b, \hat{u}_b\}$. Similarly, using the shear component definitions in (5.10) and (5.11), the cross-spectrum for rotor effective or lidar-based horizontal shear variables a_{Δ_h}, $b_{\Delta_h} \in \left\{\Delta_h, \hat{\Delta}_h\right\}$ at fixed azimuth angles ψ_m and ψ_n is given by

$$S_{a_{\Delta_h,\psi_m} b_{\Delta_h,\psi_n}}(\omega) = C_a C_b \sum_{i=1}^{3}\sum_{k=1}^{3} \sin\left(\psi_m + \frac{(i-1)\,2\pi}{3}\right) \sin\left(\psi_n + \frac{(k-1)\,2\pi}{3}\right) S_{a_{b_i,\psi_m} b_{b_k,\psi_n}}(\omega), \tag{5.13}$$

where the constants

$$C_a,\, C_b \in \left\{ \frac{2}{3\int_0^R W_b(q)\, q dq},\, \frac{2}{3r} \right\} \tag{5.14}$$

depend on the specific combination of rotor effective and lidar measurement variables for which the spectrum is being determined. Finally, the CPSD between any two vertical shear variables a_{Δ_v}, $b_{\Delta_v} \in \left\{\Delta_v, \hat{\Delta}_v\right\}$ at azimuth angles ψ_m and ψ_n can be written as

$$S_{a_{\Delta_v,\psi_m} b_{\Delta_v,\psi_n}}(\omega) = C_a C_b \sum_{i=1}^{3}\sum_{k=1}^{3} \cos\left(\psi_m + \frac{(i-1)\,2\pi}{3}\right) \cos\left(\psi_n + \frac{(k-1)\,2\pi}{3}\right) S_{a_{b_i,\psi_m} b_{b_k,\psi_n}}(\omega). \tag{5.15}$$

The rotor effective wind speed component CPSDs for all necessary combinations of fixed azimuth angles determined with the formulas given in (5.12), (5.13), and (5.15) can be used in (5.8) or (5.9) to calculate rotational spectra for rotor effective or lidar-based u_{hh}, Δ_h, and Δ_v components. These rotational spectra can then be used to determine rotor effective measurement coherence given the three-rotating lidar measurement scenario proposed in Fig. 5.1.

5.2.1 Power Spectrum Calculations for Axisymmetric Wind Conditions

Under the condition that the combined wind field and lidar measurement scenario satisfies the axisymmetric properties listed in the previous section, i.e., if $S_{a_{\psi_m} b_{\psi_n}}(\omega)$ depends on m and n only through $|n-m|$, the CPSD formulas in (5.12), (5.13), and (5.15) can be simplified, reducing the computational requirements. For axisymmetric conditions, the cross-spectrum between two hub-height components at azimuth angles ψ_m and ψ_n can be simplified as

$$\begin{aligned} S_{a_{u_{hh},\psi_m} b_{u_{hh},\psi_n}}(\omega) &= \frac{1}{9}\sum_{i=1}^{3}\sum_{k=1}^{3} S_{a_{b_i,\psi_m} b_{b_k,\psi_n}}(\omega) \\ &= \frac{1}{3}\sum_{k=1}^{3} S_{a_{b,\psi_m} b_{b,\left(\psi_n+\frac{(k-1)2\pi}{3}\right)}}(\omega) \\ &= \frac{1}{3}\sum_{k=1}^{3} S_{a_{b,\psi_0} b_{b,\left(\psi_n-\psi_m+\frac{(k-1)2\pi}{3}\right)}}(\omega) \\ &= \frac{1}{3}\sum_{k=1}^{3} S_{a_{b,\psi_0} b_{b,\left(|\psi_n-\psi_m|+\frac{(k-1)2\pi}{3}\right)}}(\omega), \end{aligned} \tag{5.16}$$

where $\psi_0 = 0$. The second line of (5.16) is possible because blades 1, 2, and 3 are offset by $2\pi/3$ radians from each other, resulting in the following equivalence:

$$S_{a_{b_i,\psi_m} b_{b_k,\psi_n}}(\omega) = S_{a_{b,\psi_m+\frac{(i-1)2\pi}{3}} b_{b,\psi_n+\frac{(k-1)2\pi}{3}}}(\omega). \tag{5.17}$$

In other words, blade i at azimuth angle ψ can be described equivalently as a blade at azimuth angle $\psi + (i-1)\,2\pi/3$. Furthermore, due to axisymmetry,

$$S_{a_{b,\psi_m+\frac{(i-1)2\pi}{3}} b_{b,\psi_n+\frac{(i-1)2\pi}{3}}}(\omega) = S_{a_{b,\psi_m} b_{b,\psi_n}}(\omega), \tag{5.18}$$

and the nine CPSDs in the first line contain only three unique CPSDs, each repeated three times. The third line, where the azimuth angles of signals a_b and b_b are both shifted by ψ_m, is also possible because of axisymmetry. Finally, for the case when $\psi_m > \psi_n$ the fourth line of (5.16) relies on the following property due to axisymmetry: $S_{a_{\psi_0} b_{\psi_m}}(\omega) = S_{a_{\psi_0} b_{\psi_{-m}}}(\omega)$, as well as the property: $S_{a_{\psi_m} b_{\psi_n+2\pi}}(\omega) = S_{a_{\psi_m} b_{\psi_n}}(\omega)$. Equation (5.16) reveals that in axisymmetric wind conditions,

$$S_{a_{u_{hh},\psi_m} b_{u_{hh},\psi_n}}(\omega) = S_{a_{u_{hh},\psi_0} b_{u_{hh},\psi_{|n-m|}}}(\omega). \tag{5.19}$$

Thus the simplified rotational spectrum formula in (5.9) can be used to calculate rotating hub-height component spectra.

To simplify the shear component spectrum calculations in (5.13) and (5.15), assuming axisymmetry, the following trigonometric identities are utilized:

$$\sin\psi_1 \sin\psi_2 = \frac{\cos(\psi_1 - \psi_2) - \cos(\psi_1 + \psi_2)}{2} \tag{5.20a}$$

$$\cos\psi_1 \cos\psi_2 = \frac{\cos(\psi_1 - \psi_2) + \cos(\psi_1 + \psi_2)}{2}, \tag{5.20b}$$

and

$$\cos(\psi) + \cos\left(\psi + \frac{2\pi}{3}\right) + \cos\left(\psi + \frac{4\pi}{3}\right) = 0. \tag{5.21}$$

With axisymmetric conditions, the cross-spectrum between two horizontal shear components at azimuth angles ψ_m and ψ_n, presented in (5.13), can be simplified as

$$\begin{aligned}
S_{a_{\Delta_h,\psi_m} b_{\Delta_h,\psi_n}}(\omega) &= C_a C_b \sum_{i=1}^{3}\sum_{k=1}^{3} \sin\left(\psi_m + \frac{(i-1)\,2\pi}{3}\right) \sin\left(\psi_n + \frac{(k-1)\,2\pi}{3}\right) S_{a_{b_i,\psi_m} b_{b_k,\psi_n}}(\omega) \\
&= C_a C_b \tfrac{3}{2} \sum_{k=1}^{3} \cos\left(\psi_m - \psi_n - \frac{(k-1)\,2\pi}{3}\right) S_{a_{b,\psi_m} b_{b,\left(\psi_n + \frac{(k-1)2\pi}{3}\right)}}(\omega) \\
&= C_a C_b \tfrac{3}{2} \sum_{k=1}^{3} \cos\left(\psi_m - \psi_n - \frac{(k-1)\,2\pi}{3}\right) S_{a_{b,0} b_{b,\left(\psi_n - \psi_m + \frac{(k-1)2\pi}{3}\right)}}(\omega) \\
&= C_a C_b \tfrac{3}{2} \sum_{k=1}^{3} \cos\left(|\psi_n - \psi_m| + \frac{(k-1)\,2\pi}{3}\right) S_{a_{b,\psi_0} b_{b,\left(|\psi_n - \psi_m| + \frac{(k-1)2\pi}{3}\right)}}(\omega)\,.
\end{aligned} \tag{5.22}$$

The second line of (5.22) relies on the same properties that were used to form the second line of (5.16) as well as the identities in (5.20) and (5.21). The product of two sines appearing in the first line can be expressed as a sum of two cosines using (5.20a). However, by applying (5.21), the second cosine in the pair is eliminated during the double summation. In the third line, the azimuth angles of the signals a_b and b_b are simply shifted by ψ_m. In the final line, the simplification made to the cross-spectra follows the same logic as described for the hub-height component derivation in (5.16), with the simplification made to the cosine term resulting from the following symmetry: $\cos(-\psi) = \cos(\psi)$. As with the hub-height component term, (5.22) shows that in axisymmetric conditions $S_{a_{\Delta_h,\psi_m} b_{\Delta_h,\psi_n}}(\omega) = S_{a_{\Delta_h,\psi_0} b_{\Delta_h,\psi_{|n-m|}}}(\omega)$, once again allowing the simplified rotational

spectrum formula in (5.9) to be applied to the rotational horizontal shear component.

Following the same approach used to simplify the horizontal shear component cross-spectra in (5.22), and utilizing the cosine product-to-sum identity in (5.20b), the cross-spectrum between two vertical shear components at azimuth angles ψ_m and ψ_n, originally presented in (5.15), can be rewritten as

$$\begin{aligned} S_{a_{\Delta_v,\psi_m} b_{\Delta_v,\psi_n}}(\omega) &= C_a C_b \sum_{i=1}^{3}\sum_{k=1}^{3} \cos\left(\psi_m + \frac{(i-1)\,2\pi}{3}\right) \cos\left(\psi_n + \frac{(k-1)\,2\pi}{3}\right) S_{a_{b_i,\psi_m} b_{b_k,\psi_n}}(\omega) \\ &= C_a C_b \tfrac{3}{2} \sum_{k=1}^{3} \cos\left(\psi_m - \psi_n - \frac{(k-1)\,2\pi}{3}\right) S_{a_{b,\psi_m} b_{b,\left(\psi_n + \frac{(k-1)2\pi}{3}\right)}}(\omega)\,. \end{aligned} \tag{5.23}$$

However, the second line of (5.23) is equivalent to the second line of the horizontal shear formula in (5.22), resulting in equivalent cross-spectra for the horizontal and vertical shear components for azimuth angles ψ_m and ψ_n:

$$S_{a_{\Delta_v,\psi_m} b_{\Delta_v,\psi_n}}(\omega) = S_{a_{\Delta_h,\psi_m} b_{\Delta_h,\psi_n}}(\omega)\,. \tag{5.24}$$

Since the horizontal and vertical shear component cross-spectra are equivalent for any pair of azimuth angles, the rotational horizontal and vertical shear components are equivalent as well:

$$S_{a_{\Delta_v,r} b_{\Delta_v,r}}(\omega) = S_{a_{\Delta_h,r} b_{\Delta_h,r}}(\omega)\,. \tag{5.25}$$

The fact that the horizontal and vertical shear components have the same spectral characteristics is expected due to the axisymmetry of the wind field. The vertical shear calculations can be thought of as equivalent to the horizontal shear calculations after rotating the wind field by an azimuth angle of 90°. Assuming axisymmetry, the frequency-domain wind field statistics remain the same even after a constant shift in azimuth angle is applied to all locations.

Although the modified linear shear terms δ_h and δ_v given in (3.43), describing the difference in the wind speed across the rotor disk normalized by the hub-height wind speed, are the standard definitions used in NREL's aeroelastic simulation and turbine model linearization code FAST [9], spectra involving these components are difficult to calculate. All of the frequency-domain calculations described in this thesis rely on the wind speed variables being linear functions of the

wind speeds at different points in the wind field. Since the definitions of δ_h and δ_v are nonlinear due to the normalization by the hub-height component, their spectra cannot be calculated using the developed techniques. The spectra of these components can be approximated, however, by fixing the hub-height component at its mean value U. By applying the definitions in (3.43), this approximation is equivalent to

$$S_{a_{\delta_h,r}b_{\delta_h,r}}(\omega) = \frac{D^2}{U^2} S_{a_{\Delta_h,r}b_{\Delta_h,r}}(\omega) \tag{5.26a}$$

$$S_{a_{\delta_v,r}b_{\delta_v,r}}(\omega) = \frac{D^2}{U^2} S_{a_{\Delta_v,r}b_{\Delta_v,r}}(\omega)\,. \tag{5.26b}$$

Using the techniques for calculating stationary and rotating power spectra and measurement coherence described in Section 4.2 and in this chapter, examples of the power spectra and measurement coherence for a stationary blade effective wind speed and corresponding lidar measurement, a rotating blade effective wind speed and lidar measurement, and rotating rotor effective hub-height and linear shear components and lidar-based estimates using (5.11) are shown in Fig. 5.2. For all three scenarios the NREL 5-MW reference turbine parameters are used, and the lidar measurements rely on a scan radius of $r = 40.95$ m (0.65 R) and preview distance of $d = 113.4$ m (0.9 D). The axisymmetric Kaimal spectral model, described at the end of Section 5.1 is used in the spectrum calculations for an above-rated mean wind speed of $U = 13$ m/s and u component turbulence intensity $TI_u = 10\%$. Instead of using the turbulence standard deviation and length scale parameters defined for the Kaimal model in Section 3.1, the parameters belonging to unstable LES wind field 11, listed in Table 3.1, are applied. Specifically, the ratios $\sigma_v/\sigma_u = 0.72$ and $\sigma_w/\sigma_u = 0.59$ as well as the length scales $L_u = 230$ m, $L_v = 90$ m, and $L_w = 62$ m are used to determine the underlying power spectra and spatial coherence functions.

As explained in Section 3.5, the torque-based blade effective weighting functions shown in Fig. 3.16 (a) are used to calculate the rotor effective hub-height component spectra in Fig. 5.2 as well as the rest of this thesis, given the interest in using collective pitch control to regulate rotor speed, which is heavily dependent on the torque produced by the hub-height wind component. On

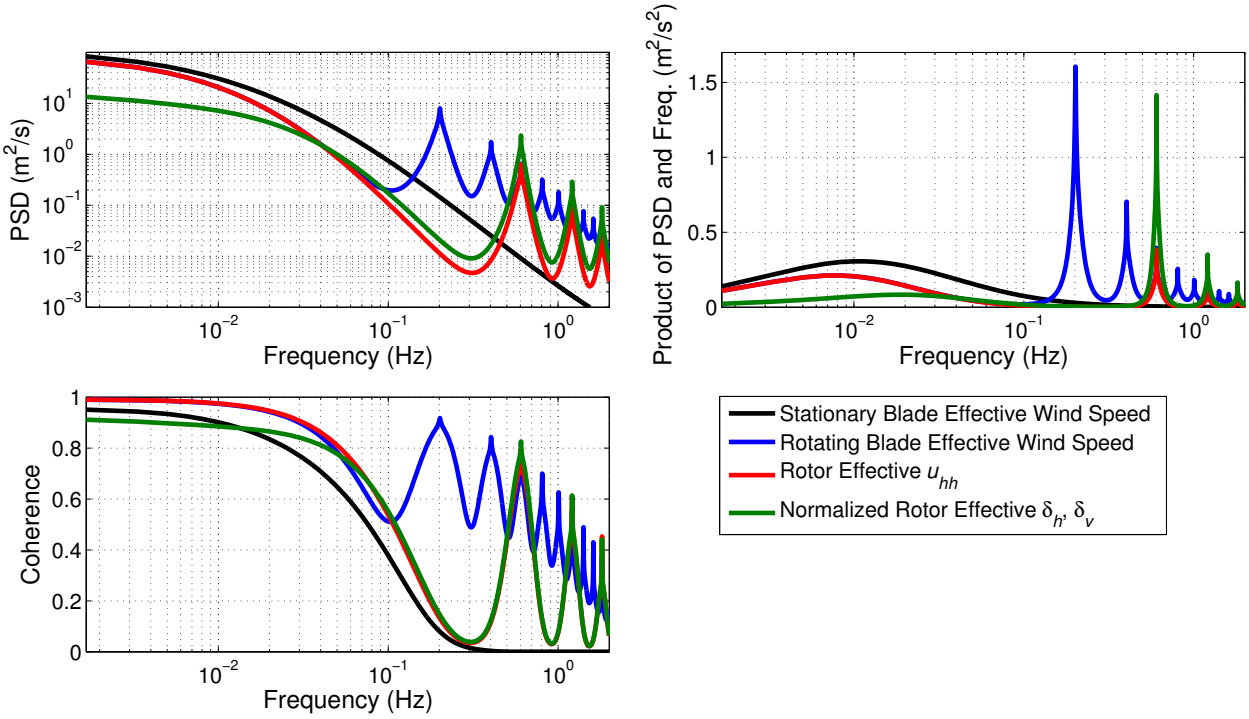

Figure 5.2: Power spectra and measurement coherence curves for a stationary blade effective wind speed (black), a rotating blade effective wind speed (blue), and rotating rotor effective hub-height (red) and shear (green) components for a lidar scan radius of $r = 40.95$ m and preview distance of $d = 113.4$ m using the NREL 5-MW reference turbine parameters. The power spectra are plotted in both unaltered form as well as multiplied by frequency. The axisymmetric Kaimal turbulence model based on LES wind field 11 is used, with $U = 13$ m/s, $TI_u = 10\%$, and $L_u = 230$ m.

the other hand, since wind shear has a greater impact on time-varying out-of-plane root bending moments experienced by the blades as they rotate through the wind field, which can be reduced using individual pitch control, than on rotor torque, the blade root bending moment-based weighting functions shown in Fig. 3.16 (b) are used to calculate the rotor effective shear components. Note that the torque-based blade effective weighting function is used to calculate the spectra for the single-rotating blade scenario in Fig. 5.2.

In order for the lidars to measure the wind at azimuth angles where the blades will be located by the time the measured wind reaches the rotor plane, the lidar measurement azimuth angle ψ_m, shown in Fig. 5.1, should be chosen as $\psi_t + (d/U) \cdot (2\pi/60) \cdot \omega_{rot}$, where ω_{rot} is the rotor speed in RPM and d/U gives the time it takes for the measured wind to reach the rotor. In the spectrum calculations performed to determine rotational measurement coherence, however, the phase shift due to the transit time d/U is subtracted from the phase of the cross-spectra between lidar measurements and wind speeds at the rotor, and the measurement azimuth angle is simply chosen as $\psi_m = \psi_t$. This simplification yields the same values of coherence that would result if the transit time were accounted for by choosing $\psi_m = \psi_t + (d/U) \cdot (2\pi/60) \cdot \omega_{rot}$.

Note that in Fig. 5.2 the power spectra of the blade effective and rotor effective quantities are displayed in their unaltered form as well as by multiplying the PSDs by frequency. As in Fig. 3.2, the latter form allows the area under the curves between any two frequencies to reflect the true fraction of the total power of the wind variable in that frequency band, i.e., to allow the dominant frequencies to be revealed. Also note that the power spectrum of the δ_h and δ_v quantities is normalized by $\left(3 \cdot U \int_0^R W_b(q)\, q dq\right)^2 / (2 \cdot D)^2$ so that its shape can be more easily compared to that of the hub-height component power spectrum.

The power spectrum of a rotating blade effective wind speed, as shown in Fig. 5.2, differs greatly from that of a stationary blade effective wind speed. While much of the energy is concentrated at low frequencies, strong peaks occur at the once-per-revolution (1P) frequency of ~0.2 Hz, corresponding to a rotor speed of 12.1 RPM, and its harmonics, due to rotational sampling of the turbulent structures in the wind field. The measurement coherence for a rotating lidar measure-

ment also peaks at the 1P frequency and its harmonics, and decays much more slowly than the coherence for a stationary blade and lidar measurement. When three rotating blade effective wind speeds are combined to form rotor effective hub-height and linear shear components, much of the energy is similarly concentrated at low frequencies, but with peaks occurring at the three-times per-revolution (3P) frequency of ∼0.6 Hz and its harmonics. Peaks occur at the 3P frequency and its harmonics because three blades are sampling the turbulent structures in the wind field every rotor revolution. A comparison between the u_{hh} component and the δ_h and δ_v components reveals that a greater fraction of the energy in the shear components is concentrated at higher frequencies such as the peak at the 3P frequency. Measurement coherence curves using the three-rotating lidar scenario follow the same trend as the power spectra. Coherence is high at low frequencies as well as the peaks at the 3P frequency and its harmonics. At low frequencies the measurement coherence for the shear components is lower than for the hub-height component, partly because the $\hat{u}_{hh}$ calculations tend to average out any uniform transverse and vertical components across the wind field, while the shear component estimates are more susceptible to the presence of transverse and vertical wind speeds.

5.3 Rotating Lidar Measurement Scenario Optimization

Similar to Fig. 4.6, which contains measurement coherence curves between stationary lidar measurements and blade effective wind speeds for different preview distances, Fig. 5.3 contains measurement coherence curves between rotating lidar-based estimates of the hub-height and shear components and the true rotor effective components based on three rotating blade effective wind speeds. Measurement coherence is calculated for the three preview distances $d = 37.8$ m, 113.4 m, and 189 m (0.3, 0.9, and 1.5 D) with fixed scan radius $r = 40.95$ m (0.65 R) using the same wind conditions that were used for the results in Fig. 5.2. As with the stationary measurement coherence curves, when the preview distance increases the low frequency coherence becomes larger because line-of-sight errors are reduced. But as preview distance increases, wind evolution becomes more severe and the coherence begins to decay at lower frequencies. However, the coherence at the

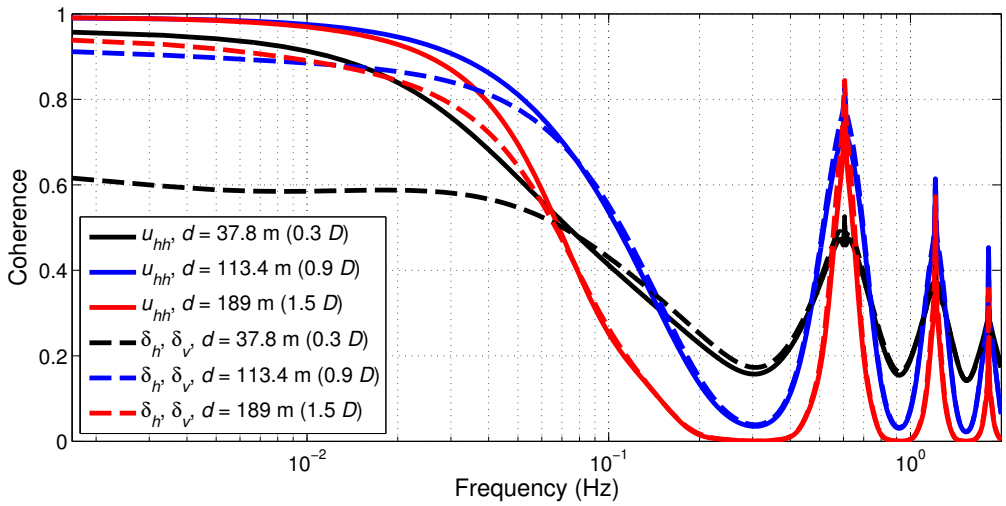

Figure 5.3: Measurement coherence for hub-height (solid) and shear (dashed) component measurements for a lidar scan radius of $r = 40.95$ m and preview distances of $d = 37.8$ m, 113.4 m, and 189 m. The axisymmetric Kaimal turbulence model based on LES wind field 11 is used, with $U = 13$ m/s, $TI_u = 10\%$, and $L_u = 230$ m.

3P frequency and its harmonics tends to reflect the low frequency behavior. As preview distance increases, thereby reducing the measurement angle indicated by θ in Fig. 5.1, the coherence at 3P and its harmonics increases, but the peaks become narrower. For all scenarios the low frequency coherence for the shear component measurements is lower than the hub-height component coherence, reflecting the larger impact that line-of-sight errors have on the shear component estimates.

By calculating measurement coherence for many different combinations of scan radius and preview distance, the dependence of the mean square measurement error on the scan parameters can be found. The optimal scan parameters that minimize MSE can then be determined for a particular wind condition. Assuming that the lidar measurements are optimally filtered using the prefilter with transfer function $H_{pre}(f) = \frac{S_{tm}(f)}{S_{mm}(f)}$ described in Section 2.2, the measurement MSE can be calculated by integrating the measurement error power spectrum given in (2.29), which depends on the PSD of the true wind speed variable $S_{tt}(f)$ as well as the measurement coherence $\gamma^2_{tm}(f)$, up to a maximum frequency f_{max} of interest:

$$\mathbf{E}\left[(w_t - H_{pre}w_m)^2\right] = \int_0^{f_{max}} S_{tt}(f)\left(1 - \gamma^2_{tm}(f)\right) df. \tag{5.27}$$

Since the analysis of lidar measurement error is primarily meant to aid the design of preview-based blade pitch control systems in above-rated conditions, f_{max} is chosen as the bandwidth of the pitch actuators, i.e., the maximum frequency for which blade pitch control can be used. The blade pitch actuator dynamics for the NREL 5-MW reference turbine are often modeled as second-order systems with a natural frequency of 1 Hz [28, 31]. Therefore, f_{max} is chosen as 1 Hz. In practice, controllers are typically designed using a lower bandwidth. For example, the baseline collective pitch controller for the NREL 5-MW reference turbine has a bandwidth of 0.25 Hz [8], while the IPC controller described in Bossanyi *et al.* [11] relies on 1P and 2P pitch control actions, i.e., ∼0.2 Hz and ∼0.4 Hz for the NREL 5-MW model's rated rotor speed of 12.1 RPM. But a value of $f_{max} = 1$ Hz is used for the measurement error calculations in this thesis to reflect the maximum possible control bandwidth that could potentially be implemented. For the majority of the MSE comparisons in this chapter, MSE is expressed not by its true value, as in (5.27), but as a fraction of the variance of the true wind component, using the following formula:

$$\mathbf{E}\left[\left(w_t - H_{pre} w_m\right)^2\right] \Big/ \sigma_t^2 = \int_0^{f_{max}} S_{tt}(f)\left(1 - \gamma_{tm}^2(f)\right) df \Bigg/ \int_0^{f_{max}} S_{tt}(f)\, df, \tag{5.28}$$

where the variance of the true wind component σ_t^2 is calculated by integrating the power spectrum $S_{tt}(f)$.

It should be noted that blade pitch control signals used to address the horizontal and vertical shear components in the non-rotating frame discussed in this thesis need to be converted into individual blade pitch commands in the rotating frame, using the MBC transformation [38], before being implemented as control actions. After applying the MBC transformation, the individual pitch commands will contain components at frequencies that are ± 1P (0.2 Hz) from the frequencies in the non-rotating frame. Therefore, given the pitch actuator bandwidth of 1 Hz, the maximum shear component frequency that can be addressed using blade pitch control is actually ∼0.8 Hz. But since there is very little power in the shear component spectra between 0.8 Hz and 1 Hz, as shown in Fig. 5.2, the integration limit of 1 Hz in (5.28) is employed without significant loss in accuracy.

Using the MSE formula in (5.27), the optimal scan radius r^* and preview distance d^* for a particular wind condition can be found according to the following formula:

$$(r^*, d^*) = \arg\min_{r,d} \int_0^{f_{max}} S_{tt}(f) \left(1 - \gamma_{tm}^2(f)\right) df, \tag{5.29}$$

where $S_{tt}(f)$ and $\gamma_{tm}^2(f)$ are replaced by the calculated PSD and measurement coherence functions corresponding to u_{hh}, δ_h, or δ_v. A brute-force approach for a range of r and d values is used to find the approximate optimal solution to (5.29) due to the complexity of the underlying spectrum and coherence formulas.

Fig. 5.4 contains the normalized measurement MSE for the hub-height and shear components as a function of scan radius and preview distance for the $U = 13$ m/s, $TI_u = 10\%$ wind condition used for the results in Figs. 5.2 and 5.3, based on LES wind field 11. For the hub-height component the optimal scan parameters are $r^* = 37.8$ m (0.6 R) and $d^* = 100.8$ m (0.8 D), producing a normalized MSE of 0.061, i.e., 6.1% of the true hub-height component variance. Slightly different optimal scan parameters of $r^* = 44.1$ m (0.7 R) and $d^* = 113.4$ m (0.9 D) yield a normalized MSE of 0.203 for the shear components. Measurement error is minimized for scan radii near 2/3 of the blade span, in the region where the blade effective weighting functions weight the wind speeds heavily, as can be inferred from Fig. 3.16. Although the peaks of the blade effective weighting functions for U= 13 m/s are closer to 80% blade span, measurements at the optimal scan radii correlate well with the overall weighted distribution of wind speeds along the blade. Measurements at 80% blade span would lose much of their correlation with wind speeds at the inboard section of the blade due to the sharp decrease in transverse and vertical spatial coherence.

As shown in Fig. 5.4, for preview distances less than the optimal preview distance, measurement error increases, due to greater line-of-sight errors caused by the larger measurement cone angle. For preview distances beyond the optimal value, on the other hand, measurement error increases due to more wind evolution. In general, close to the optimal value, measurement error is more sensitive to changes in scan radius than to variations in the preview distance. Therefore, when choosing a lidar scan scenario it is more important to measure near the optimal scan radius than

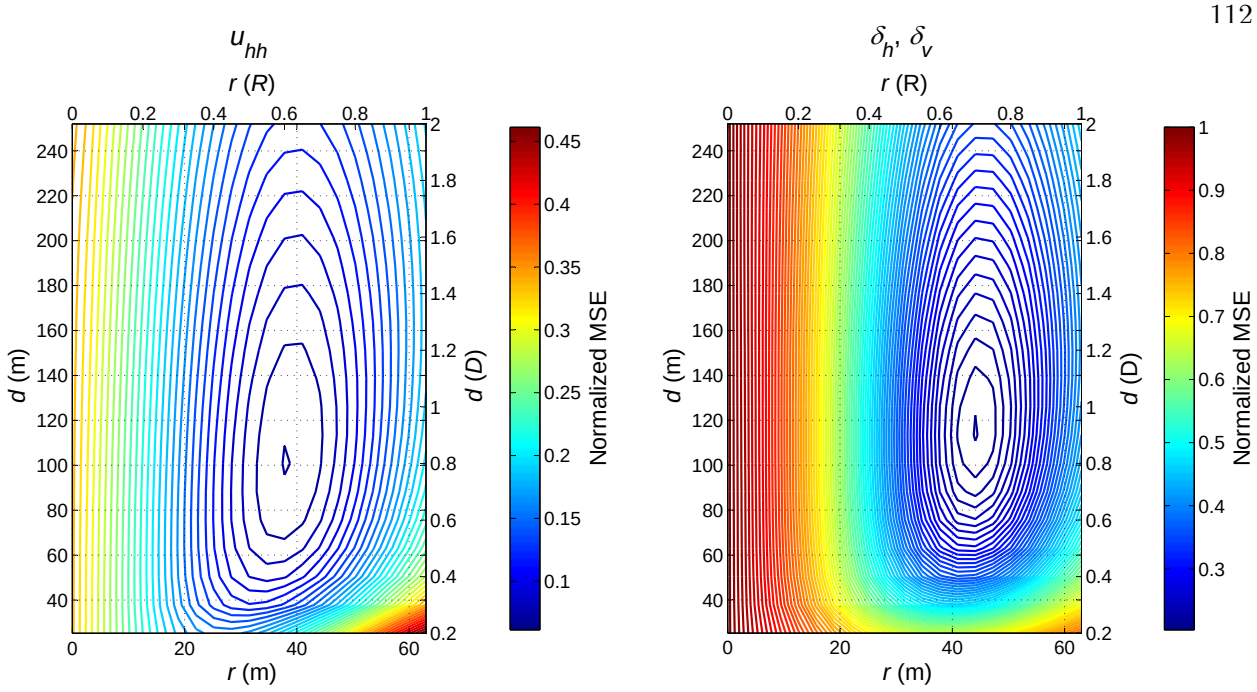

Figure 5.4: Normalized MSE as a function of scan radius r and preview distance d for the hub-height (u_{hh}) and shear (δ_h, δ_v) components using the axisymmetric Kaimal turbulence model based on LES wind field 11, with $U = 13$ m/s, $TI_u = 10\%$, and $L_u = 230$ m. The contour interval, in terms of the variance of the true wind components, is 0.01 in both plots.

to select the precise optimal preview distance, as long as the measurement angle is not too large. The hub-height component results reveal that for a scan radius of $r = 0$, equivalent to a forward staring lidar scenario, measurement error is much higher than at the optimal r value, but is still only $\sim$1/3 of the variance of the true hub-height component. However, for the shear components, scan radii close to 0 yield almost no meaningful information, i.e., a normalized MSE close to 1. This is because shear estimates require knowledge of how the wind speeds vary across the rotor area, while a point measurement at the rotor center is still a reasonable approximation of the average wind speed over the rotor disk due to the highly-correlated nature of low-frequency components of the wind over the rotor area. Note that the measurement quality for the shear components is much lower than for the hub-height component. This is partially due to line-of-sight errors affecting the shear estimates more than the hub-height component estimates, where the detected v and w components are reduced more through averaging. Another large source of the higher error is that

more of the energy in the shear components is concentrated at higher frequencies (see Fig. 5.2), which are more adversely affected by wind evolution.

5.3.1 The Impact of the Induction Zone on Rotating Measurement Coherence

The impact of the induction zone on lidar measurement quality can be assessed by including the axisymmetric induction zone model described in Section 3.3.1 in the frequency-domain power spectrum and coherence calculations. Specifically, the velocity reductions and wind direction changes illustrated in Fig. 3.12 and described in (3.26) and (3.27) are incorporated into the frequency-domain wind field model. The particular modifications to the wind field model are described below.

First of all, the corrected longitudinal wind component $u'_{\vec{x}_1}$ that interacts with the rotor at location $\vec{x}_1$ with azimuth angle ψ, longitudinal distance δ_x upstream of the rotor, and radial distance δ_{yz} from the symmetry axis is calculated as

$$u'_{\vec{x}_1} = \cos\left(\theta_{\text{ind}}\left(\delta_x, \delta_{yz}\right)\right) u_{\vec{x}_1} + \sin\left(\theta_{\text{ind}}\left(\delta_x, \delta_{yz}\right)\right)\left(\sin\left(\psi\right) v_{\vec{x}_1} - \cos\left(\psi\right) w_{\vec{x}_1}\right), \tag{5.30}$$

where $\theta_{\text{ind}}\left(\delta_x, \delta_{yz}\right)$ represents the wind direction angle in the induction zone:

$$\theta_{\text{ind}}\left(\delta_x, \delta_{yz}\right) = \arctan\left(V\left(\delta_x, \delta_{yz}\right) / U\left(\delta_x, \delta_{yz}\right)\right), \tag{5.31}$$

with $U\left(\delta_x, \delta_{yz}\right)$ representing the reduced mean longitudinal wind speed and $V\left(\delta_x, \delta_{yz}\right)$ indicating the mean radial wind speed at the longitudinal and radial distances δ_x and δ_{yz} (see Fig. 3.12). Equation (5.30) assumes that the wind speed vectors rotate along with the change in mean wind direction.

Secondly, the lidar-detected line-of-sight velocities are affected by the wind speed direction change; for a given measurement cone angle θ, the effective measurement angle at which the lidar measures the wind is larger due to the rotation of the wind speed vector in the radial direction. This change in the detected line-of-sight velocity can be described using the modified lidar direction vector $\ell'_{\vec{x}_2} = \left[\ell'_{x,\vec{x}_2}, \ell'_{y,\vec{x}_2}, \ell'_{z,\vec{x}_2}\right]$, which is a function of the intended lidar vector $\ell = [\ell_x, \ell_y, \ell_z]$ and

measurement azimuth angle ψ as well as the wind direction angle at the particular longitudinal and radial distances δ_x and δ_{yz} corresponding to the measurement point $\vec{x}_2$:

$$\ell'_{x,\vec{x}_2} = \cos\left(\theta_{\text{ind}}\left(\delta_x, \delta_{yz}\right)\right)\ell_x - \sin\left(\theta_{\text{ind}}\left(\delta_x, \delta_{yz}\right)\right)\sqrt{\ell_y^2 + \ell_z^2} \tag{5.32a}$$

$$\ell'_{y,\vec{x}_2} = -\left(\sin\left(\theta_{\text{ind}}\left(\delta_x, \delta_{yz}\right)\right)\ell_x + \cos\left(\theta_{\text{ind}}\left(\delta_x, \delta_{yz}\right)\right)\sqrt{\ell_y^2 + \ell_z^2}\right)\sin\left(\psi\right) \tag{5.32b}$$

$$\ell'_{z,\vec{x}_2} = \left(\sin\left(\theta_{\text{ind}}\left(\delta_x, \delta_{yz}\right)\right)\ell_x + \cos\left(\theta_{\text{ind}}\left(\delta_x, \delta_{yz}\right)\right)\sqrt{\ell_y^2 + \ell_z^2}\right)\cos\left(\psi\right). \tag{5.32c}$$

The corrected line-of-sight velocity $u'_{\ell,\vec{x}_2}$ detected by the lidar at the location $\vec{x}_2$ along the lidar beam is then given by

$$u'_{\ell,\vec{x}_2} = -\ell'_{x,\vec{x}_2}u_{\vec{x}_2} - \ell'_{y,\vec{x}_2}v_{\vec{x}_2} - \ell'_{z,\vec{x}_2}w_{\vec{x}_2}. \tag{5.33}$$

Finally, following the strategy used in (4.13), the estimate of the longitudinal u component is given by

$$\begin{aligned} \hat{u}'_{\vec{x}_2} &= -\tfrac{1}{\ell_x}u'_{\ell,\vec{x}_2} \\ &= \tfrac{\ell'_{x,\vec{x}_2}}{\ell_x}u_{\vec{x}_2} + \tfrac{\ell'_{y,\vec{x}_2}}{\ell_x}v_{\vec{x}_2} + \tfrac{\ell'_{z,\vec{x}_2}}{\ell_x}w_{\vec{x}_2}. \end{aligned} \tag{5.34}$$

The presence of the induction zone also influences the transverse and vertical spatial coherence within the wind field. As shown by the streamlines of the mean flow field in Fig. 3.12 (b), the wind field expands as it approaches the rotor because of conservation of mass. An assumption is made that the transverse and vertical coherence $\gamma^2_{yz,K_{\vec{x}_1}K_{\vec{x}_2}}(f)$ in the induction zone is a function of the separation distance Δ_{yz} between the points $\vec{x}_1$ and $\vec{x}_2$ prior to the wind field expansion. Therefore, the coherence parameter Δ_{yz} is calculated by first tracing the points $\vec{x}_1$ and $\vec{x}_2$ upstream outside of the induction zone and determining their freestream separation distance.

Due to the radial dependence of the mean wind speeds in the induction zone, illustrated in Fig. 3.12 (a), the time that it takes for turbulent wind speeds located the same distance upstream of the rotor, but with different radial positions, to reach the rotor can be different. In general, this variable arrival time produces non-zero mean phases between wind speeds at the same longitudinal position in the induction zone, and alters the formula relating phase to longitudinal separation described in (3.12). It is assumed that the phase of the CPSD between two wind speeds at locations $\vec{x}_1$ and $\vec{x}_2$ is a function of the different arrival times that the two wind speeds experience after

originating at the same freestream longitudinal position:

$$\measuredangle S_{K_{\vec{x}_1},K_{\vec{x}_2}}(f) = 2\pi f\left(\Delta t_{\mathrm{fr},\vec{x}_2} - \Delta t_{\mathrm{fr},\vec{x}_1}\right), \tag{5.35}$$

where $\Delta t_{\mathrm{fr},\vec{x}}$ indicates the transit time for a point in the wind field at $\vec{x}$ to travel from some fixed freestream longitudinal location.

Finally, the assumption is made that the longitudinal coherence describing wind evolution is affected by the reduced mean wind speeds in the induction zone, as described in Section 3.3.2. Specifically, the modified mean wind speed parameter U' is used, where U' describes the longitudinal distance traveled by the wind speeds between the two points of interest divided by the transit time. Similarly, the integral length scale parameters are scaled by U'/U. As discussed in Section 3.3.2, these wind parameter modifications do not account for the entire drop in longitudinal coherence in the induction zone calculated using the SOWFA-generated LES wind field. But because of uncertainty in how the true decrease in coherence varies for different wind conditions, only these simple mean wind speed and integral length scale modifications are made, which may yield a slight overestimation of the longitudinal coherence in the induction zone.

By incorporating the abovementioned wind field modifications, the impact of the induction zone on measurement error as a function of scan radius and preview distance is shown in Fig. 5.5, once again for wind conditions based on LES wind field 11 with $TI_u = 10\%$, but at the NREL 5-MW reference turbine's rated wind speed $U = 11.4$ m/s. At the rated wind speed, the axial induction factor, calculated using NREL's WT_Perf tool [88] is $\sim$0.17, close to the maximum induction factor of $\sim$0.18 in below-rated conditions [8], for which the results in Section 3.3 were created. For higher wind speeds, when the relative power capture of the turbine is reduced to maintain rated power production, the impact of the induction zone reduces rapidly; at $U = 13$ m/s, for example, $a = 0.1$. In Fig. 5.5, measurement error contours calculated by including induction zone effects are compared with the error contours calculated without incorporating the induction zone model. Note that the contour intervals are not constant, as they are in Fig. 5.4.

The contour plots in Fig. 5.5 reveal that the presence of the induction zone shifts the optimal

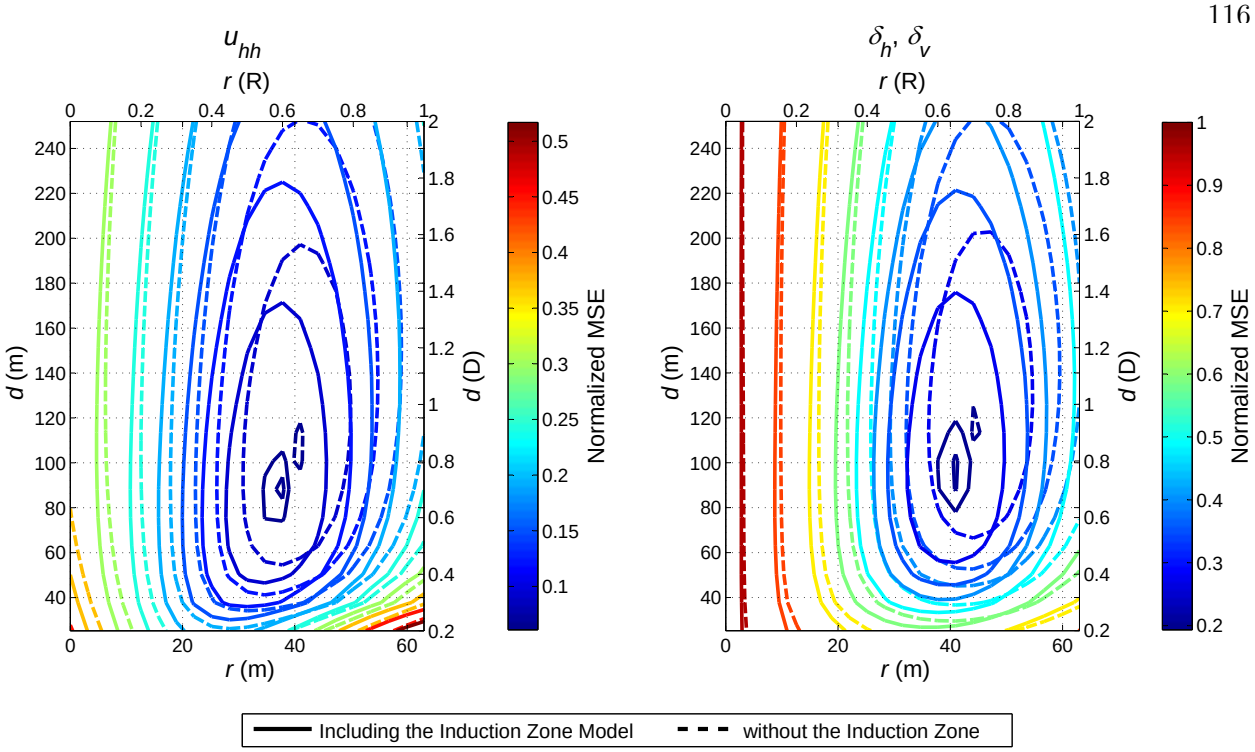

Figure 5.5: Normalized MSE as a function of scan radius r and preview distance d for the hub-height (u_{hh}) and shear (δ_h, δ_v) components with (solid) and without (dashed) the developed induction zone model using the axisymmetric Kaimal turbulence model based on LES wind field 11, with $U = 11.4$ m/s, $TI_u = 10\%$, and $L_u = 230$ m.

scan radius and preview distance to shorter values for both the hub-height and shear components. For u_{hh}, the induction zone causes the optimal scan radius to move from $r = 40.95$ m (0.65 R) to $r = 37.8$ m (0.6 R) and the optimal preview distance to shift from $d = 113.4$ m (0.9 D) to $d = 88.2$ m (0.7 D). Likewise, the inclusion of the induction zone model causes the optimal scan radius for shear component measurements to move from $r = 44.1$ m (0.7 R) to $r = 40.95$ m (0.65 R) and the optimal preview distance to relocate to $d = 100.8$ m (0.8 D) from $d = 113.4$ m (0.9 D). The shorter optimal scan radii with induction zone effects is a product of the expansion of the approaching wind field around the rotor, illustrated by the streamlines in Fig. 3.12 (b). In order to measure the wind that will interact with the rotor at a given radial position, the lidar should be focused at a smaller scan radius to account for the wind direction change. Shorter scan radii allow for shorter optimal preview distances, thereby reducing wind evolution without significantly

impacting line-of-sight errors. As a result of the shorter preview distances, the minimum achievable normalized MSE in the presence of the induction zone decreases slightly, even though the slower mean wind speeds cause a minor drop in longitudinal coherence. By including the induction zone, the minimum normalized MSE for the hub-height component changes from 0.063 to 0.061, while the error for the shear components drops from 0.2 to 0.19.

Because the developed induction zone model produces only a small change in the achievable measurement error, with diminishing impact as the wind speed increases in above-rated conditions, it is not included in the rest of the analyses in this thesis. However, it can be assumed that slightly shorter optimal scan radii and preview distances should be employed close to rated wind speed due to induction zone effects. Additional CFD data is required to determine how the true decrease in longitudinal coherence in the induction zone is related to the wind conditions.

5.3.2 The Impact of Yaw Error on Rotating Measurement Coherence

Most of the analyses in this thesis use the assumption that the turbine is perfectly aligned with the wind direction, that is, the longitudinal wind direction is perpendicular to the rotor plane. However, since yaw control on large turbines is typically performed on very long time scales compared to pitch and generator torque control [5, 6], wind turbines often operate with yaw error, or error between the longitudinal wind direction and the orientation of the rotor. If the same circularly-scanning lidar scenario explored throughout this chapter is maintained, then yaw error can lead to increased lidar measurement error. A simple top view of a turbine with a hub-mounted circularly-scanning lidar experiencing a yaw error γ is provided in Fig. 5.6. Two error sources are apparent based on the simple illustration. First of all, the wind measured by the lidar will reach the rotor at a different transverse position than anticipated. For example, the wind that interacts with the right side of the rotor, when viewing the turbine in Fig. 5.6 from upstream, is very poorly measured by the lidar. Secondly, the line-of-sight velocities measured by the lidar will contain a bias due to the yaw error. Using the specific yaw error shown in Fig. 5.6, the detected line-of-sight velocities will, on average, be higher for azimuth angles from 0 to 180°, when the lidar beam is

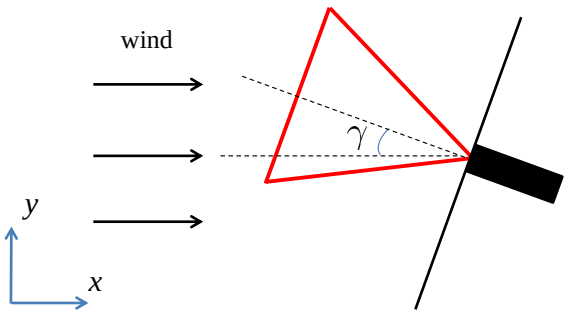

Figure 5.6: Top view of a wind turbine and lidar scan pattern with yaw error γ.

more aligned with the wind direction, than for azimuth angles between 180° and 360°, when the angle between the lidar beam and the wind direction is larger.

The effects of yaw error on measurement quality can be determined with a few simple modifications to the wind field model. First, new coordinates $[x', y', z]$ within the wind field are defined for all rotor positions and lidar measurement locations by rotating the longitudinal and transverse locations:

$$\left[x', y', z\right] = \left[\left(\cos\left(\gamma\right)x - \sin\left(\gamma\right)y\right), \left(\sin\left(\gamma\right)x + \cos\left(\gamma\right)y\right), z\right], \tag{5.36}$$

where x, y, and z are the original coordinates assuming zero yaw error. Next, the modified longitudinal wind component that interacts with the rotor at point $\vec{x}_1$, perpendicular to the rotor plane, that is used to calculate the rotor effective wind speeds, is given by

$$u'_{\vec{x}_1} = \cos\left(\gamma\right) u_{\vec{x}_1} - \sin\left(\gamma\right) v_{\vec{x}_1}, \tag{5.37}$$

where $u_{\vec{x}_1}$ and $v_{\vec{x}_1}$ are the true longitudinal and transverse wind components at point $\vec{x}_1$. Therefore, both the longitudinal and transverse wind components are used to form the rotor effective wind speeds.

Finally, the lidar direction vector is modified to reflect the projection of the velocity vector onto the lidar beam direction in the presence of yaw error. The modified lidar vector is formed as

$$\vec{\ell}' = \left[\left(\cos\left(\gamma\right)\ell_x - \sin\left(\gamma\right)\ell_y\right), \left(\sin\left(\gamma\right)\ell_x + \cos\left(\gamma\right)\ell_y\right), \ell_z\right], \tag{5.38}$$

where $\ell = [\ell_x, \ell_y, \ell_z]$ is the intended lidar direction assuming zero yaw error. Similar to (5.33), the

modified velocity $u'_{\ell,\vec{x}_2}$ detected by the lidar at point $\vec{x}_2$ along the lidar beam is equivalent to

$$u'_{\ell,\vec{x}_2} = -\ell'_x u_{\vec{x}_2} - \ell'_y v_{\vec{x}_2} - \ell'_z w_{\vec{x}_2}. \tag{5.39}$$

Assuming that the true yaw error is unknown, the strategy used in (4.13) to estimate the longitudinal u component is once again applied, yielding the following lidar-based longitudinal wind speed estimate:

$$\begin{aligned} \hat{u}'_{\vec{x}_2} &= -\tfrac{1}{\ell_x} u'_{\ell,\vec{x}_2} \\ &= \tfrac{\ell'_x}{\ell_x} u_{\vec{x}_2} + \tfrac{\ell'_y}{\ell_x} v_{\vec{x}_2} + \tfrac{\ell'_z}{\ell_x} w_{\vec{x}_2}. \end{aligned} \tag{5.40}$$

Using the $U = 13$ m/s, $TI_u = 10\%$ wind condition based on LES wind field 11, and the wind field modifications described above, the impact of yaw error on measurement coherence for the u_{hh}, δ_h, and δ_v components is shown in Fig. 5.7 for yaw errors between 2.5° and 25°. The lidar scan parameters are chosen as the optimal parameters for the hub-height and shear components with zero yaw error illustrated in Fig. 5.4: $r^* = 37.8$ m (0.6 R), $d^* = 100.8$ m (0.8 D) for u_{hh} and $r^* = 44.1$ m (0.7 R), $d^* = 113.4$ m (0.9 D) for δ_h and δ_v. While the power spectrum and measurement coherence computations used to determine measurement quality earlier in Section 5.3 relied on the simplified rotational CPSD formula for axisymmetric wind fields in (5.9) along with the simplifications discussed in Section 5.2.1, the presence of yaw error violates the axisymmetry property. The cross-spectrum between lidar measurements and/or blade effective wind speeds at two different azimuth angles no longer depends solely on the absolute difference between the azimuth angles. Therefore, the more computationally-intensive formula for calculating rotational CPSDs in (5.8) is employed. As a result, it is computationally prohibitive to calculate measurement error for as many different scan scenarios and wind conditions as are used for measurement quality analysis with zero yaw error. But the results in Fig. 5.7 illustrate the detrimental impact that yaw error has on measurement quality.

The coherence curves in Fig. 5.7 reveal that measurement quality is effected differently by yaw error depending on the particular wind component. Note that as a consequence of the lack of axisymmetry in the wind field, the coherence curves for the δ_h and δ_v components are different for $\gamma > 0$. Measurement coherence for the shear components suffers much more due to yaw error than

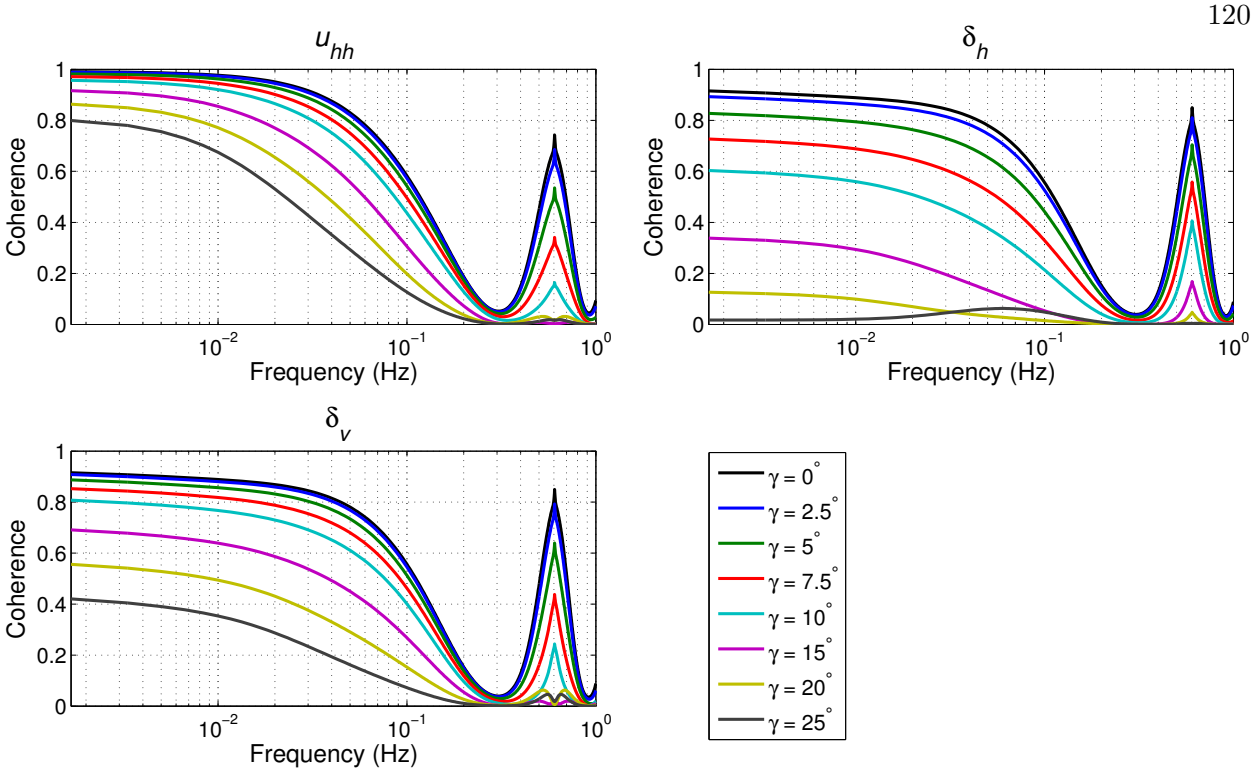

Figure 5.7: Measurement coherence for the u_{hh}, δ_h, and δ_v components as a function of yaw error using the optimal scan radii and preview distances for zero yaw error: $r^* = 37.8$ m (0.6 R), $d^* = 100.8$ m (0.8 D) for u_{hh} and $r^* = 44.1$ m (0.7 R), $d^* = 113.4$ m (0.9 D) for δ_h and δ_v. The axisymmetric Kaimal turbulence model based on LES wind field 11 is used, with $U = 13$ m/s, $TI_u = 10\%$, and $L_u = 230$ m.

for the hub-height component. Furthermore, yaw error degrades the quality of the δ_h component much more than δ_v, likely in part because of the disparity in how the wind speed vector is projected onto the lidar beam, forming line-of-sight measurements, across the scan circle in the horizontal direction. In contrast, the projection of the wind vector onto the lidar beam is much more similar across the scan circle in the vertical direction, where measurements contributing to the vertical shear estimate are formed. Additionally, measurement coherence near the peak at the 3P frequency decreases at a much faster rate because of yaw error than the low-frequency coherence, especially for the u_{hh} and δ_v components.

So that the impact of yaw error on measurement error can be more directly evaluated, Fig. 5.8 contains the normalized MSE, calculated using (5.28), for the three wind component measurements

corresponding to the coherence curves displayed in Fig. 5.7. Clearly, measurement error for the shear components increases more than the hub-height component error, although the hub-height MSE is much lower to begin with when yaw error is zero. While MSE for the horizontal and vertical shear components is identical with zero yaw error, the normalized δ_h component MSE increases faster as yaw error becomes greater, approaching 1 for $\gamma = 25°$. For a moderate yaw error of 10°, the normalized u_{hh} component MSE increases from 0.061 to 0.15, while it increases from 0.20 to 0.57 for δ_h and from 0.20 to 0.47 for δ_v.

While the impact of yaw error on measurement quality was analyzed in this section assuming that the lidar measurement scenario was the same as the scenario used for zero yaw error, it is possible to reduce measurement error by including a yaw error variable in the wind field measurement model. For example, as shown in Raach *et al.* [98], by using lidar measurements to estimate the hub-height component, horizontal and vertical linear shear, and yaw error using nonlinear techniques, the measurement coherence for the shear components is higher than when only the hub-height and shear components are estimated using linear techniques, assuming zero yaw error. However, given

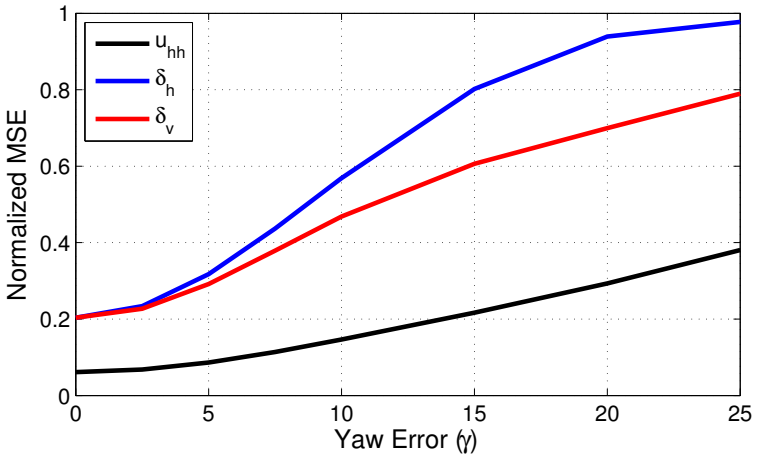

Figure 5.8: Mean square measurement error for the u_{hh}, δ_h, and δ_v components normalized by the variance of the rotor effective wind speed variables as a function of yaw error using the optimal scan radii and preview distances for zero yaw error: $r^* = 37.8$ m (0.6 R), $d^* = 100.8$ m (0.8 D) for u_{hh} and $r^* = 44.1$ m (0.7 R), $d^* = 113.4$ m (0.9 D) for δ_h and δ_v. The axisymmetric Kaimal turbulence model based on LES wind field 11 is used, with $U = 13$ m/s, $TI_u = 10\%$, and $L_u = 230$ m.

the three-beam circularly-scanning lidar scenario explored in this thesis, it is difficult to estimate both yaw error and horizontal shear. With only three unique lidar measurements each time step, only three wind field variables can be determined; either horizontal shear or yaw error can be included, but not both. In order to estimate yaw error in addition to horizontal shear using this lidar scenario, measurements over multiple time steps would have to be combined.

5.4 Rotating Lidar Measurement Scenario Optimization for Different Wind Conditions

In Section 5.3, the process of using frequency-domain measurement error calculations to optimize a scan scenario for a particular wind condition was described. The measurement error that results from a particular scan geometry varies with the wind condition, though, and the optimal scan scenario for one wind condition is not necessarily the best approach for another wind condition with a different mean wind speed, turbulence intensity, or length scale.

Measurement coherence curves and wind component power spectra are illustrated in Fig. 5.9 for four different wind conditions based on the length scales and turbulence standard deviation ratios from LES wind field 11: a mean wind speed of $U = 13$ m/s together with two different u component turbulence intensities $TI_u = 5\%$ and $TI_u = 30\%$ as well as a higher mean wind speed of $U = 23$ m/s paired with the same two turbulence intensities. The scan parameters chosen to create the measurement coherence curves consist of the optimal r and d that minimize measurement MSE for the particular wind condition. The power spectra reveal that for a fixed length scale L_u, a higher mean wind speed shifts the energy in the rotor effective wind speed components to higher frequencies. As shown in Fig. 3.16, for different mean wind speeds the blade effective weighting functions change only slightly, and thus the impact of the different blade effective weighting function shapes on the power spectra is expected to be relatively minor. As turbulence intensity increases for a given mean wind speed, measurement coherence decreases due to the additional longitudinal coherence decay from wind evolution. For a fixed turbulence intensity, increasing U causes the coherence to increase because the longitudinal coherence describing wind evolution becomes higher

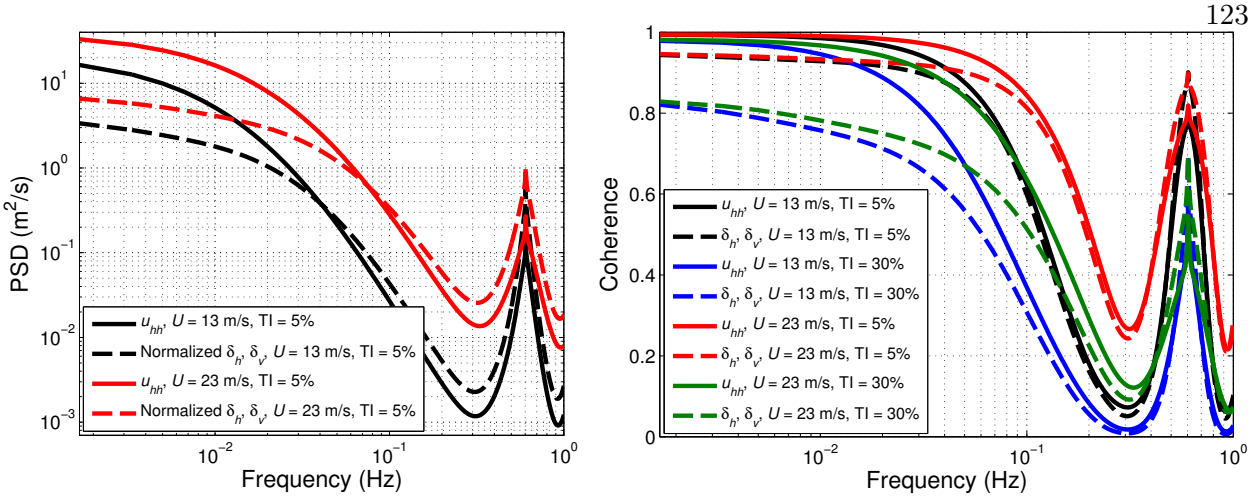

Figure 5.9: Power spectra and optimized measurement coherence for the u_{hh} as well as δ_h and δ_v components for all four combinations of low ($U = 13$ m/s) and high ($U = 23$ m/s) mean wind speeds and low ($TI_u = 5\%$) and high ($TI_u = 30\%$) u component turbulence intensities. The axisymmetric Kaimal turbulence model based on LES wind field 11 is used, with $L_u = 230$ m. Note that only the $TI_u = 5\%$ power spectra are shown because varying the turbulence intensity simply scales the PSDs by a constant.

as U increases.

By finding the optimal scan parameters for a variety of wind conditions, essentially by performing the optimization illustrated in Fig. 5.4 for each wind condition, the impact of the mean wind speed, turbulence intensity, and turbulence length scale on the minimum achievable MSE and corresponding optimal scan parameters can be found. In this section, however, rather than using the MSE objective function in (5.29), which assumes that the frequency-domain definition of the MMSE prefilter can be implemented, the preview time available to the prefilter is explicitly included in the optimization.

Following the derivation given in Section 2.3, the impulse response of the prefilter can be written as

$$\boldsymbol{h_{pre}} = \left[h_{pre}\left[-N_p\right], \quad \ldots, \quad h_{pre}\left[N_h\right] \right]^T, \tag{5.41}$$

where N_p is the number of samples of "preview" available to the filter and N_h is the number of samples into the past on which the filter operates. For simplicity, it is assumed that $N_h = N_p$. The preview time that is available to the prefilter is restricted by the preview time provided by the lidar

measurements: d/U. The number of samples of filter preview is then determined using

$$N_p = \lfloor (d/U - t_c) \cdot f_s \rfloor, \tag{5.42}$$

where f_s is the sampling frequency of the control system and t_c is a fixed preview time required by the controller. As explained in Dunne *et al.* [28], preview time is required by a feedforward controller primarily to overcome the pitch actuator delay. For the NREL 5-MW reference turbine model, the required preview time is less than 0.5 s [28], and a value of $t_c = 0.5$ s is used to calculate the results in this thesis. Note that more sophisticated controllers, such as model predictive controllers, can require preview information over some finite horizon, and could therefore require greater values of t_c.

Relying on the definitions provided in Section 2.3, particularly the MSE formula presented in (2.36), the measurement error resulting from the use of the MMSE prefilter with N_p and N_h constraints given in (2.33), normalized by the variance of the true wind component, can be calculated as

$$\mathbf{E}\left[(w_t - H_{pre} w_m)^2\right] / \sigma_t^2 = \left(R_{tt}[0] - \boldsymbol{R_{tm}}^T \boldsymbol{R_{mm}}^{-1} \boldsymbol{R_{tm}}\right) / R_{tt}[0], \tag{5.43}$$

where $R_{tt}[0]$ yields the variance of the true wind component. With implicit filter preview time constraints governed by (5.42), the scan pattern optimization objective is defined as

$$(r^*, d^*) = \underset{r,d}{\arg\min} \left(R_{tt}[0] - \boldsymbol{R_{tm}}^T \boldsymbol{R_{mm}}^{-1} \boldsymbol{R_{tm}}\right). \tag{5.44}$$

Since only the frequency-domain statistics of measurement error are calculated using the techniques described in Section 4.1 and earlier in this chapter, the time domain statistics required by (5.43) and (5.44) must be determined. The cross-correlation function between the lidar measurement and true wind speed signals $R_{tm}[n]$ is calculated using the inverse Fourier transform of the corresponding CPSD following the definition in (2.11). Similarly, the lidar measurement autocorrelation function $R_{mm}[n]$ is determined by computing the inverse Fourier transform of the lidar measurement PSD. To reflect the interest in frequencies up to 1 Hz for blade pitch control purposes, the CPSD from which $R_{tm}[n]$ is calculated contains zero power above 1 Hz. But the lidar measurement PSD used to

calculate $R_{mm}[n]$ contains higher frequencies so that the prefilter is forced to remove the undesired high frequencies of the measurement through low-pass filtering.

Using the optimization objective in (5.44) including filter preview time constraints, the three-beam lidar scan scenario is optimized for mean wind speeds from $U = 11$ m/s to the NREL 5-MW model's cut-out wind speed of $U = 25$ m/s, and for u component turbulence intensities between $TI_u = 2\%$ and $TI_u = 35\%$. The resulting optimal scan radii, preview distances, and corresponding minimum achievable normalized MSE values given by (5.43) are shown in Fig. 5.10, once again for wind conditions based on unstable LES wind field 11, i.e., for $L_u = 230$ m, $L_v = 90$ m, and $L_w = 62$ m, and $\sigma_v/\sigma_u = 0.72$ and $\sigma_w/\sigma_u = 0.59$.

Fig. 5.10 reveals that for a fixed turbulence intensity, as the mean wind speed increases

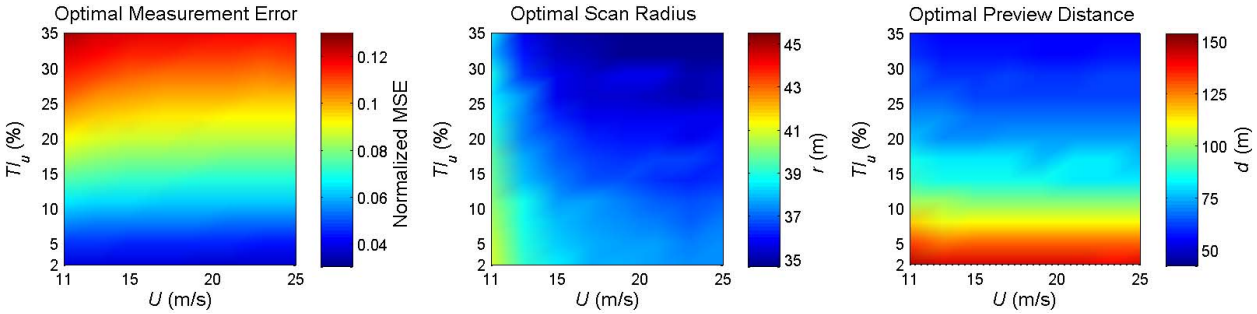

(a) Hub-height component (u_{hh}).

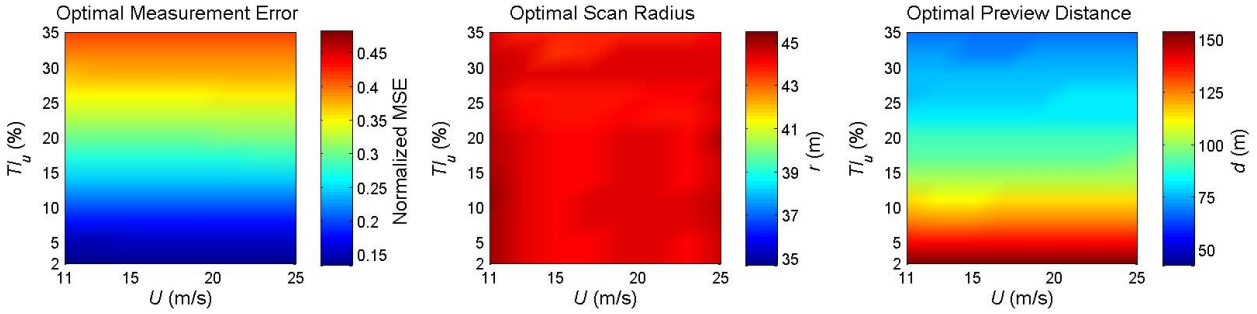

(b) Shear components (δ_h, δ_v).

Figure 5.10: Minimum achievable measurement MSE normalized by the variance of the rotor effective wind components along with the corresponding optimal scan radii r and preview distances d as a function of mean wind speed U and u component turbulence intensity TI_u for wind conditions based on unstable LES wind field 11 with $L_u = 230$ m, $L_v = 90$ m, and $L_w = 62$ m, as well as $\sigma_v/\sigma_u = 0.72$ and $\sigma_w/\sigma_u = 0.59$. Scan scenario optimization results are shown for (a) the hub-height component and (b) the linear shear components.

the optimal scan parameters and minimum achievable normalized measurement errors change very little. The optimal scan radius for hub-height component measurements becomes slightly shorter, following the tendency of the blade effective weighting functions shown in Fig. 3.16 to weight wind speeds closer to the rotor center more heavily as wind speed increases and the blades are pitched to reduce power capture. But the impact of the different optimal scan radii on optimal preview distance and achievable measurement quality is very small. For the shear components, the blade root bending moment-based weighting functions that are utilized are almost independent of U, as shown in Fig. 3.16 (b), and consequently the optimal scan radius is almost constant near $r = 45$ m ($\sim$0.7 R) over the range of wind conditions analyzed. As turbulence intensity grows, the optimal preview distance decreases to partially counter the intensifying wind evolution. The shorter preview distances, in turn, cause a minor decrease in the optimal scan radius for hub-height component measurements that mitigates line-of-sight errors slightly by reducing the measurement cone angle. But since the optimal scan radius is primarily determined by the distribution of the blade effective weighting function across the blade span, and thus remains roughly the same regardless of turbulence intensity, measurement error increases due to the rise in line-of-sight errors caused by larger measurement angles.

For both the hub-height and shear components, the minimum achievable normalized measurement error changes very little as the mean wind speed increases. As shown in Fig. 5.9, at a given frequency, the measurement coherence increases as mean wind speed becomes larger, due to the equivalent dependence of the longitudinal coherence model describing wind evolution on the mean wind speed. However, as also shown in Fig. 5.9, more of the energy in the rotor effective wind components is shifted to higher frequencies as mean wind speed increases. Therefore, the measurement coherence where most of the power in the wind is concentrated stays roughly the same, producing only a minor change in normalized measurement error as wind speed increases. Since the blade effective weighting functions in below-rated conditions are very similar to those at the rated wind speed of $U = 11.4$ m/s, the achievable measurement quality and optimal scan parameters for wind speeds below 11 m/s, not shown in Fig. 5.10, are expected to be nearly the

same as those for $U = 11$ m/s.

So that the impact of turbulence length scale on the scan scenario optimization can be examined, the optimal r and d values and corresponding minimum achievable normalized MSEs are calculated for the same range of mean wind speeds and turbulence intensities analyzed in Fig. 5.10, but for wind conditions based on stable LES wind field 12, listed in Table 3.1, with very short length scales $L_u = 56$ m, $L_v = 26$ m, and $L_w = 20$ m, and turbulence standard deviation ratios $\sigma_v/\sigma_u = 0.73$ and $\sigma_w/\sigma_u = 0.55$. The resulting optimized scan scenarios as a function of U and TI_u are provided in Fig. 5.11.

In general, the trends shown in Fig. 5.11 are similar to the optimal scan scenario behavior for the wind conditions based on LES wind field 11 presented in Fig. 5.10. But since the small

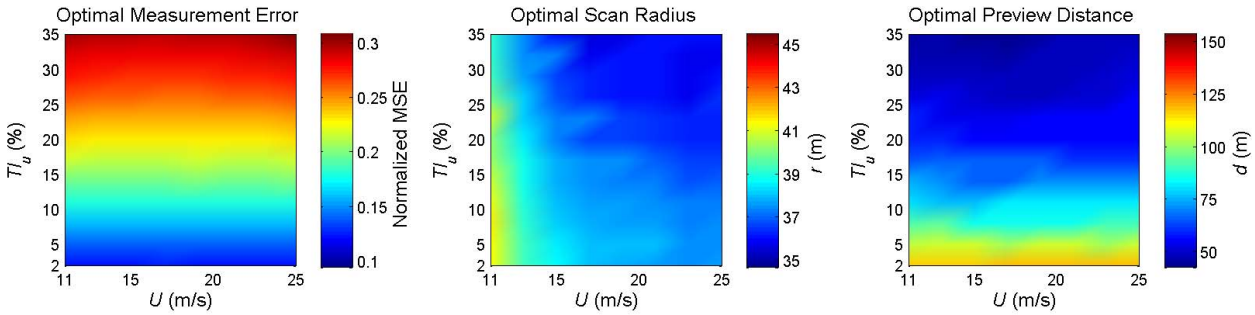

(a) Hub-height component (u_{hh}).

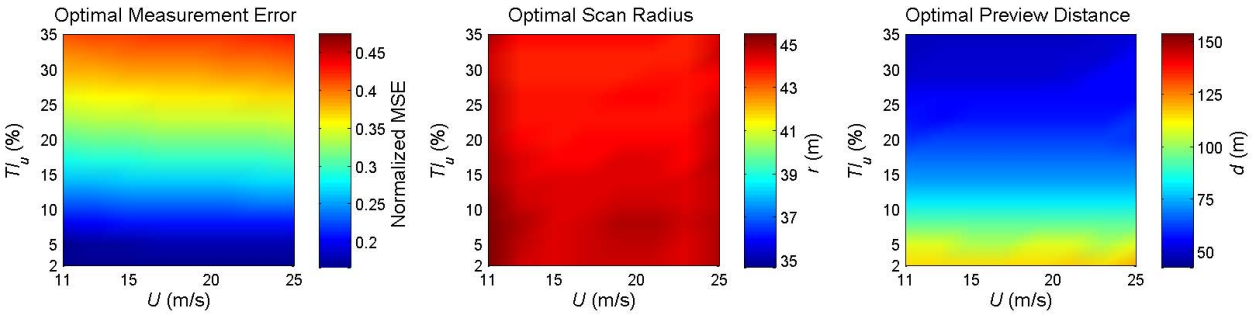

(b) Shear components (δ_h, δ_v).

Figure 5.11: Minimum achievable measurement MSE normalized by the variance of the rotor effective wind components along with the corresponding optimal scan radii r and preview distances d as a function of mean wind speed U and u component turbulence intensity TI_u for wind conditions based on unstable LES wind field 12 with $L_u = 56$ m, $L_v = 26$ m, and $L_w = 20$ m, as well as $\sigma_v/\sigma_u = 0.73$ and $\sigma_w/\sigma_u = 0.55$. Scan scenario optimization results are shown for (a) the hub-height component and (b) the linear shear components.

turbulence length scales cause the longitudinal coherence describing wind evolution to drop considerably, especially at low frequencies, the optimal preview distances are shorter. Because of the increased severity of wind evolution and the use of shorter preview distances to help counter the evolution, which in turn increases the measurement angle and causes more line-of-sight errors, the achievable normalized measurement error rises as well. Further adding to the greater measurement errors is the fact that smaller length scales shift more of the energy in the rotor effective wind speed variables to higher frequencies, which are affected by wind evolution more. It is worth noting that the relative increase in measurement error caused by shorter integral length scales is higher for the hub-height component than for the shear components.

The scan scenario optimization results presented in Figs. 5.10 and 5.11 indicate that the optimal lidar preview distance strongly depends on the turbulence intensity, while the optimal scan radius has a smaller dependence on the wind conditions. Depending on the mean wind speed the optimal scan radius ranges from 34.65 m (0.55 R) to 41.34 m (0.66 R) for the hub-height component and between roughly 43.5 m (0.69 R) and 45.5 m (0.72 R) for the shear components, while the optimal preview distance varies from 42.5 m (0.34 D) to 153.6 m (1.22 D) depending on the wind conditions. As a result, a lidar system with variable scan parameters scheduled based on the mean wind speed and estimated turbulence intensity would lead to improved measurement quality throughout a range of wind conditions. But by analyzing the normalized MSE plotted against scan radius and preview distance in Fig. 5.4, it is clear that the measurement error is much less sensitive to deviations of the preview distance from the optimal value than to deviations of the scan radius from its optimal value. Therefore it is not as important to closely track the optimal preview distance as wind conditions change. Further analyses are required to determine how much additional error would be incurred if a single fixed preview distance were used for all wind conditions. Since the optimal scan radius varies by no more than $\sim$6.7 m (0.11 R) for the hub-height component and $\sim$2 m (0.03 R) for the shear components, the performance increase made possible using a lidar system with a variable scan radius might not warrant the added complexity and cost either. However, a tradeoff between hub-height component and shear component measurement quality would have to

be made when selecting a single fixed scan radius.

5.4.1 The Impact of Filter Preview Constraints on Measurement Scenario Optimization

Although the optimization results presented in Section 5.4 show the minimum measurement errors that can be achieved given the preview time constraints imposed by the scan pattern, they do not reveal how close the errors are to the minimum normalized MSE that can be obtained with the optimal prefilter unconstrained by preview time limitations. To analyze how close the errors resulting from time-constrained prefilters are to the true optimal MSE, the optimization results for the wind conditions based on LES wind field 12, with $L_u = 56$ m, shown in Fig. 5.11, are presented in Fig. 5.12 with and without imposed filter preview time constraints. The optimization objective for the unconstrained analysis is given by the frequency-domain formula in (5.29), while the optimization objective with preview time constraints is given by (5.44). The wind condition with shorter turbulence length scales is analyzed because the shorter optimal preview distances, which result in less preview time, are expected to cause the greatest disparity between the constrained and unconstrained optimization results.

The error and scan parameter contours in Fig. 5.12 illustrate how the performance of the preview time-constrained prefilter essentially matches the performance of the unconstrained MMSE filter for low to moderate wind speeds and turbulence intensities. For very high turbulence intensities, however, the reduced optimal preview distances cause the available preview time to decrease, and thus a more noticeable difference between the constrained and unconstrained filtering scenarios can be seen. For example, when $U = 25$ m/s, and TI_u is above 15%, the time-constrained optimal preview distance is greater to allow additional filtering time. The resulting discrepancy in normalized MSE is relatively small, though. For the highest mean wind speed and turbulence intensity values analyzed, the optimal preview distance for the hub-height component of 40.95 m resulting from the time-constrained optimization allows only 1.14 s of filter preview time, but the resulting MSE is only 4% higher than the MSE yielded by the unconstrained optimization scenario.

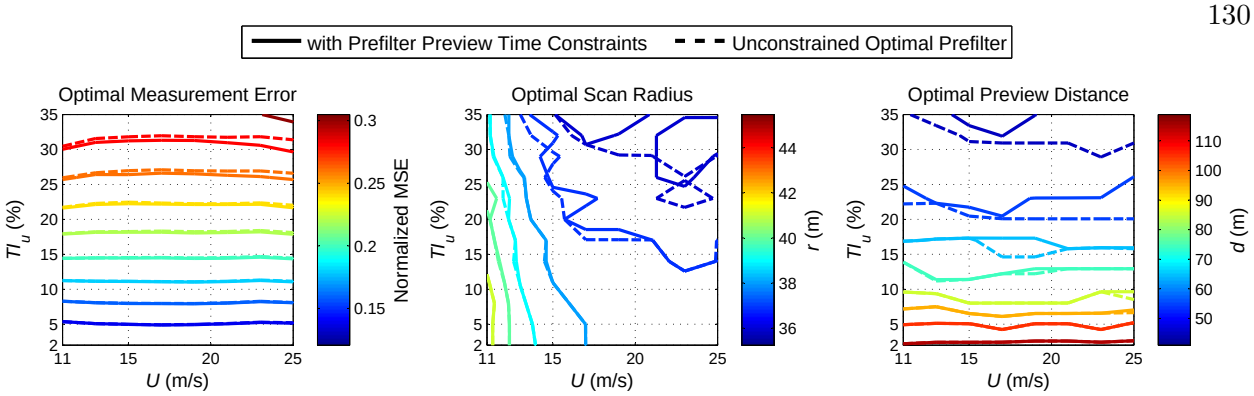

(a) Hub-height component (u_{hh}).

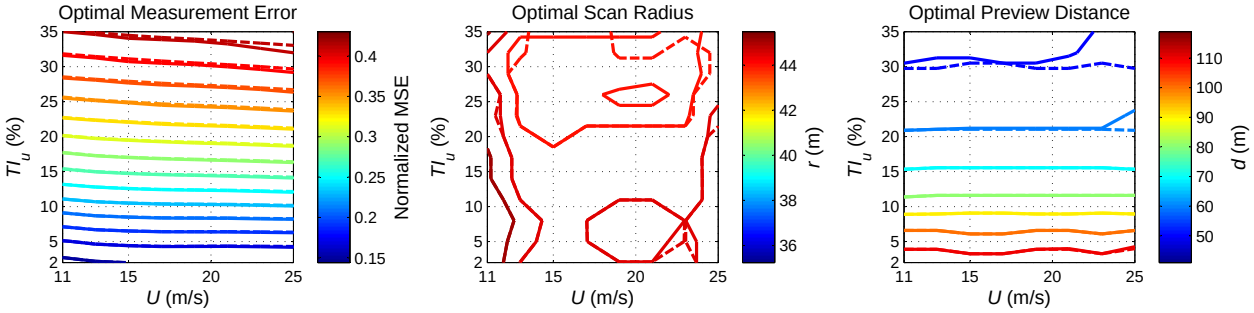

(b) Shear components (δ_h, δ_v).

Figure 5.12: Contour plots of minimum achievable measurement MSE normalized by the variance of the rotor effective wind components along with the corresponding optimal scan radii r and preview distances d as a function of mean wind speed U and u component turbulence intensity TI_u with (solid) and without (dashed) filter preview time constraints. The wind conditions are based on unstable LES wind field 12 with $L_u = 56$ m, $L_v = 26$ m, and $L_w = 20$ m, as well as $\sigma_v/\sigma_u = 0.73$ and $\sigma_w/\sigma_u = 0.55$. Scan scenario optimization results are shown for (a) the hub-height component and (b) the linear shear components.

5.5 Discussion and Conclusions

This chapter presented a technique for calculating measurement error for a three-rotating lidar scenario used to estimate rotor effective hub-height and linear shear wind variables, which are in turn calculated based on three rotating blade effective wind speeds. These three wind components can be used as inputs to a preview-based individual pitch controller designed with a non-rotating model of the turbine using the MBC transform [38]. A method for calculating the measurement quality for a single rotating lidar measurement and single rotating blade was also discussed, which can aid in the analysis of preview-based individual pitch controllers designed using rotating models of the

turbine. Measurement error is determined by calculating the power spectra of the rotor effective wind speeds and lidar measurements, the cross-spectrum between the lidar measurements and the wind variables, and the measurement coherence using frequency-domain techniques. Two methods were suggested for calculating measurement error. First, a frequency-domain measurement error calculation assuming that the optimal prefilter defined by its frequency content can be implemented was proposed. Second, a more realistic time-domain method for calculating the measurement error resulting from the use of a prefilter with time constraints imposed by the lidar preview distance was discussed.

A scan scenario optimization for a single wind condition revealed the presence of an optimal scan radius/preview distance combination that minimizes MSE. The optimal scan radius is largely determined by the shape of the blade effective weighting function, i.e., by where the wind speeds along the blade are weighted most heavily. For preview distances shorter than the optimal value, the measurement angle increases and line-of-sight errors cause measurement error to increase. On the other hand, for preview distances beyond the optimal distance, wind evolution intensifies causing higher measurement error. It was shown that by including the induction zone model described in Section 3.3, the achievable measurement error changes very little, in fact decreasing slightly, while the optimal scan radius and preview distance become smaller due to the expansion of the approaching wind field around the rotor. An investigation into the impact of yaw error on measurement quality revealed that if the yaw error is unaccounted for by the lidar scenario, measurement error can increase significantly for moderate amounts of yaw error. Yaw error affects measurements of the three wind components differently, however, with the horizontal shear component showing the most sensitivity to yaw error, followed by the vertical shear component, and finally the hub-height component, which is the most robust to yaw error. Since wind turbines are likely to encounter yaw error during operation, before the necessary error threshold is reached causing the yaw motor to activate, it could be more advantageous to use shorter-than-optimal preview distances to help mitigate the effects of yaw error. This way, errors caused by the measured wind reaching the rotor at different transverse positions than anticipated would be reduced.

Scan scenario optimizations performed for different wind conditions assuming filter preview-time constraints show that the optimal scan parameters and the achievable measurement error depend on the mean wind speed and turbulence intensity. As mean wind speed increases, the optimal scan radius for hub-height component measurements becomes slightly shorter to match the region along the blade where the mean wind speed-dependent blade effective weighting function weights the wind most heavily, although the weighting functions and thus the optimal scan radii are almost constant for wind speeds above $U = 14$ m/s. The optimal scan radius for the shear components does not vary significantly, on the other hand, regardless of mean wind speed. As turbulence intensity increases, the optimal preview distances become shorter, due to more severe wind evolution and the resulting penalty on long preview distances. The achievable measurement error therefore increases with turbulence intensity due to the intensification of wind evolution and greater line-of-sight errors caused by larger measurement angles. For both wind components, measurement error changes very little as the mean wind speed rises. A comparison of optimization results for different turbulence length scales showed that the optimal preview distances decrease as the length scale decreases, which causes wind evolution to become more severe and the achievable measurement error to rise. Finally, it was shown that the measurement error achieved by employing a measurement prefilter with time constraints imposed by the lidar scenario nearly matches the minimum error that can be achieved by ignoring filter preview time constraints.

The methods described in this chapter provide a relatively quick way to determine measurement error for different lidar scan parameters and different wind conditions using a frequency-domain wind field model, a lidar model, and knowledge of the aerodynamic properties of the turbine required to calculate the blade effective weighting functions. Many different scan scenarios and wind conditions can be analyzed directly in the frequency domain without the need to simulate any wind speed time series. But many practical issues related to implementing the optimal prefilter remain. Specifically, the cross-correlation function between the lidar measurements and the true wind disturbances that interact with the turbine, necessary to derive the optimal prefilter impulse response, needs to be calculated. The next chapter presents a wind speed estimator which can be used to

determine the "true" hub-height and shear component wind disturbances that interact with the turbine, allowing the prefilter to be implemented. In Chapter 7, the process required to estimate the prefilter coefficients given the lidar measurement and "true" wind speed signals is described.

Finally, the analyses in this chapter rely on many simplifications. First of all, it was assumed that the turbine rotates at a fixed rotational speed, although in practice, changes in wind speed cause fluctuations around the rated rotor speed. Second, the rotor effective wind variables were calculated as a linear function of the wind speeds along the three blades using torque and out-of-plane blade root bending moment-based blade effective weighting functions. In reality, the torque and thrust produced by the blades are nonlinear functions of the wind speeds interacting with the rotor, and additionally, the transverse and vertical components have an impact on the rotor aerodynamics, albeit smaller than the u component in general. To assess whether the simplified frequency-domain calculations used in this chapter accurately describe lidar measurement quality, lidar measurement simulations described in Chapter 7 are performed using NREL's aeroelastic simulator FAST [9] with stochastic spatially-varying wind inflow. Rather than relying on linearized blade effective wind speed variables to determine the rotor effective wind speeds, measurement error is determined by comparing the simulated lidar measurements with rotor effective wind speed estimates produced by the wind speed estimator discussed in the next chapter.

Chapter 6

Wind Speed Estimation

Wind speed estimation using measured outputs from a wind turbine has a variety of applications in wind turbine control. For example, the linear models of wind turbine dynamics often used in controller design vary as a function of the wind speed disturbances. Estimates of these wind speed disturbances can be used as scheduling variables as part of gain-scheduled control strategies [57, 59, 99, 100]. Additionally, the estimated wind speed can be used directly as an input to a feedforward controller that augments a typical feedback control loop [101]. To be more accurate, as noted in van der Hooft [101], this strategy is a type of "pseudo" feedforward control because the wind speed estimates are formed using the same information that is available to the feedback controller. Active power control, another application of wind speed estimation, is a strategy whereby a turbine is de-rated to produce a specific fraction of its potential power output so that it can provide additional power when needed [102]. The estimated wind speed is used to determine the maximum power that the turbine is capable of generating.

For the work discussed in this thesis, a wind speed estimator is required to determine the "true" wind disturbances that interact with the wind turbine so that the cross-spectrum (or cross-correlation) between the measured wind and the wind that interacts with the turbine can be calculated. The cross-spectrum or cross-correlation is required to determine the transfer function of the MMSE measurement filter discussed in Chapter 2. A modified block diagram of the feedforward control scenario presented in Fig. 2.1 showing how a wind speed estimator is used to determine the measurement filter is provided in Fig. 6.1. Turbine outputs and control inputs are used to estimate

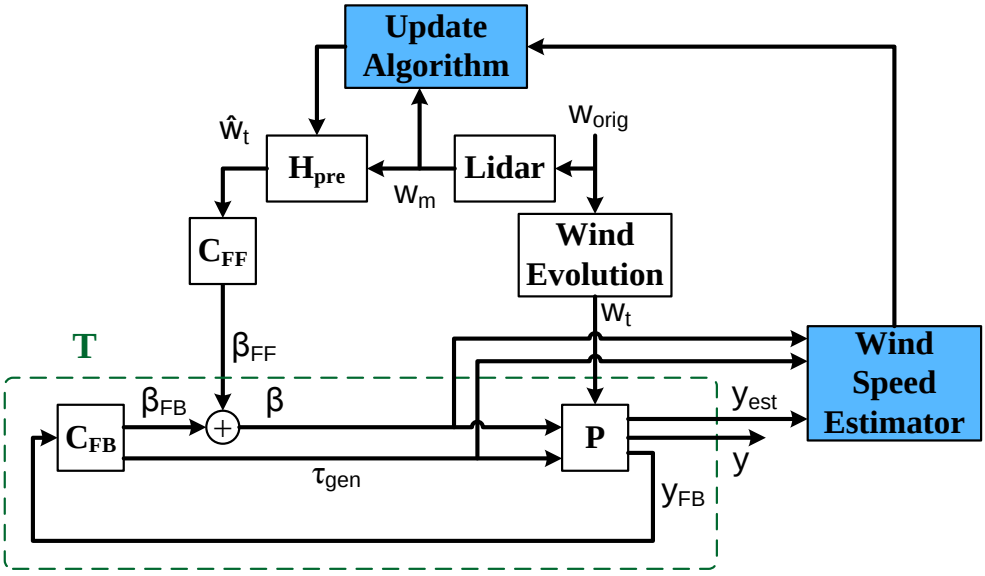

Figure 6.1: Block diagram of the original feedforward control scenario provided in Fig. 2.1 with the addition of adaptive prefiltering relying on a wind speed estimator. A vector of turbine outputs $\boldsymbol{y_{est}}$ required by the wind speed estimator together with the blade pitch and generator torque control inputs is used to estimate the wind disturbances that interact with the turbine. The estimated wind speeds and the lidar measurement time series are used by an update algorithm to adjust the prefilter coefficients based on the detected measurement correlation statistics.

the wind speeds that interact with the turbine. These wind speed estimates are combined with the lidar measurements in an update algorithm to determine the appropriate prefilter transfer function.

6.1 Wind Speed Estimation Background

A number of wind speed estimator designs have been presented in the past. Among the simplest methods are the power balance and torque balance techniques. In the power balance method, the tip speed ratio, and thus the effective wind speed, that produces the measured power output is solved for using the turbine's coefficient of power function [59]. The torque balance method, which models the conversion of energy due to rotor acceleration, uses the measured generator rotational acceleration to calculate the aerodynamic torque [44, 59, 101]. The tip speed ratio is then solved for using this aerodynamic torque value instead of the measured power. Additionally, Kalman filtering, which produces MMSE estimates of the states of a linear system, has been widely applied to the

wind speed estimation problem. A linear model of the turbine dynamics can be used to create a Kalman filter for estimating aerodynamic torque, and thereby the effective wind speed [99, 100]. By treating the effective wind speed disturbance as a dynamic state of the linearized turbine dynamics, however, wind speed can be estimated directly using a Kalman filter. Oftentimes the extended Kalman filter is employed for direct wind speed estimation, in which the full nonlinear turbine dynamics are re-linearized at every time step [58, 60, 103]. Soltani *et al.* [59] compare the performance of several wind speed estimators, finding that the power balance, torque balance, Kalman filter, extended Kalman filter, and the immersion and invariance technique for parameter estimation in nonlinear systems [104] are all promising approaches, with the best method depending on factors such as the amount of sensor noise and the turbulence intensity. While the aforementioned wind speed estimators are all concerned with estimating the effective wind speed based either directly or indirectly on the turbine's coefficient of power function, there remain a variety of other wind speed disturbance variables that are relevant to wind turbine control. Bottasso *et al.* [57] have presented an extended Kalman filter that yields estimates of the effective hub-height wind speed, horizontal and vertical shear, relative wind direction, and vertical wind speed.

In this chapter, which is based on work presented in Simley and Pao [65], a Kalman filter-based wind speed estimator for the effective hub-height and linear shear components is described. However, through (3.39) these rotor effective wind speed variables can also be used to solve for estimates of the individual blade effective wind speeds in the rotating frame. The wind speed estimator is designed using the NREL 5-MW reference turbine model for both above-rated and below-rated conditions. The performance of the estimator is analyzed in the frequency domain using outputs generated by NREL's FAST aeroelastic code for simple wind disturbances consisting of the effective hub-height and linear shear components. Note that whereas only low-frequency wind speed information is needed for wind speed estimation applications such as gain scheduling, frequencies as high as the control actuation bandwidth are required to calculate the MMSE measurement filter. Accordingly, the wind speed estimator's behavior is analyzed for frequencies up to 1 Hz.

The remainder of this chapter is organized as follows. In Section 6.2, the low-order lin-

ear model of the turbine is presented together with the Kalman filter design used for wind speed estimation. A description of the simulation environment for assessing the wind speed estimator performance is provided in Section 6.3. A frequency domain analysis of the estimator performance is provided in Section 6.4 for the NREL 5-MW reference turbine in below-rated and above-rated conditions using the two different inflow models available in FAST. The impact that blade pitch actuation has on estimator performance is investigated in Section 6.5. Section 6.6 shows the additional performance that can be gained using measurements up to 1 s after the wind speed disturbances of interest occur. Finally, in Section 6.7 the improved performance of a wind speed estimator with a gain-scheduled linear model is shown.

6.2 Kalman Filter Design for Rotor Effective Hub-Height and Shear Component Wind Speed Estimation

For estimating the effective u_{hh}, δ_h, and δ_v disturbances encountered by the turbine, Kalman filtering is employed. A Kalman filter produces MMSE estimates of the states of a linear system assuming that the states and outputs are corrupted by Gaussian noise with known covariance [105]. Kalman filtering is used as the basis of the wind speed estimator for two reasons: first of all, it is straightforward to create linearized models of the turbine that include the shear disturbance variables, whereas the previously mentioned power and torque balance methods rely on the coefficient of power to solve for the rotor effective wind speed without a way of defining or determining the effective shear disturbances; secondly, with Kalman filtering, knowledge of the sensor noise and wind speed statistics can be used to improve the estimate in the MMSE sense.

6.2.1 Linearized Wind Turbine Model

At the core of Kalman filtering is a linear state-space model of the turbine. A continuous-time linearized model of the turbine dynamics is computed for a specific operating point of interest (e.g., mean wind speed, rotor speed, generator torque, and blade pitch) using FAST [9]. The continuous-time model is then transformed into a discrete-time representation that can be used for digital

control:

$$x(k+1) = Ax(k) + B_u u_c(k) + B_w w(k) \tag{6.1a}$$

$$y(k) = Cx(k) + D_u u_c(k) + D_w w(k), \tag{6.1b}$$

where $x(k)$ is the state vector at time step k, $y(k)$ is the vector of measured turbine outputs, $u_c(k)$ is the control input vector, and

$$w(k) = \begin{bmatrix} u_{hh}(k), & \delta_h(k), & \delta_v(k) \end{bmatrix}^T \tag{6.2}$$

is the wind disturbance vector. All variables in the linear model represent zero-mean deviations from the operating-point.

The state-space model in equation 6.1 is formed using the MBC transformation method, whereby states and outputs attributed to individual rotating blades are transformed into the non-rotating frame [38]. Thus three blade-specific states are converted to a collective state, representing the average of the rotating states at the three blades, and non-rotating projections of the original states about the vertical and transverse axes. The final state-space model in equation 6.1 is formed by taking the mean value of the MBC-transformed A, B_u, B_w, C, D_u, and D_w matrices over all rotor azimuth angles. Although FAST can be used to model an onshore turbine with 18 degrees of freedom (DOF) [9], a low-order model with only 5 DOF is used for the wind speed estimator. The 10 states represent the generator rotational azimuth angle, the first tower fore-aft bending mode, and the collective, horizontal (sine), and vertical (cosine) MBC components of the first flapwise blade bending mode, as well as the first derivatives of these values. The inclusion of the tower fore-aft state helps resolve the ambiguity between the true wind speed and the apparent wind velocity caused by tower motions. Extending the linear model with additional DOF, such as drivetrain compliance or tower side-to-side motions, does not significantly improve the wind speed estimator in the frequency band of interest for blade pitch control, described in Section 6.3.

The control input vector

$$u_c(k) = \begin{bmatrix} \tau_{gen}(k), & \beta_0(k), & \beta_{sin}(k), & \beta_{cos}(k) \end{bmatrix}^T \tag{6.3}$$

consists of the generator torque command τ_{gen} as well as the collective (β_0), sine (β_{sin}), and cosine (β_{cos}) MBC components of the three independent blade pitch commands $\beta_{\{1,2,3\}}$, calculated using the MBC transformation [38]:

$$\begin{bmatrix} \beta_0(k) \\ \beta_{sin}(k) \\ \beta_{cos}(k) \end{bmatrix} = \begin{bmatrix} \frac{1}{3} & \frac{1}{3} & \frac{1}{3} \\ \frac{2}{3}\sin(\psi) & \frac{2}{3}\sin\left(\psi+\frac{2\pi}{3}\right) & \frac{2}{3}\sin\left(\psi+\frac{4\pi}{3}\right) \\ \frac{2}{3}\cos(\psi) & \frac{2}{3}\cos\left(\psi+\frac{2\pi}{3}\right) & \frac{2}{3}\cos\left(\psi+\frac{4\pi}{3}\right) \end{bmatrix} \begin{bmatrix} \beta_1(k) \\ \beta_2(k) \\ \beta_3(k) \end{bmatrix}. \tag{6.4}$$

Five output measurements are included in the linear model:

$$y(k) = \left[\omega_{gen}(k), \quad M_{root,y,0}(k), \quad M_{root,y,sin}(k), \quad M_{root,y,cos}(k), \quad a_{nac,x}(k)\right]^T, \tag{6.5}$$

where ω_{gen} is the generator speed, $a_{nac,x}$ is the nacelle acceleration in the fore-aft direction, and $M_{root,y,0}$, $M_{root,y,sin}$, and $M_{root,y,cos}$ are the collective, sine, and cosine MBC components of the out-of-plane blade root bending moments. These MBC bending moment values are calculated from measurements at the individual blades $M_{root,y,\{1,2,3\}}$ using load sensors at the blade roots. Strain gauge sensors have been considered for measuring blade bending moments, although they have often been found to be unreliable for commercial operation [6]. Recently, optical-based sensors such as fiber optic Bragg grating sensors have been developed for load monitoring on wind turbine blades as well [106]. While not all turbines are currently equipped with load sensors at each blade, it is assumed that any turbine using individual pitch control contains appropriate sensors for measuring blade root bending at each blade [10]. The measurement $M_{root,y,sin}$ represents the net bending of the rotor around the vertical axis and $M_{root,y,cos}$ corresponds to the rotor bending around the horizontal transverse axis. Accordingly, the estimate of the hub-height wind component is primarily formed using the generator speed, nacelle fore-aft acceleration, and collective blade bending moment measurements along with the collective pitch angle, whereas the horizontal and vertical shear estimates are based principally on the cosine and sine components of blade root bending as well as blade pitch angle.

6.2.2 Kalman Filter Model

As mentioned earlier, Kalman filtering produces MMSE estimates of the states of a linear system; but the wind speed variables of interest instead appear as disturbances in the model in equation 6.1. To address this conflict, the manipulation used previously in Bottasso *et al.* [57], Knudsen *et al.* [58], and Henriksen *et al.* [60] is utilized, where the state equations are rearranged so that the wind disturbances appear as system states. The resulting model that the Kalman filter design is based on is given by

$$\begin{bmatrix} x(k+1) \\ w(k+1) \end{bmatrix} = \begin{bmatrix} A & B_w \\ \mathbf{0} & \boldsymbol{I}_{3\times 3} \end{bmatrix} \begin{bmatrix} x(k) \\ w(k) \end{bmatrix} + \begin{bmatrix} B_u \\ \mathbf{0} \end{bmatrix} u_c(k) + v_x(k) \tag{6.6a}$$

$$y(k) = \begin{bmatrix} C & D_w \end{bmatrix} \begin{bmatrix} x(k) \\ w(k) \end{bmatrix} + D_u u_c(k) + v_y(k), \tag{6.6b}$$

where $v_x(k)$ is Gaussian process noise that represents modeling errors, such as nonlinearities, in the state-space model and, similarly, $v_y(k)$ is Gaussian output noise that represents modeling errors and sensor noise. The dynamics of the wind speed disturbances are modeled as random walks driven by the corresponding elements of the process noise vector [57, 60]. Although the effective wind speed signals differ from random walks, this model is adequate for estimating more complex wind disturbances such as the rotor effective wind quantities described in Chapter 5. However, it is possible to add additional dynamics to the wind disturbance model to improve the accuracy of the Kalman filter model [58].

Estimates of the wind turbine states $\hat{x}(k)$, including the wind disturbance states $\hat{w}(k)$, are formed using the two-step Kalman filtering process [105]:

$$\begin{bmatrix} \hat{x}_p(k) \\ \hat{w}_p(k) \end{bmatrix} = \begin{bmatrix} A & B_w \\ \mathbf{0} & \boldsymbol{I}_{3\times 3} \end{bmatrix} \begin{bmatrix} \hat{x}(k-1) \\ \hat{w}(k-1) \end{bmatrix} + B_u u_c(k-1) \tag{6.7a}$$

$$\begin{bmatrix} \hat{x}(k) \\ \hat{w}(k) \end{bmatrix} = \begin{bmatrix} \hat{x}_p(k) \\ \hat{w}_p(k) \end{bmatrix} + K \left(y(k) - \begin{bmatrix} C & D_w \end{bmatrix} \begin{bmatrix} \hat{x}_p(k) \\ \hat{w}_p(k) \end{bmatrix} - D_u u_c(k) \right). \tag{6.7b}$$

In the first stage, the predicted states $\hat{x}_p(k)$ and $\hat{w}_p(k)$ at the current time step are generated by feeding the previous state estimates $\hat{x}(k-1)$ and $\hat{w}(k-1)$ through the state-space model along with the previous control actions $u_c(k-1)$. In the second stage of the Kalman filter, the predicted states are updated based on the current sensor outputs $y(k)$. The update terms are formed by multiplying the error between the measured output $y(k)$ and the predicted output by the Kalman gain matrix K. The optimal Kalman gain matrix K is calculated using the state-space matrices together with the covariance matrices Q_x and R_y corresponding to the process noise vector $v_x(k)$ and output noise vector $v_y(k)$. Further information about Kalman filtering can be found in Grewal and Andrews [105].

It is difficult to estimate the exact covariance matrices of the process and output noise because the true turbine states are unknown. Therefore, to calculate the Kalman gain matrix K, estimates $\hat{Q}_x$ and $\hat{R}_y$ of the true covariance matrices are typically needed. In this work, the design of the Kalman filter is simplified by treating the $\hat{Q}_x$ and $\hat{R}_y$ matrices as tuning variables used to achieve acceptable estimator performance. To reduce the dimension of the tuning variables, and because the off-diagonal terms of the covariance matrices are expected to be much smaller than the diagonal terms, $\hat{Q}_x$ and $\hat{R}_y$ are chosen to be diagonal. The process noise covariance matrix parameter is structured as

$$\hat{Q}_x = \text{diag}\left(\begin{array}{ccccccc} \epsilon_Q, & \ldots, & \epsilon_Q, & \sigma^2_{v_x,\,u_{hh}}, & \sigma^2_{v_x,\,\delta_h}, & \sigma^2_{v_x,\,\delta_v} \end{array} \right), \tag{6.8}$$

where ϵ_Q is a process noise tuning parameter for the original states $x(k)$ of the turbine. The values $\sigma^2_{v_x,\,u_{hh}}$, $\sigma^2_{v_x,\,\delta_h}$, and $\sigma^2_{v_x,\,\delta_v}$ are estimates of the variances of the wind disturbance changes after one time step, keeping in line with the random walk model in equation 6.6. Similarly, the output noise covariance parameter depends on a tuning parameter ϵ_R:

$$\hat{R}_y = \epsilon_R \cdot \text{diag}\left(\begin{array}{ccccc} \sigma^2_{y_1}, & \ldots, & \sigma^2_{y_5} \end{array} \right), \tag{6.9}$$

where $\sigma^2_{y_i}$ is the estimated variance of output variable i.

6.3 Wind Speed Estimator Simulation Description

The wind speed estimator is evaluated using outputs generated by FAST with the NREL 5-MW reference turbine model. Performance is evaluated during both above-rated and below-rated conditions using the baseline generator torque controller in all operating conditions and the baseline proportional-integral (PI) collective blade pitch controller [8] with additional individual pitch actuation during above-rated operation. The individual pitch controller uses PI control on the sine and cosine MBC components of flapwise blade root bending moment to mitigate cyclic blade loads [10]. The linearized model of the turbine dynamics for designing the Kalman filter is generated in FAST using the equilibrium inflow model, based on blade element momentum theory, to calculate aerodynamic forces [9, 87]. A sampling rate of 80 Hz is used for the linear model, although a lower sampling rate could be used while still capturing the relevant turbine modes modeled in the Kalman filter. While linearization in FAST can only be performed using equilibrium inflow [9], the higher-fidelity dynamic inflow model is more realistic [87]. Consequently, the wind speed estimator is analyzed using FAST outputs generated with both equilibrium inflow, so that the estimator performance can be assessed when the Kalman filter model is more accurate, and dynamic inflow, in order to investigate how the inflow modeling error affects estimator quality. Furthermore, the simulations performed using dynamic inflow also include dynamic stall [9].

The aim of the wind speed estimator design in this chapter is to provide estimates of the wind speed disturbances to aid in the implementation of blade pitch control. As discussed briefly in Section 5.3, the blade pitch actuators for the NREL 5-MW reference turbine are often modeled as having a bandwidth of 1 Hz [28, 31]. Due to this bandwidth limitation on the pitch actuation, it is desired that the Kalman filter at least provide accurate estimates of wind speed up to a bandwidth of 1 Hz. To continue the emphasis on frequency-domain analysis of lidar measurement quality throughout this thesis, the spectra of the wind speed estimates are compared to the spectra of the true wind speeds. Specifically, the power spectra as well as the coherence and phase between the estimates and the true values are discussed. All results are produced using outputs from 50

separate 20-minute simulations.

The wind speed estimator is tested in both below-rated and above-rated conditions using modeled hub-height and shear components due to three rotating blade effective wind speeds, as described in Sections 3.4 and 3.5. The wind speed component power spectra are calculated using the methods described in Section 5.2 with the von Kármán turbulence model. Below-rated wind conditions with mean wind speed $U = 8$ m/s are calculated using a fixed rotor speed of 9.2 RPM and above-rated wind conditions with a mean wind speed of $U = 13$ m/s are calculated using a fixed rotor speed of 12.1 RPM, the 5-MW reference turbine's rated speed. In order to evaluate the wind speed estimator, random Gaussian realizations of the time series of the three independent components are generated, adhering to the desired power spectra. The power spectral densities of the generated hub-height and shear components for the below-rated and above-rated conditions are shown in Fig. 6.2 for turbulence intensity TI = 10%. Note that with the axisymmetric von Kármán turbulence model, the resulting spectra of the horizontal and vertical shear components are identical. While a wind turbine will experience a variety of wind conditions during operation, the wind speed power spectra used to test the wind speed estimator shown in Fig. 6.2 are meant

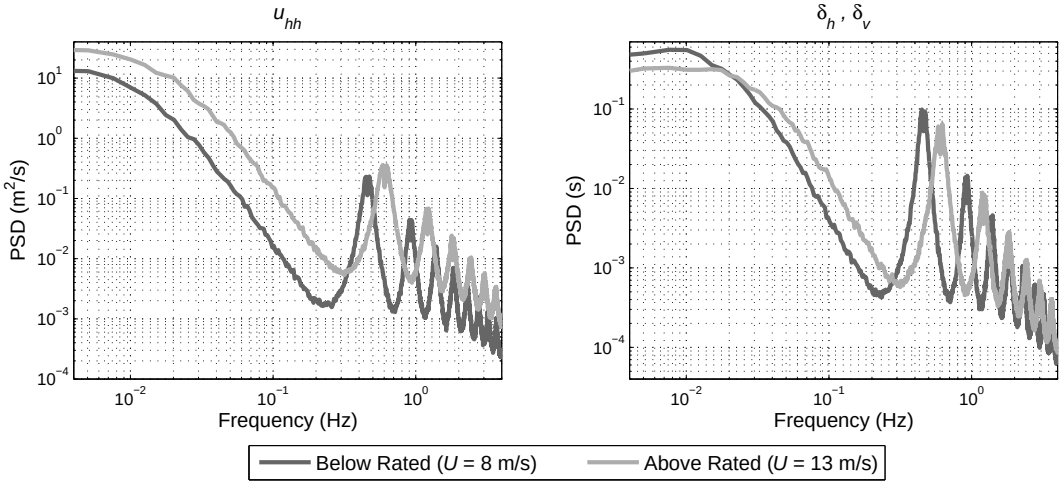

Figure 6.2: Power spectral densities of the effective hub-height and shear components resulting from three rotating blade effective wind speeds using the von Kármán turbulence model with turbulence intensity TI = 10% at the below-rated operating point of $U = 8$ m/s and above-rated operating point of $U = 13$ m/s.

to represent examples of wind disturbances with the salient features that any particular wind condition is likely to contain, i.e., a large concentration of power at low frequencies as well as the 3P frequency and its harmonics, with the shear components containing higher dominant frequencies than the hub-height component.

Zero mean vertical wind shear is included in the simulated wind fields because only the time-varying components are of interest for the lidar measurement quality analyses in this thesis; it is assumed that the turbine's feedback control loop can adequately mitigate the impacts of mean wind shear disturbances. However, if non-zero mean vertical shear is present, a linear dynamic model of the turbine derived using an operating point with non-zero vertical shear could be used in the Kalman filter.

The state-space models used for the below-rated and above-rated Kalman filters are created by linearizing the turbine dynamics around the appropriate operating points determined by the baseline torque and blade pitch controller characteristics [8]. The operating points used for linearization are provided in Table 6.1. As discussed in Section 6.7, in order to use the wind speed estimator over the entire operating range of a wind turbine, gain scheduling of the underlying linear model should be employed. For example, the generator speed ω_{gen} can be used as a scheduling variable in below-rated conditions while the collective pitch angle β_0 can be used in above-rated conditions. Together, these two variables allow the estimator to be gain scheduled over the turbine's entire operating range.

Table 6.1: Linearization operating points for state-space models.

Operating Condition	u_{hh} (m/s)	τ_{gen} (kN·m)	β_0 (deg)	$\beta_{\{sin,cos\}}$ (deg)	ω_{gen} (RPM)
Below-Rated	8	20.37	0	0	891.8
Above-Rated	13	43.09	6.62	0	1,173.7

6.3.1 Kalman Filter Parameters

The covariance matrix parameters used to define the Kalman filter behavior are based on the diagonal matrices in equations 6.8 and 6.9. The covariance parameters were chosen by first setting the variances of the wind disturbance changes after one time step $\sigma^2_{v_x,\,u_{hh}}$, $\sigma^2_{v_x,\,\delta_h}$, and $\sigma^2_{v_x,\,\delta_v}$ to their true values calculated using wind disturbances with power spectra shown in Fig. 6.2 with a turbulence intensity of 10%. The measurement variance parameters $\sigma^2_{y_i}$ in equation 6.9 are simply set to the calculated variances of the corresponding outputs with TI = 10%. For all cases analyzed in Section 6.4, a value of $\epsilon_R = 10^{-6}$ was found to provide satisfactory results. Different values of ϵ_Q were chosen for estimating the hub-height and shear components in the above-rated scenario while a single value was found to provide the best performance for both the hub-height and shear terms in the below-rated conditions. Table 6.2 contains the resulting covariance matrix parameters used for the Kalman filter in both operating conditions. Although these parameters were chosen for a specific turbulence intensity, it was found that they provided good performance for all TI values investigated.

Table 6.2: Kalman filter covariance matrix parameters.

Operating Condition	$\sigma^2_{v_x,\,u_{hh}}$ (m^2/s^2)	$\sigma^2_{v_x,\,\delta_h}$, $\sigma^2_{v_x,\,\delta_v}$	ϵ_R	ϵ_Q, u_{hh} est.	ϵ_Q, δ_h, δ_v est.
Below-Rated	$3.6 \cdot 10^{-4}$	$1.1 \cdot 10^{-4}$	10^{-6}	$8.7 \cdot 10^{-8}$	$8.7 \cdot 10^{-8}$
Above-Rated	$1.2 \cdot 10^{-3}$	$1.5 \cdot 10^{-4}$	10^{-6}	10^{-6}	10^{-9}

6.3.2 Sensor Noise

Sensor noise is introduced to the turbine outputs used for the Kalman filter to approximate realistic operating conditions. Sensor noise is simulated by introducing independent zero-mean additive white Gaussian noise signals at each turbine output. The standard deviation of the generator speed noise is set equal to 2% of the nominal generator speed as is suggested in Knudsen *et al.* [58]. The standard deviation of the nacelle longitudinal accelerometer noise is set to 4% of the standard deviation of the true tower acceleration as suggested in Knudsen and Bak [107]. Following a similar

guideline, the blade root bending moment sensor noise is simulated using a standard deviation equal to 2% of the actual out-of-plane blade root bending moment standard deviation. This choice of sensor noise variance is based on an estimation of the high-frequency noise floor using a short period of data from the blade root strain gauges on NREL's 600 kW CART3 research turbine [59].

After MBC-transforming the bending moment measurements to form inputs to the Kalman filter, the equivalent noise signals corrupting the collective, sine, and cosine components of bending moment are given by

$$\begin{bmatrix} n_{M_{root,y,0}} \\ n_{M_{root,y,sin}} \\ n_{M_{root,y,cos}} \end{bmatrix} = \begin{bmatrix} \frac{1}{3} & \frac{1}{3} & \frac{1}{3} \\ \frac{2}{3}\sin(\psi) & \frac{2}{3}\sin\left(\psi+\frac{2\pi}{3}\right) & \frac{2}{3}\sin\left(\psi+\frac{4\pi}{3}\right) \\ \frac{2}{3}\cos(\psi) & \frac{2}{3}\cos\left(\psi+\frac{2\pi}{3}\right) & \frac{2}{3}\cos\left(\psi+\frac{4\pi}{3}\right) \end{bmatrix} \begin{bmatrix} n_{M_{root,y,1}} \\ n_{M_{root,y,2}} \\ n_{M_{root,y,3}} \end{bmatrix}, \tag{6.10}$$

where $n_{M_{root,y,i}}$ is the sensor noise at blade i. The resulting variances of the independent MBC-transformed noise components are

$$\sigma^2_{n_{M_{root,y,0}}} = \frac{1}{3}\sigma^2_{n_{M_{root,y,i}}} \tag{6.11}$$

and

$$\sigma^2_{n_{M_{root,y,sin}}} = \sigma^2_{n_{M_{root,y,cos}}} = \frac{2}{3}\sigma^2_{n_{M_{root,y,i}}}. \tag{6.12}$$

The variance parameters for the sensor noise are summarized in Table 6.3. The blade pitch and generator torque commands are treated as noise-free control inputs.

Table 6.3: Variance parameters used to simulate white Gaussian sensor noise.

$\sigma^2_{n_{\omega_{gen}}}$	$\sigma^2_{n_{M_{root,y,0}}}$	$\sigma^2_{n_{M_{root,y,sin}}}$	$\sigma^2_{n_{M_{root,y,cos}}}$	$\sigma^2_{n_{a_{nac,x}}}$
$(0.02 \cdot \overline{\omega_{gen}})^2$	$\frac{1}{3}\left(0.02 \cdot \sigma_{M_{root,y,i}}\right)^2$	$\frac{2}{3}\left(0.02 \cdot \sigma_{M_{root,y,i}}\right)^2$	$\frac{2}{3}\left(0.02 \cdot \sigma_{M_{root,y,i}}\right)^2$	$\left(0.04 \cdot \sigma_{a_{nac,x}}\right)^2$

6.4 Wind Speed Estimator Performance

In this section, comparisons are made between the wind speed estimator performance in below-rated and above-rated conditions using both the equilibrium and dynamic inflow settings in

FAST. Examples of the time series for the true hub-height and vertical shear wind speed disturbances along with the estimates using both inflow settings are shown in Fig. 6.3 for the below-rated mean wind speed 8 m/s and the above-rated wind speed 13 m/s. Both the estimates and the true wind speed disturbances shown in Fig. 6.3 are low-pass filtered using a cutoff frequency of 1 Hz to reflect the approximate bandwidth of interest for blade pitch control. The estimator performance results for the horizontal shear component are very similar to the vertical shear results for all analyses in the remainder of this chapter and therefore, for simplicity, are not included. In above-rated conditions, the Kalman filter underestimates the hub-height wind speed when the wind deviates significantly from the operating point of 13 m/s, but, in general, appears to perform well otherwise. In below-rated conditions, however, the hub-height estimates are much more accurate, even when the wind deviates far from the operating point of 8 m/s. For both operating conditions, the estimates of the shear components are very accurate with equilibrium inflow; with dynamic inflow, on the other hand, the magnitude of the shear component is underestimated, particularly in below-rated conditions.

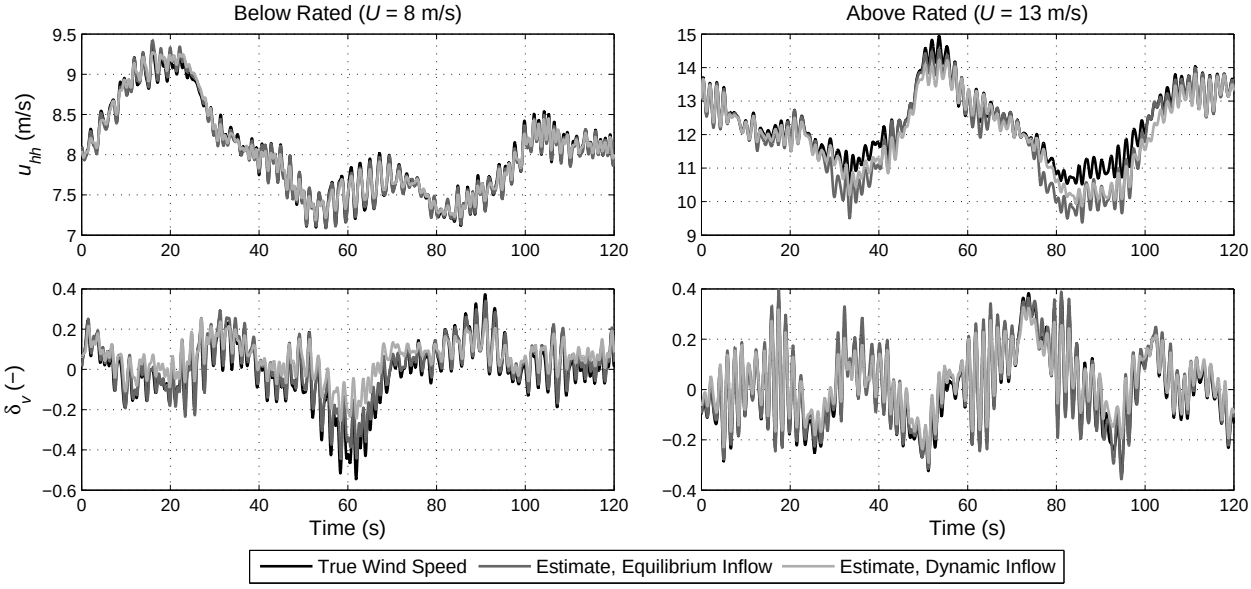

Figure 6.3: Effective hub-height and vertical shear wind disturbances and their Kalman filter estimates using outputs from FAST with equilibrium and dynamic inflow. The below-rated and above-rated wind fields with $U = 8$ m/s and $U = 13$ m/s, respectively, are generated for TI = 10%. All time series are low-pass filtered with a cutoff frequency of 1 Hz.

Figs. 6.4 and 6.5 contain spectral information relevant to the wind speed estimator performance for the below-rated and above-rated scenarios shown in Figure 6.3. The coherence between the estimates and the true disturbances is provided along with the ratio between the power spectra of the estimates and the true disturbances, and the phase between the estimates and the true wind components. The three different frequency domain plots are used to show whether errors are caused by poor correlation, misestimation of the disturbance magnitude, or phase mismatch.

From the below-rated spectra in Fig. 6.4, it can be seen that the hub-height estimator coherence is high at low frequencies as well as near the 3P frequency (0.46 Hz) and its harmonics, where the energy in the wind disturbances is concentrated, as revealed in Fig. 6.2. Sensor noise causes the estimation coherence to suffer at frequencies where the power spectral density of the wind disturbance is low, but because there is very little energy in the wind at these frequencies, the poor performance does not cause overall estimation error to degrade significantly. Above approx-

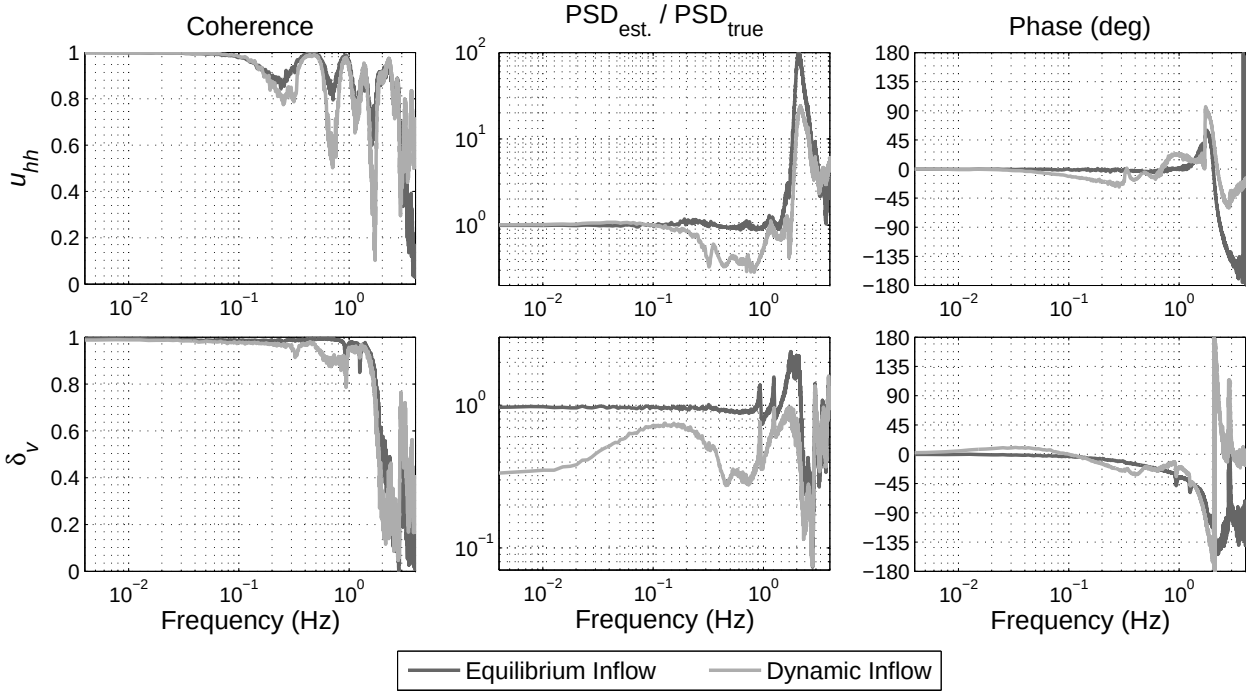

Figure 6.4: Coherence between estimated and true hub-height and vertical shear components, ratios between power spectral densities of estimated and true wind components, and phases between the estimates and the true wind components at the below-rated operating point of $U = 8$ m/s.

imately 2 Hz, the coherence begins to decay. For equilibrium inflow, the power spectral density and phase of the hub-height component estimate are very accurate below 1 Hz. With dynamic inflow, the magnitude of the hub-height component spectrum is underestimated between 0.2 Hz and 1 Hz, and the phase distortion is much worse. The coherence of the shear component estimates remains high at all frequencies until about 1.5 Hz, with the exception of 0.9 Hz and 1.25 Hz, where minor errors occur due to the unmodeled asymmetric edgewise blade modes [8]. With equilibrium inflow, the power spectrum of the shear component is generally very accurate below 1.5 Hz, aside from the modes at 0.9 Hz and 1.25 Hz, whereas for dynamic inflow, the power spectrum is severely underestimated. There is a clear phase lag in the shear estimates for both inflow models. For both the hub-height and shear components, there are significant errors above 1.5 Hz caused by the unmodeled second flapwise blade modes as well as sensor noise. Consequently, the estimates require additional low-pass filtering to remove the high frequency errors.

Generally, the quality of the estimates with equilibrium inflow is expected to be higher than the quality with dynamic inflow since the Kalman filter relies on a turbine model linearized using equilibrium inflow. This discrepancy between the estimator's underlying model and the dynamic inflow model used in simulation explains the noticeable difference in the power spectra of the estimates. Also, the phase lag in the shear estimates above 1 Hz is larger than for the hub-height estimates. This indicates that there might be a lag between when the shear disturbances occur and when their effect is felt by the chosen sensors. Thus a causal estimator might not be able to accurately determine the shear disturbances at the current time step. In Section 6.6, a non-causal estimator is presented, which is shown to reduce this phase lag.

From the above-rated spectra in Fig. 6.5, it can be seen that the hub-height estimator coherence is very high at low frequencies and between 0.3 Hz and 2 Hz. The power spectra of the estimates are distorted at most frequencies, although the distortion is much more significant with the dynamic inflow model. For equilibrium inflow, the estimator phase is very accurate below 1.5 Hz, while there is more distortion with dynamic inflow. Above 1 Hz, the power spectra reveal large errors caused by the unmodeled second flapwise blade modes that need to be removed through

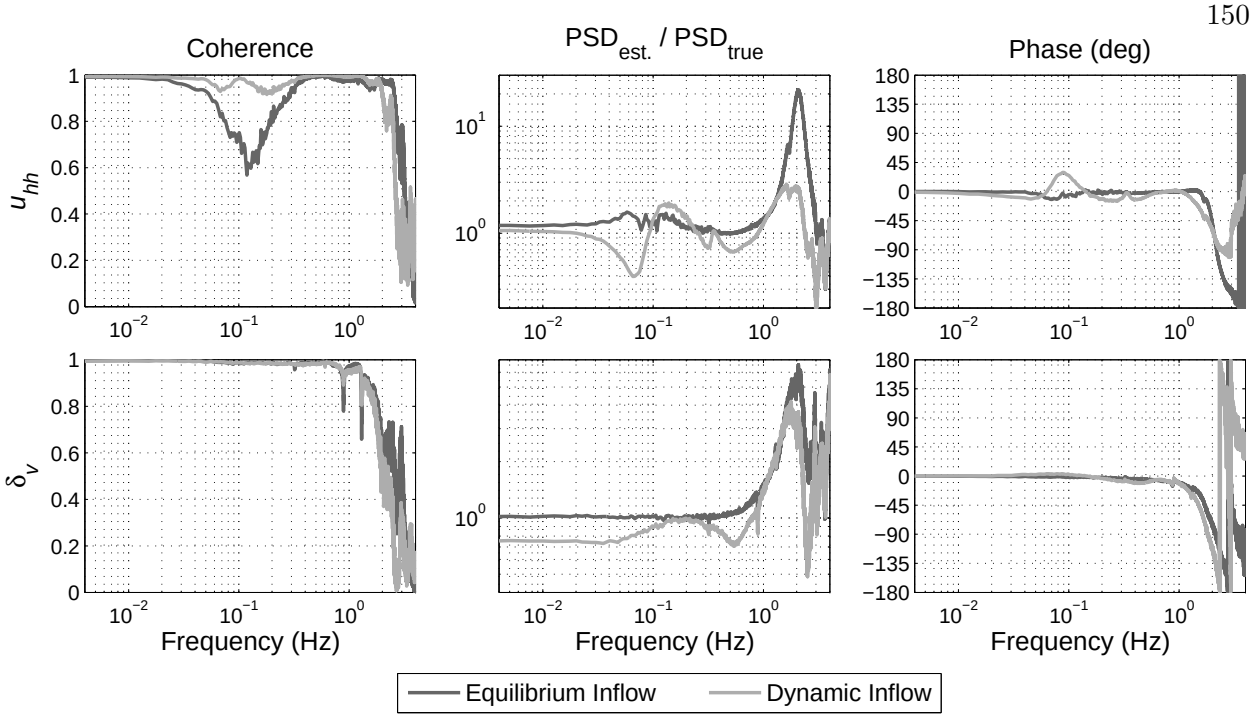

Figure 6.5: Coherence between estimated and true hub-height and vertical shear components, ratios between power spectral densities of estimated and true wind components, and phases between the estimates and the true wind components at the above-rated operating point of $U = 13$ m/s.

additional low-pass filtering. In contrast to the estimator performance in below-rated conditions, the estimator accuracy between 0.03 Hz and 0.3 Hz is strikingly low, but in different ways depending on the inflow model. For the equilibrium inflow setting, the coherence of the estimate is relatively poor and the power spectrum is slightly higher than the true spectrum, while for dynamic inflow, the coherence is remains high, but the power spectrum is severely distorted. Additionally, there is significant phase error between the estimate and the true wind speed. As discussed in the next section, the errors in the band between 0.03 Hz and 0.3 Hz are caused by the use of blade pitch control during above-rated operation.

The coherence of the vertical shear component estimate is very high up until roughly 1.3 Hz, where it begins to decay. However, there are minor inaccuracies at 0.9 Hz and 1.3 Hz where unmodeled asymmetric edgewise blade bending modes occur [8]. Again, the power spectra of the estimates diverge from the true spectrum above 1 Hz due to unmodeled second flapwise blade modes

and sensor noise. With dynamic inflow, the low-frequency magnitude of the shear component is underestimated, but not as significantly as for the below-rated estimates. A possible explanation for the decreased shear component estimator accuracy with dynamic inflow in below-rated conditions is related to the higher induction factors experienced in below-rated conditions, when the turbine is maximizing power capture. As explained in Henriksen *et al.* [60], the effects of dynamic inflow, not included in the equilibrium inflow model, are much more pronounced with higher induction factors.

To reflect overall estimator accuracy, root mean square (RMS) estimation errors for the hub-height and shear components with both inflow models are provided in Table 6.4. All RMS errors are normalized by the standard deviation of the true wind disturbances. Errors are listed for unfiltered estimates and true disturbances as well as low-pass filtered estimates and true wind speeds using a cutoff frequency of 1 Hz. The errors for the filtered signals reflect the estimator accuracy in the frequency band of interest for blade pitch control purposes.

Table 6.4: Normalized RMS estimation errors for hub-height and vertical shear components in below-rated and above-rated conditions with 10% turbulence intensity using equilibrium and dynamic inflow. The RMS errors are normalized by the standard deviation of the true wind disturbances. Error values are provided for the unfiltered signals as well as for estimates and true wind disturbances that have been low-pass filtered with a cutoff frequency of 1 Hz.

Estimation Category	Unfiltered		Filtered	
	Equil.	Dyn.	Equil.	Dyn.
Below-Rated, u_{hh}	0.562	0.437	0.0662	0.154
Above-Rated, u_{hh}	0.448	0.33	0.232	0.223
Below-Rated, δ_v	0.658	0.8	0.263	0.603
Above-Rated, δ_v	1.52	1.35	0.169	0.254

6.5 The Impact of Blade Pitch Control on Estimator Performance

Fig. 6.6 contains examples of turbine outputs as well as the collective and cosine MBC components of the blade pitch commands along with the hub-height and vertical shear wind speed

estimates at the above-rated mean wind speed 13 m/s with both equilibrium and dynamic inflow. The hub-height wind speed estimator clearly performs most poorly when the wind speed deviates farthest from the operating point of $U = 13$ m/s, causing the wind speeds to be underestimated. However, it is unlikely that the deviation in the wind speed from the operating point is solely responsible for the drastic loss in estimation performance between 0.03 Hz and 0.3 Hz. In below-rated conditions, the wind speed also deviates significantly from $U = 8$ m/s but the low-frequency hub-height component estimate is very accurate.

The times when the hub-height component estimation errors are highest correspond to times when the collective blade pitch is far from its operating point of 6.62°. Nonlinearities in the effect of blade pitch actuation on the rotor aerodynamics appear to be the cause of the poor

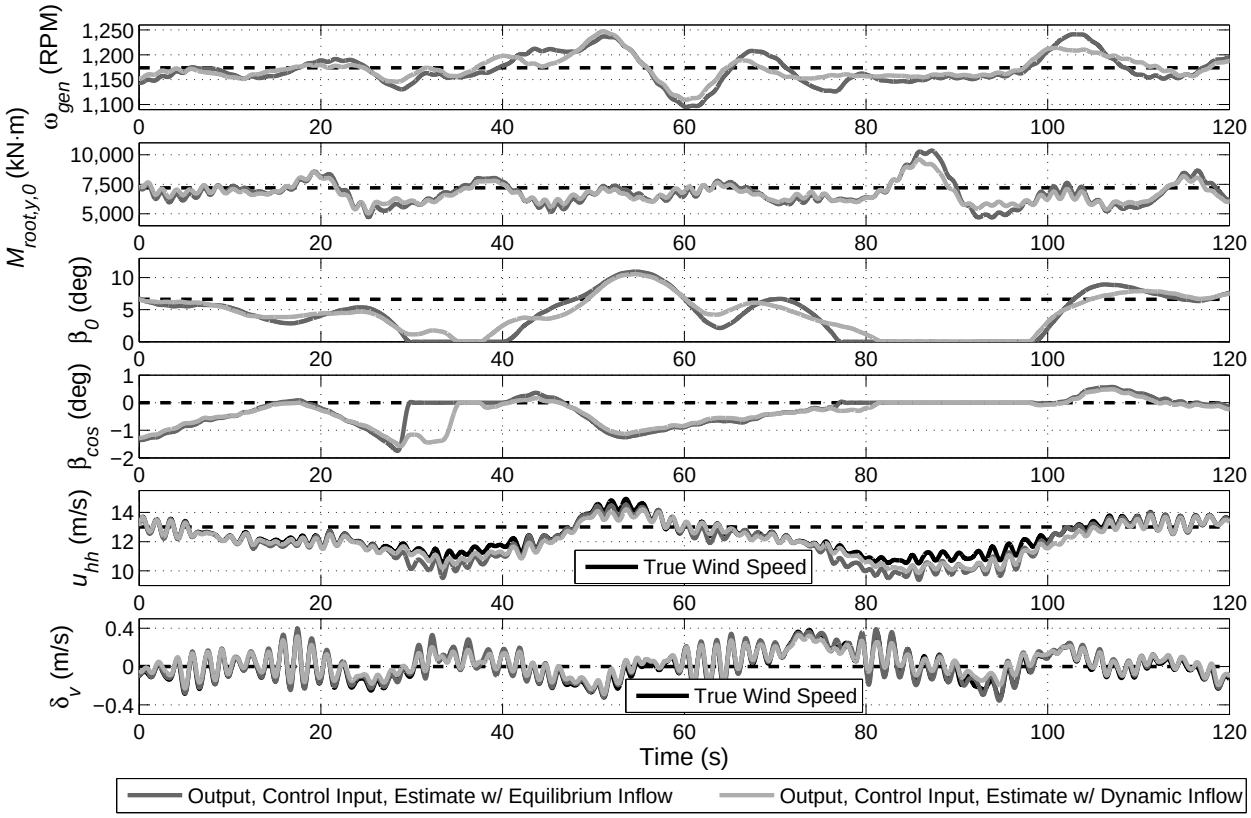

Figure 6.6: Examples of turbine outputs, control actions, and wind speed estimates in above-rated conditions with mean wind speed $U = 13$ m/s and TI = 10%. The dashed lines indicate the nominal variable values used for linearization.

estimator performance. As blade pitch angle increases, the sensitivity of the power produced by the rotor to small changes in pitch angle increases as well [8]. For blade pitch angles higher than the linearization operating point (e.g., around 55 seconds), the linearized dynamics of the state-space model underestimate how much the increased pitch angle decreases the aerodynamic power; the Kalman filter solution, therefore, attributes the measured power to wind speeds that are lower than the true values. Similarly, when the blade pitch angle is lower than the operating point used for linearization (e.g., at 35 and 90 seconds), the state-space model overestimates how much the change in pitch increases the power. Consequently, the Kalman filter falsely attributes the measured power to wind speeds that are again lower than the true values. However, as the cosine component of the pitch angles deviates from zero, the shear estimates remain close to their true values. The shear estimates likely remain robust to the sine and cosine components of blade pitch because the individual pitch control inputs are smaller than the collective pitch commands.

Based on the estimator behavior corresponding to large deviations in blade pitch angle, it seems wise to only use a particular linear model of the turbine in above-rated conditions during operation very close to the linearization operating point. Spectral results are used in Fig. 6.7 to show how the estimator performance for the hub-height component improves as the deviation of the turbine variables from the operating point becomes smaller. This is done by simulating the turbine with wind fields containing a range of turbulence intensities. The impact of reducing the deviation of the turbine variables from the operating point on estimator quality for the shear components is not analyzed since the shear component estimation error (for equilibrium inflow) is much lower to begin with, as shown in Fig. 6.5. Sensor noise is not included for the results in this section so that the impact of modeling errors can be isolated. Individual pitch control is disabled as well. When equilibrium inflow is used and the turbulence intensity decreases, the coherence approaches 1, the power spectral density approaches the true spectrum, and the phase distortion decreases for frequencies below 1 Hz. These results are expected because as the TI decreases, the turbine operation remains closer to the operating point; since the inflow model used for simulation matches the inflow model in the linear model, the linear model becomes more accurate for frequencies

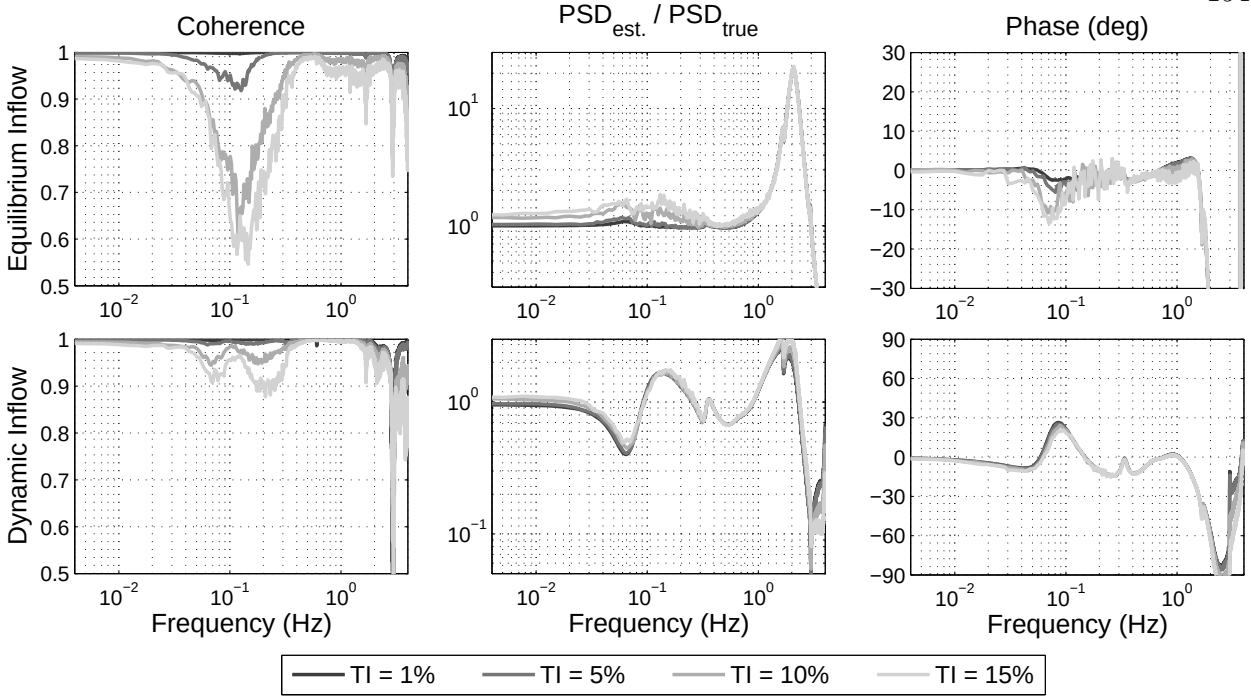

Figure 6.7: Coherence between estimated and true hub-height components, ratios between power spectral densities of estimated and true wind components, and phases between the estimates and the true wind components at the above-rated operating point of $U = 13$ m/s with turbulence intensities from 1% to 15%. Individual pitch control and sensor noise are not included.

below 1 Hz. But with dynamic inflow, as the wind speed deviations from the operating point become smaller, the power spectrum errors and phase distortion do not improve significantly; only coherence increases. This is likely due to the dynamics between blade pitch and other turbine variables not being represented correctly in the Kalman filter model linearized using equilibrium inflow. The frequencies where the power spectra and phase distortion occur roughly correspond to a closed-loop mode at 0.09 Hz caused by the feedback controller where blade pitch activity is high. It is possible that the coherence remains higher when using dynamic inflow because, as shown in Fig. 6.6, the blade pitch angle variations are not as extreme as they are with equilibrium inflow. In summary, the estimation errors with equilibrium inflow are mostly caused by nonlinearities when the turbine operation deviates far enough from the operating point, but with dynamic inflow, they are caused primarily by fundamental modeling inaccuracies.

Normalized hub-height component RMS estimation errors are provided in Table 6.5 for the

range of turbulence intensities investigated in Fig. 6.7. Because there is a very small mean estimation error that would dominate the overall estimation error for very low turbulence intensities, the errors are calculated after first removing the mean values of the signals. As turbulence intensity decreases, the unfiltered RMS errors do not change significantly, because the errors are dominated by the unmodeled turbine modes above 1 Hz. But the RMS errors for the low-pass filtered signals using a cutoff frequency of 1 Hz show that the estimator accuracy improves much more for equilibrium inflow as turbulence intensity decreases than it does for dynamic inflow. For a turbulence intensity of 1% using equilibrium inflow, the RMS error of the filtered signals is less than 2% of the standard deviation of the true wind disturbance.

Table 6.5: Normalized RMS hub-height component estimation errors for above-rated conditions with turbulence intensities from 1% to 15% using equilibrium and dynamic inflow. The RMS errors are normalized by the standard deviation of the true wind disturbances and do not include the mean estimation error. Error values are provided for the unfiltered signals as well as for estimates and true wind disturbances that have been low-pass filtered with a cutoff frequency of 1 Hz.

Turbulence Intensity	Unfiltered		Filtered	
	Equil.	Dyn.	Equil.	Dyn.
TI = 1%	0.344	0.221	0.0174	0.121
TI = 5%	0.357	0.226	0.073	0.125
TI = 10%	0.386	0.233	0.187	0.145
TI = 15%	0.423	0.258	0.239	0.169

6.6 Performance of a Non-Causal Wind Speed Estimator

For some wind speed estimation applications, such as direct feedforward control using the estimated wind speed [101], it is important to obtain the wind speed value at the current time step. For other applications, some delay in the wind speed estimates can be tolerated, especially if estimation error is reduced. For example, for the preview-based control scenario discussed in this thesis, the controller depends on the statistics of the wind speed disturbances rather than the

exact values. Since wind speed statistics typically vary slowly compared to control time scales, a few seconds of estimator delay is acceptable. The estimator described by equation 6.7 is the causal formulation of the Kalman filter, which only relies on past and present measurements. However, the Kalman filter can be extended to account for measurements after the time step of interest occurs. One possible non-causal design is the fixed-lag estimator [105], which provides estimates of the states that occur at a fixed time delay in the past.

In this section, a simple fixed-lag estimator is created by augmenting the state-space model in equation 6.6 with additional states representing the past wind speeds. Note that more efficient implementations of the fixed-lag estimator exist, which are outside the scope of this work [105]. In the augmented state model, no additional dynamics are introduced; instead, states are simply added to store the past wind speed values:

$$\begin{bmatrix} x(k+1) \\ w(k+1) \\ \vdots \\ w(k+1-P) \end{bmatrix} = \left[\begin{array}{c|cc|c} A & B_w & \mathbf{0} & \\ \mathbf{0} & \boldsymbol{I}_{3\times 3} & \mathbf{0} & \mathbf{0} \\ \hline \mathbf{0} & \boldsymbol{I}_{3P\times 3P} & & \mathbf{0}_{3P\times 3} \end{array}\right] \begin{bmatrix} x(k) \\ w(k) \\ \vdots \\ w(k-P) \end{bmatrix} + \begin{bmatrix} B_u \\ \mathbf{0}_{3P\times 4} \end{bmatrix} u_c(k) + \begin{bmatrix} v_x\,(k) \\ \mathbf{0}_{3P\times 1} \end{bmatrix} \tag{6.13a}$$

$$y(k) = \begin{bmatrix} C & D_w & \mathbf{0}_{5\times 3P} \end{bmatrix} \begin{bmatrix} x(k) \\ w(k) \\ \vdots \\ w(k-P) \end{bmatrix} + D_u u_c(k) + v_y\,(k)\,, \tag{6.13b}$$

where the wind disturbances of interest $w(k-P)$ are estimated after P samples of delay. Because of the lack of dynamics necessary to describe the past wind speed states, there is no process noise corresponding to $w(k-1)$ through $w(k-P)$. As a result, the Kalman filter need only rely on the covariance matrix $\hat{Q}_x$ for the original system (equation 6.8) appended with zeros to obtain the proper dimension. For the investigations using this non-causal estimator, a fixed lag time of 1 s, or $P = 80$ samples is chosen.

The improvement made possible by the use of estimator delay is analyzed by comparing the estimates of the non-causal Kalman filter, with 1 s of estimation lag, with the results of the original causal estimator. It was found that for the non-causal estimator in above-rated conditions, covariance tuning parameters of $\epsilon_Q = \epsilon_R = 10^{-5}$ provide good performance for estimating the hub-height component while $\epsilon_Q = 10^{-5}$ and $\epsilon_R = 10^{-6}$ work well for estimating the shear components. The spectral results for the fixed-lag filter tested in above-rated wind fields with $U = 13$ m/s and TI = 10% for both inflow models are provided in Fig. 6.8.

Fig. 6.8 reveals that the non-causal estimator is an improvement over the causal estimator in a couple of ways. First of all, as made evident by the power spectrum ratios, the non-causal estimator further low-pass filters the estimates to remove the high frequency errors due to unmodeled dynamics and sensor noise. Whereas the high frequency noise in the standard causal estimates

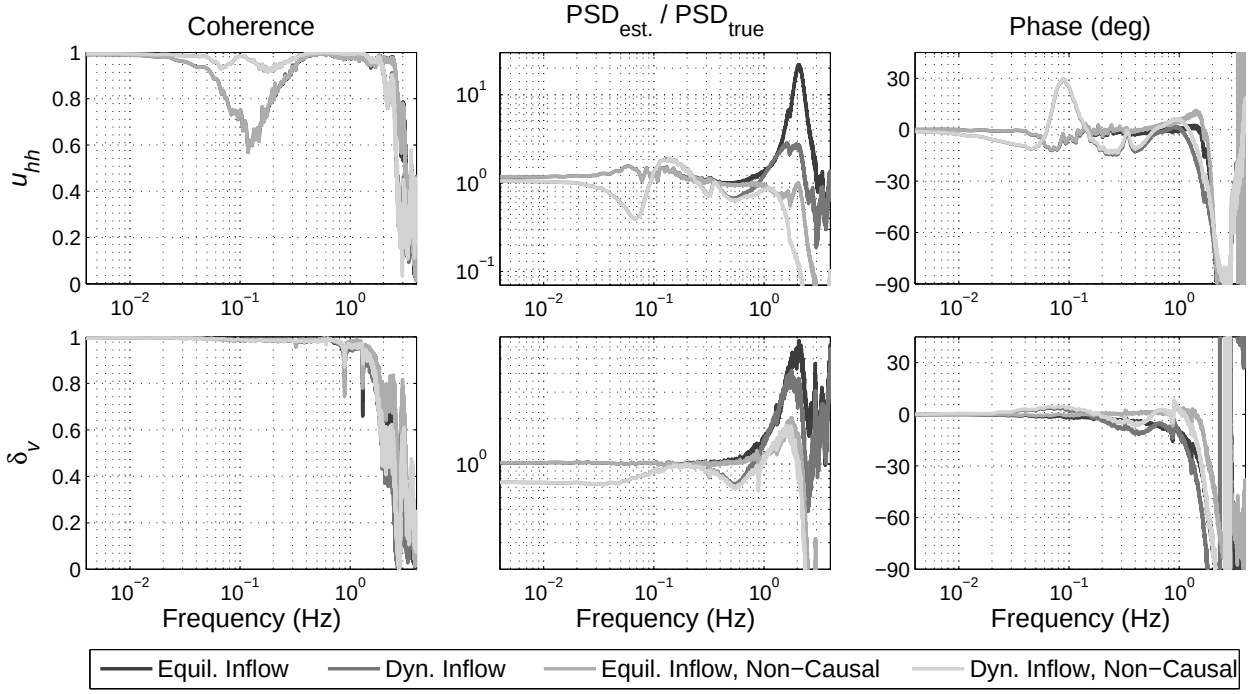

Figure 6.8: Coherence between estimated and true hub-height and vertical shear components, ratios between power spectral densities of estimated and true wind components, and phases between the estimates and the true wind components at the above-rated operating point of $U = 13$ m/s with TI = 10%. Non-causal estimates using a Kalman filter based on the model in equation 6.13 with 1 s of estimator delay are compared with causal estimates using the Kalman filter and covariance matrix parameters described in Sections 6.2.2 and 6.3.

necessitates additional low-pass filtering, the non-causal estimator inherently provides this filtering. The additional low-pass filtering does not come at the price of additional phase delay however. In fact, the non-causality allows the Kalman filter to eliminate the phase delay up to a frequency of roughly 1.5 Hz, as can be seen in the phase curves corresponding to the shear component estimates. Table 6.6 compares the normalized RMS errors of the causal and non-causal estimators. For the unfiltered signals, the non-causal estimator is a considerable improvement over the standard estimator. When considering the frequency band below 1 Hz, the non-causal estimator provides modest reductions in RMS error aside from the hub-height component errors with dynamic inflow.

Table 6.6: Normalized RMS hub-height component estimation errors in above-rated conditions with 10% turbulence intensity for standard and non-causal wind speed estimators using equilibrium and dynamic inflow. The RMS errors are normalized by the standard deviation of the true wind disturbances. Error values are provided for the unfiltered signals as well as for estimates and true wind disturbances that have been low-pass filtered with a cutoff frequency of 1 Hz.

Estimation	Unfiltered		Filtered	
Category	Equil.	Dyn.	Equil.	Dyn.
Standard, u_{hh}	0.448	0.33	0.232	0.223
Non-Causal, u_{hh}	0.27	0.256	0.231	0.224
Standard, δ_v	1.52	1.35	0.169	0.254
Non-Causal, δ_v	0.285	0.38	0.151	0.249

6.7 Performance of a Gain-Scheduled Wind Speed Estimator

The results of Section 6.5 showed that when using equilibrium inflow, the hub-height component estimation error improves significantly when the turbine operation, particularly the blade pitch actuation, remains close to the operating point at which the linear Kalman filter model is calculated. For very low turbulence intensities, the error is reduced such that measurement coherence and the ratio between the PSDs of the estimated and true components both approach 1 for frequencies below $\sim$1 Hz. During realistic operating conditions with potentially high turbulence intensity and fluctuating mean wind speeds, the turbine operation can be kept close to the lin-

earization operating point of the Kalman filter model by switching between different linear models depending on the value of measurable turbine variables. An estimator using this strategy, called gain-scheduling, is implemented here by scheduling the precalculated linear Kalman filter models using values of the generator torque command in below-rated conditions, i.e., when the blade pitch command is 0, and collective blade pitch angle in above-rated conditions. The different linear models are scheduled using the control variables such that any given linear model is only used for wind speeds $+/-$ 0.5 m/s from the operating point. Note that some additional overhead is required to ensure that the state, input, and output variables are correctly represented as the difference from the operating point of the current linear model. The controller design is simplified by using the covariance matrix parameter structure in (6.8) and (6.9) with the below-rated parameter values listed in Table 6.3.1 at all times when the blade pitch angle is 0 and the above-rated parameter values when blade pitch is greater than 0.

In Fig. 6.9, the performance of the gain-scheduled hub-height component estimator is compared to that of the standard estimator relying on a single linear model linearized at $U = 13$ m/s, for the $U = 13$ m/s, TI = 10% wind condition and equilibrium inflow. As seen in the time-domain comparison, the gain-scheduled estimates are much closer to the true hub-height wind speeds, especially when the wind speed drops far below 13 m/s. The spectral results show that the ratio of the estimated and true PSDs is significantly improved, the measurement coherence is much closer to 1, and the estimator phase distortion is reduced considerably below 1 Hz using the gain-scheduled estimator. Thus a gain-scheduled estimator can be used to sufficiently estimate the wind speeds, assuming the inflow model used in the calculation of the linear models matches the true aerodynamic inflow behavior; the gain-scheduled estimator derived assuming equilibrium inflow will still suffer from the same errors shown in Section 6.5 when dynamic inflow is present. An evaluation of the shear component estimator is not provided because of the relatively low estimation error that can already be achieved using the standard estimator, as shown in Fig. 6.5. However, the estimation error for the shear components is also reduced using gain-scheduling.

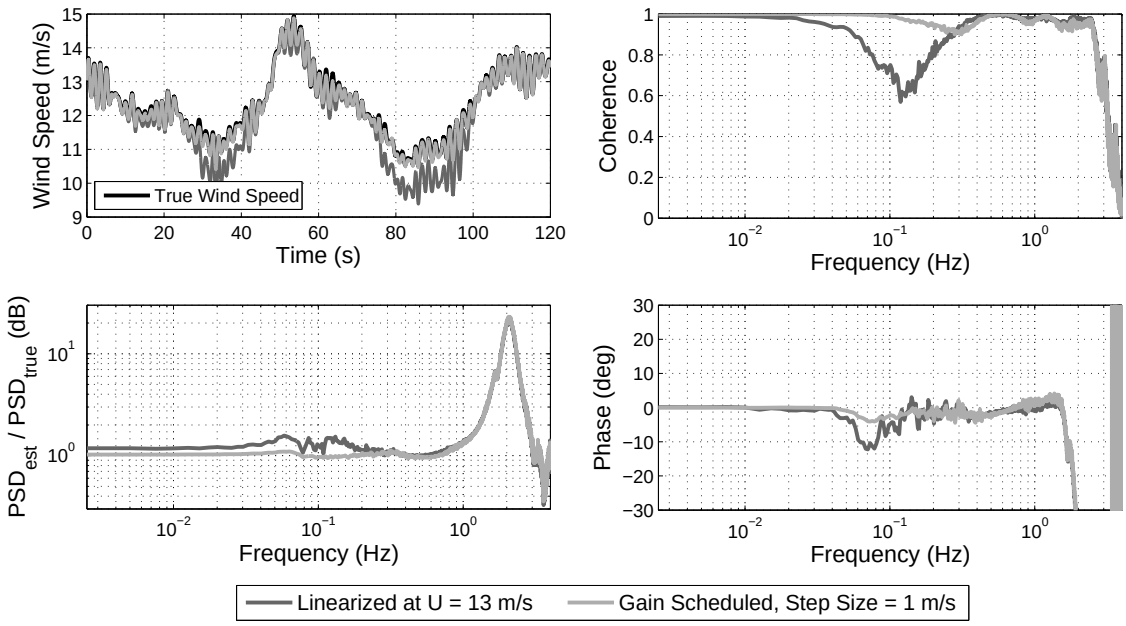

Figure 6.9: Comparison between the performance of a wind speed estimator using a dynamic model linearized at 13 m/s and a gain-scheduled estimator with different linear models corresponding to every 1 m/s step in wind speed at the above-rated operating point of $U = 13$ m/s with TI = 10%. Time series are shown for the hub-height component estimates and true hub-height wind speeds filtered with a cutoff frequency of 1 Hz. Spectrum-based results include the coherence between estimated and true hub-height wind components, ratios between power spectral densities of estimated and true wind components, and phases between the estimates and the true hub-height components.

6.8 Discussion and Conclusions

A wind speed estimator for rotor-effective hub-height and linear horizontal and vertical shear components based on Kalman filtering was described and evaluated in this chapter. The linear turbine model used in the Kalman filter includes relevant degrees of freedom such that the turbine dynamics for frequencies below 1 Hz, the approximate bandwidth of interest for blade pitch control applications, are well modeled. It was found that the estimator quality is very high when the turbine operation remains close to the operating point used to create the Kalman filter's underlying linear dynamic turbine model and when the aerodynamic inflow model used to simulate the turbine response to the wind field matches the inflow model included in the linearized turbine model. A gain-scheduled estimator was developed that schedules the dynamic Kalman filter model based on control signals such that a specific turbine model is only used when the wind speed is within 0.5 m/s

of the linearization operating point. When using this gain-scheduled estimator and simulating the turbine response with NREL's FAST code with the equilibrium inflow setting enabled, which is the required setting when using FAST to create the linearized turbine models included in the Kalman filter, the estimator performs very well. However, when the more realistic dynamic inflow setting is enabled in FAST, the estimator performance suffers. Therefore, the estimator could be improved by introducing a model of dynamic inflow to the linear turbine model as described in previous work on hub-height component estimation: Henriksen *et al.* [60] and Knudsen and Bak [107].

Although the frequency content of the wind speed estimates above 1 Hz is not of interest for blade pitch control applications, the estimates are very noisy above 1 Hz due to unmodeled turbine dynamics and sensor noise. In order to remove the frequency content of the estimates above 1 Hz, additional low-pass filtering is required. It was shown that if a fixed estimation lag time can be tolerated, the estimator phase delay can be reduced using non-causal Kalman filtering. In addition, the non-causal estimator inherently provides some low-pass filtering above 1 Hz. For the purpose of using the wind speed estimator to determine the correlation between the lidar measurements and the true wind speed disturbances, as illustrated in Fig. 6.1, some delay, either for non-causal estimation or to low-pass filter the estimates, can be tolerated. In other words, it is necessary to determine the wind speed correlation statistics, which will not change significantly after a few seconds of delay; possessing the true wind speed disturbance values at the current time step is not important.

In the next chapter, the gain-scheduled wind speed estimator will be used to estimate the measurement correlation statistics based on FAST simulations, with equilibrium inflow enabled, so that the optimal measurement prefilter can be calculated for different wind conditions. However, instead of simulating the turbine response using simple three-component wind fields with time varying u_{hh}, δ_h, and δ_v components, as was done in this chapter, full-field spatially-varying turbulent wind fields will be used. Therefore, the wind speed estimator will provide estimates of the equivalent rotor effective u_{hh}, δ_h, and δ_v wind disturbances that would have produced the measured turbine response rather than "true" u_{hh}, δ_h, and δ_v components present in the wind field. By

comparing these estimated equivalent wind disturbances with simulated lidar measurements, the optimal measurement filter can be estimated without any prior information about the measurement correlation statistics.

Acknowledgements

Dr. Paul Fleming from the National Renewable Energy Laboratory is acknowledged for providing data from NREL's CART3 wind turbine, which was used to help determine realistic sensor noise parameters.

Chapter 7

Time-Domain Lidar Measurement Simulation and Optimal Filter Estimation

While the focus of much of this thesis has been on the direct calculation of lidar measurement error using frequency-domain techniques, the objective of this chapter is to present measurement quality results based on time-domain simulations. The direct frequency-domain calculations discussed in Chapters 4 and 5 yield the same measurement error statistics that would be obtained from stochastic lidar measurement and rotor effective wind speed time series with the same statistics described by the frequency-domain model. Therefore, it is not useful to merely simulate lidar measurement and rotor effective wind speed time series with the same underlying model as the frequency-domain approach. However, time-domain simulations do not have to be performed using the simplifications and assumptions made in the frequency-domain calculations, and can thus provide more realistic measurement quality results. One goal of this chapter is to validate the method of modeling rotor effective wind speeds based on three rotating linear blade effective wind speeds by using the wind speed estimator analyzed in Chapter 6 to determine rotor effective wind speeds resulting from aeroelastic simulations with full-field spatially varying turbulence. Another aspect explored in this chapter is the method through which the optimal prefilter, assumed to be known *a priori* in the frequency-domain calculations, can be calculated using lidar measurement and estimated rotor effective wind speed time series.

In Section 7.1, a lidar measurement scenario is optimized using wind field and turbine output data resulting from the SOWFA simulation used to create the induction zone model in Section 3.3.1. The LES wind field created by SOWFA allows a comparison between results based on the statistical

wind field model discussed in Chapter 3 and results formed from physics-based simulations more characteristic of the atmospheric boundary layer. Section 7.2 discusses a method for extending the stochastic wind field simulation technique assuming frozen turbulence employed by TurbSim [71] to four dimensions, allowing wind evolution to be included. Measurement coherence and rotor effective wind speed power spectra determined using frequency-domain methods are compared with the corresponding spectra calculated using simulated lidar measurements as well as wind speed estimator outputs resulting from aeroelastic simulation in Section 7.2.1. Practical considerations regarding the time-domain implementation of the optimal MMSE prefilter, discussed in Section 2.3, are presented in Section 7.3, including the impact of filter preview time and the estimation of the underlying correlation statistics used to calculate the filter. Finally, in Section 7.3.2 the performance of the optimal filter is assessed as a function of the time permitted to estimate the underlying correlation statistics.

7.1 Lidar Measurement Simulations using a Large-Eddy Simulation Wind Field

The SOWFA simulation with $U = 8$ m/s below-rated wind conditions similar to LES wind field 1 described in Table 3.1 that was used to develop the induction zone model in Section 3.3.1 can also be used for time-domain lidar measurement simulations. Wind speed data from the 1000 s simulation was saved with a 3 m spatial resolution and a 0.2 s time step in the region around the NREL 5-MW turbine model, extending 760 m (6 D) upstream of the rotor. Lidar measurements can be simulated by sampling points along the lidar beam in the three-dimensional wind field and applying the range weighting function. Outputs from the FAST simulation within SOWFA can be used to determine the rotor effective wind speeds encountered by the turbine using the wind speed estimator described in the previous chapter. By comparing simulated lidar measurements, using many different scan parameter combinations, with the wind speed estimator outputs, the measurement scenario can be optimized. The SOWFA simulation allows measurement quality to be assessed in realistic, physics-based wind conditions, as opposed to the stochastic wind field model

analyzed in the previous sections.

7.1.1 Lidar Measurement Simulation Scenarios

The main objective of the measurement simulations performed using the SOWFA wind field is to determine the relative impact of the induction zone on measurement quality compared to other error sources, such as wind evolution, line-of-sight effects, and lidar range weighting. Three measurement simulation scenarios are investigated. A baseline simulation case is created to reveal measurement quality with neither wind evolution nor induction zone effects. A second scenario introduces wind evolution errors while the third scenario adds induction zone effects. The three measurement scenarios investigated are:

- Scenario I: FAST, No Evolution. A 144 m $\times$ 144 m (1.14 D $\times$ 1.14 D) slice of wind speeds in the yz plane, at an imaginary turbine location 315 m (2.5 rotor diameters) upstream of the turbine location in SOWFA, where induction effects are negligible, is extracted from the LES wind field and used as an input to a separate FAST simulation with the NREL 5-MW turbine model using the equilibrium inflow setting [9]. The hub-height and shear wind disturbances at the turbine are estimated using turbine outputs from FAST and the wind speed estimator for below-rated conditions developed in the previous chapter. Lidar measurements are simulated in the original SOWFA wind field such that the lidars measure at the extracted wind field location but are located behind the imaginary rotor plane by an amount equal to the intended preview distance. This way, the proper range weighting and directional bias effects are included, but wind evolution does not occur.

- Scenario II: FAST, with Evolution. This scenario is identical to Scenario I, except that the lidar is located at the hub location of the imaginary turbine and measurements are taken at the intended preview distance upstream of the turbine. This allows the wind measured by the lidar to evolve before it reaches the location of the extracted wind field.

- Scenario III: SOWFA, with Evolution. Lidar measurements are simulated for a lidar located

at the hub of the original 5-MW turbine in the SOWFA simulation. Thus the lidar measures wind that is disturbed by the rotor induction and that undergoes wind evolution. The wind disturbances at the rotor are estimated using outputs from the original turbine in SOWFA.

The three abovementioned simulation scenarios are illustrated in Fig. 7.1, where the location of the virtual turbine for Scenarios I and II and the SOWFA turbine for Scenario III as well as the location of the lidars are shown using a top view and a side view.

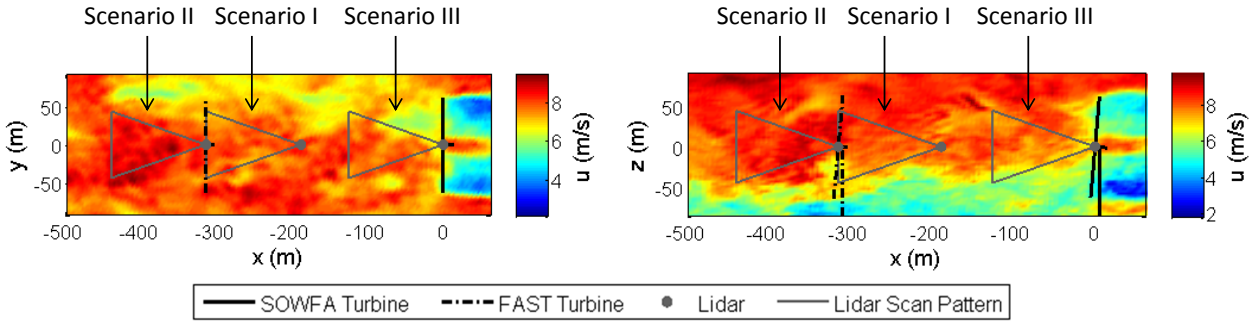

Figure 7.1: The three lidar measurement scenarios that are investigated using the SOWFA simulation.

The three-beam, circularly-scanning lidar scenario illustrated in Fig. 5.1 and analyzed throughout Chapter 5 is used to estimate the rotor effective hub-height and shear components provided by the wind speed estimator. Examples of the simulated lidar measurement time series and the wind speed estimator outputs resulting from Scenario III are shown for all three wind components Fig. 7.2. Note that the lidar measurement time series have been shifted to account for the preview time delay. The wind speed estimator outputs as well as the lidar measurements exhibit the 3P components predicted by the frequency-domain calculations in Chapter 5. Because the lidar measurements are simulated within the induction zone created by SOWFA, the mean value of u_{hh} measured by the lidar is lower than the wind speed estimator output. Furthermore, it should be noted that the δ_v component contains a non-zero mean value due to the presence of non-zero mean vertical shear over the rotor plane, which was not included in the wind field model analyzed earlier in the thesis.

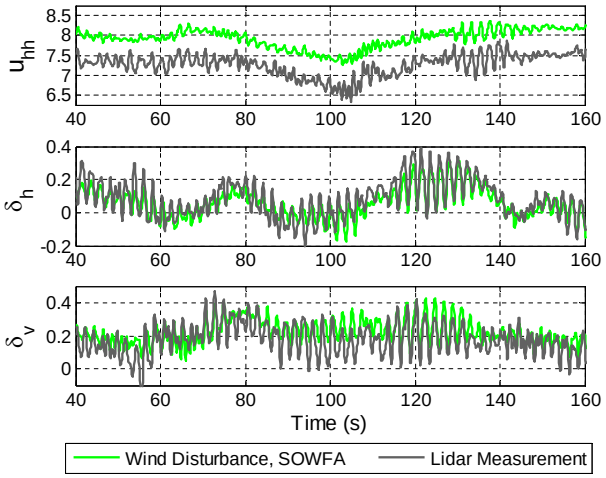

Figure 7.2: Estimated and measured hub-height and shear components, low-pass filtered with a cutoff frequency of 1 Hz, for measurement scenario III using a scan radius $r = 47.25$ m ($0.75\ R$) and preview distance $d = 88.2$ m ($0.7\ D$.

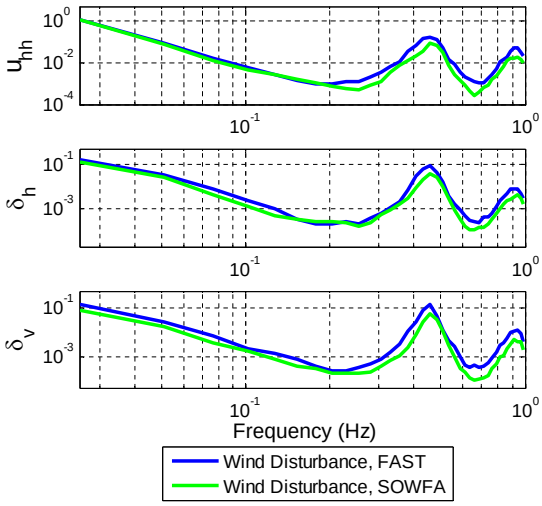

Figure 7.3: Power spectral densities of the estimated hub-height and shear wind disturbances for the FAST and SOWFA turbine simulations.

The power spectra of the hub-height and shear components given by the wind speed estimator are shown in Fig. 7.3 for the FAST simulations used in Scenarios I and II as well as the FAST simulation embedded within SOWFA from Scenario III. All power spectra exhibit the trends predicted by the frequency-domain calculations from Chapter 5. Specifically, strong peaks in the spectra occur at the 3P frequency (∼0.46 Hz, corresponding to the mean rotor speed of ∼9.2 RPM) as well as the harmonic at 6P, and the hub-height component contains a higher concentration of its power at low frequencies than the shear components. The discrepancy between the power spectra resulting from the stand-alone FAST simulation and the SOWFA simulation at higher frequencies is partially due to the different aerodynamic inflow models employed. The FAST simulations are performed using equilibrium inflow while the SOWFA simulation relies on LES calculations to determine the induced velocities at the rotor plane, and is more similar to the dynamic inflow setting discussed in Chapter 6.

7.1.2 Measurement Simulation Results

The lidar scan parameters are optimized for all three scenarios by simulating lidar measurements for a range of scan radii and preview distances and calculating the normalized MSE by way of the estimated measurement coherence and rotor effective wind component PSDs, assuming ideal prefiltering without preview time constraints, using the frequency-domain formula in (5.27), as in Section 5.3. The measurement azimuth angle (shown in Fig. 5.1) is determined so that each lidar measures the wind that will reach its corresponding blade, using the formula: $\psi_m = \psi_t + \omega_{rot} \cdot (2\pi/60) \cdot (d/U_{hh} + t_{offset})$, where ω_{rot} is the rotational rate of the rotor in RPM, U_{hh} is the mean hub-height wind speed, and t_{offset} is a tuning parameter that is used to correct for the arrival time of the wind potentially differing from d/U_{hh}. In the results presented here, optimal values of t_{offset} are found for each combination of scan radius and preview distance investigated using a brute-force approach.

So that the results of scenario III can be fairly compared with scenarios I and II, the wind disturbance power spectra from the FAST simulation, which are expected to be more accurate due to the lack of dynamic inflow, are used for $S_{tt}(f)$ when calculating the normalized MSE in all scenarios. Figure 7.4 shows the measurement quality plotted against r and d for the three wind disturbance components and the three measurement scenarios. However, instead of plotting the normalized MSE, the difference between the variance of the true rotor effective wind speed and the MSE, normalized by the variance of the true component, equivalent to

$$1 - \mathbf{E}\left[\left(w_t - H_{pre} w_m\right)^2\right] \Big/ \sigma_t^2 = \int_0^{f_{max}} S_{tt}\left(f\right) \gamma_{tm}^2\left(f\right) df \Bigg/ \int_0^{f_{max}} S_{tt}\left(f\right) df, \tag{7.1}$$

is shown. This way, the optimal scan scenario is given by the parameters that produce the maximum value of (7.1).

Table 7.1 displays the optimal scan radii and preview distances corresponding to the maxima in Figure 7.4, i.e., the parameters that minimize the MSE of the wind measurements for all components and scenarios. Additionally, Table 7.1 lists the normalized MSE values that are achieved by these r and d using (5.27).

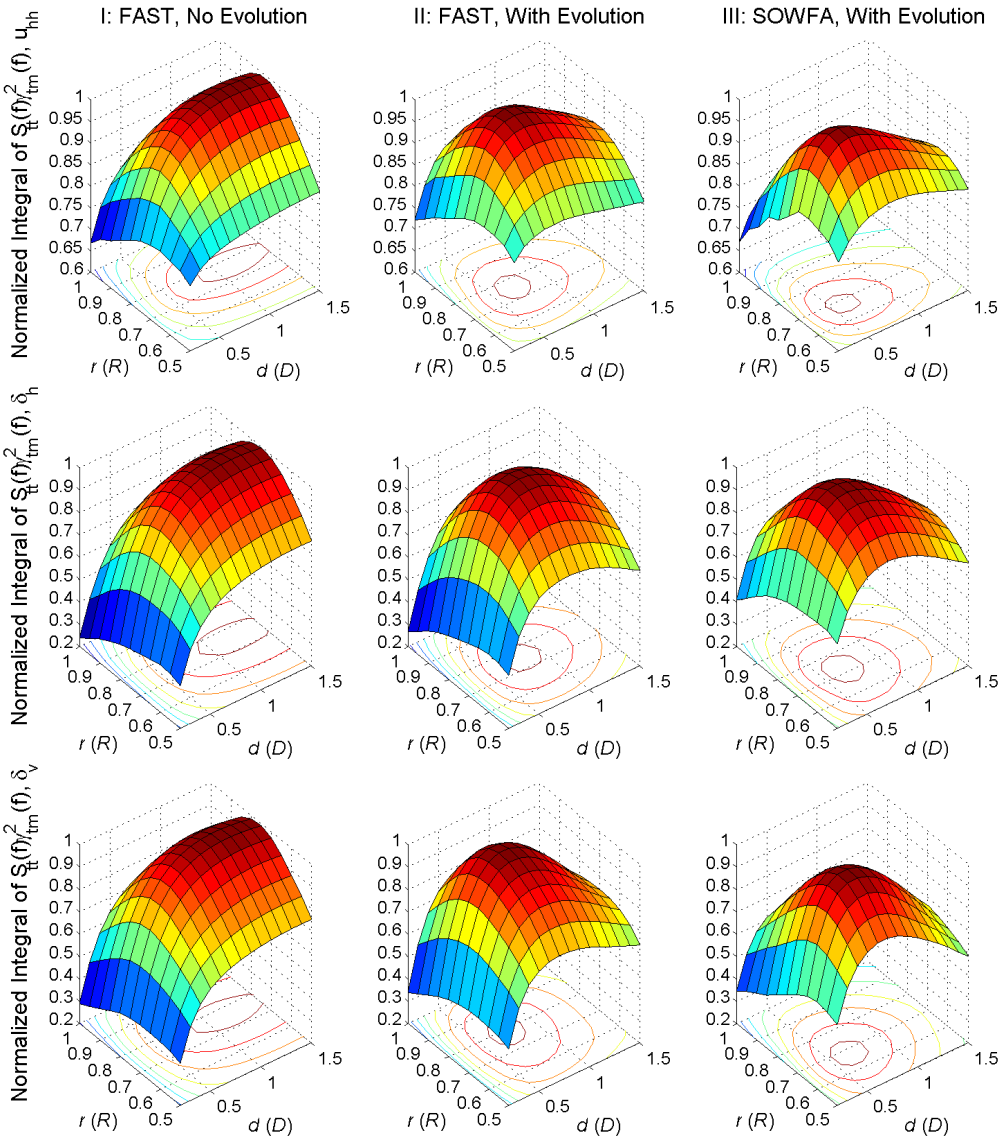

Figure 7.4: Measurement quality, defined in (7.1), as a function of r (in rotor radii $R = 63$ m) and d (in rotor diameters $D = 126$ m) for all three disturbances (rows) and all measurement scenarios (columns).

Table 7.1: Optimal scan radii (in units of rotor radii R), preview distances (in units of rotor diameters D), and minimum achievable normalized MSE, defined in (5.27).

	r (R)			d (D)			Measurement Error		
Scenario	u_{hh}	δ_h	δ_v	u_{hh}	δ_h	δ_v	u_{hh}	δ_h	δ_v
I	0.75	0.75	0.75	1.1	1.2	1.2	0.09	0.13	0.16
II	0.75	0.75	0.80	0.7	0.8	0.7	0.15	0.23	0.28
III	0.70	0.70	0.70	0.6	0.7	0.7	0.14	0.21	0.26

7.1.3 Discussion of Results

Figure 7.4 and Table 7.1 reveal that lidar scan radii between 70% and 80% blade span yield the best measurement correlation, slightly higher than the optimal scan radii found for rated wind conditions in Chapter 5. For scenario I, the optimal preview distances are between 1.1 and 1.2 rotor diameters. Shorter preview distances suffer from directional bias errors because of large measurement angles. But greater preview distances cause the lidar probe volumes to become too large, resulting in excessive spatial averaging [39]. As shown in Table 7.1, when wind evolution is introduced to the measurement simulations, the optimal preview distances are reduced to between 0.7 and 0.8 rotor diameters (Scenario II) and between 0.6 and 0.7 rotor diameters (Scenario III). In addition to the fact that wind evolves more over larger distances, greater preview distances exaggerate errors caused by both wind shear (wind speeds measured at different heights reach the turbine at different times) and uncertainty in the rotor azimuth angle when the wind arrives at the turbine due to variable rotor speed, thus contributing to shorter optimal preview distances.

As revealed in Table 7.1, measurement correlation is higher for the hub-height component than for the shear components in all three cases, as also shown by the frequency-domain calculations in Chapter 5. Figure 7.5 shows the measurement coherence curves corresponding to the optimal scan radii and preview distances for all scenarios. When wind evolution is introduced to the simulations (Scenario II), normalized MSE increases by 6–12%. This is most evident at the coherence peaks around the 3P and 6P frequencies. However, when induction zone effects are included, measurement error decreases slightly. This improvement is largely due to the increased measurement coherence around 0.1 Hz in all components. For comparison, measurement coherence curves for scenario III using the optimal scan parameters from scenario II, without the induction zone, are also plotted in Figure 7.5.

The slight improvement to measurement quality in Scenario III, when the induction zone is included, confirms the results obtained by including the induction zone model in the frequency-domain calculations in Section 5.3.1. For Scenario III as well as the frequency-domain calculations,

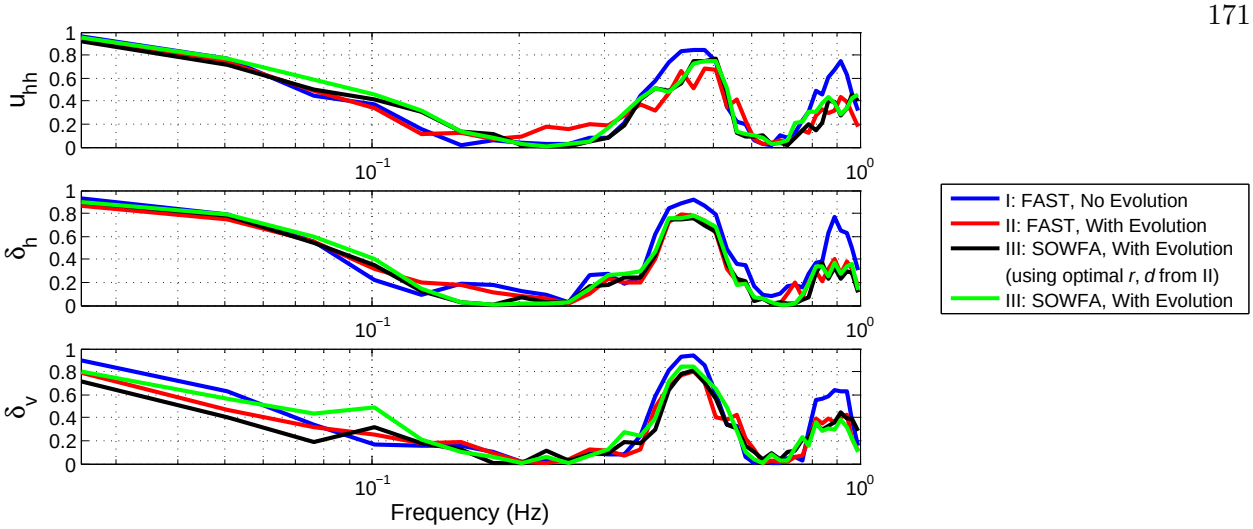

Figure 7.5: Measurement coherence curves corresponding to the optimal scan radii and preview distances listed in Table 7.1 for all three SOWFA simulation scenarios.

the optimal scan radii and preview distances are reduced in the presence of the induction zone, and the achievable measurement error decreases slightly. As discussed in Section 5.3.1, the shorter optimal scan radii result from the expansion of the approaching wind around the rotor plane illustrated in Fig. 3.12 (b). In order to measure the wind that reaches the rotor at 75% to 80% blade span, which is optimal for Scenario II, the lidar should actually be focused at slightly smaller scan radii. The smaller scan radii allow for shorter preview distances, while only slightly increasing the measurement angles, and thus not increasing line-of-sight errors by much. The shorter preview distances, in turn, result in less wind evolution which likely accounts for the higher measurement coherence.

Results from the three lidar scenarios investigated suggest that wind evolution is a significant source of error while the induction zone, rather than acting as a further error source, allows marginally better measurement coherence with slightly different optimal lidar scan parameters. Thus, the additional drop in longitudinal coherence measured in the induction zone in Section 3.3.2, not accounted for by the modified mean wind speed and length scale parameters, appears to be small enough that the higher severity of wind evolution in the induction zone does not increase measurement error. However, only a 1000 s period of data was analyzed, leading to noisy spec-

tral calculations. To increase the statistical significance of the comparisons between the three scenarios, longer simulations should be performed. Furthermore, simulations using different wind conditions should also be investigated to determine how the dependence of measurement quality on the induction zone is affected by stability, mean wind speed, and turbulence intensity.

7.2 Stochastic Wind Field Simulation with Wind Evolution

Aeroelastic wind turbine simulations are often performed using full-field stochastic wind fields which contain turbulent wind speed time series at a number of grid points in the yz plane encompassing the rotor, e.g., the blue points in Fig. 7.6. For the wind fields generated by NREL's TurbSim code [71], wind speeds at non-zero longitudinal positions are determined by assuming Taylor's frozen turbulence hypothesis [76] using (3.10). In the previous section, full-field turbulent wind fields were created by extracting wind velocities at points on a grid in an existing LES wind field. Since LES is very computationally expensive, however, aeroelastic simulations are typically performed using efficiently computed stochastic wind fields. Stochastic wind fields typically contain turbulence that is approximately Gaussian with second order statistics defined by turbulence power spectra and spatial coherence functions, such as those described in Section 3.1.

Two methods for generating stochastic wind fields are commonly used: the Mann method, described in Mann [74], and the Veers method implemented in TurbSim, described in Veers [72]. In this section, an extension of the Veers method will be described which allows for stochastic lidar measurement time series to be generated in addition to the grid of wind velocities at the rotor plane. Such a modified wind field allows simulated lidar measurement time series to be used in aeroelastic wind turbine simulations with preview-based controllers such that the effects of wind evolution are included, as presented in Laks *et al.* [34]. Additionally, as investigated in this chapter, a wind field containing a grid of wind velocities that interacts with the turbine as well as lidar measurement time series can be used to determine measurement coherence based on the wind speeds provided by a wind speed estimator.

The Veers method for generating a grid of stochastic wind velocity time series can be sum-

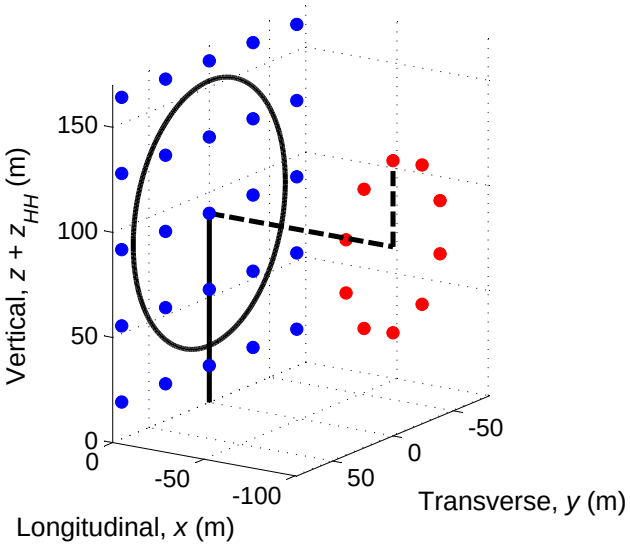

Figure 7.6: Diagram showing the grid of locations at the rotor plane where stochastic wind speed time series are generated (blue) as well as the locations on a scan circle where lidar measurement time series are generated (red).

marized as consisting of the following steps:

- For a series of discrete frequencies up to half the wind field sampling frequency, approximately unity-magnitude Fourier components corresponding to the wind speeds at each grid point are determined such that their phases are correlated according to the spatial coherence model used.
- The proper magnitude is introduced to the correlated Fourier components according to the power spectra defined by the wind field model.
- The inverse Fourier transform [67] is applied to the Fourier coefficients for each grid point, forming zero-mean velocity time series.
- Mean wind speed values are added to each velocity time series, introducing wind shear if applicable.

For a particular frequency bin, the vector of Fourier coefficients describing the longitudinal wind speeds at all N grid points at the rotor plane can be represented as $\boldsymbol{U}(f)$. The Veers method

can be extended to include lidar measurements on a scan circle upstream of the rotor, indicated by the red points in Fig. 7.6. By representing the vector of Fourier coefficients at the M lidar measurement points on the scan circle as $\hat{\boldsymbol{U}}(f)$, the wind speed and lidar measurement Fourier coefficients for a particular frequency bin are calculated as

$$\begin{bmatrix} \boldsymbol{U}(f) \\ \hat{\boldsymbol{U}}(f) \end{bmatrix} = \begin{bmatrix} \sqrt{S_{uu}(f)}\boldsymbol{I_N} & \mathbf{0} \\ \mathbf{0} & \sqrt{S_{\hat{u}\hat{u}}(f)}\boldsymbol{I_M} \end{bmatrix} \boldsymbol{L}(f)\,\boldsymbol{z}(f), \tag{7.2}$$

where $\boldsymbol{z}(f)$ is a vector of uncorrelated unity-magnitude Fourier components, $\boldsymbol{L}(f)$ is a lower-triangular correlating matrix, $S_{uu}(f)$ is the PSD of the u components at the grid points encompassing the rotor, and $S_{\hat{u}\hat{u}}(f)$ is the PSD of the lidar measurements, assuming axisymmetry. $\boldsymbol{I_N}$ represents the N-by-N identity matrix.

Specifically, each of the $M+N$ elements of $\boldsymbol{z}(f)$ is defined as

$$\boldsymbol{z}_i(f) = e^{j\phi_i}, \tag{7.3}$$

where ϕ_i are independent and identically distributed uniform random variables where $\phi_i \in [0, 2\pi]$. The lower-triangular matrix $\boldsymbol{L}(f)$ is found using the Cholesky decomposition of $\boldsymbol{\Gamma}(f)$:

$$\boldsymbol{\Gamma}(f) = \boldsymbol{L}(f)\,\boldsymbol{L}^T(f), \tag{7.4}$$

where $\boldsymbol{\Gamma}(f)$ is a matrix defining the coherence between each of the $M+N$ wind speed frequency components in the wind field. The elements of $\boldsymbol{\Gamma}(f)$ are defined as

$$\boldsymbol{\Gamma}_{i,j}(f) = \sqrt{\gamma^2_{\{u,\hat{u}\}_i,\{u,\hat{u}\}_j}(f)}, \tag{7.5}$$

where $\gamma^2_{\{u,\hat{u}\}_i,\{u,\hat{u}\}_j}(f)$ is the coherence between the u component or lidar measurement $\hat{u}$ at point i and the u component or lidar measurement at point j. In the standard method employed in TurbSim, the spatial coherence between wind speeds is simply given by a coherence formula, such as (3.7). But in the extended method presented here, the coherence between lidar measurements at two points, or between a lidar measurement and a wind speed at the rotor grid, is calculated using the measurement coherence formulas derived in Section 4.2.

After calculating the $M + N$ Fourier coefficients for each frequency bin using (7.2) to form a frequency-domain representation of each signal, the inverse Fourier transform is applied to yield the time series. The wind velocities and lidar measurements are properly correlated, including the effects of wind evolution, line-of-sight errors, and range weighting. Many different realizations of the wind field and lidar measurements with the same statistics can be generated using different random $\boldsymbol{z}(f)$ vectors for each realization. Although (7.2) through (7.5) only describe calculations for lidar measurements and the u components, the v and w components can be easily included as well.

7.2.1 Comparison between Frequency Domain Measurement Coherence Model and Time Domain Simulations

In this section, the stochastic wind field simulation method described in the previous section is used to create collections of 10-minute wind fields with corresponding lidar measurements so that measurement coherence and the wind component power spectra can be determined using wind speed estimator outputs based on FAST simulations. The stochastic wind fields are generated using the axisymmetric Kaimal turbulence model analyzed in Chapter 5 based on LES wind field 11, with $TI_u = 10\%$ and $L_u = 230$ m, for low and high above-rated mean wind speeds: $U = 13$ m/s and $U = 23$ m/s. The lidar scan scenario is based on the optimal parameters determined from the measurement optimization illustrated in Fig. 5.4; a scan radius of $r = 40.95$ m ($0.65\ R$) and a preview distance of $d = 107.1$ m ($0.85\ D$) are used, which, for both mean wind speeds, are halfway between the optimal parameters for the hub-height and shear components. A collection of 30 unique 10-minute wind fields with a 0.05 s time step and 4.83 m grid spacing over the rotor plane is generated for the two mean wind speeds analyzed. The corresponding lidar measurements consist of measurement time series at 60 azimuth angles around the scan circle (see the red points in Fig. 7.6). Rotating three-beam lidar-based wind component estimates using (5.11) are formed by interpolating between the time series at the 60 discrete azimuth angles depending on the current rotor azimuth angle.

For each of the unique wind fields generated, a FAST aeroelastic simulation is performed using the NREL 5-MW reference turbine model with equilibrium inflow and all DOF enabled. The gain-scheduled wind speed estimator described in Section 6.7 is then used to determine the effective hub-height and shear components encountered by the rotor given the full-field turbulent inflow. Using the history of rotor azimuth angles from each simulation, lidar-based estimates of the three wind components are formed based on the formulas in (5.11). Fig. 7.7 contains an example of the wind speed estimator outputs and corresponding lidar measurements for the hub-height and vertical shear components resulting from one of the 30 simulations with $U = 13$ m/s. As in Chapter 6, since the results for the horizontal shear component are very similar to those for vertical shear, due to axisymmetric wind conditions, only the vertical shear results are shown for simplicity. Note that the time series are low-pass filtered with a cutoff frequency of 1 Hz so that the measurement quality in the frequency band of interest for blade pitch control purposes can be

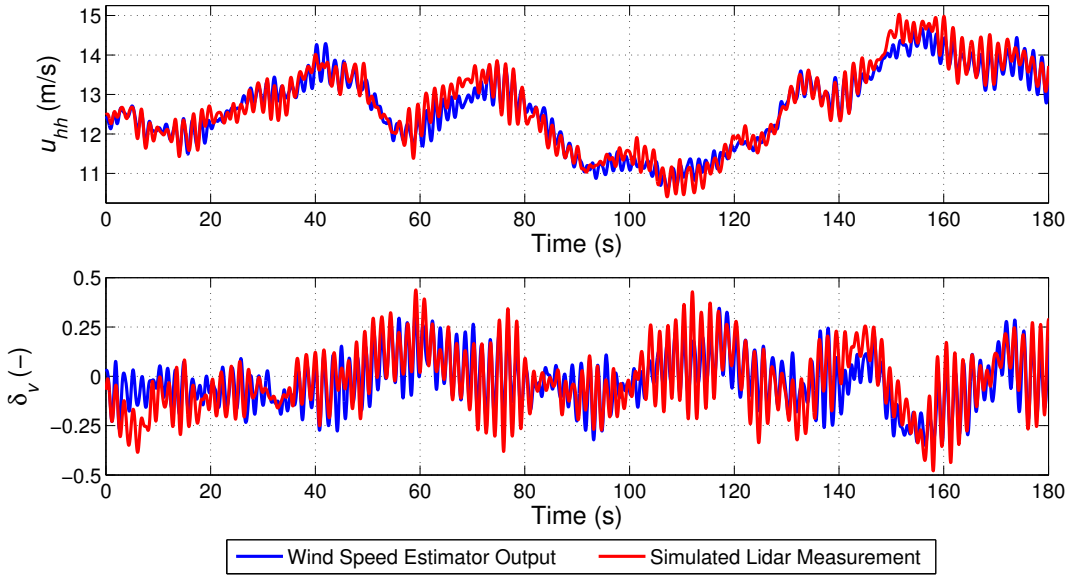

Figure 7.7: A comparison between wind speed estimator outputs resulting from FAST simulations with full-field stochastic wind inflow (blue) and simulated lidar measurements (red) for hub-height and vertical shear components. The simulated wind field is formed using the axisymmetric Kaimal turbulence model based on LES wind field 11, with $U = 13$ m/s, $TI_u = 10\%$, and $L_u = 230$ m. Lidar scan parameters of $r = 40.95$ m and $d = 107.1$ m are used. All time series are low-pass filtered with a cutoff frequency of 1 Hz.

shown. The strong 3P components resulting from rotational sampling of the wind field are clearly visible, with the 3P fluctuations being more dominant for the shear component as expected based on the spectra shown in Fig. 5.2.

Comparisons of the wind component power spectra and measurement coherence curves determined using the frequency-domain calculations described in Chapter 5 as well as from the wind speed estimator outputs resulting from FAST simulations with full-field turbulent inflow are provided in Figs. 7.8 and 7.9 for the $U = 13$ m/s and $U = 23$ m/s wind conditions, respectively. The power spectra and coherence curves for the time-domain simulations are estimated using all 30 10-minute simulations. In general, the power spectra and measurement coherence curves resulting from aeroelastic simulation match the direct frequency-domain calculations very well for the

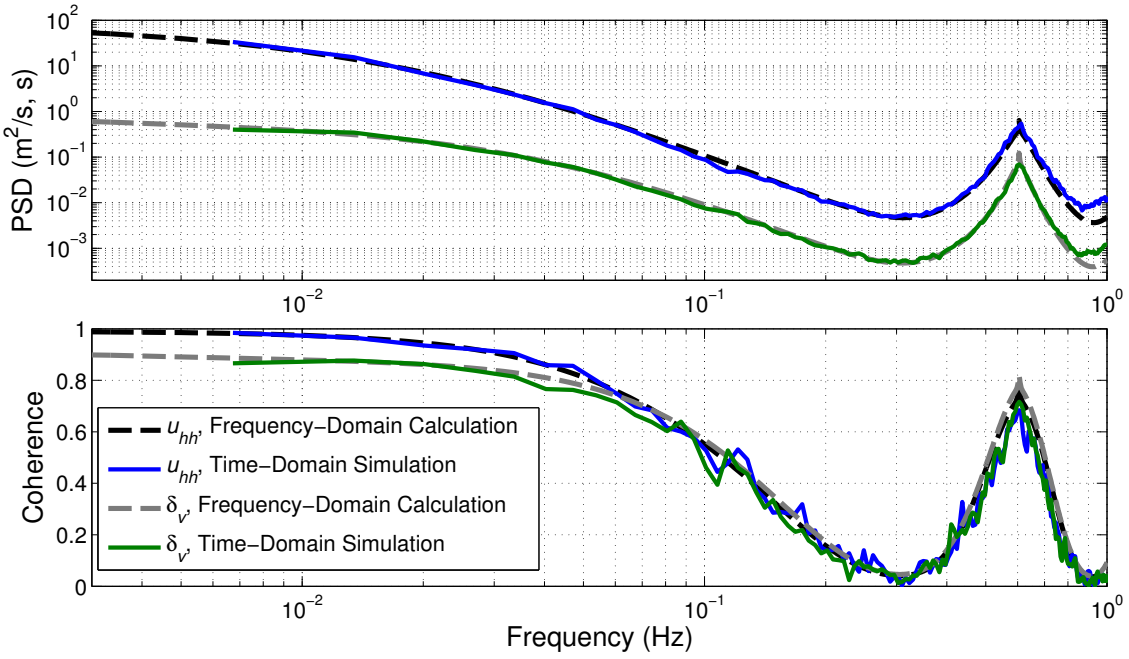

Figure 7.8: Hub-height and vertical shear component power spectra and measurement coherence curves determined using frequency-domain calculations as well as time-domain simulations. The rotor effective wind components in the time-domain simulations are determined using wind speed estimator outputs resulting from FAST simulations with full-field stochastic wind inflow. The simulated wind field is formed using the axisymmetric Kaimal turbulence model based on LES wind field 11, with $U = 13$ m/s, $TI_u = 10\%$, and $L_u = 230$ m. Lidar scan parameters of $r = 40.95$ m and $d = 107.1$ m are used.

$U = 13$ m/s wind condition despite the simplifications included in the latter approach. For the simulations with $U = 23$ m/s, however, the frequency-domain calculations overpredict the measurement coherence slightly, especially for the shear components. For both mean wind speeds and both wind components, the measurement coherence is significantly overpredicted by the frequency-domain calculations near the 3P frequency.

Many modeling details are included in the time-domain simulations using FAST that are ignored in the simplified frequency-domain calculation method. For example, the frequency-domain calculations assume linearized rotor effective wind speeds based solely on the u component while the wind speed estimator outputs are calculated based on nonlinear aeroelastic simulations where all three wind components affect the rotor aerodynamics. Additionally, a 5° rotor shaft tilt angle and

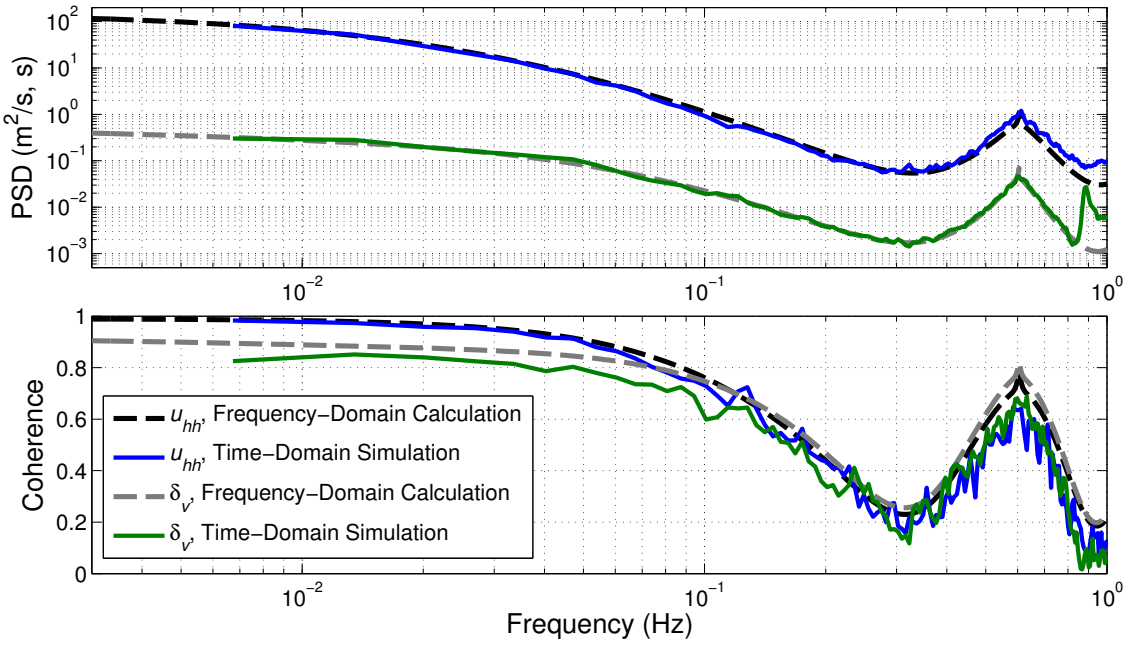

Figure 7.9: Hub-height and vertical shear component power spectra and measurement coherence curves determined using frequency-domain calculations as well as time-domain simulations. The rotor effective wind components in the time-domain simulations are determined using wind speed estimator outputs resulting from FAST simulations with full-field stochastic wind inflow. The simulated wind field is formed using the axisymmetric Kaimal turbulence model based on LES wind field 11, with $U = 23$ m/s, $TI_u = 10\%$, and $L_u = 230$ m. Lidar scan parameters of $r = 40.95$ m and $d = 107.1$ m are used.

2.5° rotor precone angle are present in the aeroelastic simulations while the frequency-domain calculations assume that the rotor is two-dimensional and perpendicular to the longitudinal direction. Furthermore, the direct frequency-domain method relies on a constant rotor speed of 12.1 RPM (the rated rotor speed), but the wind speed estimator outputs are calculated using FAST simulations with a rotor speed that fluctuates around the average value of 12.1 RPM. Yet the frequency-domain calculations describe the spectra that result from the higher fidelity time-domain simulation approach reasonably well. The presence of lower measurement coherence near the 3P frequency based on the wind speed estimator outputs and simulated lidar measurements than predicted by the frequency-domain approach is likely due to a combination of the abovementioned modeling details not present in the frequency-domain approach, particularly the variable rotor speed and the rotor geometry. For the $U = 23$ m/s wind condition, the lower measurement coherence at low frequencies calculated using the time-domain simulations, particularly for the shear component, is likely due to the transverse and vertical wind speed components, ignored when calculating the rotor effective wind component spectra in the frequency-domain calculations, affecting the rotor aerodynamics more at higher wind speeds than at lower wind speeds such as $U = 13$ m/s.

Given the reasonably good agreement between the simplified frequency-domain calculations and the more realistic time-domain simulations using FAST, the computationally efficient linearized frequency-domain method can be used to determine lidar measurement quality for different scan geometries and wind conditions without the need to perform computationally burdensome high-fidelity time-domain simulations. However, the slightly lower coherence near the 3P frequency as well as the slightly lower measurement coherence for the shear components at high wind speeds observed using the more realistic time-domain simulations should be considered.

7.3 Determining the Optimal Filter

The time-domain prefilter implementation with preview time constraints described in Section 2.3 and analyzed in Section 5.4 allows the MMSE prefilter to be derived given the cross-correlation function between the lidar measurements and the true wind components along with

the autocorrelation function of the lidar measurements. In Section 7.2.1, it was shown how the gain-scheduled wind speed estimator developed in the previous chapter can be used to accurately determine the rotor effective wind components encountered by the turbine. These wind speed estimates can then be compared with the lidar measurement time series to determine the necessary correlation functions required to derive the optimal filter. In this section, practical issues related to the derivation of the optimal prefilter are addressed. In Section 7.3.1, the effect of the filter preview time on measurement error is analyzed, while Section 7.3.2 discusses how the correlation functions can be estimated given the wind speed estimator outputs and lidar measurement time series. Finally, in Section 7.3.2, the impact of different combinations of filter preview time and the time provided to estimate the correlation statistics on measurement error is assessed.

7.3.1 Impact of Filter Length on Measurement Error

In Section 5.4, lidar measurement scenarios were optimized for different wind conditions assuming that all of the available preview time provided by the lidar's preview distance was used for the prefilter implementation, except for 0.5 s required by the feedforward controller to overcome pitch actuator delay. The performance of the prefilter with preview time constraints was compared to the performance of an ideal unconstrained filter in Section 5.4.1. Here, it will be shown how the achievable measurement error varies as a function of the preview time allocated to the prefiltering process, while not necessarily using all of the available time. Once again, the assumption is made that the number of samples of filter history N_h in the filter impulse response given by (5.41) is equal to the specified number of samples of filter preview N_p.

For the axisymmetric Kaimal turbulence model based on LES wind field 11, with $U = 13$ m/s, $TI_u = 10\%$, and $L_u = 230$ m, analyzed in Section 7.2.1, Fig. 7.10 shows how the normalized measurement MSE varies with the allocated preview time for both hub-height and shear components using the near-optimal preview distance $d = 107.1$ m ($0.85\ D$) and near-optimal scan radius $r = 40.95$ m ($0.65\ R$). The correlation functions $R_{tm}[n]$ and $R_{mm}[n]$ are determined by computing the inverse Fourier transforms of the CPSDs and lidar measurement PSDs resulting from frequency-domain

calculations using a sampling rate of $f_s = 50.82$ Hz. As in Section 5.4, the bandwidth of the rotor effective wind speed signals is limited to 1 Hz to reflect the frequencies of interest for blade pitch control purposes, but the lidar measurement autocorrelation function is calculated with higher frequency components included to force the prefilter to low-pass filter the measurements above 1 Hz. In Fig. 7.10, the achievable MSE as a function of the preview time is compared with the MSE resulting from the optimal unconstrained prefilter, given by (5.28), as well as the MSE that results from no prefiltering at all, calculated by integrating (2.17).

Fig. 7.10 reveals that very little prefilter preview time is required to approach the error reduction possible with an unconstrained MMSE filter. Even with a filter preview time of 0 s, i.e., a one-sample filter used to scale the lidar measurements, the normalized MSE is significantly reduced, especially for the shear components. Most of the available MSE reduction is made possible with only 0.2 s of filter preview. With 2 s of filter preview time (out of the maximum allowable time of ∼8 s given the lidar preview time of $d/U = 8.72$ s), the normalized measurement error is reduced

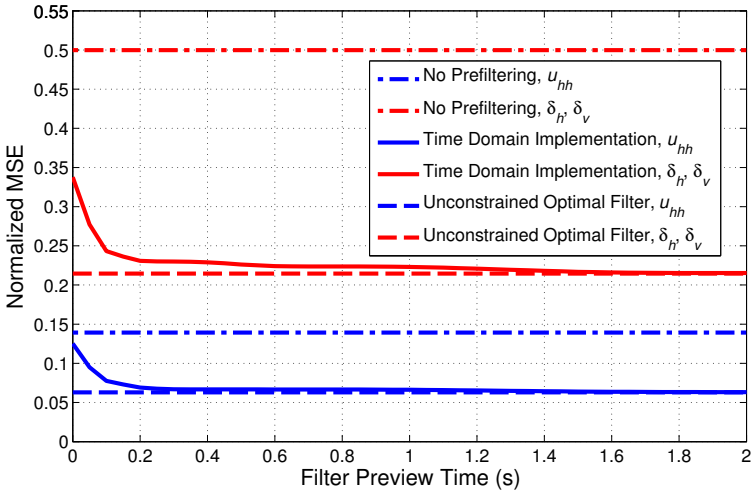

Figure 7.10: Normalized mean square measurement error for the hub-height and vertical shear components as a function of prefilter preview time using correlation statistics obtained from frequency-domain calculations. The MSE achieved using prefilter implementations with time constraints is compared with the MSE resulting from no prefiltering as well as the MSE that is obtained with the unconstrained optimal filter. The axisymmetric Kaimal turbulence model based on LES wind field 11 is used, with $U = 13$ m/s, $TI_u = 10\%$, and $L_u = 230$ m. Lidar measurement error is calculated using $r = 40.95$ m (0.65 R) and $d = 107.1$ m (0.85 D).

to within $3.5 \cdot 10^{-4}$ of the unconstrained optimal error. Therefore, should a preview-based control system require more preview time than is necessary simply to overcome the pitch actuator delay, prefilter preview times of only a couple seconds can be employed while causing only a negligible loss in performance.

7.3.2 Measurement Filter Performance with Estimation Time Constraints

Since the correlation statistics necessary to calculate the optimal prefilter with time-domain constraints given by (2.33) are unknown *a priori*, they must be estimated during operation of the preview-based wind turbine control system. Specifically, the autocorrelation matrix $\boldsymbol{R_{mm}}$ in (2.34) and the cross-correlation vector $\boldsymbol{R_{tm}}$ in (2.35) must be estimated yielding the optimal prefilter estimate

$$\hat{h}_{pre} = \hat{\boldsymbol{R}}_{\boldsymbol{mm}}^{-1} \hat{\boldsymbol{R}}_{\boldsymbol{tm}}. \tag{7.6}$$

Because wind conditions vary depending on many factors including the atmospheric stability and wind direction, the correlation statistics will vary as well. Therefore the correlation statistics must be estimated using a relatively short history of wind speed estimator outputs and lidar measurements such that the estimated prefilter can adapt to changing wind conditions and variable measurement quality. Given a time history of N samples, the cross-correlation function between the rotor effective wind components, determined from the wind speed estimator, and the lidar measurements as well as the autocorrelation function for the lidar measurements can be determined using the following estimate of the cross-correlation function $R_{ab}[n]$ for time lags from $-N+1$ to $N-1$:

$$\hat{R}_{ab}[n] = \frac{1}{N} \sum_{m=\max(0,n)}^{\max(0,n)+N-1-|n|} a[m+n]\, b^*[m]. \tag{7.7}$$

The performance of estimated prefilters for hub-height and shear components using the cross-correlation function estimator given in (7.7) is analyzed as a function of the estimation time, which is related to N through the sampling rate, for the axisymmetric Kaimal wind condition based on LES wind field 11 analyzed in Sections 7.2.1 and 7.3.1, with $U = 13$ m/s, $TI_u = 10\%$, and

L_u = 230 m, using the lidar scan parameters r = 40.95 m (0.65 R) and d = 107.1 m (0.85 D). Wind speed estimator outputs resulting from FAST simulations with full-field turbulent inflow as well as the simulated lidar measurements, as in Section 7.2.1, are used to determine the correlation statistics for a 20 Hz sampling rate, resulting in the estimated prefilter. Measurement error is then determined by comparing the filtered measurements with the low-pass filtered wind speed estimator outputs using a cutoff frequency of 1 Hz. Fig. 7.11 contains the measurement MSE for the hub-height and vertical shear terms as a function of not only the estimation time utilized to estimate the correlation functions leading to the filter calculations, but also the prefilter preview time. The plotted measurement MSE values are normalized such that a value of 0 corresponds to the MSE resulting from the use of the unconstrained optimal prefilter without preview time constraints and a value of 1 corresponds to the MSE resulting from no prefiltering at all. The measurement errors

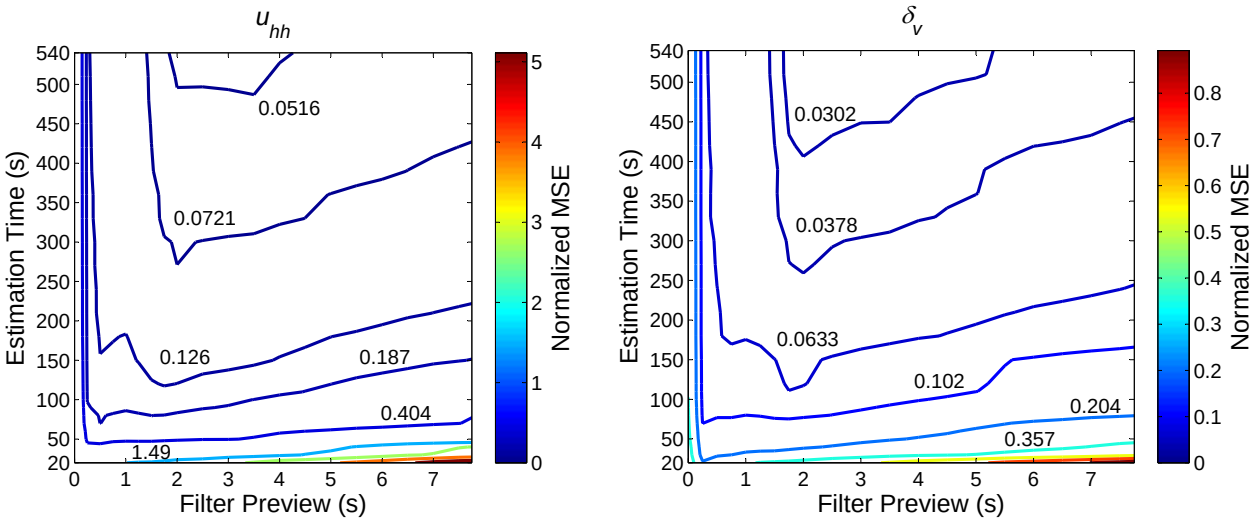

Figure 7.11: Normalized measurement error for the hub-height and vertical shear components as a function of prefilter preview time and the time used to estimate the lidar measurement and rotor effective wind speed correlation statistics. The measurement MSE is normalized such that a value of 0 corresponds to the MSE achieved with the unconstrained optimal prefilter and a value of 1 corresponds to the MSE resulting from no prefiltering. The rotor effective wind components are determined using wind speed estimator outputs resulting from FAST simulations with full-field stochastic wind inflow. The simulated wind field is formed using the axisymmetric Kaimal turbulence model based on LES wind field 11, with U = 13 m/s, TI_u = 10%, and L_u = 230 m. Lidar scan parameters of r = 40.95 m and d = 107.1 m are used.

are determined by forming 30 different estimates of the prefilter, one corresponding to each of the 30 10-minute wind fields, and then applying each filter estimate to all 30 lidar measurement time series.

Fig. 7.11 reveals that only 1-2 minutes of correlation function estimation time is required to yield relatively low measurement errors. Less than one minute of prefilter estimation time is required to achieve better error performance than would result from no prefiltering. For reference, the normalized MSEs that result from no prefiltering at all are 0.159 for u_{hh} and 0.642 for δ_v, while normalized MSEs of 0.0765 for u_{hh} and 0.250 for δ_v are achieved using the unconstrained optimal prefilter. The contour plots for both components show that as the filter preview time increases above roughly 2 s, the time needed to estimate the filter increases as well. In other words, provided with a certain amount of time to estimate the correlation statistics, a filter with a preview time close to 2 s will yield the lowest measurement error. While the available prefilter estimation time depends on how long the wind conditions remain approximately stationary, which can vary depending on location and time, as long as at least 1-2 minutes of estimation time is utilized and a filter preview of 1-3 s is implemented, the resulting measurement error will be relatively close to the minimum possible MSE compared to the error that would result without any prefiltering.

In order to analyze the ability of the optimal prefilter to adapt to different wind conditions likely to be encountered by a wind turbine, lidar field measurement data are used to determine realistic wind parameters. Specifically, lidar data provided by researchers at the University of Colorado Boulder obtained using a ground-based vertically-profiling WindCube lidar system during the Crop/Wind-Energy Experiments (CWEX) campaign [108, 109, 110] are used to calculate wind speed parameters that occur at different times during a 24-hour period. The CWEX lidar data were acquired during the summer of 2013 at a wind farm in central Iowa. A 24-hour period of longitudinal wind speeds measured at a height of 100 m with a sampling rate of 1 s during August 2013 is shown in Fig. 7.12. Although the wind direction varies throughout the 24-hour period, the longitudinal components of the wind are formed based on the mean wind direction calculated for each 10-minute block of measurement data. Fig. 7.12 reveals that the wind conditions can be

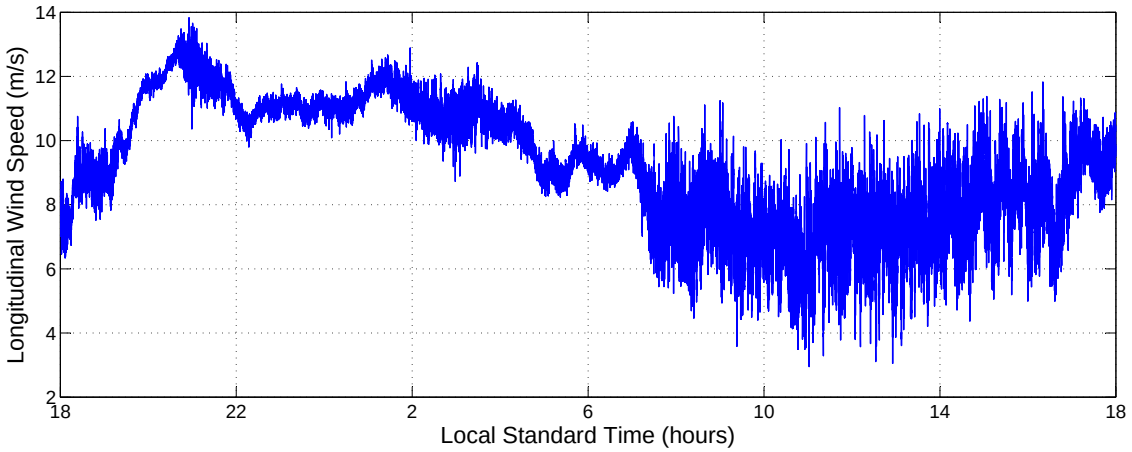

Figure 7.12: A 24-hour period of longitudinal wind speeds at a height of 100 m in central Iowa measured using a WindCube pulsed lidar during the CWEX campaign in August 2013.

divided into two distinct periods: nighttime wind conditions, typically coinciding with a stable atmospheric boundary layer, with higher mean wind speeds and lower turbulence intensities, and daytime conditions, commonly resulting in an unstable atmospheric boundary layer, with lower mean wind speeds but higher turbulence intensities.

Two sets of wind conditions representative of the low-turbulence stable atmosphere as well as the high-turbulence unstable atmosphere are selected to simulate the adaptive filtering process. The low-turbulence wind parameters are calculated using a 20-minute period of measurements beginning at 00:20 while the high-turbulence parameters are based on 20 minutes of measurement data beginning at 10:20. During the low-turbulence conditions at 00:20, the calculated wind parameters are $U = 8.95$ m/s, $TI_u = 2.0\%$, and $L_u = 98$ m. The remaining parameters are estimated as $TI_v = 1.8\%$, $TI_w = 0.65\%$, $L_v = 52$ m, and $L_w = 31$ m. For the high-turbulence wind conditions occurring at 10:20, the wind parameters are estimated as $U = 6.1$ m/s, $TI_u = 17.4\%$, $TI_v = 17.0\%$, $TI_w = 8.8\%$, $L_u = 149$ m, $L_v = 79$ m, and $L_w = 48$ m. Both sets of wind conditions are simulated using the axisymmetric Kaimal spectral model employed throughout this thesis. Note that while most of the analyses in this thesis have focused on above-rated operation, the available CWEX measurement data contained below-rated mean wind speeds. The WindCube lidar system estimates

the u, v, and w wind components by measuring the line-of-sight wind speeds along four beam directions evenly spaced around a scan cone. At a height of 100 m, the 30° half-opening angle of the scan cone [111] results in a distance of 115 m between measurement locations opposite each other in the scan circle. Therefore, due to the spatial averaging inherent in the wind component estimates, the length scales and turbulence intensities measured by the lidar could differ from those provided by measurements at a single point.

For both the high-turbulence and low-turbulence wind conditions, 30 different 10-minute realizations of the lidar measurements and rotor effective wind speed disturbances were simulated using frequency-domain techniques to calculate the power spectra and cross-spectra and applying the stochastic wind field simulation technique explained in Section 7.2 to obtain the time series, rather than using a wind speed estimator together with aeroelastic simulation data. The mean square measurement error normalized by the variance of the true wind components is shown as a function of the filter estimation time in Fig. 7.13 for the hub-height and shear components, using a filter preview time of 2 s. The normalized MSE is compared with the MSE produced by the unconstrained optimal prefilter as well as the measurement error that would result if the optimal unconstrained prefilter for the other wind condition were used. In other words, for the high-turbulence wind conditions in Fig. 7.13 (a), the dash-dotted lines represent the errors that would result if the optimal unconstrained prefilters derived for the previous low-turbulence wind conditions that occurred at 00:20 were used; similarly, the dash-dotted lines in Fig. 7.13 (b) indicate the measurement error that would result if the optimal prefilter for the high-turbulence conditions were used during the low-turbulence conditions that occurred earlier in the day. The results in Fig. 7.13 suggest that with less than 10 minutes of filter estimation time, the prefilters are able to adapt to changing wind conditions such that measurement errors are lower than those produced by fixed prefilters derived for the other turbulence condition. However, the estimation time required to exceed the performance of a fixed prefilter varies depending on the wind conditions. For the high-turbulence conditions, approximately 8 minutes of estimation time are required for the hub-height component prefilter to exceed the performance of the optimal filter derived for the low-turbulence

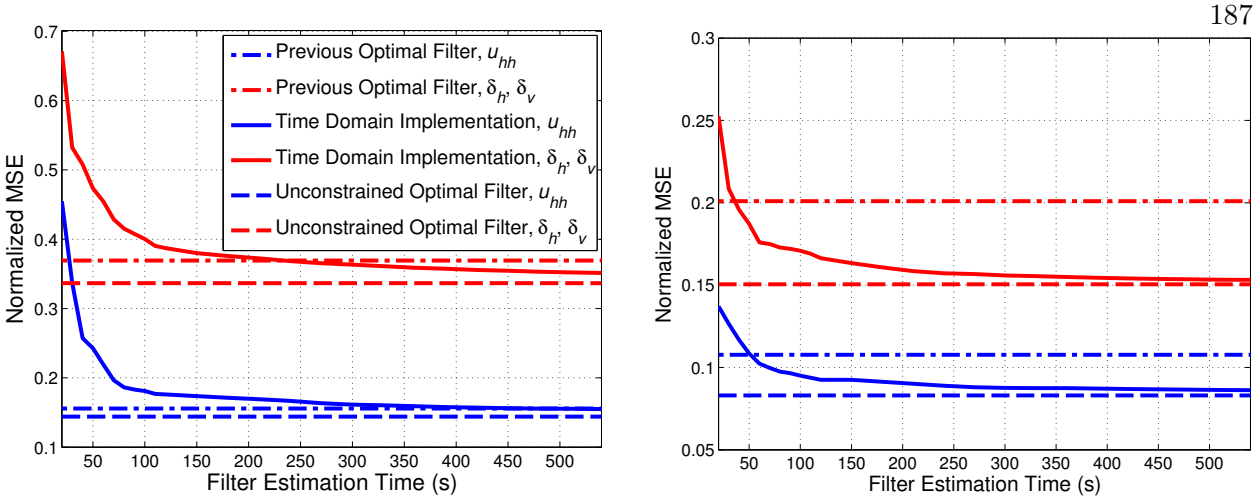

(a) $U = 6.1$ m/s, $TI_u = 17.4\%$.

(b) $U = 8.95$ m/s, $TI_u = 2\%$.

Figure 7.13: Normalized measurement error for the hub-height and shear components as a function of the estimation time for the correlation statistics with a filter preview time of 2 s for two different wind conditions measured during during the CWEX campaign in August 2013: (a) $U = 6.1$ m/s, $TI_u = 17.4\%$, and $L_u = 149$ m observed at 10:40, and (b) $U = 8.95$ m/s, $TI_u = 2.0\%$, and $L_u = 98$ m observed at 00:20. The normalized MSE curves are compared with the minimum achievable measurement errors using unconstrained optimal filters as well as the measurement errors that would result if the unconstrained optimal filters from the *other* wind condition were used (i.e., if the optimal filters for wind condition (b) were used for measurements in wind condition (a) and vice versa).

conditions. But for the low-turbulence conditions, less than 1 minutes of estimation time is needed to exceed the performance of the optimal prefilter derived for the high-turbulence conditions.

7.4 Discussion and Conclusions

The investigations in this chapter served one of two general purposes. First, time-domain simulations using wind speed estimator outputs determined from aeroelastic wind turbine simulations with full-field turbulent inflow were performed in order to validate the simplified frequency-domain calculations of measurement quality presented in Chapter 5. Second, practical issues related to implementing the optimal measurement prefilter were discussed, such as the impact of filter preview time and how the prefilter coefficients can be estimated from a finite amount of estimated wind speed and lidar measurement information.

In Section 7.1, lidar measurement error was determined using a SOWFA simulation com-

bining a wind field generated using LES with a FAST aeroelastic wind turbine simulation. The measurement error calculated using a wind speed estimator to determine the true rotor effective wind quantities confirmed some of the findings of the direct frequency-domain calculations. First of all, the rotor effective wind speed power spectra and corresponding measurement coherence curves contain peaks at the 3P frequency and its harmonics, as predicted by the frequency-domain calculations. Second, the measurement quality for the shear components is lower than for the hub-height component. The optimal scan parameters are also close to those predicted from frequency-domain methods. Finally, results from simulations performed both with and without the induction zone included agree with the calculations in Section 5.3.1. Specifically, the presence of the induction zone results in slightly shorter optimal scan radii and preview distances, producing slightly lower measurement error.

In Section 7.2, rotor effective wind speed power spectra and measurement coherence curves were calculated using simulated lidar measurements and wind speed estimator outputs resulting from aeroelastic simulations with stochastic full-field turbulent inflow. The power spectra and coherence curves that result from the time-domain simulations generally agree closely with those predicted using the simplified frequency-domain calculations, indicating that many of the modeling assumptions made in the latter method are justified. Specifically, the method of modeling rotor effective wind speeds using the combined impact of three rotating linear blade effective wind speeds very closely approximates the rotor effective wind speeds given by a wind speed speed estimator using outputs from aeroelastic simulations with full-field turbulent inflow. Because the simpler frequency-domain calculations agree reasonably well with the time-domain simulations, they can be used in lieu of the computationally expensive time-domain approach. However, it should be taken into consideration that the measurement coherence near the 3P frequency is overpredicted slightly using the frequency-domain calculations, as is the low-frequency measurement coherence for the shear components at high mean wind speeds.

Finally, in Section 7.3, it was shown that a prefilter implemented using only 1-2 s of preview time can achieve nearly the same error reduction performance as the unconstrained optimal filter.

Therefore, controllers that require more preview time than a simple model-inverse feedforward controller that merely needs to overcome pitch actuator delay can use the majority of the preview time provided by the lidar preview distance, while the measurements can be effectively filtered using a MMSE prefilter needing only 1-2 s of preview time. By investigating how the time allowed to estimate the prefilter correlation statistics affects the resulting measurement quality, it was found that only a couple minutes of estimation time are required to achieve most of the benefit that can be provided from prefiltering. Since wind conditions can vary rapidly, such a short filter estimation time allows the prefilter to effectively adapt to changing wind speed and lidar measurement statistics. As a reference, in wind turbine control simulations, 10-minute stationary wind fields are often employed, leaving adequate time for the prefilter to adapt to the specific wind conditions.

Simulations using two different wind conditions based on field measurements (low turbulence intensity and high turbulence intensity conditions) showed that the amount of estimation time required for prefilters to perform better than fixed prefilters that are optimal for the other condition is less than 10 minutes. Therefore, while prefilters can quickly adapt to changing wind conditions in 1-2 minutes such that they reduce measurement error compared to no prefiltering at all, more time could be required for the estimated prefilters to exceed the performance of some fixed prefilter which is determined as a tradeoff between the optimal filters corresponding to different wind conditions. Ultimately, the ability of the measurement prefilters to adapt to changing wind conditions depends on how long the wind conditions tend to remain approximately stationary, which is an area of research beyond the scope of this thesis.

Acknowledgements

As in Chapter 3, the SOWFA data used to determine lidar measurement quality, including the effects of wind evolution and the induction zone, via time-domain simulations in Section 7.1 was provided by Dr. Pieter Gebraad. The contributions of Dr. Gebraad as well as Dr. Matthew Churchfield, who provided information about the SOWFA simulation method and the specific data analyzed, are greatly appreciated. Prof. Julie Lundquist, from the University of Colorado Boulder,

is greatly acknowledged for providing the lidar measurement data from the Crop/Wind-Energy Experiments (CWEX) campaign utilized in Section 7.3.2, and for helping to select appropriate periods of data to analyze. Joseph C.-Y. Lee and Brian Vanderwende provided additional support preparing the lidar measurement data.

Chapter 8

Conclusions and Future Work

8.1 Discussion and Conclusions

The objective of this thesis was to determine how accurately lidar can be used to provide preview measurements of the approaching wind field for preview-based control applications through wind field modeling and optimization of the lidar measurement scenario. Lidar measurement quality was determined using the mean square error (MSE) between the lidar wind speed measurements and the true wind speeds that interact with the rotor. The minimum achievable MSE for any measurement scenario is achieved by filtering the measurements using a minimum mean square error (MMSE) prefilter, which is based on the statistics of the correlation between the measurements and the true wind speeds. As discussed in Chapter 2, the optimal preview-based control system that minimizes the variance of an output variable of interest, e.g., rotor speed error, using the lidar-based preview measurements as input, is given by the ideal model-inverse feedforward controller in series with the MMSE prefilter. Therefore, throughout the thesis MSE was calculated assuming that a MMSE prefilter was employed. For more advanced multi-objective control scenarios such as model predictive control or optimal control, discussed briefly in Chapter 1, the relationship between preview measurement MSE and the controller objectives is not necessarily as straightforward. However, measurement MSE is a relatively simple error metric to analyze given the statistical wind field model employed throughout the thesis, and MMSE preview measurements are expected to benefit a variety of control applications.

Mean square measurement error can be determined by integrating the measurement MSE

power spectrum, which can be calculated using a statistical frequency-domain wind field model. In Chapter 3, an existing frequency-domain wind field model given by turbulence power spectrum and spatial coherence formulas, assuming Gaussian turbulence, was described. A longitudinal coherence formula, developed based on data from large-eddy simulations (LES), was incorporated into this wind field model to describe wind evolution. A method was proposed for describing the wind speeds encountered by a wind turbine as the combined impact of three "blade effective" wind speeds, calculated by integrating the longitudinal wind speeds along a blade weighted by the spanwise sensitivity of aerodynamic torque production or the contribution to out-of-plane blade root bending moment to wind speed changes. It was shown how three blade effective wind speeds can be equivalently described as the hub-height wind component, i.e., the average wind speed encountered by the three blades, and linear horizontal and vertical shear components. These three rotor effective wind components are common wind speed disturbance variables for which linear dynamic turbine models can be created using aeroelastic tools such as NREL's FAST code [9]. The dynamic turbine models can then be used to develop model-based control systems. Typically, collective pitch control is used to mitigate the impact of the rotor effective hub-height component on rotor speed error and structural loads, while individual pitch control can be employed to reduce structural loads caused by the effective horizontal and vertical shear using the multiblade coordinate (MBC) transformation [38]. Therefore, torque-based blade effective weighting functions were used to calculate the hub-height component, to reflect the large impact that the hub-height component has on rotor speed via aerodynamic torque, while blade root bending moment-based weighting functions were used to determine the shear components, due to the interest in mitigating blade loads caused by shear across the rotor using individual pitch control.

Using the statistical frequency-domain wind field model, together with the lidar range weighting model described in Chapter 4 as well as the torque and bending moment-based blade effective weighting functions presented in Section 3.4, a method was described for calculating measurement MSE directly in the frequency domain using the NREL 5-MW reference turbine model. The NREL 5-MW model is representative of large utility-scale wind turbines and is commonly used to compare

controller performance in the wind turbine control community. A simple hub-mounted circularly-scanning lidar measurement scenario was analyzed, in which three lidar measurement points (one for for each blade) are obtained on a scan circle upstream of the rotor. A model of the commercially-available ZephIR continuous-wave lidar was used for all analyses. The lidar measurement points rotate along with the rotor so that each lidar measures the wind encountered by a specific blade. Using the MBC transformation, the lidar measurements are converted to estimates of the rotor effective hub-height and shear components. Assuming that the optimal MMSE prefilter is included in the measurement scenario, the MSE calculations rely on the power spectrum of the true wind speeds encountered by the turbine as well as the coherence between the lidar measurements and the true wind speeds. Methods were developed for calculating these spectra resulting from three rotating blade effective wind speeds and three corresponding rotating lidar measurements. Directly calculating the measurement MSE using the developed frequency-domain techniques is much more efficient than performing time-domain simulations, allowing measurement error for many different lidar and wind field scenarios to be calculated relatively quickly. In contrast, time-domain simulations rely on stochastic wind fields, which are computationally expensive to generate. Furthermore, lidar measurements must be simulated in many different wind field realizations in order for the calculated measurement error statistics to converge.

In Chapter 5, the optimal lidar scan radius and preview distance that minimize mean square measurement error were found for a variety of wind conditions. For the above-rated mean wind speed of 13 m/s and a moderate u component turbulence intensity of 10%, with other turbulence parameters based on one of the unstable LES wind fields analyzed in Chapter 3, it was shown that the optimal scan radius is 37.8 m (0.6 R) for the hub-height component and 44.1 m (0.7 R) for the shear components, corresponding to the general regions along the blade were the impact of wind speed variations on torque production and blade root bending moment are greatest, respectively. The optimal preview distance is 100.8 m (0.8 D) for the hub-height component and 113.4 m (0.9 D) for the shear components, where tradeoffs between line-of-sight errors caused by large measurement angles and errors caused by wind evolution, which grow as preview distance increases, are achieved.

With the optimal scan parameters, a very low measurement error of only 6.1% of the variance of the true wind component is achieved for the hub-height component. The achievable measurement quality for the shear components (both horizontal and vertical) is worse, with a MSE equal to 20.3% of the true wind component variance. As wind speed increases, the weighting functions used to calculate blade effective wind speed change very little, but the region along the blade where torque production is most sensitive to wind speed variations shifts slightly toward the root of the blade, causing the optimal scan radius for the hub-height component measurements to decrease by a small amount. Measurement error changes very little, however, when the wind speed increases but all other turbulence parameters remain the same. As turbulence intensity increases, wind evolution intensifies causing shorter optimal preview distances and increased measurement error. By varying the integral length scale of the turbulence, it was found that shorter length scales result in shorter optimal preview distances because of greater wind evolution, and consequently higher measurement errors.

The lidar scenario optimization results for different wind conditions suggest that measurement quality would benefit from lidar systems with variable scan geometries. The optimal scan radii do not change significantly for different wind conditions, however. Over the range of all above-rated mean wind speeds, the optimal scan radius for hub-height component measurements changes by less than 7 m ($\sim$0.11 R), while for shear component measurements, the optimal scan radius varies by less than 2 m ($\sim$0.03 R). Therefore, measurement quality would likely not be significantly improved by using a lidar system with a variable scan radius. On the other hand, depending on the turbulence intensity, the optimal preview distance varies considerably, ranging from $\sim$0.35 D to $\sim$1.2 D. But finding the optimal preview distance, which depends strongly on turbulence statistics that must be estimated during turbine operation, could be difficult. However, as can be seen in Fig. 5.4, measurement error is not as sensitive to changes in the preview distance as it is to changes in the scan radius. Thus it is not necessarily important to aggressively track the optimal preview distance. Finally, while scan scenario optimization results for the hub-height and shear components were presented individually in this thesis, a single set of lidar parameters must be implemented at

any given time. Therefore a tradeoff between the measurement quality of the hub-height component and the shear components must be found.

By incorporating a model of the upstream induction zone based on a simulation performed with NREL's SOWFA tool [78], it was found that for the NREL 5-MW turbine's rated wind speed $U = 11.4$ m/s, the induction zone has very little impact on measurement quality, although the optimal scan radius is reduced slightly to account for the expansion of the wind around the rotor. Consequently, the optimal preview distance is reduced as well. These trends were later confirmed using time-domain simulations performed with SOWFA in Section 7.1. The induction zone has an even smaller impact on measurement quality for higher wind speeds when the turbine's axial induction factor is reduced. Note that an additional induction zone investigation, using ground-based lidars to measure the wind inflow upstream of a 225 kW wind turbine, is discussed in Appendix A. An investigation into the effects of yaw error on measurement quality for the $U = 13$ m/s, $TI_u = 10\%$ wind condition revealed that measurement MSE more than doubles for a yaw error of 10° when the optimal scan geometry, assuming zero yaw error, is employed. The drastic reduction in measurement quality due to yaw error suggests that the measurement scenario might benefit from shorter-than-optimal preview distances, which reduce the undesired transverse distance that the measured wind speeds travel before they reach the rotor plane.

While the scan scenario optimizations performed in Chapter 5 relied on the assumption that the optimal MMSE prefilter was employed, in practice the correlation statistics required to determine the filter need to be estimated. Specifically, the cross-correlation function between the lidar measurements and the true wind speeds encountered by the turbine, as well as the lidar measurement autocorrelation function must be determined. Since there is no way to directly determine the "true" wind speeds encountered by the turbine, a wind speed estimator needs to be employed. In Chapter 6, it was shown that a gain-scheduled Kalman filter-based wind speed estimator relying on generator speed, tower fore-aft acceleration, and flapwise blade root bending moment measurements can accurately determine the hub-height and shear components encountered by the turbine. The wind speed estimator's accuracy depends on which aerodynamic inflow model

is used during simulation, however, since the Kalman filter model is based on the less realistic equilibrium inflow model. When the more realistic dynamic inflow model is used in simulation, the estimation error increases. Therefore, an improved wind speed estimator that includes the effects of dynamic inflow should be utilized. Methods for incorporating dynamic inflow into linear turbine models are discussed in Henriksen *et al.* [60] and Knudsen and Bak [107].

The rotor effective wind speed power spectra and measurement coherence curves calculated using direct frequency-domain techniques as well as obtained using wind speed estimator outputs based on aeroelastic simulations with full-field stochastic wind inflow were compared. The spectra obtained from both approaches agree reasonably well, suggesting that the linear frequency-domain calculations are sufficient for determining approximate measurement error. As the mean wind speed increases in above-rated conditions, however, the accuracy of the direct frequency-domain approach diminishes slightly. Using the wind speed estimator outputs together with simulated lidar measurements, it was shown how the MMSE prefilter can be determined by estimating the required correlation functions. The impact of the time used to estimate the correlation statistics, as well as the preview time available to the filter, on the achievable measurement MSE was investigated for the $U = 13$ m/s, $TI_u = 10\%$ wind condition analyzed throughout the thesis. However, as was shown in Section 5.4.1, the difference between the measurement error achievable with filter time constraints imposed by the lidar scenario and the optimal MSE possible with an unconstrained prefilter is negligible except when the preview distance is very short (resulting from very high wind speeds or turbulence intensities). In terms of the difference in MSE between measurement scenarios without any prefiltering and with the optimal unconstrained MMSE prefilter employed, after only 2 minutes of correlation function estimation time approximately 87% of the possible MSE reduction is achieved for the hub-height component, with roughly 94% of the improvement resulting for the shear components. After 9 minutes of estimation time, the estimated prefilters achieve 95% of the potential MSE reduction for the hub-height wind speed and 97% of the potential improvement for the shear components. These results suggest that the optimal prefilters can quickly adapt to changing wind conditions and measurement quality. By comparing the performance of estimated

prefilters for two different wind conditions with low and high turbulence intensities determined using field observations, it was observed that a longer period of estimation time is required for the prefilters to perform better than a fixed prefilter derived for the wind condition not being investigated. But less than 10 minutes of estimation time was found to be sufficient to perform better than the optimal prefilter for the other turbulence intensity.

Finally, lidar scenarios were optimized in this thesis in the minimum mean square measurement error sense. However, as discussed in Chapter 2, if the objective of the preview-based controller is to minimize the variance of an output error variable, such as generator speed, then the output variance should be reflected in the optimization objective. As shown in Section 2.2.1, the variance of an output variable can be calculated by integrating the product of the power spectrum of the MSE and the squared magnitude of the transfer function from the measured wind disturbance to the output. It is possible that the lidar scan scenario that minimizes the output variance, assuming an ideal model-inverse feedforward controller, is not the MMSE scan configuration. For example, if the transfer function from the wind speed to the output contains a resonant mode at a particular frequency, the optimal lidar scan scenario in the minimum variance sense might yield very low measurement error at that frequency even though the total MSE is minimized by some other scan configuration. In this thesis, though, MSE was treated as the optimization variable because it is a much more general metric. In contrast, the minimum-variance scan parameters and achievable output variance depend on the behavior of the specific feedback controller utilized as well as on the specific output variable of interest. But by incorporating the transfer function of interest into the optimization objective, the frequency-domain approaches developed in this thesis can very easily be extended to find the optimal lidar scan configuration that minimizes output variance.

8.2 Areas of Future Work

Opportunities exist to introduce additional modeling details to the frequency-domain techniques for calculating measurement error used to generate the primary results of this thesis. For example, the wind field model that was used contains zero mean vertical shear, although in reality

some vertical shear is almost always present in the atmospheric boundary layer. The impact that the height-dependent variable arrival time between wind measured by the lidar and the wind that reaches the rotor has on measurement quality can be analyzed by incorporating height-dependent phase delays in the cross-spectrum calculations. Because introducing vertical shear causes a wind field to no longer remain axisymmetric, the more computationally intensive spectrum calculations used to incorporate yaw error would have to be used. Furthermore, wind veer (height-dependent wind direction), which is also common in the atmospheric boundary layer, could be incorporated into the wind field model by extending the procedure used to analyze the impact of yaw error on measurement quality. Additionally, different lidar measurement scenarios can be investigated, including those used in commercially-available lidars. A rotating three-beam scenario was analyzed because it forms a relatively accurate measurement of the wind components encountered by three rotating blades. However, the frequency-domain methods presented in Chapters 4 and 5 can be used to calculate measurement quality for lidar scan scenarios with additional beams or fixed measurement points, for example. But the techniques developed in this thesis would need to be heavily modified to allow the analysis of lidar scan patterns with a scan period different from the rotational period of the rotor.

Other lidar models and wind turbine models can easily be included in the measurement error calculations performed in this thesis by replacing the lidar range weighting functions and blade effective weighting functions with those calculated for other models. Although the optimal measurement scenarios and achievable measurement errors depend on the specific rotor size and its aerodynamic properties as well as the specific lidar range weighting function shape, the general trends found in this thesis are expected to hold for any measurement scenario. Specifically, the optimal lidar scan radius depends on where along the blade the sensitivity of torque production or blade root bending moment to wind speed variations is highest, while the optimal preview distance occurs where a tradeoff between line-of-sight errors and wind evolution-induced errors takes place.

Many of the analyses in this thesis would benefit from wind speed statistics obtained from field data. First, in Section 7.3.2 it was shown that only a couple minutes are required to obtain a

relatively accurate estimate of the MMSE prefilter, but measurement error can still be significantly improved with more filter estimation time. Wind speed field data obtained from a meteorological tower, for example, could be used to examine how long wind conditions tend to remain stationary and thus how much filter estimation time should be afforded to the prefilter calculation so that it can adapt to changing conditions quickly enough. Given the amount of filter estimation time utilized, it could then be determined if the adaptive filtering strategy can perform better than a non-adaptive filter formed as a tradeoff between the optimal filters corresponding to different wind conditions likely to be encountered during turbine operation. Secondly, statistics about the distribution of mean wind speeds and turbulence intensities at a particular site could be used to further optimize the measurement scenario. For example, if only a single set of lidar scan parameters can be implemented, then the scan radius and preview distance that minimize measurement error over the lifetime of the turbine should be determined. The optimization could be performed by summing the errors that occur for a particular scan geometry over a variety of wind conditions weighted by the probability of each particular wind condition occurring.

A number of models presented in the thesis were developed with the aid of computational fluid dynamics simulations performed using NREL's SOWFA tool. LES provides the opportunity to develop models using physics-based wind field simulations, but in a much more controlled manner than field measurements could allow. Although a collection of 12 different LES wind conditions was used to develop the longitudinal coherence formula describing wind evolution in Section 3.2, the model should be validated using LES wind fields with a greater range of mean wind speeds and turbulence intensities. Ultimately, the wind evolution model should also be validated using field observations. The 1000 s SOWFA simulation used to develop the induction zone model is sufficient for creating a model of the mean velocity reductions and direction changes upstream of the turbine, but longer simulations should be performed to validate the true impact that the induction zone has on measurement quality. As can be seen in the coherence plots in Fig. 7.5, a single 1000 s lidar measurement simulation using the SOWFA wind field does not provide enough data for the frequency-domain statistics to be precisely determined. It is difficult to conclude whether the slight

difference in measurement quality with and without the induction zone is significant, or if it is simply a result of noise in the coherence calculations caused by insufficient data. Furthermore, although it was observed that longitudinal coherence decreases in the induction zone close to the turbine, and that simply adjusting the mean wind speed and length scale wind evolution model parameters to account for the velocity reductions close to the turbine does not yield the true coherence drop, more data is required to determine how the induction zone affects wind evolution for different wind conditions.

One of the drawbacks to using a statistical frequency-domain wind field model or stochastic wind field simulations to analyze lidar measurement error is that the turbulence is modeled as Gaussian, which is a simplification compared to the actual behavior of turbulence. The method of incorporating a linear MMSE prefilter to find the optimal lidar scenario and the minimum achievable measurement MSE is, in general, an optimal strategy in the MSE sense only if the lidar measurements and wind speeds encountered by the turbine are jointly Gaussian. For non-Gaussian wind conditions, such as those generated by LES, nonlinear prefilters or estimation techniques could perform better than the linear prefilters employed in this thesis. As an example, the speed at which different turbulent structures advect downstream for short periods of time varies throughout an LES simulation; not all turbulent structures advect at the mean wind speed at all times. As was discovered by Dunne *et al* [41] using turbine-mounted lidar measurement data obtained in the field, employing a time-varying preview time delay when determining the wind speeds that interact with a turbine, a form of nonlinear estimation, allows a reduction in measurement error. By performing additional lidar measurement simulations using SOWFA, or other LES tools, other nonlinear measurement filtering techniques could be developed to determine the potential improvement in measurement quality. Machine learning techniques, which rely on a "training" period to learn the complex relationships between measurements and outputs, could be applied to the preview measurement scenario. A period of time could be dedicated to learning the nonlinear model describing the relationship between lidar preview measurements and the wind that arrives at the turbine. Next, the resulting model could be used to estimate the true wind speeds at the turbine based on

the time history of lidar measurements and previous "true" wind speeds encountered by the turbine obtained from a wind speed estimator. After some period of time, the learning stage could then be performed again in order to adapt to changing wind conditions.

Perhaps the most useful extension of this research is the incorporation of the lidar measurement model into preview-based control simulations. A lidar model including range weighting and line-of-sight effects was incorporated into FAST simulations used to evaluate controller designs performed by Laks *et al.* [23] as well as Dunne *et al.* [24, 28]. Using the Kristensen wind evolution model and the stochastic wind field/lidar measurement simulation technique described in Section 7.2, the impact of wind evolution on an $\mathcal{H}_2$ optimal preview-based controller's performance was analyzed in Laks *et al.* [34]. However, the more recent LES-based wind evolution model developed in this thesis could be used to model wind evolution in future controller simulations. Many lidar-assisted controllers are designed assuming perfect lidar preview measurements, and are then analyzed when lidar measurement errors are introduced. By incorporating lidar and wind evolution models into the controller design process, however, the controller and measurement scenario could be jointly optimized, leading to improved performance.

Bibliography

[1] IEA wind 2013 annual report. Technical report, International Energy Agency, 2014.

[2] Global Wind Energy Council. Global statistics. http://www.gwec.net/global-figures/graphs/, February 2015.

[3] R. Wiser and M. Bolinger. 2013 wind technologies market report. Technical report, U.S. Department of Energy, DOE/GO-102014-4459, 2014.

[4] 20% wind energy by 2030: Increasing wind energy's contribution to U.S. electricity supply. Technical report, U.S. Department of Energy, DOE/GO-102008-2567, 2008.

[5] L. Y. Pao and K. E. Johnson. Control of wind turbines: Approaches, challenges, and recent developments. IEEE Control Systems Magazine, 31(2):44–62, 2011.

[6] T. Burton, D. Sharpe, and E. Jenkins, N. Bossanyi. Wind Energy Handbook. John Wiley & Sons, Chichester, UK, 2011.

[7] J. F. Manwell, J. G. McGowan, and A. L. Rogers. Wind Energy Explained: Theory, Design and Application, Second Edition. John Wiley & Sons, Chichester, UK, 2009.

[8] J. Jonkman, S. Butterfield, W. Musial, and G. Scott. Definition of a 5-MW reference wind turbine for offshore system development. Technical report, National Renewable Energy Laboratory, NREL/TP-500-38060, Golden, CO, 2009.

[9] J. Jonkman and M. Buhl. FAST user's guide. Technical report, National Renewable Energy Laboratory, NREL/EL-500-38230, Golden, CO, 2005.

[10] E. A. Bossanyi. Individual blade pitch control for load reduction. Wind Energy, 6(2):119–128, 2003.

[11] E. A. Bossanyi, A. Wright, and P. Fleming. Validation of individual pitch control by field tests on two- and three-bladed wind turbines. IEEE Transactions on Control Systems Technology, 21(2):1067–1078, 2013.

[12] N. Kodama, T. Matsuzaka, K. Tuchiya, and S. Arinaga. Power variation control of a wind generator by using feed-forward control. Renewable Energy, 16:847–850, 1999.

[13] M. Harris, M. Hand, and A. Wright. Lidar for turbine control. Technical report, National Renewable Energy Laboratory, NREL/TP-500-39154, Golden, CO, 2006.

[14] D. Schlipf, S. Kapp, J. Anger, O. Bischoff, M. Hofsäß, A. Rettenmeier, U. Smolka, and M. Kühn. Prospects of optimization of energy production by lidar assisted control of wind turbines. In Proc. European Wind Energy Association Annual Event, Brussels, Belgium, March 2011.

[15] K. A. Kragh, M. H. Hansen, and T. Mikkelsen. Precision and shortcomings of yaw error estimation using spinner-based light detection and ranging. Wind Energy, 16(3):353–366, 2013.

[16] P. A. Fleming, A. K. Scholbrock, A. Jehu, S. Davoust, E. Osler, A. D. Wright, and A. Clifton. Field-test results using a nacelle-mounted lidar for improving wind turbine power capture by reducing yaw misalignment. In Proc. The Science of Making Torque from Wind, Lyngby, Denmark, June 2014.

[17] N. Wang, K. Johnson, and A. Wright. Combined feedforward and feedback controllers for turbine power capture enhancement and fatigue loads mitigation with pulsed lidar. In Proc. AIAA Aerospace Sciences Meeting, Nashville, TN, January 2012.

[18] E. A. Bossanyi, A. Kumar, and O. Hugues-Salas. Wind turbine control applications of turbine-mounted lidar. In Proc. The Science of Making Torque from Wind, Oldenburg, Germany, October 2012.

[19] D. Schlipf, P. Fleming, S. Kapp, A. Scholbrock, F. Haizmann, F. Belen, A. Wright, and P. W. Cheng. Direct speed control using lidar and turbine data. In Proc. American Control Conference, Washington, D.C., June 2013.

[20] D. Schlipf and M. Kühn. Prospects of a collective pitch control by means of predictive disturbance compensation assisted by wind speed measurements. In Proc. German Wind Energy Conference (DEWEK), Bremen, Germany, November 2008.

[21] D. Schlipf, S. Schuler, P. Grau, F. Allgöwer, and M. Kühn. Look-ahead cyclic pitch control using lidar. In Proc. The Science of Making Torque from Wind, Heraklion, Greece, June 2010.

[22] D. Schlipf, T. Fischer, C. E. Carcangiu, M. Rossetti, and E. Bossanyi. Load analysis of look-ahead collective pitch control using LIDAR. In Proc. German Wind Energy Conference (DEWEK), Bremen, Germany, November 2010.

[23] J. Laks, L. Pao, E. Simley, A. Wright, N. Kelley, and B. Jonkman. Model predictive control using preview measurements from LIDAR. In Proc. AIAA Aerospace Sciences Meeting, Orlando, FL, January 2011.

[24] F. Dunne, L. Y. Pao, A. D. Wright, B. Jonkman, N. Kelley, and E. Simley. Adding feedforward blade pitch control for load mitigation in wind turbines: Non-causal series expansion, preview control, and optimized FIR filter methods. In Proc. AIAA Aerospace Sciences Meeting, Orlando, FL, January 2011.

[25] J. Laks, L. Pao, A. Wright, N. Kelley, and B. Jonkman. The use of preview wind measurements for blade pitch control. IFAC J. Mechatronics, 21(4):668–681, June 2011.

[26] F. Dunne, L. Y. Pao, A. D. Wright, B. Jonkman, and N. Kelley. Adding feedforward blade pitch control to standard feedback controllers for load mitigation in wind turbines. IFAC J. Mechatronics, 21(4):682–690, June 2011.

[27] J. Laks and L. Y. Pao. Preview-enabled set-point scheduling for model predictive control of wind turbines. In Proc. AIAA Aerospace Sciences Meeting, Nashville, TN, January 2012.

[28] F. Dunne, D. Schlipf, L. Y. Pao, A. D. Wright, B. Jonkman, N. Kelley, and E. Simley. Comparison of two independent lidar-based pitch control designs. In Proc. AIAA Aerospace Sciences Meeting, Nashville, TN, January 2012.

[29] N. Wang, K. E. Johnson, and A. D. Wright. FX-RLS-based feedforward control for lidar-enabled wind turbine load mitigation. IEEE Transactions on Control Systems Technology, 20(5):1212–1222, 2012.

[30] D. Schlipf, L. Y. Pao, and P. W. Cheng. Comparison of feedforward and model predictive control of wind turbines using lidar. In Proc. IEEE Conference on Decision and Control, Maui, HI, December 2012.

[31] D. Schlipf, D. J. Schlipf, and M. Kühn. Nonlinear model predictive control of wind turbines using LIDAR. Wind Energy, 16(7):1107–1129, 2013.

[32] F. Dunne and L. Y. Pao. Benefit of wind turbine preview control as a function of measurement coherence and preview time. In Proc. American Control Conference, Washington, D.C., June 2013.

[33] M. Mirzaei, M. Soltani, N. K. Poulsen, and H. H. Niemann. Model predictive control of wind turbines using uncertain lidar measurements. In Proc. American Control Conference, Washington, D.C., June 2013.

[34] J. Laks, E. Simley, and L. Y. Pao. A spectral model for evaluating the effect of wind evolution on wind turbine preview control. In Proc. American Control Conference, Washington, D.C., June 2013.

[35] M. Kristalny, D. Madjidian, and T. Knudsen. On using wind speed preview to reduce wind turbine tower oscillations. IEEE Transactions on Control Systems Technology, 21(4):1191–1198, 2013.

[36] C. L. Bottasso, P. Pizzinelli, C. E. D. Riboldi, and L. Tasca. LiDAR-enabled model predictive control of wind turbines with real-time capabilities. Renewable Energy, 71:442–452, November 2014.

[37] K. A. Kragh, M. H. Hansen, and L. C. Henriksen. Sensor comparison study for load alleviating wind turbine pitch control. Wind Energy, 17(12):1891–1904, 2014.

[38] G. Bir. Multiblade coordinate transformation and its application to wind turbine analysis. In Proc. AIAA Aerospace Sciences Meeting, Reno, NV, January 2008.

[39] E. Simley, L. Y. Pao, R. Frehlich, B. Jonkman, and N. Kelley. Analysis of light detection and ranging wind speed measurements for wind turbine control. Wind Energy, 17(3):413–433, 2014.

[40] E. A. Bossanyi. Un-freezing the wind: improved wind field modelling for investigating lidar-assisted wind turbine control. In Proc. European Wind Energy Association Annual Event, Copenhagen, Denmark, April 2012.

[41] F. Dunne, L. Y. Pao, D. Schlipf, and A. K. Scholbrock. Importance of lidar measurement timing accuracy for wind turbine control. In Proc. American Control Conference, Portland, OR, June 2014.

[42] E. Simley and L. Y. Pao. Reducing LIDAR wind speed measurement error with optimal filtering. In Proc. American Control Conference, Washington, D.C., June 2013.

[43] A. Scholbrock, P. Fleming, L. Fingersh, A. Wright, D. Schlipf, F. Haizmann, and F. Belen. Field testing lidar-based feed-forward controls on the NREL controls advanced research turbine. In Proc. AIAA Aerospace Sciences Meeting, Grapevine, TX, January 2013.

[44] D. Schlipf, P. Fleming, F. Haizmann, A. K. Scholbrock, M. Hofsäß, A. Wright, and P. W. Cheng. Field testing of feedforward collective pitch control on the CART2 using a nacelle-based lidar scanner. In Proc. The Science of Making Torque from Wind, Oldenburg, Germany, October 2012.

[45] M. Harris, D. Bryce, A. Coffey, D. Smith, J. Birkemeyer, and U. Knopf. Advance measurements of gusts by laser anemometry. Wind Engineering and Industrial Aerodynamics, 95(12):1637–1647, June 2007.

[46] A. Rettenmeier, O. Bischoff, M. Hofsäß, D. Schlipf, and J. J. Trujillo. Wind field analysis using a nacelle-based LIDAR system. In Proc. European Wind Energy Conference, Warsaw, Poland, April 2010.

[47] T. Mikkelsen, N. Angelou, K. Hansen, M. Sjöholm, M. Harris, C. Slinger, P. Hadley, R. Scullion, G. Ellis, and G. Vives. A spinner-integrated wind lidar for enhanced wind turbine control. Wind Energy, 16(4):625–643, 2013.

[48] M. Sjöholm, N. Angelou, T. Mikkelsen, A. T. Pedersen, S. Kapp, M. Harris, and C. Slinger. Two-dimensional structures in wind turbine inflow studied by a spinner-mounted lidar. In Proc. International Symposium for the Advancement of Boundary Layer Remote Sensing, Auckland, New Zealand, January 2014.

[49] A. T. Pedersen, M. Sjöholm, N. Angelou, T. Mikkelsen, B. F. Montes, J. E. Pedersen, C. Slinger, and M. Harris. Full-scale field test of a blade-integrated dual-telescope wind lidar. In Proc. European Wind Energy Association Annual Event, Vienna, Austria, February 2013.

[50] D. Schlipf, J. Mann, and P. W. Cheng. Model of the correlation between lidar systems and wind turbines for lidar-assisted control. J. Atmospheric and Oceanic Tech., 30(10):2233–2240, 2013.

[51] L. Kristensen. On longitudinal spectral coherence. Boundary-Layer Meteorology, 16(2):145–153, 1979.

[52] R. A. Pielke and H. A. Panofsky. Turbulence characteristics along several towers. Boundary-Layer Meteorology, 1(2):115–130, 1970.

[53] D. Medici, S. Ivanell, J.-Aa. Dahlberg, and P. H. Alfredsson. The upstream flow of a wind turbine: blockage effect. Wind Energy, 14(5):691–697, 2011.

[54] C. Slinger, M. Leak, M. Pitter, and M. Harris. Relative power curve measurements using turbine mounted, continuous-wave lidar. In Proc. European Wind Energy Association Annual Event, Vienna, Austria, February 2013.

[55] M. Asimakopoulos, P. Clive, G. More, and R. Boddington. Offshore compression zone measurement and visualisation. In Proc. European Wind Energy Association Annual Event, Barcelona, Spain, March 2014.

[56] I. Antoniou, S. M. Pedersen, and P. B. Enevoldsen. Wind shear and uncertainties in power curve measurement and wind resources. Wind Engineering, 33(5):449–468, 2009.

[57] C. L. Bottasso, A. Croce, C. E. D. Riboldi, and G. S. Bir. Spatial estimation of wind states from the aeroelastic response of a wind turbine. In Proc. The Science of Making Torque from Wind, Heraklion, Greece, June 2010.

[58] T. Knudsen, T. Bak, and M. Soltani. Prediction models for wind speed at turbine locations in a wind farm. Wind Energy, 14(7):877–894, 2011.

[59] M. Soltani, T. Knudsen, M. Svenstrup, R. Wisniewski, P. Brath, R. Ortega, and K. Johnson. Estimation of rotor effective wind speed: a comparison. IEEE Transactions on Control Systems Technology, 21(4):1155–1167, 2013.

[60] L. C. Henriksen, M. H. Hansen, and N. K. Poulsen. A simplified dynamic inflow model and its effect on the performance of free mean wind speed estimation. Wind Energy, 16(8):1213–1224, 2013.

[61] E. Simley and L. Y. Pao. A longitudinal spatial coherence model for wind evolution based on large-eddy simulation. In Proc. American Control Conference, Chicago, IL, July 2015.

[62] E. Simley, L. Y. Pao, P. Gebraad, and M. Churchfield. Investigation of the impact of the upstream induction zone on lidar measurement accuracy for wind turbine control applications using large-eddy simulation. In Proc. The Science of Making Torque from Wind, Lyngby, Denmark, June 2014.

[63] E. Simley, L. Y. Pao, N. Kelley, B. Jonkman, and R. Frehlich. Lidar wind speed measurements of evolving wind fields. In Proc. AIAA Aerospace Sciences Meeting, Nashville, TN, January 2012.

[64] E. Simley and L. Y. Pao. Correlation between rotating lidar measurements and blade effective wind speed. In Proc. AIAA Aerospace Sciences Meeting, Grapevine, TX, January 2013.

[65] E. Simley and L. Y. Pao. Evaluation of a wind speed estimator for hub-height and shear components. Wind Energy, accepted in 2014, *online early view*.

[66] E. Simley, N. Angelou, M. Mikkelsen, T. Sjöholm, J. Mann, and L. Y. Pao. Characterization of wind velocities in the upstream induction zone of a wind turbine using scanning continuous-wave lidars. *submitted to* J. Renewable and Sustainable Energy, 2015.

[67] A. V. Oppenheim, A. S. Willsky, and S. Hamid. Signals and Systems, Second Edition. Prentice Hall, Upper Saddle River, NJ, 1996.

[68] H. Stark and J. W. Woods. Probability and Random Processes with Applications to Signal Processing, Third Edition. Prentice Hall, Upper Saddle River, NJ, 2002.

[69] P. Stoica and R. Moses. Spectral Analysis of Signals. Pearson Prentice Hall, Upper Saddle River, NJ, 2005.

[70] T. Kailath, A. H. Sayed, and B. Hassibi. Linear Estimation. Prentice Hall, Upper Saddle River, NJ, 2000.

[71] B. Jonkman. TurbSim user's guide: Version 1.50. Technical report, National Renewable Energy Laboratory, NREL/TP-500-46198, Golden, CO, 2009.

[72] P. Veers. Three-dimensional wind simulation. Technical report, Sandia National Laboratories, SAND88-0152, Albuquerque, NM, March 1988.

[73] J. Mann. The spatial structure of neutral atmospheric surface-layer turbulence. J. Fluid Mechanics, 273:141–168, 1994.

[74] J. Mann. Wind field simulation. Probabilistic Engineering Mechanics, 13(4):269–282, 1998.

[75] IEC 61400-1 "Wind turbines-part 1: Design requirements." 3rd edition. Technical report, International Electrotechnical Commission, Geneva, Switzerland, 2005.

[76] G. Taylor. The spectrum of turbulence. In Proceedings of the Royal Society of London, 1938.

[77] A. G. Davenport. The spectrum of horizontal gustiness near the ground in high winds. J. Roy. Meteor. Soc., 87:194–211, 1961.

[78] M. Churchfield and S. Lee. NWTC Information Portal (SOWFA), National Renewable Energy Laboratory. https://wind.nrel.gov/SOWFA/, September 2014.

[79] OpenFOAM the open source CFD toolbox, user's manual, version 1.7.1. Technical report, OpenCFD, Reading, UK, 2010.

[80] M. J. Churchfield, S. Lee, J. Michalakes, and P. J. Moriarty. A numerical study of the effects of atmospheric and wake turbulence on wind turbine dynamics. J. Turbulence, 13(14):1–32, 2012.

[81] R. B. Stull. An Introduction to Boundary Layer Meteorology. Kluwer Academic Publishers, Dordrecht, The Netherlands, 1988.

[82] M. J. Churchfield, S. Lee, and P. J. Moriarty. Adding complex terrain and stable atmospheric condition capability to the OpenFOAM-based flow solver of the simulator for on/offshore wind farm applications (SOWFA). In Proc. 1st Symposium on OpenFOAM in Wind Energy, Oldenburg, Germany, March 2013.

[83] P. L. O'Neill, D. Nicolaides, D. Honnery, and J. Soria. Autocorrelation functions and the determination of integral length with reference to experimental and numerical data. In Proc. 15th Australasian Fluid Mechanics Conference, Sydney, Australia, December 2004.

[84] S. Kay. Modern Spectral Estimation: Theory and Application. Prentice Hall, Englewood Cliffs, NJ, 1999.

[85] R. W. Thresher, W. E. Holley, C. E. Smith, N. Jafarey, and S.-R. Lin. Modeling the response of wind turbines to atmospheric turbulence. Technical report, Department of Mechanical Engineering, Oregon State University, RL0/2227-81/2, Corvallis, OR, August 1981.

[86] M. Wilczek, R. J. A. M. Stevens, and C. Meneveau. Spatio-temporal spectra in the logarithmic layer of wall turbulence: large-eddy simulations and simple models. J. Fluid Mechanics, 769:1–12, 2015.

[87] P. J. Moriarty and A. C. Hansen. Aerodyn theory manual. Technical report, National Renewable Energy Laboratory, NREL/TP-500-36881, Golden, CO, January 2005.

[88] A. D. Platt and M. L. Buhl Jr. WT_Perf user guide for version 3.05.00. Technical report, National Renewable Energy Laboratory, NREL/TP, Golden, CO, November 2012.

[89] M. Pitter, C. Slinger, and M. Harris. Introduction to continuous-wave Doppler lidar, chapter 4 in Remote Sensing for Wind Energy. Technical report, DTU Wind Energy, DTU Wind Energy-E-Report-0029(EN), Roskilde, Denmark, June 2013.

[90] J.-P. Cariou. Pulsed lidars. Technical report, DTU Wind Energy, DTU Wind Energy-E-Report-0029(EN), Roskilde, Denmark, June 2013.

[91] T. Mikkelsen. On mean wind and turbulence profile measurements from ground-based wind lidars: limitations in time and space resolution with continuous wave and pulsed lidar systems – a review. In Proc. European Wind Energy Conference, Stockholm, Sweden, March 2009.

[92] R. Frehlich and M. Kavaya. Coherent laser performance for general atmospheric refractive turbulence. Applied Optics, 30(36):5325–5352, December 1991.

[93] R. Frehlich, Y. Meillier, M. Jensen, B. Balsley, and M. Sharman. Measurements of boundary layer profiles in an urban environment. Applied Meteorology and Climatology, 45(6):821–837, June 2006.

[94] N. Angelou, F. F. Abari, J. Mann, T. Mikkelsen, and M. Sjöholm. Challenges in noise removal from doppler spectra acquired by a continuous-wave lidar. In Proc. 26th International Laser Radar Conference, Porto Heli, Greece, June 2012.

[95] M. Sjöholm, N. Angelou, P. Hansen, K. H. Hansen, T. Mikkelsen, H. Steinar, J. A. Silgjerd, and N. Starsmore. Two-dimensional rotorcraft downwash flow field measurements by lidar-based wind scanners with agile beam steering. J. Atmospheric and Oceanic Tech., 31(4):930–937, April 2014.

[96] E. Branlard, A. T. Pedersen, J. Mann, N. Angelou, A. Fischer, T. Mikkelsen, M. Harris, C. Slinger, and B. F. Montes. Retrieving wind statistics from average spectrum of continuous-wave lidar. Atmospheric Measurement Techniques, 6:1673–1683, 2013.

[97] R. G. Frehlich. Velocity error for coherent doppler LIDAR with pulse accumulation. Atmospheric and Oceanic Technology, 21(6):905–920, June 2004.

[98] S. Raach, D. Schlipf, F. Haizmann, and P. W. Cheng. Three dimensional dynamic model based wind field reconstruction from lidar data. In Proc. The Science of Making Torque from Wind, Lyngby, Denmark, June 2014.

[99] K. Z. Østergaard, P. Brath, and J. Stoustrup. Estimation of effective wind speed. In Proc. The Science of Making Torque from Wind, Lyngby, Denmark, August 2007.

[100] D. Bourlis and J. A. M. Bleis. Gain scheduled controller with wind speed estimation via Kalman filtering for a stall regulated variable speed wind turbine. In Proc. Universities Power Engineering Conference, Glasgow, UK, September 2009.

[101] E. L. van der Hooft and T. G. van Engelen. Estimated wind speed feedforward control for wind turbine operation optimisation. In Proc. European Wind Energy Conference, London, UK, November 2004.

[102] J. Aho, A. Buckspan, L. Pao, and P. Fleming. An active power control system for wind turbines capable of primary and secondary frequency control for supporting grid reliability. In Proc. AIAA Aerospace Sciences Meeting, Grapevine, TX, January 2013.

[103] X. Ma, N. K. Poulsen, and H. Bindner. Estimation of wind speed in connection to a wind turbine. Technical report, Technical University of Denmark, IMM-Technical Report-1995-26, Lyngby, Denmark, December 1995.

[104] R. Ortega, F. Mancilla-David, and F. Jaramillo. A globally convergent wind speed estimator for windmill systems. In Proc. Joint IEEE Conference on Decision and Control and European Control Conference, Orlando, FL, December 2011.

[105] M. S. Grewal and A. P. Andrews. Kalman Filtering: Theory and Practice using MATLAB. Wiley, New York, NY, 2008.

[106] T. W. Verbruggen. Load monitoring for wind turbines: Fibre optic sensing and data processing. Technical report, Energy Research Centre of the Netherlands, ECN-E–09-071, Petten, The Netherlands, 2009.

[107] T. Knudsen and T. Bak. Simple model for describing and estimating wind turbine dynamic inflow. In Proc. American Control Conference, Washington, D.C., June 2013.

[108] E. S. Takle, D. A. Rajewski, J. K. Lundquist, W. A. Gallus, Jr., and A. Sharma. Measurements in support of wind farm simulations and power forecasts: The crop/wind-energy experiments (CWEX). In Proc. The Science of Making Torque from Wind, Lyngby, Denmark, June 2014.

[109] B. Vanderwende, J. K. Lundquist, M. E. Rhodes, G. S. Takle, and S. I. Purdy. Observing and simulating the summertime low-level jet in central Iowa. Monthly Weather Review, 143(6):2319–2336, June 2015.

[110] J. K. Lundquist *et al.* Shearing of wind turbine wakes in a large wind farm. *in preparation for submission to* Environmental Research Letters.

[111] M. E. Rhodes and J. K. Lundquist. The effect of wind turbine wakes on summertime Midwest atmospheric wind profiles. Boundary-Layer Meteorology, 149(1):85–103, 2013.

[112] K. Modarresi and R. H. Kirchhoff. The flow field upstream of a horizontal axis wind turbine. Technical report, University of Massachusetts Wind Energy Center, Amherst, MA, 1979.

[113] Vestas V27-225 kW, 50 Hz wind turbine with tubular/lattice tower — general specification. Technical report, Item no. 941129, version 1.2.0.24, Vestas, 1994.

[114] S. M. Petersen. Wind turbine test — Vestas V27-225 kW. Technical report, Risø National Laboratory, Risø–M–2861, Roskilde, Denmark, 1990.

[115] T. Mikkelsen, J. Mann, M. M. Courtney, and M. Sjöholm. Windscanner: 3-D wind and turbulence measurements from three steerable Doppler lidars. In Proc. International Symposium for the Advancement of Boundary Layer Remote Sensing, Roskilde, Denmark, June 2008.

Appendix A

Induction Zone Measurements Upstream of a 225 kW Wind Turbine using Scanning Continuous-Wave Lidars

In addition to the SOWFA LES-based investigations described in Sections 3.3 and 7.1, several approaches have been previously used to investigate the induction zone. In Modarresi and Kirchhoff [112] an analytic model of the velocity field and streamlines upstream of a wind turbine rotor in steady flow is presented. Particle image velocimetry (PIV) and hot-wire anemometry were used in Medici *et al.* [53] to measure the wind velocities upstream of rotating model turbines in a wind tunnel. High resolution longitudinal and radial velocities in the near upstream region of the 18 cm diameter rotor are provided from the PIV analysis. Hot-wire anemometry revealed that velocity reductions between 2% and 5% of the freestream wind speed were present two rotor diameters upstream of the turbine, while velocity deficits of less than 1% were detected 3 D upstream of the turbine. Medici *et al.* [53] also presents a CFD investigation of the induction zone, finding that the numerical simulations predict lower wind speed deficits in the induction zone than exhibited by the experimental results. At 2 D upstream of the turbine, velocity deficits of only $\sim$1% are produced using CFD. Recently, lidar remote sensing has been used to measure the induction zone on full-scale wind turbines. In Slinger *et al.* [54] the reduction in wind speed up to 1.5 D upstream of the rotor was verified by measuring at several upstream distances using a circularly-scanning lidar located on the nacelle. Different power curves were measured using reference lidar measurements at five distances between 0.14 D and 2.5 D upstream of the turbine. A nacelle lidar was also employed in Asimakopoulos *et al.* [55] to determine how far upstream of the turbine the induction

zone extends, using forward-staring measurements as well as a horizontal arc scan at hub height. The authors conclude that at the upstream distance of 2.5 D, where power curve measurements are conventionally performed, velocity reductions between 1% and 3% of the freestream velocity are still detectable.

In this study, three scanning ground-based lidars, the short-range "WindScanner" lidars, are used to measure the induction zone upstream of a 225 kW Vestas V27 wind turbine at the Danish Technical University (DTU) Wind Energy department's Risø campus. Whereas the aforementioned lidar studies relied on a single nacelle-mounted lidar to provide line-of-sight velocity measurements, the three ground-based lidars are used to solve for the three wind components, namely the longitudinal, radial, and tangential (aligned with the rotational direction of the rotor) components. Mean velocities in the induction zone are determined by scanning a horizontal plane at hub height on one side of the nacelle extending roughly 1.5 D upstream of the rotor for various wind speeds resulting in a wide range of induction factors a. A similar scan is employed to measure mean velocities in a vertical plane extending from the bottom to the top of the rotor up to 1.5 D upstream of the turbine. Therefore, while much of the focus of previous induction zone investigations was on finding the velocity deficits that are present far upstream of the turbine, this study focuses on the near region of the induction zone. Finally, the impact of the induction zone on turbulence statistics is analyzed by rapidly scanning along lines perpendicular to the rotor plane at different radial positions and forming velocity time series at regular intervals up to 1 D upstream of the rotor.

The remainder of this appendix is organized as follows. Section A.1 describes the experimental setup for the induction zone measurements. A description of the Vestas V27 wind turbine is included in Section A.1.1. Section A.1.2 contains information about the WindScanner lidars used for the measurements, Section A.1.3 summarizes the lidar data processing procedures, and Section A.1.4 discusses the different scan patterns employed. The resulting measurements of 10-minute mean longitudinal, radial, and tangential velocities in the induction zone are provided in Section A.2 for a variety of mean freestream wind speeds. Section A.2.1 contains the results of the horizontal plane

scans and Section A.2.2 illustrates the results of a vertical plane scan. Turbulence statistics in the induction zone are presented in Section A.3. Finally, Section A.4 concludes the appendix with a brief discussion of the experimental methods and results.

A.1 Experimental Methods

The induction zone measurements are performed using the 27 meter rotor diameter, 225 kW Vestas V27 wind turbine at DTU Wind Energy's Risø campus. As shown in Fig. A.1, the turbine is located on relatively flat agricultural land approximately 225 m to the east of Roskilde fjord. The terrain is gently sloping up from the shore of the fjord and a meteorological (met) mast used for reference measurements is located approximately 73 m (2.7 D) away from the turbine at a heading of 283°. The positions of the scanning lidars around the turbine are chosen to produce measurements of the induction zone up to ∼1.5 D upstream of the rotor for wind directions from 221° to 281°, with an ideal wind direction of 251°, indicated in Fig. A.1. To improve the quality of the lidar scans, as will be explained in Section A.1.2, the lidar positions are chosen to measure only the left side of the rotor when looking upstream.

A.1.1 Wind turbine description

With a hub height of 32.5 m and a rotor diameter of 27 m, the three-bladed, pitch-regulated, 225 kW Vestas V27 turbine (pictured in Fig. A.2) was chosen for the measurement campaign because its design is similar to that of larger utility-scale turbines, yet it is small enough to allow for rapid scanning of its induction zone while keeping the lidars relatively close to the turbine. A list of the parameters for the V27 is included in Table A.1. For wind speeds below ∼5.5 m/s, power is generated using a 50 kW generator and the rotor's rotational speed is fixed at 33 RPM [113]. At higher wind speeds, power is generated using the 225 kW generator with a constant rotational speed of 43 RPM. When wind speeds exceed 14 m/s, rated wind speed for the V27, blade pitch control is used to regulate power capture. The published power curve for the V27 turbine [113] is shown in Fig. A.3 (a). Using data collected during early testing of the V27 at Risø [114], the estimated C_P

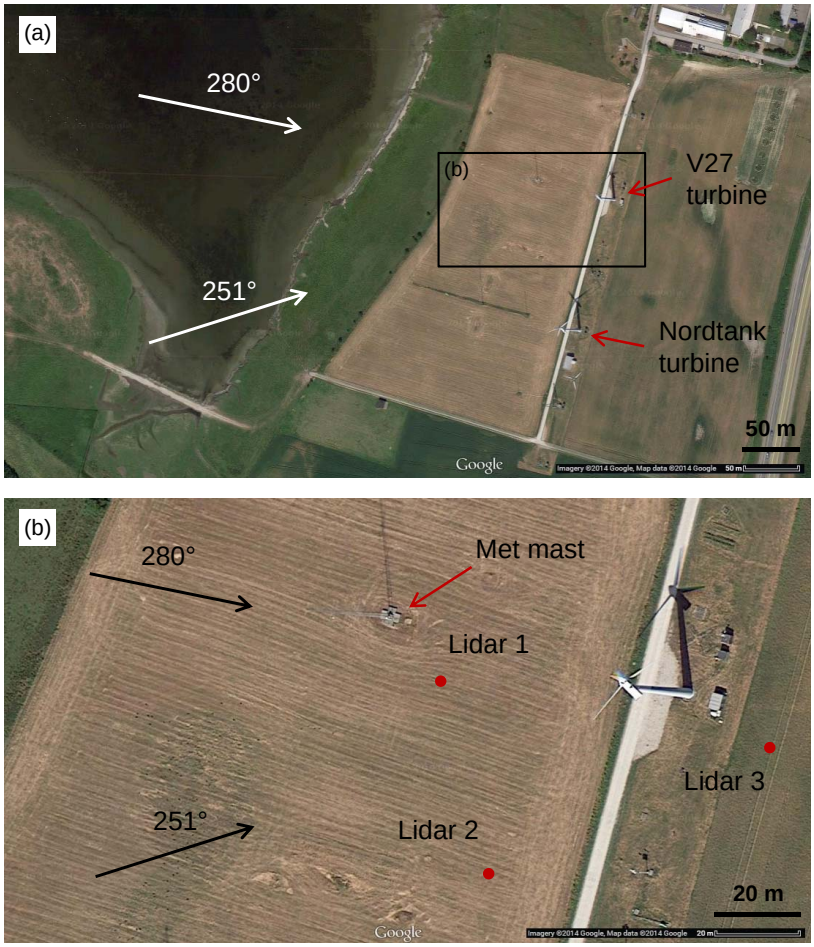

Figure A.1: Location of measurement campaign at the Danish Technical University's Risø campus. (a) Map of the terrain surrounding the Vestas V27 turbine used for the inflow measurements. Inflow measurements were acquired for intended wind directions between 251 and 280 degrees. (b) Close-up of the region near the V27 turbine where the experiment took place (indicated by the rectangular region in (a)). The locations of the three WindScanner lidars are indicated by the red points and are chosen to provide the highest inflow scan quality for a wind direction of 251 degrees. Map imagery ©2014 Google, Map data ©2014 Google.

curves based on electrical power production and mechanical power production (the latter relying on modifying the electrical C_P curve using measurements of the generator transmission efficiency) are plotted in Fig. A.3 (b). Note that values of mechanical C_P above the Betz limit of ∼0.59 at low wind speeds are due to small errors in the estimation of the generator efficiency. Fig. A.3 (b) also includes the estimated axial induction factor curve for the V27 calculated by solving for a using the mechanical C_P curve and (3.25). Although two solutions for a exist for a given C_P value, it

was assumed that the turbine operates at induction factors below the optimal value of 1/3. Higher values of a would cause unnecessarily high rotor thrust.

Figure A.2: Lidar 2 positioned in the field with V27 wind turbine in the background (left). Close-up of V27 nacelle and rotor (right).

Table A.1: Vestas V27 wind turbine parameters [113].

Parameter	Value
Type	3 bladed, upwind oriented
Rated power	225 kW
Rotor diameter	27 m
Hub height	32.5 m
Power regulation	Pitch control
Rotor speed, 50 kW generator (U $<$ $\sim$5.5 m/s)	33 RPM
Rotor speed, 225 kW generator (U $>$ $\sim$5.5 m/s)	43 RPM
Cut-in wind speed	3.5 m/s
Rated wind speed	14 m/s
Cut-out wind speed	25 m/s

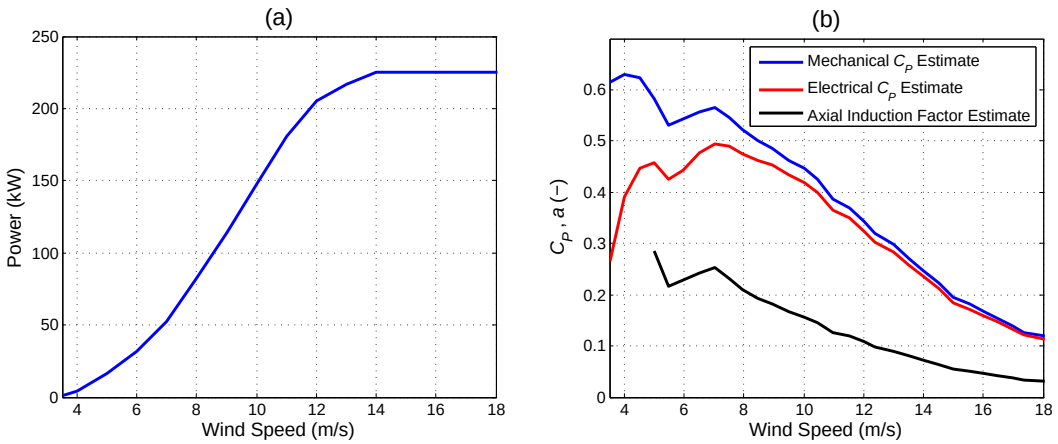

Figure A.3: (a) Vestas V27 power curve listed in [113]. (b) Estimated coefficient of power curves based on generated electrical power and mechanical power produced by the low-speed shaft listed in [114] as well as estimated axial induction factor curve using (3.25).

A.1.2 Lidar system

The short-range WindScanner lidar system (see Fig. A.2) developed by DTU Wind Energy is used to measure the wind inflow to the V27 turbine. The short-range WindScanner system consists of three continuous-wave (CW) lidars developed by ZephIR that have been modified with dual-prism scanning systems capable of orienting the beam in any direction within 60° of the adjustable center axis [95, 115]. Two motors are used to orient the beam while a third motor is used to control the focus distance of the lidars between 10 m and 200 m. The short-range WindScanners are capable of sampling the wind speed at 400 Hz, but a sample rate of 100 Hz is used for this campaign. All three WindScanner lidars can be synchronized to scan the same pattern in space simultaneously allowing for line-of-sight measurements from three unique directions, and therefore the ability to solve for the three wind speed components.

As described in Section 4.1.1, particularly in (4.2) through (4.5), rather than measuring the line-of-sight velocities at precisely the point where the lidars are focused, some volume averaging, or "range weighting" occurs along the beam. The ZephIR CW range weighting function and parameters listed in Section 4.1.1 are roughly equivalent to those for the short-range WindScanner lidars. As previously mentioned, the resulting full-width-at-half-maximum (FWHM) width of the

range weighting function, centered at the focus point, with focus distance F, can be approximated as $0.0013 \cdot F^2$. For this measurement campaign, the focus distances during the lidar scans range from approximately 33 m to 75 m resulting in range weighting FWHM widths between approximately 1.5 m and 7 m.

A.1.3 Lidar data processing

At every time sample, a Doppler velocity spectrum is provided by each lidar. As discussed in Section 4.1.2, each Doppler spectrum is formed by computing the discrete Fourier transform of the backscattered light and contains 255 frequency bins, where the width of each frequency bin represents a velocity change of 0.153 m/s. Approximately 2000 individual 255-bin Doppler spectra are averaged together during the sampling period to reduce noise; for longer sampling periods, noise suppression is higher. Because of range weighting, the Doppler spectrum contains energy at frequencies corresponding to all of the velocities detected along the beam, weighted by $W(F, R)$. After subtracting the mean background noise spectrum, only frequency bins containing energy in excess of some multiple of the standard deviation of the remaining noise floor are considered in the final Doppler spectrum [94]. In this investigation, threshold values of either 3 or 5 standard deviations of the noise floor are used, depending on the lidar scan. Once the background noise is removed from the Doppler spectrum, a single value of the line-of-sight velocity detected by the lidar is estimated. As outlined in Section 4.1.2, the more robust approach of identifying the velocity representing the median value of the energy in the Doppler spectrum is used. More information about estimating the line-of-sight velocity from a Doppler spectrum is provided in Angelou *et al.* [94].

Once the line-of-sight velocities for the three lidars focusing at the same point in space are known, the measurements are used to estimate the orthogonal u, v, and w wind components of interest. This estimation is achieved by solving the inverse detection problem to find the u, v, and w components that would have produced the three line-of-sight measurements. In reality, due to range-weighting, the line-of-sight measurements are only approximations of the true line-of-sight

velocities at the focus point. However, by ignoring the range-weighting effect in (4.2), the u, v, and w components at the common focus point can be solved for using

$$\begin{bmatrix} u \\ v \\ w \end{bmatrix} = - \begin{bmatrix} \ell_{x,1} & \ell_{y,1} & \ell_{z,1} \\ \ell_{x,2} & \ell_{y,2} & \ell_{z,2} \\ \ell_{x,3} & \ell_{y,3} & \ell_{z,3} \end{bmatrix}^{-1} \begin{bmatrix} u_{\ell,1} \\ u_{\ell,2} \\ u_{\ell,3} \end{bmatrix} \tag{A.1}$$

where $[\ell_{x,i}, \ell_{y,i}, \ell_{z,i}]$ and $u_{\ell,i}$ are the beam direction unit vector and measured line-of-sight velocity, respectively, for lidar i. It is desirable to choose lidar positions and scan patterns that result in a well-conditioned matrix in (A.1) to minimize the sensitivity of the u, v, and w component estimates to errors in the line-of-sight measurements and beam direction vectors.

A.1.4 Lidar scan scenarios

Three lidar scan patterns were used to measure wind velocities in the induction zone: two used to measure the mean velocity components upstream of the rotor and one used to measure turbulence characteristics. The lidar positions were chosen to allow measurements for a 60° range of wind directions, up to 30° away from an ideal wind direction. A 60° range of acceptable wind directions allows a trade-off between optimizing for a single wind direction and enabling enough data to be collected during the campaign given the variability in wind direction. After analyzing the distribution of wind directions encountered by the V27, it was decided to allow measurements for directions from 221° to 281°, with 251° as the ideal direction. In practice, only lidar scans intended for wind directions between 251° and 280° were performed during the campaign (see Fig. A.1).

When choosing the lidar positions, an additional guideline was the desire to avoid measuring line-of-sight velocities close to 0. To allow the ability to distinguish between negative and positive velocities, the Doppler spectrum detected by a WindScanner lidar is shifted by 27 MHz using an acousto-optic modulator (AOM) so that frequencies from 0 to 27 MHz represent negative velocities and frequencies from 27 MHz to 50 MHz represent positive velocities [94]. However, low-frequency noise caused by laser light leakage in the lidar optics and mechanical vibrations in the optical fiber, which is shifted by the AOM to the frequency band near 27 MHz, makes it difficult to detect

velocities between approximately -0.5 m/s and 0.5 m/s. Therefore, the lidar positions and scan patterns were chosen to avoid measuring perpendicular to the intended mean wind directions. To minimize volume averaging due to range weighting, yielding measurement scans with higher spatial resolution, the lidars were placed as close to the intended scan pattern locations as possible while avoiding measurements perpendicular to the mean wind direction. To minimize the lidar focus distances, resulting in less range weighting, only locations up to roughly 1.5 D upstream of the turbine were scanned. Furthermore, only the area upstream of the left side of the rotor (when looking upstream) was measured, under the assumption that the behavior of the induction zone is symmetric about the rotor center. The chosen lidar positions are shown in Fig. A.1 (b). Lidar 1 is positioned upstream and to the right of the intended scan area, lidar 2 is positioned upstream and to the left, and lidar 3 is located downstream of the scan area resulting in a diversity in measurement angles at all points throughout the scan. While the lidar positions were not chosen to produce measurement matrices (see (A.1)) with condition numbers above a specific threshold, the diverse measurement angles help reduce the sensitivity of the u, v, and w component estimates to measurement and beam direction errors.

The majority of the lidar scans performed during the measurement campaign were horizontal planes at hub height extending from 0.1 D (2.7 m) downstream of the rotor to 1.6 D upstream and from 1/8 D beyond the left edge of the rotor, when looking upstream, to 1/8 D to the right of the hub. The scan is performed by repeating a 10-second pattern covering the area of interest, which is plotted in Fig. A.4 (a) for a wind direction, and therefore x axis direction, of 251°. Note the positions of the lidars in Fig. A.4, plotted as red points, which result in no measurements perpendicular to the wind direction of 251°. For wind directions far enough above 251°, however, lidar 2 measures perpendicular to the wind direction during portions of the scan. Measurement periods with such wind directions are still analyzed in this study, but the distance upstream of the rotor for which data can be analyzed is limited. In terms of the rotor diameter D, the 10-second

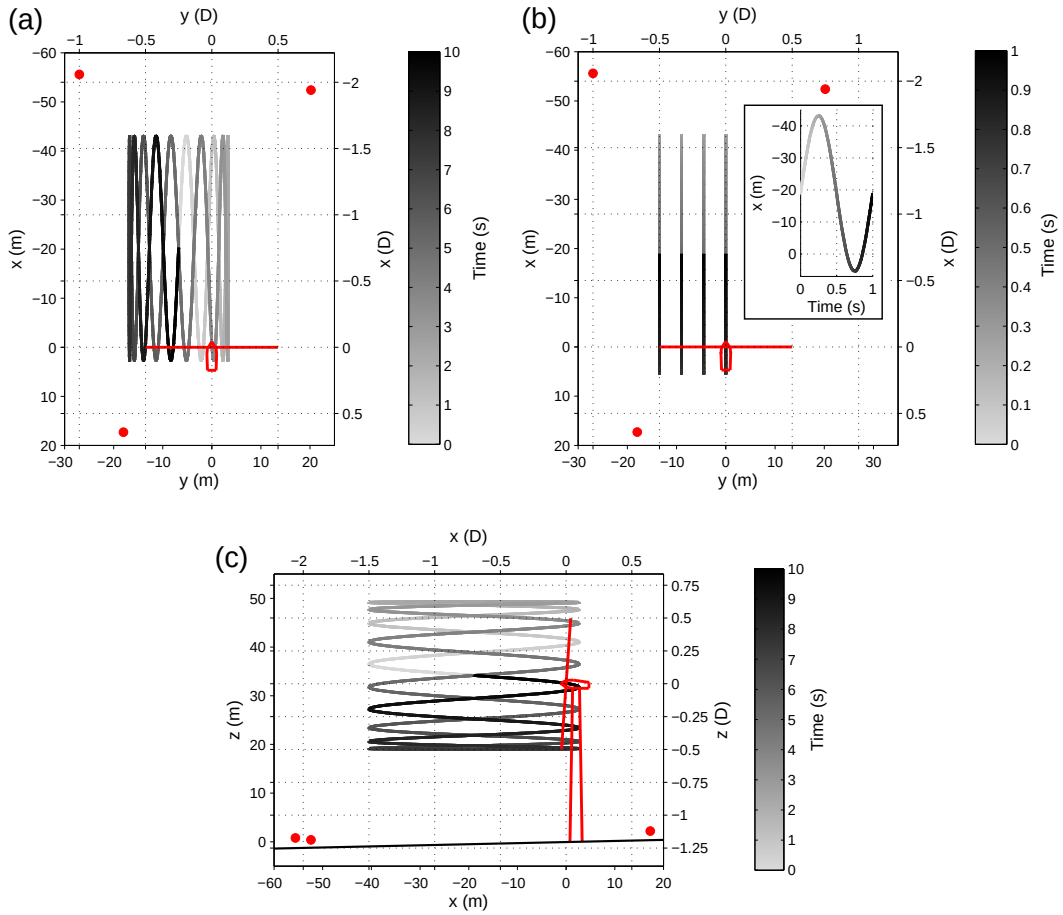

Figure A.4: Lidar scan patterns used to measure the induction zone. (a) Top view of horizontal scan plane at hub height. (b) Top view of longitudinal line scans at hub height for radial positions at 0, 1/6, 1/3, and 1/2 D. An inset plot shows the longitudinal scan position as a function of time. (c) Side view of vertical scan plane located at the center of the rotor in the transverse direction ($y = 0$). The lidar positions are indicated by the red points.

scan is defined as

$$\vec{x}\,(t) = \begin{cases} x\,(t) &= -0.85D\sin\left(2\pi t\right) - 0.75D \\ y\,(t) &= 0.375D\sin\left(2\pi t/10\right) - 0.25D \\ z\,(t) &= 32.5 \text{ m}, \end{cases} \tag{A.2}$$

where sinusoidal scan positions are used to reduce the acceleration of the WindScanners' prism and focus motors. This scan pattern is used to form 10-minute mean values of the wind velocities to reveal the behavior of the longitudinal (u), radial, and tangential wind speeds in the induction zone. The radial wind speed is defined as the wind speed component oriented away from the rotor

center, perpendicular to the longitudinal direction, and the tangential wind speed is defined as the component of the wind aligned with the rotational direction of the rotor, i.e., perpendicular to the radial component in the yz plane. Thus, for the horizontal plane scan, the radial wind speed is equivalent to the v component and the tangential wind speed is equivalent to the w component. All scan patterns described in this section can be adjusted so that the x axis is aligned with any wind direction between 221° and 281°.

A second scan pattern, consisting of a vertical scan plane, was used to measure mean velocities in the induction zone as well. The scan plane extends from 0.1 D downstream of the rotor to 1.5 D upstream of the rotor and from the bottom of the rotor to 1/8 D above the top of the rotor, located at the center of the rotor in the transverse direction, i.e., intersecting the hub position. This 10-second vertical scan pattern, which allows measurements upstream of the entire rotor diameter, is shown in Fig. A.4 (c) and is defined as

$$\vec{x}\left(t\right) = \begin{cases} x\left(t\right) &= -0.8D\sin\left(2\pi t\right) - 0.7D \\ y\left(t\right) &= 0 \\ z\left(t\right) &= 0.5625D\sin\left(2\pi t/10\right) + 0.0625D + 32.5 \text{ m}. \end{cases} \tag{A.3}$$

As with the horizontal scan plane, this 10-second pattern is repeated to form 10-minute averages of the measured inflow.

The third scan pattern used during the measurement campaign is designed to measure the turbulence characteristics in the induction zone. Similar to the horizontal scan plane, this scan pattern measures the wind upstream of the left side of the rotor at hub height, but along lines perpendicular to the rotor plane extending from 0.2 D downstream of the rotor to 1.6 D upstream at different radial positions. The line scans are performed at radial distances of 0 (the hub location), 1/6 D, 1/3 D, and 1/2 D. Each complete line scan, pictured in Fig. A.4 (b), is a 1-second sinusoidal pattern defined for radial positions $i \in \{1, 2, 3, 4\}$ as

$$\vec{x}\left(i,t\right) = \begin{cases} x\left(t\right) &= -0.9D\sin\left(2\pi t\right) - 0.7D \\ y\left(i,t\right) &= -\left(i-1\right)D/6 \\ z\left(t\right) &= 32.5 \text{ m}. \end{cases} \tag{A.4}$$

During the field measurements, the 1-second line scans were repeated for 2.5 minutes at each radial position before advancing to the next position, forming a sequence which was repeated every 10 minutes. In contrast to the horizontal and vertical plane scans, these line scans were used to determine wind velocity time series, instead of mean values. Time series at various longitudinal distances from the rotor plane are formed by grouping the measurements by their x positions using a bin size of 1 m and interpolating the resulting data for each bin to form 1 Hz time series.

A.2 Results: Radial and Longitudinal Dependence of Mean Wind Speeds in the Induction Zone

Data were collected using the three different scan patterns from mid March to early May 2014 at the Risø campus. In order to identify acceptable data for analysis, all 10-minute periods where the intended wind direction of the lidar scan differs by the mean wind direction reported by the met mast by more than 15° were discarded, leaving roughly 35 hours of acceptable measurements. For the horizontal scan at hub height, six 10-minute periods were chosen for analysis when the turbine was running, with wind speeds representing axial induction factors between $\sim$0.25 ($U = \sim$6.89 m/s) and the minimum induction factor that occurred during all acceptable scan periods ($a = \sim$0.041, $U = \sim$16.29 m/s), according to the estimated induction factor curve in Fig. A.3 (b), in wind speed intervals of approximately 1–3 m/s. By visually inspecting the met mast and lidar data, a 10-minute period for each desired wind speed interval was selected by identifying the period with the lowest error between mean wind direction and the chosen lidar scan direction, while maintaining low wind speed and direction variability. Because very few lidar scans were acquired using the vertical plane scan and line scan patterns, only a small number of scan periods for these categories are analyzed and results for a wide range of mean wind speeds are not included. A summary of all the lidar scans that were chosen for analysis in this study is provided in Table A.2. Measurement cases 1–7 are 10-minute horizontal plane scans chosen from the collected data to provide a wide range of mean wind speeds and thus axial induction factors. Case 7 consists of measurements performed when the V27 was stopped, providing a reference scan. Case 8 contains one of the few satisfactory

Table A.2: Summary of lidar measurement cases. Cases 1–8 consist of 10-minute measurement periods while cases 9–16 are 2.5-minute scans. Wind direction is calculated using the mean lidar-measured wind speed values as far upstream of the rotor as possible. Turbulence intensity (TI) and wind direction standard deviation are calculated using met tower measurements at a height of 32 meters. Case 7 was performed with the turbine stopped.

Case	Date/Time (all 2014)	Scan Type	Scan Dir.	$\hat{U}_\infty$	$\hat{a}$	Wind Dir.	TI	Wind Dir. Std. Dev.
1	3/17 10:57	xy plane	275°	16.29 m/s	0.041	289.5°	8.9%	4.8°
2	3/18 12:00	xy plane	251°	8.93 m/s	0.18	254.8°	9.0%	5.1°
3	3/18 14:09	xy plane	251°	10.01 m/s	0.16	260.2°	11.0%	5.0°
4	3/19 13:32	xy plane	260°	11.49 m/s	0.12	259.1°	9.4%	4.9°
5	3/19 16:18	xy plane	260°	13.26 m/s	0.085	263.4°	12%	6.1°
6	3/21 10:44	xy plane	251°	6.89 m/s	0.25	250.8°	10.6%	5.0°
7	3/21 12:09	xy plane	251°	5.67 m/s	0	249.8°	15.2%	7.0°
8	4/30 22:19	xz plane	270°	7.17 m/s	0.25	269.8°	13.6%	6.7°
9	5/07 14:05	line, y = -4.5 m	260°	6.23 m/s	0.24	262.5°	12.8%	7.2°
10	5/07 14:08	line, y = -9 m	260°	6.25 m/s	0.24	260.1°	11.8%	7.0°
11	5/07 14:10	line, y = -13.5 m	260°	5.95 m/s	0.23	264.1°	10.4%	5.5°
12	5/07 14:13	line, y = 0	260°	6.15 m/s	0.23	259.3°	7.8%	4.4°
13	5/07 16:03	line, y = -4.5 m	275°	7.60 m/s	0.22	281.2°	10.5%	5.0°
14	5/07 16:05	line, y = -9 m	275°	7.49 m/s	0.22	277.8°	7.0%	5.8°
15	5/07 16:08	line, y = -13.5 m	275°	8.09 m/s	0.20	275.9°	10.9%	6.0°
16	5/07 16:10	line, y = 0	275°	7.40 m/s	0.23	278.6°	9.4%	6.5°

10-minute measurement periods using the vertical scan plane. Cases 9–16 consist of 2.5-minute line scan periods. Cases 9–12 represent successive line scans at radial positions of 1/6 D (y = -4.5 m), 1/3 D (y = -9 m), 1/2 D (y = -13.5 m), and at the hub location (y = 0) as do cases 13–16, but for higher wind speeds. The similar sequences of scan cases 9–12 and 13–16 are both analyzed to help confirm the identified trends, since each case contains only a short measurement period.

The scan direction column in Table A.2 indicates the wind direction that the x axes of the scan patterns were aligned with in anticipation of the true wind direction. The wind direction

column contains the actual mean wind directions present during the scan periods, calculated from the lidar measurements. It is difficult to determine the true freestream mean wind speeds from the lidar measurements, given that the farthest measurement locations from the turbine are roughly 1.5 D upstream of the rotor, within the expected extent of the induction zone. Furthermore, there are occasionally significant discrepancies between the mean wind speeds measured by the nearby met mast and those detected by the lidars far upstream of the turbine. Therefore, the mean wind speeds (under the $\hat{U}_\infty$ column) are estimated by solving the vortex sheet theory formula presented in Medici *et al.* [53] giving the velocities upstream of the rotor center, plotted in Fig. 3.9, for the freestream velocities using the measured wind speeds at either x = -1 D or x = -1.5 D and the estimated axial induction factors. The estimated axial induction factors ($\hat{a}$) are based on the induction factor curve plotted in Fig. A.3 and the mean velocities measured at x = -1 D or x = -1.5 D. After applying the vortex sheet theory formula the estimated freestream velocities only differ from the values at x = -1 D or x = -1.5 D by up to 3% or 1%, respectively, however. Finally, the u component turbulence intensity and wind direction standard deviation columns contain values measured at a height of 32 m on the met tower 2.7 D to the west of the turbine. Measurement periods with low wind direction standard deviations were selected for analysis to keep the instantaneous wind directions close to the lidar scan direction.

A.2.1 Horizontal scan plane at hub height

Fig. A.5 shows the 10-minute mean longitudinal (U), radial (V), and tangential (W) velocities measured in the horizontal scan plane at hub height for cases 5, 6, and 7. In order of increasing mean freestream wind speed U_∞, case 7 has an estimated wind speed of 5.67 m/s, with the wind turbine stopped to provide a reference measurement case free of rotor induction effects, case 6 has a value of $\hat{U}_\infty$ = 6.89 m/s with a relatively high estimated induction factor of $\hat{a}$ = 0.25, and case 5 contains an estimated freestream wind speed of $\hat{U}_\infty$ = 13.26 m/s with a relatively low $\hat{a}$ value of 0.085. The velocity plots are formed by grouping the measurements by their (x, y) positions using 1 m-by-1 m bins and averaging all Doppler spectra belonging to each bin. Line-of-sight velocities are

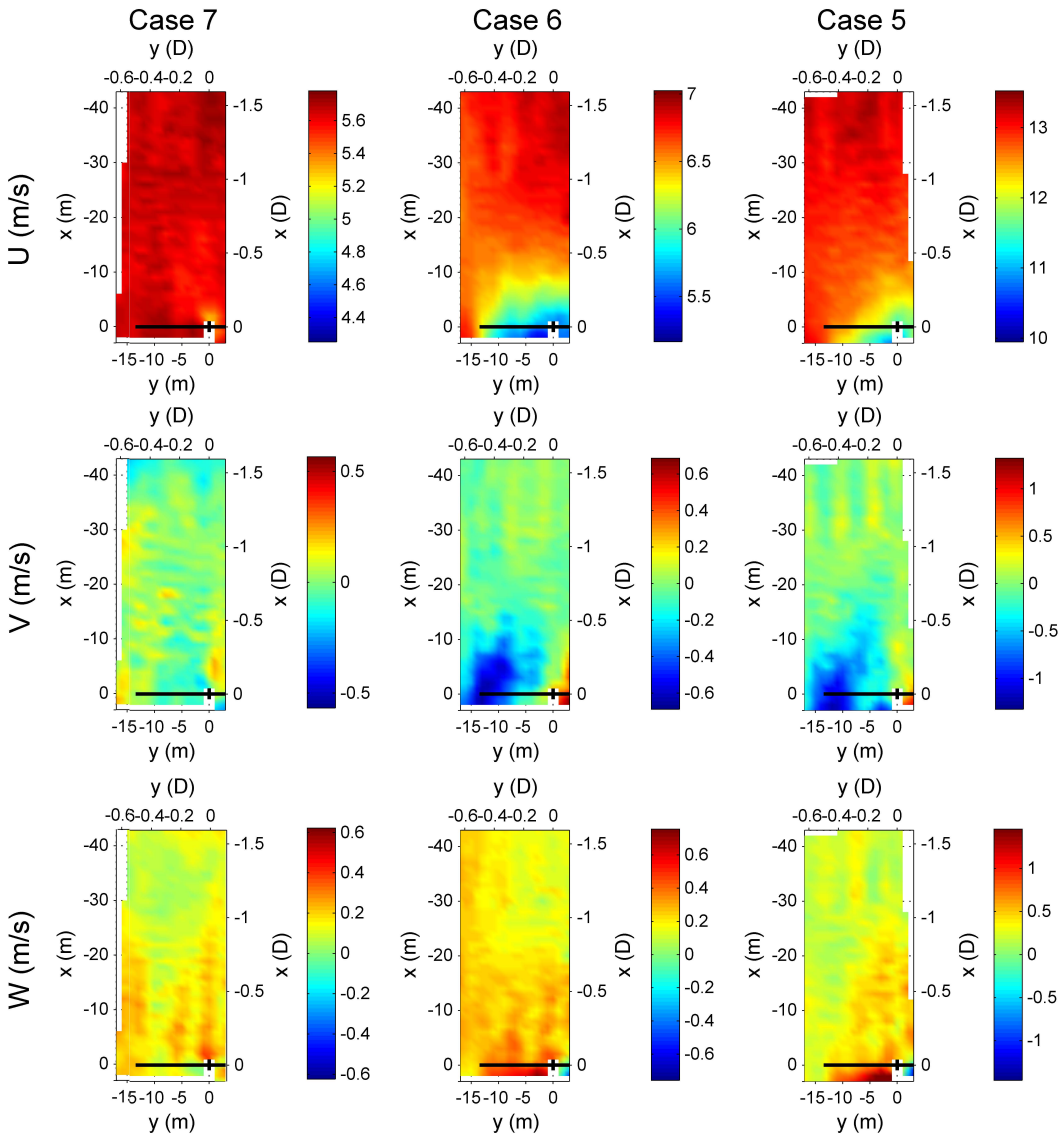

Figure A.5: Measured U, V, and W wind components (top, middle, and bottom rows, respectively) for a horizontal scan plane at hub height for measurement cases 7 ($\hat{U}_\infty = 5.67$ m/s, turbine stopped), 6 ($\hat{U}_\infty = 6.89$ m/s), and 5 ($\hat{U}_\infty = 13.26$ m/s).

determined from the averaged Doppler spectra at each of the bin locations and bilinear interpolation in the xy plane is used to find values at bins in the scan plane for which no measurements were acquired during the scan period. The line-of-sight velocities at each bin location in the xy plane are then transformed to the U, V, and W components using (A.1). By averaging the Doppler spectra prior to determining the velocities, the background spectral noise is significantly reduced. Measurements corresponding to lidar beam directions pointing at the turbine, including the blades,

are detected and removed before calculation of the velocities. Note that the scan patterns plotted in Fig. A.5 are rotated so that the x axis is aligned with the true wind direction rather than the original scan direction.

For measurement case 7, with the turbine stopped, there are no drastic variations in the U, V, and W components within the scan plane, aside from a drop in the longitudinal wind speed near the nacelle. To allow easier visual comparison between the relative velocity variations for the three cases shown in Fig. A.5, the limits of the color axes are identical across each row after normalization by the estimated mean freestream wind speed $\hat{U}_\infty$. For case 6, significant longitudinal velocity deficits occur in the induction zone, especially within 0.5 D of the rotor. The U component velocity reductions are present in case 5 as well, although, as expected given the lower induction factor, they are less drastic and are also more concentrated near the center of the rotor, possibly due to lower induction at the outboard region of the blades. Consistent with the expected expansion of the wind inflow around the rotor disk, illustrated in Fig. 3.12 (b), the radial V components are negative (directed away from the rotor center) near the edge of the rotor for cases 5 and 6. Thus the mean wind direction changes in that region, deflecting away from the rotor center. Significant positive vertical W components can be seen behind the rotor when the turbine is operating. This behavior is expected because the blades are traveling downward on the left half of the rotor and the induced tangential velocities should be opposite the direction of rotor rotation [7]. For all three cases in Fig. A.5 the mean W component upstream of the rotor is slightly positive (0.1 m/s for case 7, 0.18 m/s for case 6, and 0.2 m/s for case 5), likely due to the gently sloping nature of the terrain between the fjord and the V27. The vertical wind speeds do not vary significantly upstream of the rotor, however, and are therefore not analyzed in depth in this study.

The velocity plots in Fig. A.5 reveal longitudinal stripe patterns which are artifacts of the lidar scan process. There are two reasons why these stripes appear. First of all, there are very minor timing errors between the lidar motor position values, used to determine the scan positions, and the corresponding Doppler spectra. This results in small offsets between the detected velocities and their reported locations in the scan plane, and has the effect of causing the detected velocities

to either lead or lag the actual measurement positions. As can be seen in Fig. A.4 (a) and (c), there are alternating regions of the scan plane where the lidar focus positions are moving in either the positive x direction or in the negative x direction. The line-of-sight velocities detected by the lidars tend to either increase or decrease along the x direction due to the changing lidar beam angles. As a result, depending on the x direction the lidar scan is moving in, the lead or lag in the velocity measurements will cause the detected line-of-sight velocities to be either slightly higher or slightly lower than their true values, on average. These errors are then transferred to the calculated u, v, and w components. The motor position timing errors are minimized as much as possible however, to within the sampling period of 10 ms, and therefore cause only minor artifacts in the measurements. A second, unavoidable reason for the artifacts in the velocity plots is due to the lidars measuring different areas of the scan plane at different times. Although all regions in the scan pattern are sampled every 10 seconds, the regions are measured at different times. Due to the turbulent nature of the inflow, the 10-minute averages of the velocities are slightly different depending on exactly when the velocities are sampled during the 10-minute period. The artifacts caused by different sampling times for different regions cannot be avoided, but are also relatively small when using a 10-minute measurement period.

Measurement cases 1–7 are used to determine how the behavior of the induction zone changes as the turbine's induction factor decreases. U velocities normalized by $\hat{U}_\infty$, determined from the horizontal plane scans, are plotted as a function of longitudinal distance from the rotor in Fig. A.6 for six different radial positions from the hub location to 1/8 D beyond the edge of the rotor. Cases 6, 2, 3, 4, 5, and 1 represent wind speeds from 6.89 m/s to 16.29 m/s with estimated axial induction factors of 0.25, 0.18, 0.16, 0.12, 0.085, and 0.041, respectively, while case 7, with the turbine stopped, acts a reference case. Note that velocities could only be calculated for case 1 up to 19 m upstream of the rotor because the actual wind direction of nearly 290° causes lidar 2 to measure close to perpendicular to the wind direction for greater longitudinal distances, thus making it difficult to estimate the low line-of-sight velocities. In general, the velocity reductions are largest at the rotor center as well as the radial position of 1/8 D and become smaller towards the edge

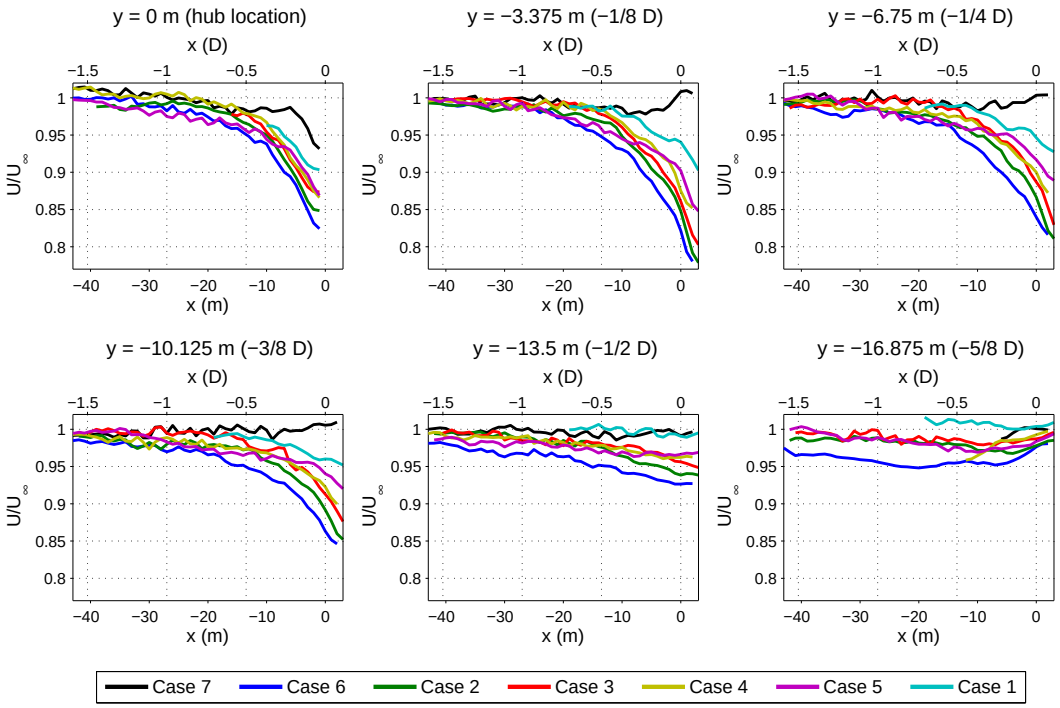

Figure A.6: Measured U wind components as a function of radial and longitudinal position for measurement cases 7 ($\hat{U}_\infty = 5.67$ m/s, turbine stopped), 6 ($\hat{U}_\infty = 6.89$ m/s), 2 ($\hat{U}_\infty = 8.93$ m/s), 3 ($\hat{U}_\infty = 10.01$ m/s), 4 ($\hat{U}_\infty = 11.49$ m/s), 5 ($\hat{U}_\infty = 13.26$ m/s), and 1 ($\hat{U}_\infty = 16.29$ m/s). For each case, the velocities are normalized by the corresponding estimated freestream longitudinal wind speed.

of the rotor until they are no longer noticeable beyond the rotor disk. The velocity deficits are a strong function of the turbine's induction factor, with a maximum deficit at the rotor plane of 20% U_∞ occurring for case 6, which has the highest estimated induction factor. The measurements for case 1, with the lowest estimated induction factor, reveal velocity reductions of only 6% U_∞ at the rotor plane. When the turbine is stopped there is still a slight reduction in wind speed upstream of the rotor center due to the presence of the nacelle.

Similar to Fig. A.6, the radial V velocities for cases 1–7, normalized by $\hat{U}_\infty$, are plotted as a function of longitudinal position in Fig. A.7 for different radial positions. Significant changes in the V velocities due to the induction zone begin occurring between 0.5 D and 0.75 D upstream of the rotor and are noticeable at radial distances between 1/8 D and 5/8 D. The maximum magnitude of the radial V component occurs at the edge of the rotor, where the magnitude of V for case 6,

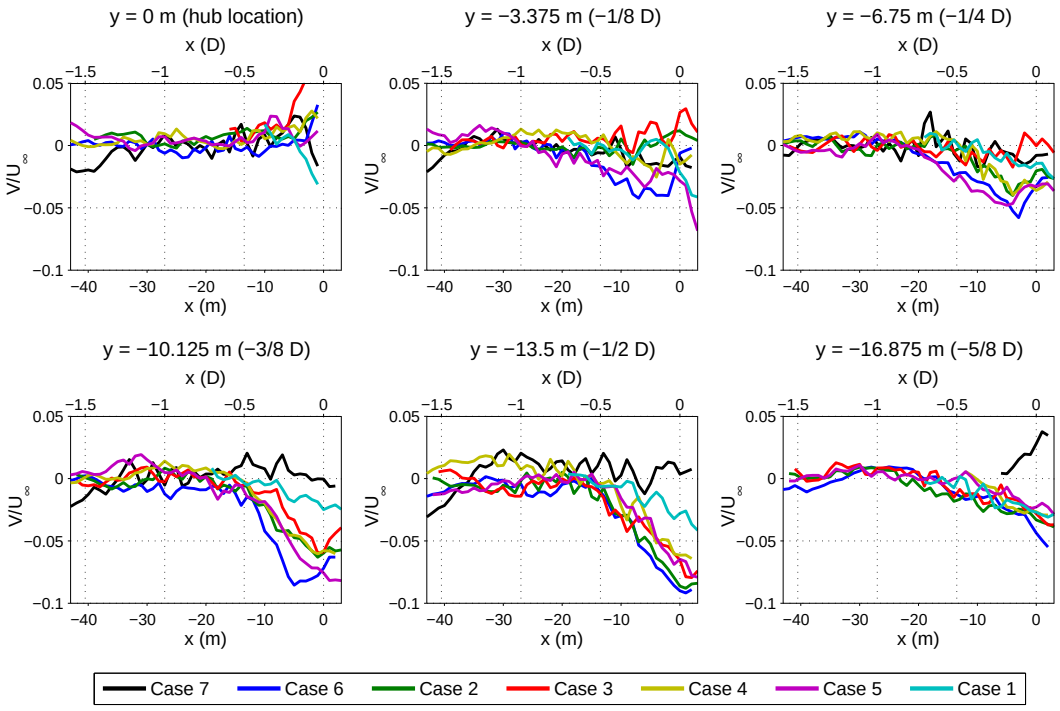

Figure A.7: Measured V wind components as a function of radial and longitudinal position for measurement cases 7 ($\hat{U}_\infty = 5.67$ m/s, turbine stopped), 6 ($\hat{U}_\infty = 6.89$ m/s), 2 ($\hat{U}_\infty = 8.93$ m/s), 3 ($\hat{U}_\infty = 10.01$ m/s), 4 ($\hat{U}_\infty = 11.49$ m/s), 5 ($\hat{U}_\infty = 13.26$ m/s), and 1 ($\hat{U}_\infty = 16.29$ m/s). For each case, the velocities are normalized by the corresponding estimated freestream longitudinal wind speed.

with the highest induction factor, is 9% U_∞ at the rotor plane. In general, the magnitude of the V component decreases for lower induction factors with only very minor radial velocities equal to 3% U_∞ occurring at the rotor plane for case 1, with the lowest induction factor. However, this trend is not as strong as with the U velocities. For example, at a radial position of 3/8 D case 5, which has a low induction factor of 0.085, shows V magnitudes almost as high as case 6. Because the V component magnitudes are significantly smaller than the U component deficits, they may be more difficult to accurately measure, however. In addition, the yaw angle of the turbine does not perfectly track the wind direction; potentially time-varying yaw error during the 10-minute measurement periods could also contribute to variations in the V component estimates.

By combining the U and V velocities measured in the horizontal scan planes, the wind direction changes in the induction zone can be determined. Fig. A.8 shows streamlines formed

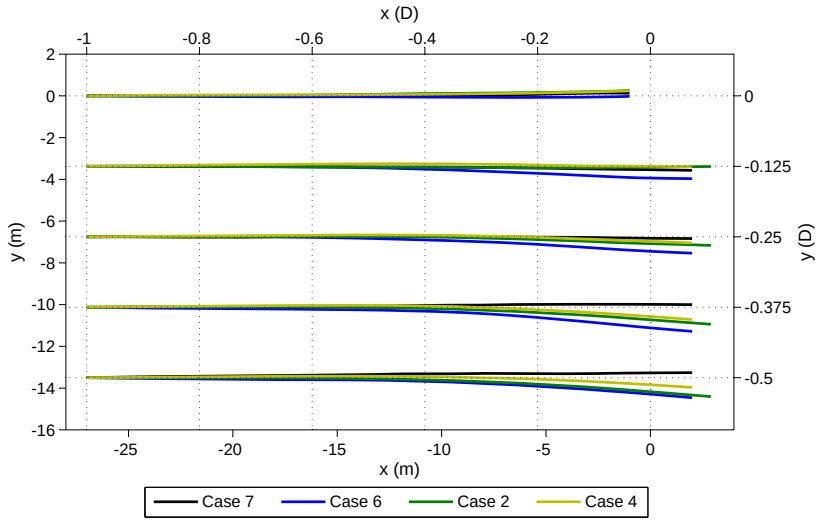

Figure A.8: Streamlines of the measured U and V components for measurement cases 7 ($\hat{U}_\infty = 5.67$ m/s, turbine stopped), 6 ($\hat{U}_\infty = 6.89$ m/s), 2 ($\hat{U}_\infty = 8.93$ m/s), and 4 ($\hat{U}_\infty = 11.49$ m/s).

from the U and V velocities starting at 1 D upstream of the rotor for four measurement cases. As expected, the wind directions are relatively unchanged for case 7, with the turbine stopped. The direction changes are greatest for case 6 with an estimated induction factor of 0.25. Near the edge of the rotor the wind direction changes the most, such that a particle released 1 D upstream of the rotor at radial position 3/8 D will, on average, end up nearly 0.04 D closer to the edge of the rotor when it reaches the rotor plane. For the remaining two cases the wind direction changes along the streamlines decrease as the estimated induction factor decreases ($\hat{a} = 0.18$ for case 2 and 0.12 for case 4).

A.2.2 Vertical scan plane

A small amount of data was collected using the vertical plane scan pattern. Velocities calculated from a 10-minute measurement period with an estimated hub-height freestream wind speed of 7.17 m/s, with a wind direction that was very close to the scan direction (case 8), are shown in Fig. A.9. Velocities are only shown for x distances up to 30 m upstream of the rotor because the wind direction of roughly 270° caused lidar 2 to once again measure close to perpendicular to the wind direction for locations farther from the rotor, making the velocities at those positions

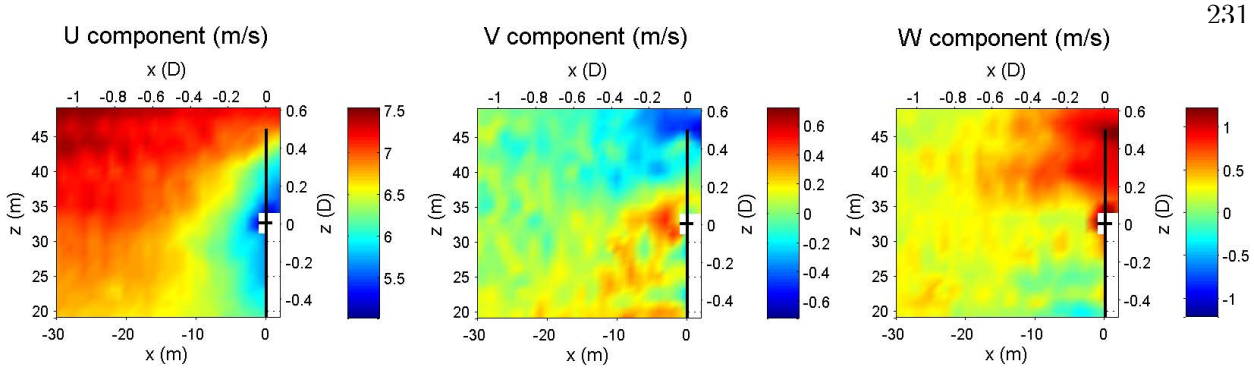

Figure A.9: Measured U, V, and W wind components for a vertical xz scan plane at the center of the rotor for measurement case 8 ($\hat{U}_\infty = 7.17$ m/s).

difficult to estimate. As shown in the U component plot, the velocity deficits in the induction zone are present upstream of the entire diameter of the rotor. The velocities at the same radial positions above and below the hub are different due to the wind shear present across the rotor plane extending into the induction zone. Due to the slightly negative V velocities above hub height, it appears that there is wind veer across the rotor plane causing a slight change in wind direction with height. But the source of the strong V components near the top of the rotor disk, as well as the source of the positive V components near the hub location, is unknown. For the vertical scan plane orientation, the w component represents the radial wind speed instead of v, and therefore strong vertical W velocities are present near the top of the rotor disk, indicating expansion of the wind inflow around the rotor, as was seen in the horizontal scan results. However, even though there are positive mean vertical components due to the sloping of the terrain ($W = 0.22$ m/s at hub height), the radial wind speed magnitudes are unexpectedly very low near the lower edge of the rotor disk. This could possibly be caused by the lower freestream velocities near the bottom of the rotor as well as the presence of the ground 20 m below the bottom of the rotor plane.

A.3 Results: Turbulence Statistics in the Induction Zone

Measurement cases 9–16 are used to determine how turbulence is affected by the induction zone. Specifically, the standard deviations of the u, v, and w wind components are calculated for

different distances upstream of the rotor at different radial positions at hub height. Cases 9–12 consist of consecutive 2.5-minute line scans performed at radial positions of -4.5 m (1/6 D), -9 m (1/3 D), -13.5 m (1/2 D), and 0 (hub location), respectively. Cases 13–16 represent the same sequence of scans but at a later time with a different wind direction and higher wind speeds. For both line scan sequences, the estimated induction factors are relatively high, between 0.2 and 0.24. To calculate the turbulence standard deviation values, a single 1 Hz time series is formed for each 1 m-wide x position bin between x = -27 m (1 D upstream of the rotor) and $x = 0$ by interpolating between all of the lidar measurements occurring in each respective bin. Due to the lidar scan directions intersecting with the nacelle for scan positions close to the turbine, results for scan cases 12 and 16, with $y = 0$, are only analyzed at longitudinal distances beyond x = -3 m.

Examples of the time series calculated from the lidar line scans in case 13 are provided in Fig. A.10. The time-varying u', v', and w' components are plotted for five different distances upstream of the rotor at radial position y = -4.5 m where zero-mean u', for example, is equal to $u - U$. Therefore, the reduction in the mean U wind speed approaching the rotor is not visible (although it is shown in Fig. A.12). To allow easier comparison of the turbulence at the different x positions, the signals in Fig. A.10 are shifted in time by time lag values that produce the highest cross correlation with the wind speeds at x = -14 m. In general, the large scale structures in the turbulence remain unchanged as the wind passes through the induction zone. At the rotor plane, however, small time scales of the turbulence are altered; more high frequency content is added to the turbulence. This is likely due to the altering of the wind speeds caused by rotor induction at the blade passage frequency of 2.15 Hz. The turbulence in the radial v component appears to change the most close to the rotor plane due to rotor induction.

Statistics for the wind speed time series calculated for cases 9–12 and 13–16 are shown in Figs. A.11 and A.12, including the mean values and standard deviation values calculated at 1 m intervals between x = -27 m and $x = 0$. The mean velocity plots reveal slightly different conditions during each 2.5-minute line scan for both sequences, but for each sequence the four mean wind directions deviate by less than 6°. The differences in mean freestream wind speed within the two

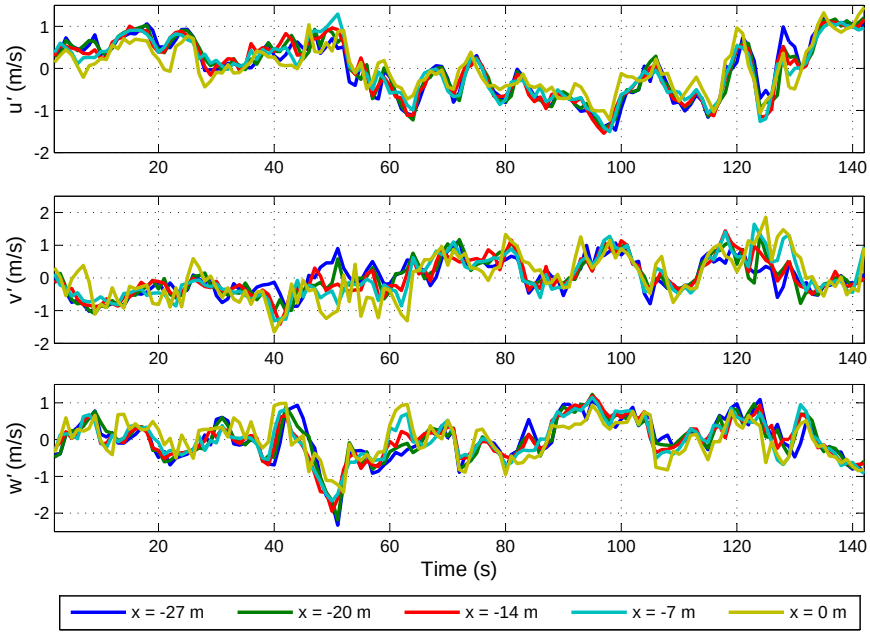

Figure A.10: Time series of measured longitudinal, transverse, and vertical wind speeds in the induction zone upstream of radial position y = -4.5 m (-1/6 D) for measurement case 13. Time series are shown for longitudinal positions x = -27 m (-1 D), x = -20 m (-0.74 D), x = -14 m (-0.52 D), x = -7 m (-0.26 D), and $x = 0$. All time series are plotted with their mean values subtracted and are time-shifted to correct for their different positions along the mean wind direction to allow for easier comparison.

scan sequences are primarily caused by the use of different averaging periods. As revealed by the presence of positive V components close to the rotor in case 9 and negative W components upstream of the rotor in case 10, a 2.5-minute averaging period is not as capable of revealing mean wind speed trends as the 10-minute averaging period used for cases 1–8. The measurements in cases 9–12 in Fig. A.11 show that the standard deviation of the longitudinal u component is relatively unaltered as the wind travels through the induction zone, with a slight decrease close to the rotor at radial positions $y = 0$ and y = -4.5 m. In general, the standard deviations of the radial v component and vertical w component, on the other hand, increase close to the rotor plane. Fig. A.12, which contains measurement results for cases 13–16, shows a stronger decrease in u component standard deviation close to the rotor for all four radial positions investigated. Similar to cases 9–12, the standard deviations of the v component also increase as the wind inflow travels toward the rotor. The w component standard deviations remain relatively unchanged in the induction zone.

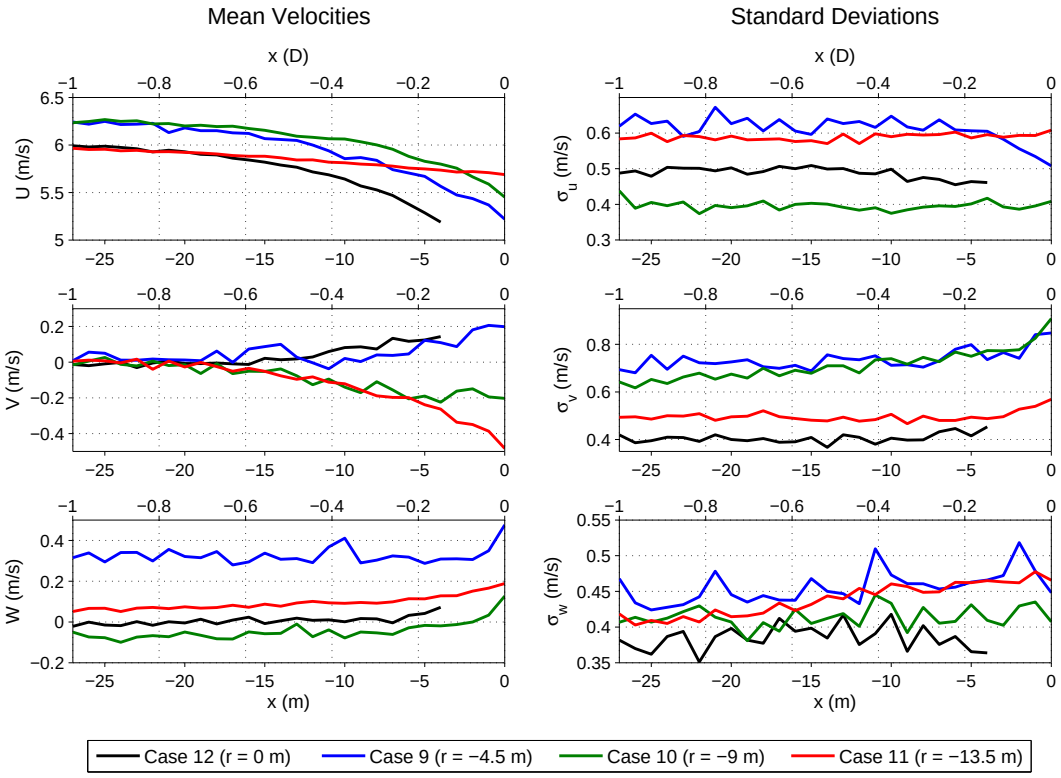

Figure A.11: Mean and standard deviation of the measured longitudinal, transverse, and vertical wind speeds upstream of radial positions $y = 0$ (hub location, case 12), y = -4.5 m (-1/6 D, case 9), y = -9 m (-1/3 D, case 10), and y = -13.5 m (-1/2 D, case 11).

It is difficult to infer the exact behavior of turbulence in the induction zone from the relatively short time series in cases 9–16. However, the u component standard deviations decrease slightly close to the rotor for the majority of the measurement periods. The greatest reductions occur close to the rotor center. It appears that the velocity reductions present in the mean wind speeds extend to the time-varying part of the wind inflow as well. All eight cases indicate that the radial v component standard deviation increases as the inflow moves closer to the rotor. The expansion of the inflow around the rotor disk seems to create larger variations in the radial component. It is more difficult to draw conclusions about the w component turbulence. Cases 9–11 reveal a slight increase in the standard deviation close to the rotor while cases 12–16 show very little variation in the induction zone. Thus the w component turbulence does not appear to change significantly as the inflow approaches the rotor.

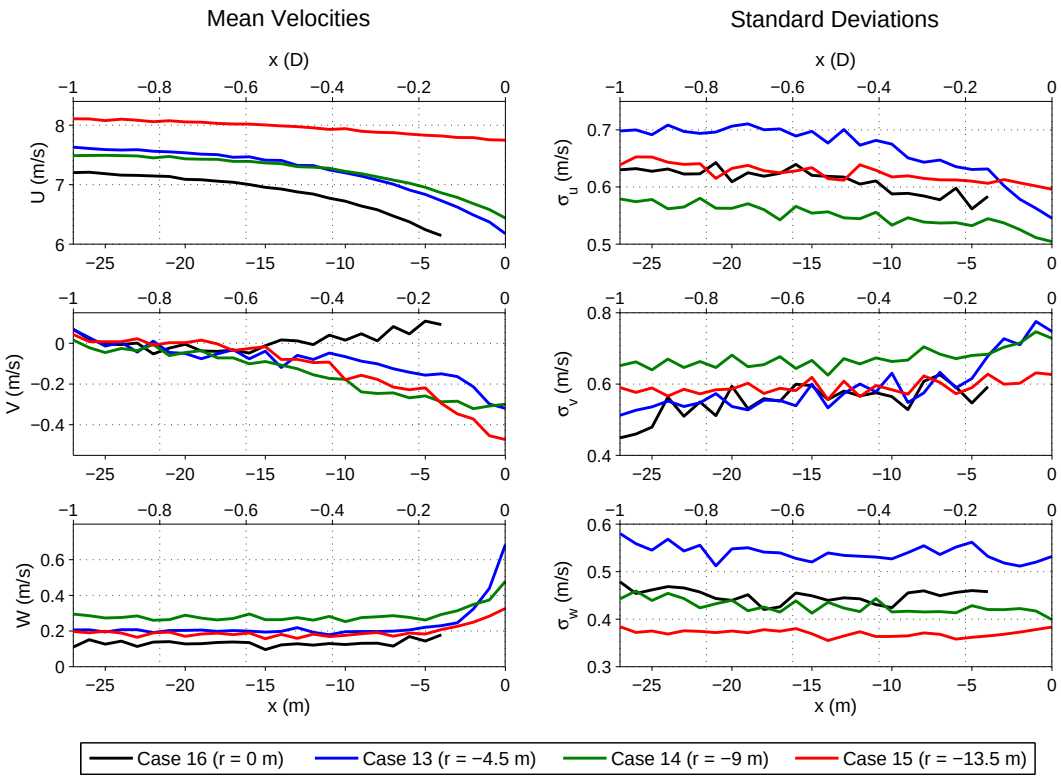

Figure A.12: Mean and standard deviation of the measured longitudinal, transverse, and vertical wind speeds upstream of radial positions $y = 0$ (hub location, case 16), y = -4.5 m (-1/6 D, case 13), y = -9 m (-1/3 D, case 14), and y = -13.5 m (-1/2 D, case 15).

Complicating the estimates of turbulence standard deviation is the fact that the lidar spatially averages the wind speeds along the beam, as described by (4.2) and (4.3). The range weighting along the beam can filter out small-scale turbulent fluctuations in the measurements. Additionally, the lidar probe volume, and therefore the amount of spatial averaging, changes depending on where in the scan pattern the lidar is measuring. Consequently, lidar range weighting could produce artificial trends in the turbulence statistics that vary depending on the distance from the turbine rotor. Regardless, the changing turbulence trends close to the rotor are believed to be caused by rotor induction. First of all, the probe volumes of lidars 1 and 2 are relatively large in this region, which should cause some amount of reduction in measured turbulence, yet the measured v and w component turbulence intensities close to the rotor increase rather than decrease. Moreover, the rapid nature of the decrease in u component standard deviation close to the rotor at $y = 0$ and

y = -4.5 m is unlikely to be caused solely by the increasing lidar probe volumes.

A.4 Conclusions

In this appendix, results from lidar measurements of the upstream induction zone of a 27 m rotor diameter Vestas V27 wind turbine were presented. In contrast to the majority of previous wind turbine induction zone studies, which have focused on finding the velocity deficits that are present far upstream (2–3 D) of the turbine, this investigation focused on the region of the induction zone close to the turbine (within 1.5 rotor diameters). Whereas the previous lidar-based induction zone studies discussed here relied only on line-of-sight velocities from nacelle lidars, this work was performed with three scanning ground-based lidars so that the three components of the wind could be detected. The experimental setup was designed to minimize instances when the lidars measure close to perpendicular to the wind direction, where it is difficult to estimate the very small velocity magnitudes, as well as to minimize the lidar focus distances and thus the amount of volume averaging due to range weighting. To help achieve these objectives, only wind speeds upstream of one half of the rotor plane were measured. The results of the investigations showed that the reductions in the mean longitudinal wind speed in the induction zone due to rotor induction increase as the turbine's axial induction factor increases. The radial component of wind becomes non-zero near the edge of the rotor due to the expansion of the wind inflow around the rotor disk present in actuator disk theory. The relative magnitude of the radial component increases as the axial induction factor increases as well. No significant change in the mean tangential wind component (equivalent to the vertical component for the horizontal plane scan at hub height) was detected upstream of the turbine. Measurements of the wind speed time series upstream of the turbine reveal a general decrease in the longitudinal component turbulence standard deviation close to the rotor and an increase in the radial component standard deviation, while the tangential component standard deviation is relatively unchanged. Very close to the rotor plane, high frequency turbulence components are added to the wind speeds, likely caused by the periodic induction effects due to blade passage.

The conclusions drawn in this study relied on measurements upstream of half of the rotor and it was assumed that velocity reductions and radial wind speeds are similar on the other half of the rotor. Future investigations including measurements across the entire rotor disk would be useful to verify this assumption. Additionally, although the range weighting, inherent in all lidar technologies, was minimized through the choice of lidar positions, it is possible that the volume averaging present in the measurements as well as the uneven volume averaging across the scan patterns somewhat influence the results. Finally, future investigations using CFD to simulate the induction zone of the V27 turbine would be of interest for comparison with the lidar measurements presented in this work.

Acknowledgements

The measurement campaign described in this appendix was performed in conjunction with Nikolas Angelou, Prof. Torben Mikkelsen, Dr. Mikael Sjöholm, and Prof. Jakob Mann from DTU Wind Energy. Per Hansen, Claus Brian Munk Pedersen, and Kasper Hjorth Hansen, also from DTU Wind Energy, are acknowledged for their invaluable assistance deploying, operating, and troubleshooting the lidar system during the measurement campaign. Financial support from the Danish Agency for Science, Technology and Innovation through Grant 2136-08-0022 for support to the Danish research infrastructure facility WindScanner.dk (http://www.windscanner.dk) is gratefully acknowledged. Further support for this work was provided by NREL as well as by a Fulbright US Student Program fellowship administered through the Danish-American Fulbright Commission.